DEPARTAMENTO DE FÍSICA TEÓRICA Y DEL COSMOS

Universidad de Granada

ANALYSIS OF THE BRIGHT GALAXY POPULATION IN THE CORE OF CLUSTERS OF GALAXIES AT MEDIUM REDSHIFT

Begoña Ascaso Anglés

Memoria de Tesis

presentada en la Universidad de Granada

para optar al grado de Doctor en Astrofísica.

Director de la Tesis

Prof. Mariano Moles Villamate

INSTITUTO DE ASTROFÍSICA DE ANDALUCÍA-CSIC

Junio-2008

A mis padres

Lo mejor para la tristeza -contestó Merlin, empezando a soplar y resoplar- es aprender algo. Es lo único que no falla nunca. Puedes envejecer y sentir toda tu anatomía temblorosa; puedes pemanecer durante horas por la noche escuchando el desorden de tus venas; puedes echar de menos a tu único amor, puedes ver al mundo a tu alrededor devastado por locos perversos; o saber que tu honor es pisoteado por las cloacas de inteligencias inferiores. Entonces sólo hay una cosa posible: aprender. Aprender por qué se mueve el mundo y lo que hace que se mueva. Es lo único que la inteligencia no puede agotar, ni alienar, que nunca la torturará, que nunca le inspirará miedo ni desconfianza y que nunca soñará con lamentar, de la que nunca se arrepentirá. Aprender es lo que te conviene. Mira la cantidad de cosas que puedes aprender: la ciencia pura, la única pureza que existe. Entonces puedes aprender astronomía en el espacio de una vida, historia natural en tres, literatura en seis. Y entonces después de haber agotado un millón de vidas en biología y medicina y teología y geografía e historia y economía, pues, entonces puedes empezar a hacer una rueda de carreta con la madera apropiada, o pasar cincuenta años aprendiendo a empezar a vencer a tu contrincante en esgrima. Y después de eso, puedes empezar de nuevo con las matemáticas hasta que sea tiempo de aprender a arar la tierra."

Terence White, 'The Once and Future King'

Acknowledgements

A lo largo de esto cuatro años de doctorado, además de realizar una tesis, he tenido la ocasión de conocer y trabajar con muchísimas personas. Muchas de ellas, son hoy las responsables de que esta tesis se haya llevado a cabo por una infinidad de motivos que voy a intentar resumir.

En primer lugar, quiero agradecer a las personas que han hecho posible que mi sueño de trabajar en Astrofísica haya sido posible. A Mariano Moles, mi jefe, y la persona que me brindó la oportunidad de hacer un doctorado en Astrofísica y a mis dos jefes 'adoptivos', Alfonso Aguerri, quien en mi etapa inicial del doctorado puso a mi disposición gran parte de su tiempo y sus conocimientos, enseñándome a ser rigurosa y metódica en la Ciencia y a Txitxo Benítez, quien en mi etapa final, me ofreció la oportunidad de trabajar con él y su equipo en Estados Unidos, me dió el privilegio de intercambiar todo tipo de ideas científicas y siempre fue raudo en prestarme su apoyo y sus consejos. Millones de gracias.

Seguidamente, debo mi agradecimiento a otras tres personas por su ayuda directa con el trabajo de esta tesis. Jesús Varela, quien con paciencia y amabilidad, siempre estuvo dispuesto a ayudarme a solventar cualquier pequeño detalle que pudiera surgir con el tratamiento de los datos y fue una fuente de inspiración para seguir muchos de sus pasos. Ruben Sánchez-Janssen, por sus pacientes lecciones de IDL y sus valiosos comentarios y Jairo Méndez-Abreu por el enorme trabajo de calidad realizado en en análisis de brillo superficial.

Aussi, je suis très reconnaissant à Chantal Balkowski, qui m'a fait sentir à la maison dans mon étape à Paris et má encouragé à interagir et de discuter de nombreux sujets astrophysiques. Thanks a lot to Holland Ford too, who let me collaborate with him and his group and gave me many good pieces of advice during my stage in Baltimore. Gracie mille to Daniella Bettoni and Giuseppe Galletta, for leading me in my first steps in Astrophysics, not only during my stage in Padova but with my first observations in La Palma. Asímismo, nunca dejaré de agradecer a una de las personas que me dió el lujo y la oportunidad de aprender a su lado, me introdujo en la Astrofísica y me dió la llave para continuar después, Guillermo González-Casado.

Por otra parte, quiero agradecer a esas personas que hemos coincidido en Granada y que me han prestado su apoyo en cualquier momento difícil y su sonrisa en cualquier otro. En primer lugar, a Carlos Barceló, desde la primera semana uno de mis pilares granainos, un buen amigo y una de las personas más sabias del mundo. Gracias, mozo, por todos los consejos, el apoyo y las laaaargas conversaciones sobre la vida, la cosmología, la filosofía y cualquier cosa que se nos viniera a la cabeza.

A Silbieta López de Lacalle, una de las personas más honesta que he conocido a lo largo de mi vida, y que me ha brindado la oportunidad de ser su amiga. Gracias por todo, día tras día, conversación tras conversación, risa tras risa, bajón tras bajón, paseo tras paseo. A Cristiñiña Rodríguez, que su ejemplo de esfuerzo continuo y su apuesta por un sueño, me han dado fuerza en muchas ocasiones para seguir adelante. Además, un placer arreglar el mundo cuando éste se nos venía encima, y volver a levantarlo, y volver a sonreír. Graciñas. A Emilio García, un cielazo siempre dispuesto a ayudarme en cualquier momento, ya sea empollándose los paquetes de Fortran para explicármelos luego, con una palabra de ánimo en el momento justo o con un muñequito de la suerte. Mil gracias también por hacer de los meses de escritura mucho más llevaderos.

A Geli Martínez y Omaira González, por todos los momentos que caben en estos cuatro años y la suerte de haber compartido piso, despacho(s), nombres falsos (Yenni, Monica y Sofía) y muchas cosas más con ellas. Gracias por todos los ánimos, cables, plastilina y muchos etcéteras prestados. A Susi Vidal, esa personita que aún tarde nos dimos cuenta que estábamos hechas de material muy parecido, y disfrutamos de todo ello. A David Orozco, una ayuda de IDL andante eternamente despistado. A Yoli Jimenez, por sus 'claridades', que han hecho esfumar cualquier 'bulto' que se infiltrara por el camino y por su admirable tenacidad, que me ha servido de ejemplo en numerosas ocasiones. Infinitas gracias, quilla. A Gabriella Gilli, por lo bien que me sientan esos paseos Albayzineros o en cualquier lugar del mundo, que hayan muchos más.

También quiero agradecer a Pepa Masegosa, Isabel Márquez y Chony del Olmo por ayudarme a entender que si no hubiera bajadas no habría subidas en el camino. Gracias guapas. A Jaime Perea por sus valiosas indicaciones sobre cualquier asunto informático. A Juande, por estar siempre dispuesto a echar un cable, de cualquier tipo, desinteresadamente, y en cualquier momento. A Antxon Alberdi, por esa honestidad combinada siempre con una palabra amable para Carmencita. A Lucas Lara, por haber sido un ejemplo de ilusión y entusiasmo en todos los aspectos. A Benja Montesinos, por esos ánimos y esa buena memoria. A Jose Luis Jaramillo, por todas las largas conversaciones sobre ciudades remotas o granadas. Y a todos y cada uno de los becarios, gracias por todos los buenos ratos que hemos pasado.

Cómo no, a Silvia y a Carmen, por enseñarme a vivir al 100% y a saber apreciar lo que es realmente importante de manera definitiva. Mi gratitud también a Simon Verley, quién desinteresadamente, me ofreció su apartamento en Paris, con vistas a la Torre Eiffel, y él, junto con su familia, me trataron como una más de su familia haciendo de Paris uno de los mejores períodos de mi vida. Y a Vic Serey y Nacha Echevarría, quienes me acogieron, me cuidaron y me trataron tan bien, en mi estancia en Baltimore. Gracias por el mapa tan genial con las zonas chungas de Baltimore y por las buenas conversaciones, la buena música, y los buenos momentos.

Por último, he de agradecer a todos mis amigos que aunque estén fuera de Granada, me siguen apoyando en cualquiera de mis empresas y que han permitido conservar nuestra amistad a pesar de la distancia.

A mis clavelinas oscenses: Aneta O., Cristifina, Blanquita, Mariajo, Jareta C, Marieta G., Maria S., Patri, Jareta S., Aneta B., Beita, Marcus, Vane, Eva.. por llenar mi vida de alegría continua, de amparo, de buenos consejos, de risas, juergas cubiteras, de San Lorenzos increíbles, y también por hacerme partícipe de vuestras penas e ilusiones. En concreto a Patricia, por esas largísimas conversaciones que nunca acabamos, y que me tanto bien me hacen.

Al meus primitivos (i allegados) barcelonins: Gemma, Laia, Meritxell, Gemmita, Maria, Miquel, Tito, Pau, Rut, Ferran, Francesc, Aly, Marc, Marcel, Helena, Eva, Joan, Arruebo, Àngel, M. Carmen, Beto... merci per ser així. Ja sabeu la meva teoría sobre la formació definitiva de cadascú. Jo estic segura que tots estem fets de la mateixa pasta i m'encanta. Gràcies. A Gemmita, en particular, per obligar-me a ser feliç definitivament i donar-me el millor dels consells.

A Núria Font, per la seva força i el seu empeny de ser feliç. A Pere Pascual, por haberme animado a hacer el doctorado y haber sido mi 'padre adoptivo' durante los años de facultad, a la vez que un amigo. A Ade La Sierra, por todos las palabras de ánimo regaladas desde siempre. A los Agripinos oscenses, en especial a Elena Alayeto, por esos tropecientos años que llevamos arreglando el mundo y a Jorge Vidal, por el ímpetu que le pones a la vida. A Lloi Burdalo, por tener siempre la mesa del cafetín lista para un café. A Manu, por esos largos mails llenos de luz y fuerza, y por todos los lazos de lana rojos diseminados por el mundo. A Maca, por toda la fuerza, ánimos, ejemplo y alegría que me ha proporcionado desde que nos conocemos.

Finalmente, a mis padres, Leoné y Carmencita y mi a hermana y 'cuñao', Magda y Albert. Millones de gracias por respetar y apoyar cada una de mis decisiones, por estar siempre, inquebrantablemente allí y por haber sido el mejor de los ejemplos de esfuerzo, tenacidad, alegría y sabiduría. Os quiero.

Y, a todos aquellos que estos años han pasado a ser parte de mi vida, no los cito, porque afortunadamente, son muchos, pero no les olvido.

Contents

List of Figures

List of Tables

Part I

Introduction

Resumen

Yo deshojé las constelaciones, hiriéndome,
afilando los dedos en el tacto de estrellas,
hilando hebra por hebra la contextura
helada de un castillo sin puertas,
oh estrellados amores cuyo
jazmín detiene su transparencia en vano.

Pablo Neruda, 'El hondero. Canto General. Yo Soy.'

Partiendo de los datos de cinco cúmulos de galaxias en un rango de *redshift* de $0.18 \leq z \leq 0.25$, observados con el *Nordic Optical Telescope (NOT)* en muy buenas condiciones de *seeing* por una parte, y datos de cinco cúmulos de galaxias más en un rango de *redshift* de $0.17 \leq z \leq 0.39$, observados con la *Advanced Camera of Surveys (ACS)* en el $\approx Mpc^2$ central, hemos realizado un análisis exhaustivo de su población galáctica brillante. Este rango de *redshift*, en el que solo se dispone una pequeña cantidad de datos de calidad, con la resolución adecuada, es particularmente importante para el entendimiento de la formación y evolución de los cúmulos de galaxias.

Hemos inspeccionado la relación color-magnitud (CMR) para estos cúmulos y hemos medido la fracción de galaxias azules en sus núcleos para buscar evidencia de evolución, como la que se ha encontrado en otros trabajos. Además, se ha realizado la clasificación visual de la morfología de las galaxias y se ha examinado la relación morfologia-radio. Además, hemos analizado también los perfiles de brillo superficial, estudiando los parametros estructurales que se derivan y la función de luminosidad también se ha ajustado dando resultados fiables para este rango de *redshift*. Finalmente, hemos explorado las principales características de las galaxias más brillantes de los cúmulos (BCGs).

La pendiente de la CMR aparece prácticamente constante hasta *reshift* $\sim$ 0.4 y en acuerdo con los valores de la pendiente a *redshift* más alto. No hemos encontrado signos de evolución con *redshift* ni en la pendiente de la CMR, ni en la fracción de galaxias azules, o en la Función de Luminosidad. Estos resultados

están a favor de que el contenido estelar de las galaxias en nuestros cúmulos ya estaban asentados a z $\sim$ 0.2.

Se ha encontrado una diversidad de situaciones en cuanto a la mezcla morfológica. La fracción de galaxias en interacción en los cúmulos parece que es mayor que en cúmulos como Coma, aunque el número de cúmulos en la muestra es pequeño para dar conclusiones definitivas.

En cuanto a los parámetros estructurales de la población galáctica, las galaxias ajustadas con una componente de Sersic presentan una dicotomía para la población roja y azul, obteniendo valores $2 \leq n \leq 4$ para las galaxias rojas y $n \sim 1$ para las azules. Hemos encontrado parametros estructurales del bulbo similares a los que se encuentran en el cúmulo de Coma. Aunque las escalas de los discos en nuestra muestra y en las galaxias de campo se han detectado que son estadísticamente diferentes de las del cúmulo de Coma, lo que indica mayores escalas de discos a este rango de *redshift*.

Finalmente, BCGs encontradas en cúmulos más ricos parecen tener un alto nivel de homogeneidad en cuanto a su luminosidad, mientras que para el resto, parece ser necesaria una corrección de riqueza. Su brillo superficial, por el contrario, no se muestra tan homogéneo como su luminosidad.

Abstract

Using data of five clusters of galaxies within the redshift range $0.18 \leq z \leq 0.25$, imaged with the Nordic Optical Telescope (NOT) in very good seeing conditions on one hand, and data of five more clusters of galaxies within a redshift range of $0.17 \leq z \leq 0.39$ imaged with the Advanced Camera of Surveys (ACS) in the central ≈ 1 Mpc^2, we have performed an exhaustive inspection of their bright galaxy population. This range of redshift, where only a small amount of data with the required resolution and quality is available, is particularly important for the understanding of the formation and evolution of clusters of galaxies.

We have inspected the color-magnitude relation (CMR) for these clusters and measured the blue fraction of galaxies in their cores to check for evidence of evolution as found in other works. Moreover, the visual classification of the galaxy morphology has been performed and the morphology-radius relation has been examined. Additionally, we have also analyzed the surface brightness profiles, studying their derived structural parameters and the luminosity function has been also fitted providing reliable parameters for this range of redshift. Finally, we have explored the main characteristics of the Brightest Cluster Galaxies (BCGs).

The slope of the CMR appears nearly constant up to redshift ~ 0.4 and in agreement with the slope values found at higher redshift. We have not found any signs of evolution with redshift neither in the slope of the CMR, nor in the blue fraction of galaxies or even in the Luminosity Function. These results support the view that the stellar content of the galaxies in our clusters have been already settled at $z \sim 0.2$.

A diversity of situations regarding the morphological mixing has been noticed. The fraction of interacting galaxies in the clusters appear to be larger than in clusters like Coma although the number of clusters in the sample is small to give a definitive conclusion.

Regarding to structural parameters of the galactic population, one Sersic component galaxies show a dichotomy for the red and blue galactic population, obtaining $2 \leq n \leq 4$ values for red galaxies and $n \sim 1$ for blue galaxies. We have also found bulge structural parameters similar to those found in Coma Cluster. However, disc scales in our sample and in field local galaxies have been detected to be statistically different from those in Coma Clusters, which goes in the sense of larger disc galaxies at this range of redshift.

Finally, BCGs found in richer clusters seem to have a high level of homogeneity regarding to their luminosity, while for the rest, a correction richness need to be performed. Their surface brightness, instead, have been shown not to be so homogeneous as their luminosity,

Chapter 1

Introduction

Recordo una nit, a l'altra banda del Pirineu,
que sortí de la fosca una nena que cantava amb veu de fada.
Vaig demanar-li que em digués quelcom en la seva llengua pròpia
i ella, tota admirada, signà'l cel estrellat i féu només així:
'Lis esteles...'

Joan Maragall, 'Elogi de la Paraula Viva'

To wonder about our origins is an inherent characteristic of humanity. Who we are, what we are doing here, how the world around us is, how the Universe in which we are embedded is, what all the infinity of points up there are, etc... At the end of the XX century, people in the world seemed to forget about that, as the skies were not clear anymore and everytime is more and more difficult to find a piece of clean sky.

It is however, in this century, when the greatest steps for understanding our Universe, outside our local Solar System, have been performed. Between 1920 and 1924, Edwin Hubble proved that Andromeda nebula was a Galaxy and that, many point of lights were huge stellar universes, placed much farther than our own Galaxy, the Milky Way. With the development of the photography and the building of more powerful telescopes, the Galaxies were observed to move away from each other with a velocity that was proportional to their distances, as well as they increased, at the same time, the size of the Universe.

At present, the Astrophysics has experimented a stunning progress thanks to the development in the last decades of observational resources (spacial telescopes, like Hubble Space Telescope (HST), XMM-Newton, Chandra...) and calculus tools (simulations with more and more powerful computers). We are living an astonishing era of discoveries. The Humankind realizes about its smallness, day after day.

This thesis is based on one of the most exciting structures in the Universe: Clusters of Galaxies. It is entitled *Analysis of Bright Galaxy Population in the Core of Clusters of Galaxies at medium redshift.* Throughout this introduction, we have elaborated a historical and conceptual motivation of the objects we are going to study in this thesis.

1.1 Clusters of Galaxies

Cluster of galaxies are the largest structures, gravitationally bounded, in the Universe, with sizes of several Mpc and masses from $10^{14} - 10^{16}$ $M_{\odot}$. They are composed by many to thousand galaxies and millions of stars. Clusters are usually formed by a core, where the highest concentration of galaxies are found. Moreover, between the galaxies, a **plasma or gas** composed mainly by ionized hydrogen exits, which is detected due to its X-ray emission. In addition, studies of gas and galaxy dynamics in cluster show that the largest part of these systems is distributed continously, througout the region occupied by gas and galaxies. This component, known as **dark matter** does not emit any kind of electromagnetic radiation (but possible, γ-rays from neutralino annihilation) and it is only interacting gravitationally with gas and galaxies, forming the **halo**.

Prior to 1949, only a few dozen clusters were known. In the fifties and early sixties, the first catalogues of hundreds to thousands of clusters were published (Zwicky, 1951; Zwicky et al., 1953, 1956; Abell, 1958). In particular, two main catalogs of rich clusters of galaxies established the definitive criteria for the present definition of a cluster: the catalog of rich clusters by Abell (1958) and the Catalogue of Galaxies and Clusters of Galaxies by Zwicky et al. (1961). Both authors identified clusters on the Palomar Sky Survey plates.

Abell catalogue lists 2712 clusters in the redshift range $0.02 \leq z \leq 0.2$. He set some requirements for including the clusters in his catalogue regarding to their richness, compactness or galactic-latitude. On the other hand, Zwicky catalogue contained more clusters and also systems that are less rich than those of Abell, as he set less strict criteria concerning their properties.

Different classifications schemes for clusters were developed in the early seventies. Rood & Sastry (1971) classified clusters according the distribution of the ten brightest members, the so called **Rood-Sastry (RS) classification**. The **Bautz-Morgan (BM) classification system** was introduced by Bautz & Morgan (1970) who based this on the relative contrast of the brightest galaxy to the other galaxies in each cluster. In addition, Morgan (1962); Oemler (1974) introduced the classification of clusters according to the morphological type of their bright members.

A number of fenomena is produced in clusters of galaxies. They are real laboratories to study processes such as **Gravitational Lensing** (Tyson & Fischer, 1995; Kneib et al., 1996; Broadhurst et al., 2005b; Diego et al., 2005). Also,

theoretical studies about modeling their dark matter halo density profiles can be tested on clusters of galaxies (Navarro et al., 1995; Łokas & Mamon, 2001; Ascaso & González-Casado, 2003) or even in dwarf galaxies (Burkert, 1995).

Additionally, clusters of galaxies are potential candidates to produce irregularities in the Cosmic Microwave Background (CMB) through the **Sunyaev-Zel'dovich (SZ) effect** (Sunyaev & Zeldovich, 1970, 1972; Bonamente et al., 2006; Ascaso & Moles, 2007). At present, a number of studies (Uyaniker et al., 1997; Tsuboi et al., 1998; Lieu, Mittaz & Zhang, 2006; Bonamente et al., 2006; LaRoque et al., 2006; Morandi, Ettori & Moscardini, 2007; Hashimoto et al., 2007; Morandi, Ettori & Moscardini, 2007; Zemcov et al., 2007), have detected an analyzed this signal in X-ray massive clusters, providing constraints on the values of the cosmological parameters of our universe.

The shape of clusters of galaxies is the result of the initial conditions on the formation and subsequent evolution of the galaxies contained in them, as well as the interaction with the environment. Up to date, numerous studies have been devoted to the formation of clusters of galaxies. However, two main scenarios for its clarification still remain. On one hand, we have the monolithic collapse scenario in which the clusters were formed first in a single event through the gravitational collapse of a cloud of primordial gas, very early in the universe (Bower, Kodama & Terlevich, 1998), and on the other, we have the hierarchical merging scenario (Kauffmann, Guiderdoni & White, 1994; De Lucia & Blaizot, 2007b), in which the galaxies were formed at the outset and were gradually assembled through multiple mergers of smaller subgalactic units.

The monolithic scenario implies that the galaxies of different morphological types are born intrinsically different and are not suffering substantial transformations after the cluster collapse (Merritt, 1984) while the hierarchical scenario would imply that galaxies end up as spiral or elliptical galaxies depending on their merger history and that the environmental effects and interactions are transforming the galaxy population due to mechanisms that were operational until recent epochs, such as harassment (Moore et al., 1996), gas-stripping (Gunn & Gott, 1972; Quilis, Moore & Bower, 2000), starvation (Bekki, Couch & Shioya, 2002), or merging (Gerhard & Fall, 1983; Aguerri, Balcells & Peletier, 2001; Eliche-Moral et al., 2006). Likewise, the evolution of the galaxy population in clusters of galaxies has been broadly studied in many works.

Attempts to discriminate between the two models have focused mostly on elliptical galaxies. Present-epoch elliptical galaxies have been selected to be a very homogeneous family with very similar intrinsic properties. Compared with the heterogeneous family of spiral galaxies, elliptical ones in the local universe have been found to have little or no dust, gas, and star formation activity (Roberts & Haynes, 1994).

Moreover, the stellar population of elliptical galaxies is mostly as old as the universe, with very similar relative ages. This fact is responsible for the most distinctive property of ellipticals: their color. Elliptical galaxies are the reddest galaxies in the local universe (Roberts & Haynes, 1994).

Indeed, the Color-Magnitude Relation for elliptical galaxies was already noticed in a earlier work by Baum (1959). Later on, Rood (1969) analyzed data from the center of the Coma Cluster, where the tendency found was that more luminous galaxies present redder colors. Some years later, Visvanathan & Sandage (1977); Visvanathan & Griersmith (1977) showed the Universality to this relation for Early-types (E and S0) and Early Spirals.

One of the best studied subjects regarding the galactic population in galaxies has been the evolution of the slope of the color-magnitude with redshift in clusters of galaxies (van Dokkum & Franx, 1996; Kelson et al., 1997; Ellis et al., 1997; Andreon, Davoust & Heim, 1997; Bender et al., 1998; López-Cruz, Barkhouse & Yee, 2004; Mei et al., 2006; Driver et al., 2006; De Lucia et al., 2007a). As we are going to discuss throughout this thesis, this slope appears to be constant up to redshift z $\sim$1 at least. As a consequence, this results suggests that the formation of the stellar population in early-type galaxies in clusters ocurred before z=1. This feature is very interesting in itself because it gives information about the metallicity and age of the galaxy population (Kodama, 1999).

Another attribute that is considered in the context of the evolution of clusters of galaxies is the blue fraction of the galaxy population in clusters. In the early work by Butcher & Oemler (1984), an increase of this blue fraction with redshift was found for clusters up to redshift ≈ 0.5. That fact indicates that the galaxy population would be evolving. However, as shown by Aguerri, Sánchez-Janssen & Muñoz-Tuñón (2007), this variation would happen only for some redshift range. They studied a large sample of SDSS clusters up to redshift $z \leq 0.1$ and did not see any significant change of the blue fraction with the redshift. Therefore, exploring the next redshift range, $0.1 \lesssim z \lesssim 0.3$, would be relevant to clarify the situation. In particular, since several works have explored and noticed the Butcher-Oemler effect with samples of clusters at lower (De Propris et al., 2004) and higher (De Lucia et al., 2007a) redshift.

The Morphology-Density relation in clusters of galaxies has also been widely explored (Dressler, 1980; Dressler et al., 1997). At the beginning of the XX century, Curtis (1918); Hubble & Humason (1931) already observed that early-type galaxies were more concentrated in denser regions. Later on, Oemler (1974); Melnick & Sargent (1977); Dressler (1980) discovered a dependence with the distance to the center of the fraction of lenticular and spiral galaxies, the so-called morphology- density relation. The extension of this relation to higher redshift was performed by Dressler et al. (1997); Postman et al. (2005), obtaining this relation but only for more compact and regular clusters and with lower density of elliptical galaxies.

Additionally, the Luminosity Function in clusters of galaxies, in contrast with the Field Luminosity Function has been extensively studied. After several attempts to give a reasonable analytical function that describes the luminosity function (Hubble & Humason, 1931; Abell, 1958; Zwicky et al., 1961) basing them on their empirical behaviur, the concluding description was given by Schechter (1976). The matter regarding to the universality of the Luminosity

Function has been deeply explored. A number of studies give support to this assumption (Dressler, 1978; Lugger, 1986; Colless, 1989; Gaidos, 1997; Yagi et al., 2002; De Propris et al., 2003a) while, many other works argue the contrary (Godwin & Peach, 1977; Dressler, 1978; Binggeli, Sandage & Tammann, 1988; Piranomonte et al., 2001; Hansen et al., 2005; Popesso et al., 2006; Barkhouse, Yee & López-Cruz, 2007). We have found in this work, that the LF does not seem to be universal but some trends regarding to the color of the different galactic population seem to be present.

Few works have been dedicated to study the morphology of the galaxy population at z$\approx$ 0.2. The morphological studies have been generally confined to rather local samples, in part due to the need of establishing a visual classification (Dressler, 1980; Fasano et al., 2000), and more generally, to the difficulties to get deep and high-resolution images for relatively large fields. Some of these studies have tried to establish an automatic morphological classifications by inspecting the galaxies surface brightness and their main structural parameters. Nevertheless, those samples have often been preselected to be only late type (de Jong, 1996; Graham & de Blok, 2001), or early type (Graham, 2003). As a consequence, the present number of clusters that have been studied in that redshift range is small (Fasano et al., 2000; Trujillo et al., 2001c; Fasano et al., 2002).

An additional advantage of studying clusters of galaxies is that we can consider that all the galaxy population remains at the same distance as the cluster sizes are much smaller than the distance at which they are found (with the exception to the more local ones). Thanks to that, the galactic population in clusters of galaxies were analyzed, providing relations between physical parameters for different morphological types that otherwise, it would be much more complicated to get to know.

Among these discoveries, we stand out the **Faber- Jackson relation** (Faber & Jackson, 1976), which gives a relationship between the luminosity and central stellar velocity dispersion of elliptical galaxies, the **Tully-Fisher relation** (Tully & Fisher, 1977), that shows correlations for spiral galaxies between luminosity and rotation velocity, **the Fundamental Plane** (Djorgovski & Davis, 1987; Dressler et al., 1987) that set constraints between surface brightness, radius and velocity dispersion or the already commented **Color-Magnitude relation** (Visvanathan & Griersmith, 1977).

On the other hand, one of the objects that deserve great interest at studying clusters of galaxies are the **Brightest Cluster Galaxies (BCGs)** as their origin is thought to be closely connected to the formation of the cluster. BCGs are the most luminous and massive galaxies in the universe. They are usually placed close to the center of its host cluster and seem to be aligned with the cluster galaxy distribution. As a consequence, they have been suggested to lie at the bottom of the cluster's gravitational potential well.

The typical characteristics of the BCGs can be summarized as elliptical galaxies that are much brighter and much more massive than the average, with luminos-

ity's $\approx 10L_*(L_* = 1.0 \times 10^{10}h^2L_\odot)$ (Schombert, 1986; Dubinski, 1998; Seigar, Graham & Jerjen, 2007), with very little rotational support and central velocity dispersions around $\approx 300 - 400kms^{-1}$ (Fisher, Illingworth & Franx, 1995).

BCGs have been shown not to be extracted from the same luminosity distribution as the Schechter luminosity function for the rest of the galaxies, as it has been shown in this thesis. As in clusters of galaxies, two main theories remain to explain the formation of the BCGs.

The hierarchical simulations of BCG formation performed by De Lucia & Blaizot (2007b) suggested that the stellar population in BCGs were formed nearly at z ~ 5 to 3. On the other side, a number of observations indicates that BCGs were formed at high redshift and have been passively evolving to the now (Bower, Lucey & Ellis, 1992b; Aragon-Salamanca et al., 1993; Stanford, Eisenhardt & Dickinson, 1998; van Dokkum et al., 1998).

In addition, these objects has been set as candidates to 'standard candles' for the measurement of cosmological distances (Sandage, 1972a,c; Gunn & Oke, 1975; Hoessel & Schneider, 1985; Lauer & Postman, 1994; Postman & Lauer, 1995). In fact, one of the most studied subjects in the literature is the increase of the number of observed BCGs in the K-band Hubble Diagram, (Aragon-Salamanca, Baugh & Kauffmann, 1998; Collins & Mann, 1998; Burke, Collins & Mann, 2000; Brough et al., 2005), achieving a dispersion of 0.3.

Additionally, although many attempts have been devoted to model the surface brightness of these objects (Schombert, 1986; Graham et al., 1996; Lin & Mohr, 2004; Seigar, Graham & Jerjen, 2007), this matter is still not solved. In this thesis, we have shown that a diversity is manifest as far as the best model of the surface brightness is concerned.

Although a remarkably homogeneity in luminosity of the BCGs is evident, a great amount of these studies have been performed by selecting very rich and massive clusters. In fact, in this thesis, we have shown that if we consider BCGs belonging to poorer clusters or less massive, the dispersion increases. These facts seem to indicate that a richness correction, as already stated by Sandage, Kristian & Westphal (1976); Kristian, Sandage & Westphal (1978); Postman & Lauer (1995), is necessary to consider these objects as 'Standard Candles'.

In this thesis, we have widely analyzed a great number of the properties regarding to the galactic population in our sample of medium redshift clusters. We have aimed to study the degree of variance of their properties and their evolution with redshift by comparing the results found in with lower and higher redshift samples.

1.2 Motivations and Aims of the thesis

This thesis collects a complete study performed in a sample of ten clusters of galaxies at medium redshift (z $\approx$ 0.2-0.25). Clusters of galaxies are great structures with largest concentration of galaxies in similar environment, providing an ideal frame to study the behavior and characteristic of the galactic population. In particular, the main motivations for the study of these particular objects are the following.

A small number of analyzed clusters in this medium range of redshift up to date is found (Fasano et al., 2000; Trujillo et al., 2001c; Fasano et al., 2002). This fact is due to difficulties in the depth and quality of the observations.

With the advent of spatial telescopes, the number of clusters imaged at higher and higher redshift has grown but that range of redshift continues being overlooked. However, we think that this range of redshift can be specially interesting and surprising as far as the examination of the speed of the evolution of the galaxies' features is concerned. The study of the cosmic evolution or the properties of clusters of galaxies and their variance with redshift is a basic point for understanding the origin and formation of these objects, and likewise, the Universe.

Throughout this thesis, we have adopted the standard ΛCDM cosmology with H_0=71 km s^{-1} Mpc^{-1}, Ω_m=0.27 and Ω_Λ=0.73.

1.3 Brief description of the thesis chapters

In this thesis, we have structured the contents into four parts. The first part is devoted to the introduction of the general subjects we have worked, together with a presentation of the sample of clusters of galaxies we have analyzed and an explanation of the reduction and calibration process of this sample set.

The second part is dedicated to the analysis of the main characteristics of the bright galaxy population in the central part of the clusters samples. It comprises five Chapters. Chapter 3 studies the Color- Magnitude Relation and the Butcher-Oemler Effect, examining also their relation with the morphology. We have also compared the results we have found with samples at lower redshift.

Chapter 4 is dedicated to the Galaxy Visual Morphology. We have assigned morphological visual types to the galaxy population, checking that our classification corresponds statistically with the reported in the literature. Moreover, we have looked into the concentration parameter of the clusters in the sample that have enough coverage. Finally, we have examined the interaction degree in the sample by analyzing the tidal forces distribution.

The subsequent Chapter, 5 refers to the analysis of the surface brightness of the NOT galaxy population. We have previously performed several simulations in

order to check the best conditions for fitting the Surface Brightness of the galaxies. The final classification carried out by elaborating an algorithm that decides the best fit into one or two component model. Additionally, we have investigated into the derived bulge and disc structural parameters of the galaxies.

Further on, Chapter 6 describes the research performed in the spatial distribution of the sample. We have analyzed the local density and the radial distribution of the galaxies in our sample. Several relations have been examined, in particular, the Morphology-Density relation, or the Radius density relation.

Finally, the last Chapter in this part, Chapter 7 examines the analysis of the Luminosity Function by providing different methods for performing the fits. The Morphology and Color Luminosity Function have also been analyzed and consequently, we have attempted to extract conclusions about the Universality of the Luminosity Function.

The third part of the thesis is completely dedicated to the Brightest Cluster Galaxies or BCGs. We have detailed an algorithm for the extraction of the BCG from the cluster potential in the first part and subsequently, we have analyzed the main characteristics of the BCG population, regarding to the degree of dominance, morphology or surface brightness. We have dedicated the last part to the study of the identity of these objects as Standard Candles.

Finally, the last part is a compilation of the main conclusions of the work developed in the thesis, with a final remark on the future prospects.

The Annex contains four chapters. The first one Annex A, collects the catalogue of the galaxies detected in NOT sample. Annex B shows the information for the galaxies in NOT sample to analyze their surface brightness profile and finally, Annex C and D, gather the results of the extraction of the BCG for the NOT and ACS sample, respectively.

Chapter 2

Clusters Sample

Mercurio de rampas y hélices,
grumos de luna entre tensores y placas de bronce;
pero el hombre ahí, el inversor, el que da vuelta a las suertes,
el volatinero de la realidad:
contra lo petrificado de una matemática ancestral,
contra los husos de la altura destilando sus hebras
para una inteligencia cómplice,
telaraña de telarañas,
un sultán herido de diferencia yergue su voluntad enamorada,
desafía un cielo que una vez más propone las cartas transmisibles.

Julio Cortazar, 'Prosa del Observatorio'

In this Chapter, the observational cluster sample at medium redshift is described. The sample consists on ten clusters of galaxies within the medium redshift range $0.17 \leq z \leq 0.39$. On one hand, five of those clusters were imaged with the Nordic Optical Telescope (NOT) from the Ground and, hereafter, we will refer to them as the **NOT sample**. On the other hand, the other half of the sample consist on five more clusters imaged with the Advanced Camera of Surveys (ACS) in the Hubble Space Telescope (HST) and, we will allude to them as the **ACS sample**.

All the images are centered in the very central part or the core, covering the $\approx 1\ Mpc^2$, being somewhat smaller for the ACS sample. The NOT sample is complete up to $\approx M_r^* + 1$, while the ACS sample achieves the completeness at $\approx M_r^* + 3$. As a consequence, we will perform most of the work in the $M_r^* + 1$ magnitude range, except in some cases that we will take advantage of the good quality of the ACS data set.

This medium redshift galaxy cluster sample was elaborated in order to continue the exploration and establishment of the clusters properties in the immediately

following redshift range respect to local samples (such as Wide-Field Imaging Nearby Galaxy-Cluster Survey (WINGs) (Fasano et al., 2006), Sloan Digital Sky Survey (SDSS) (York et al., 2000)). This range of redshift ($0.15 \lesssim z \lesssim 0.4$) has been very little observed for a long time, due to technical limitations. They need a very good seeing quality to be observed from the Ground, to be able to resolve the galactic population inside the clusters, for example. In addition, the size of the CCD needs to be large enough to be able to sample a sustancial part of the cluster. With the advent of the Hubble Space Telescope (HST), those compromises were solved at the same time, as we will see in the ACS sample. However, the NOT sample is the first cluster sample at medium redshift, observed from the Ground with very good conditions of seeing.

2.1 Nordic Optical Telescope Cluster Sample

The first half of the sample consists on five galaxy clusters imaged at the 2.5m Nordic Optical Telescope (NOT). That Telescope is located at the Roque de Los Muchachos Observatory (La Palma, Canary Islands). The observations were taken from May to June 1995 with the Stand Camera whose field of view is $3^{'} \times 3^{'}$. This CCD has a plate scale of $0.176^{''}$/pix, a gain of 1.69 e^{-}/ADU and a readout noise of 6.36 e^{-}.

In Table 2.1, the information about the observed galaxy clusters is collected. Columns 1, 2,3 and 4 show the cluster name and the center obtained from the Nasa Extragalactic Data Base (NED)[1]. The redshift, Bautz-Morgan Type, Rood-Sastry type and Richness Class are listed in the four last columns, respectively.

Table 2.1: NOT Clusters Global Sample

Name	α(2000)			δ(2000)			z	BM type	RS type	RC
A 1643	12	55	54	+44	04	46	0.198	III	B	1
A 1878	14	12	49	+29	12	59	0.220	II	C	1
A 1952	14	41	04	+28	38	12	0.248	III	C	2
A 2111	15	39	38	+34	24	21	0.229	II – III	C	3
A 2658	23	44	58	−12	18	20	0.185	III	F	3

These clusters were selected from the catalogue by Abell, Corwin & Olowin (1989) to fulfill the requirements of being massive, apparently relaxed systems, with an intermediate richness class and high galactic latitudes to avoid problems with extinction.

[1]The NASA/IPAC Extragalactic Database (NED) is operated by the jet propulsion laboratory, California Institute of Technology, under contract with the national Aeronautics and Space Administration

The clusters were observed through two broad-band optical filters: Gunn-r (r) and Bessel B (B). In Table 2.2, the information about the observations is collected. The number of pointings observed for each cluster are indicated in column 1. These pointings cover different cluster areas which are showed in column 2. The third and fourth columns of the Table give the exposition time in the r and B filters respectively for the different clusters. The last column of the table shows the seeing of the images. The different areas covered were sampled as an effort to sample the whole cluster in a considerable part of the ≈ 1 Abell diameter. Due to the relative medium-redshift of those clusters, that aim was achieved. Note that all images were taken under photometric sky conditions and very good seeing (between 0.5 and $0.8''$).

Table 2.2: NOT Clusters Observations

Name	$\#Frames$	Area (Mpc) ^{2}	Exp Time(r) (s)	Exp Time(B) (s)	seeing ($''$)
A 1643	2	0.6810	600	900	0.55
A 1878	2	0.7894	600	600	0.7
A 1952	2	0.7989	900	900	$0.55 - 0.8$
A 2111	2	0.8030	600	900	0.7
A 2658	1	0.3055	600	1200	0.7

2.1.1 Comments on the sample

Given the scarce information on those clusters, we have gathered the few available literature, which refers, above all, to redshift data and the environmental situation of each of them.

A1643. The redshift of this cluster was given from the work by Humason, Mayall & Sandage (1956), who obtained a spectrum of the brightest galaxy in the area, finding z = 0.198. Our images were centered at that position, $\alpha(J2000)$=12h 55m 54.4s, $\delta(J2000)$= +44d 04m 46s. More recently, Gal et al. (2003) detected an overdense region centered at $\alpha(J2000)$=12h 55m 42.4s, $\delta(J2000)$= +44d 05m 22s, identified as a cluster designed by NSC J125542+440522. They have determined a photometric redshift of 0.2515. Both clusters do appear in our frames where we can identify A1643 as the one dominated by the galaxy observed by Humason, Mayall & Sandage (1956) and, therefore, at z = 0.198. This is the value we adopt in this work. We will exclude the frames that could be contaminated by the presence of NSC J125542+440522 in all the analysis regarding the galactic content of A1643. The area and number of frames values given in Table are already corrected.

A1878. This clusters appears with z = 0.254 in the NED. A closer inspection shows that there is another value given to a galaxy in the field, namely z = 0.222. Both redshift values come from Sandage, Kristian & Westphal (1976), who observed the brightest galaxy in the field, placed at $\alpha(J2000)$=14h 12m 52.13s, $\delta(J2000)$ = +29d 14m 29s, and another, fainter galaxy at $\alpha(J2000)$=14h 12m 49.13s, $\delta(J2000)$ = +29d 12m 59s. As quoted by the authors, the spectra were of low quality. The low z value corresponds to the brightest object that appears at the center of a strong concentration of galaxies that do correspond to the cluster catalogued as A1878. More recently, Gal et al. (2003), identified a cluster labeled as NSCJ141257+291256, with a photometric redshift z = 0.22. Its position and redshift value coincide with that of the bright galaxy observed by Sandage, Kristian & Westphal (1976) that is accepted here as the brightest galaxy of A1878.

A1952. The redshift attributed to this cluster, z = 0.248, also comes from the work by Sandage, Kristian & Westphal (1976) who observed the brightest cluster galaxy. The possible confusion regarding this cluster comes from the fact that the position given by Abell, Corwin & Olowin (1989), $\alpha(J2000)$=14h 41m 04.2s, $\delta(J2000)$= +28d 38m 12s, does not coincide with that of its Brightest Cluster Galaxy (BCG) as given by Sandage, Kristian & Westphal (1976), $\alpha(J2000)$= 14h 41m 03.6s, $\delta(J2000)$= +28d 36m 59.68s. To add to the confusion, Gal et al. (2003) detected a cluster designed by NSC J144103+283622, at almost exactly the position of A1952's BCG, but the redshift they have determined photometrically amounts to 0.2084. Taking all the information at hand, we consider that the cluster identified by Gal et al. (2003) is A1952, but the redshift we adopt here is that measured by Sandage, Kristian & Westphal (1976), z = 0.248. The analysis we present of the Color-Magnitude Relation in Chapter 3, supports this conclusion.

A2111. This cluster has the largest amount of information available in the literature of all the clusters in that sample. The redshift was established from spectroscopic observations by Lavery & Henry (1986). The center given by NED comes from the ACO catalogue given by Abell, Corwin & Olowin (1989), namely, $\alpha(J2000)$=15h 39m 38.3s, $\delta(J2000)$ = +34d 24m 21s. However, the subsequent analysis of the X-ray data by Wang, Ulmer & Lavery (1997); Henriksen, Wang & Ulmer (1999); Miller, Oegerle & Hill (2006), let them to conclude that the cluster center position is at $\alpha(J2000)$=15h 39m 40.9s , $\delta(J2000)$= +34d 25m 04s, only 5.04 kpc away from the Brightest Cluster Galaxy. Miller, Oegerle & Hill (2006) also provides a large number of spectra.

Interestingly, this cluster is thought to be a merger of two clusters due to the fact that the cluster contains a distinct comet-shaped X-ray subcomponent that appears hotter than the rest of the cluster Wang, Ulmer & Lavery (1997). Furthermore, the orientation between the two central major galaxies coincides with the elongation of both the galaxy and X-ray distributions. And also it has the distinction of being the richest cluster in the original Butcher & Oemler (1984) study. A2111 was also among the larger blue fraction clusters noted in Butcher & Oemler (1984), at f_b=0.16 $\pm$ 0.03.

A2658. This cluster is the only one from the sample that is observable from the South Hemisphere. The redshift of that cluster is set from Fetisova (1982). The center, as given by Abell, Corwin & Olowin (1989) is found at $\alpha(J2000)$ =23h 44m 58.8s, $\delta(J2000)$= -12d 18m 20s. However, our BCG is located at $\alpha(J2000)$=23h 44m 49.83s, $\delta(J2000)$= -12d 17m 38.93. After a visual inspection of the cluster image in the Digital Sky Survey, we conclude that the center of the cluster is given by the BCG, where a high concentration of galaxies is visually detected.

In Chapter 6, we will discuss the determination of the center of the cluster, giving the final coordinates in Table 6.3.

In the following sections, we are going to summarize the procedure for the reduction, calibration, (already performed by Fasano et al. (2002)), astrometrization of the clusters, and extraction of the sources.

2.1.2 Data reduction

At least two exposures for each field in both filters (r) and (B) were usually taken, allowing to clean-up the combined images for cosmic-rays and spurious events. Here, we sum up the basic steps of the data reduction process, following the procedure explained in Fasano et al. (2002).

The bulk of the data reduction of the images was achieved using standard IRAF tasks. The electronic bias level was removed from the CCD by fitting a Chebyshev function to the overscan region and subtracting it from each column. By averaging ten bias frames, a master bias per night was created and subtracted from the images in order to remove any remaining bias structure.

Dark images were also observed in order to remove the dark signal from the CCD. This correction turned out to be negligible, and was not considered. Additionally, twilight flats were taken at the beginning and at the end of every observing night. They were combined and used for removing the pixel-to-pixel structure of the images.

2.1.3 Calibration

The photometric calibration of the images was obtained by observing several standard stars from the Landolt (1992), Jorgensen (1994), and Montgomery, Marschall & Janes (1993) catalogues. They were observed every night at different zenith distances in order to measure the atmospheric extinction. The calibration constant was taken from Fasano et al. (2002).

Table 2.3 shows the calibration coefficients with their error in the r band for each cluster. As different clusters were observed different nights, the information in the log of the observations has been compiled to know which night a

particular galaxy cluster was observed. In the two first columns, the photometric zero points Z_c and the color coefficients C_c is set, the third column shows the extinction coefficients and the last column shows the calibration errors.

Table 2.3: Calibration Coefficients in NOT Clusters Sample

Name	Z_c	C_c	k_r	rms
A 1643	24.704 ± 0.004	0.085 ± 0.003	-0.128 ± 0.013	0.0222
A 1878	24.704 ± 0.004	0.085 ± 0.003	-0.128 ± 0.013	0.0222
A 1952	25.111 ± 0.005	0.117 ± 0.005	-0.088 ± 0.005	0.0232
A 2111	24.704 ± 0.004	0.085 ± 0.003	-0.128 ± 0.013	0.0222
A 2658	25.111 ± 0.005	0.117 ± 0.005	-0.088 ± 0.005	0.0232

2.1.4 Astrometrical Calibration.

Images need to be calibrated spatially. In other words, we need to obtain world (α,δ) coordinates from the CCD pixels (x, y) in order to locate an object exactly in the sky. This procedure is commonly known as **astrometrization**.

Usually, the field can be geometrically distorted by the optical layout of the camera. Such distortions can significantly affect the astrometric measurements as well as the photometry, due to the mis-shaped smearing of the light on the pixel array. In order to map and correct distortions in the images, it is quite useful to compare coordinates for a given sample of point-like sources (stars) in the field. Strong distortions require sizeable astrometric samples of stars uniformly spread throughout the field.

Hence, we have used an interactive software developed and maintained by the *Centre de Données astronomiques de Strasbourg*, called **Aladin Sky Atlas** (Bonnarel et al., 2000). *Aladin* visualizes digitized astronomical images and place entries from astronomical catalogues or databases over them. It also has the capability of access related data and information from the different databases and archives for all known sources in the field interactively. In the following, we summarize the steps required for achieving the astrometrization of the NOT sample images.

- Digitalizated Sky Survey (DSS) images of the different NOT clusters were downloaded, ensuring that their sizes were larger than our $3^{'} \times 3^{'}$ fields. A typical size of $14^{'} \times 14^{'}$ was selected. These images are previously astrometrizated.
- A NOT image, previously reduced, was opened with *Aladin*.
- We performed a visual comparison between both images to identify the same object, ideally stars, in both images. We obtain a list of (x, y) pixels

in our observed frame and the corresponding (α,δ) coordinates for the DSS.

- In *Aladin*, we select the options: *Tools*, *Image astrometrical (re)calibration* and finally *By matching stars*. An iterative window will open and we can introduce the pixels and their relative world coordinates.

- An initial astrometrization of the image is shown. Then we superimpose a star catalogue in that frame to improve the initial astrometrical solution. In *Aladin*, we select: *Load*, *All VO* and *Catalogs* where we can choose a number of different catalogues. In that case, we selected NOMAD.

- If desired, we can manually re-astrometrizate the result by selecting the option *Modify*.

- Once we are satisfied, we can save the image by selection *Save* and *Export some planes* and we obtain the NOT original image with galactic astrometry.

2.1.5 Extraction of the sources

We have selected and extracted the sources of our images in order to study their individual characteristics. For that purpose, we used *SExtractor* (Source-Extractor) (Bertin & Arnouts, 1996), which is a well-known astronomical program that builds a catalogue of objects from an astronomical image and measures their photometry.

We have included here an explanation about the most essential parameters for the extraction of the objects in our images. SExtractor gets some image information from the FITS header of the image but it also needs some of the parameters to be specified in the configuration file.

- Extraction Parameters

  They are setting the constraints for the objects to be detected. The most relevant parameters are *DETECT_THRESH* and *DETECT_MINAREA* . The first one determines the level of brightness we want to detect, usually specifying a number of times over the σ of the image and the second one sets up the minimum number of pixels above a threshold that the object has to have to be selected.

  As far as the deblending is concerned, the most interesting and important parameters are *DEBLEND_NTHRESH*, which designates the number of intensity levels that each detection is going to be divided in to analyze the deblending and *DEBLEND_MINCONT*, which stipulates the minimum contrast to split one detection into one or more detections.

  We decided to fix the *DETECT_THRESH*=1.5σ in order to detect galaxies which arrived to Gunn-r isophote of 25.3 and *DETECT_MINAREA*

=150 pixels, which corresponds to galaxies with radius at least of 7 pixels, which is twice the medium full-width at half maximum ($FWHM$) for our images. After performing different tests in our images and checking that the deblending was accurately performed, we resolved to set *DEBLEND_NTHRESH*= 32 and *DEBLEND_MINCONT*=0.0001.

- Photometry Parameters

  SExtractor allows to choose between five different magnitudes for each detected galaxy on our images: isophotal, isophotal-corrected, automatic, best estimate and aperture. We have chosen two of them.

  The first one corresponds to a fixed-aperture *MAG_APER* of radius five kpc, useful to compare colors in the same physical region (Bernardi et al., 2003; Varela, 2004). The other one is the magnitude called by SExtractor 'MAG_BEST' that is determined in an automatic aperture which depends on the neighbours around the galaxy. If those neighbours are bright enough to affect the magnitude corresponding to an aperture enclosing the whole object by more than 10%, then that magnitude is taken as the corrected isophotal magnitude, which corresponds to the isophotal magnitude together with a correction. This magnitude provides the best measures of the total light of the objects (Nelson et al., 2002; Stott et al., 2008).

- Star/Galaxy Separation Parameters

  In a catalogue of objects, we expect to know the kind of object we're dealing with. SExtractor is able to work out the probability (*stellar index*), that an object is an star (a point-source) by using a neural network which was trained with more than 10^6 images of stars and galaxies simulated with different conditions of pixel-scale, seeing and detection limits. Therefore, if the *Stellar index* is close to 1, the object is predictable a star and if it is close to 0., it is likely to be a galaxy. The parameter demanding by SExtractor is the *SEEING_FWHM* which is the $FWHM$ of the image and can be measured directly from the image.

  For our sample, we have considered that an object was a galaxy when its stellar index was smaller then 0.2. In contrast, an object was considered a star if the stellar index was larger than 0.8. The rest of the objects were considered as doubt objects. Those values were selected as the best partition of the galaxy population. As the field of view of our frames is not large we have considered the FWHM being constant in the whole image.

- Background Parameters

  Estimating the local background is a crucial step in achieving good quality photometry. SExtractor estimates the background of the image as well as the RMS noise in that background. The most important values for a proper estimation of the background are *BACK_SIZE* and *BACK_FILTERSIZE*. The first parameter, *BACK_SIZE* is the size of

the area where SExtractor works out the mean and the σ of the distribution of pixel values is computed. The process consists then on discarding the most deviant values and working out again the median and standard deviation σ until all the remaining pixel values are within the mean $\pm$ 3 σ. Then, the value for the background in the area is the mean of those pixels. The background map is a bi-cubic-spline interpolation over all the area's of size *BACK_SIZE*, after filtering.

The second parameter, *BACK_FILTERSIZE* is the median filter for the background map. That is, before the fit of the background values is done, the background image is smoothed over this number of meshes. In order to obtain a good value of these parameters, we have measured the largest objects in our images and we have set *BACK_SIZE* parameter larger than them, that is 128, and a *BACK_FILTERSIZE* of at least 3, in order to get rid of the possible deviations between different estimations in contrasting parts of the image. However, as the field of view is relatively small, the background maintains nearly constant, what implies a good quality subtraction.

SExtractor is also capable of performing on-line cross-identifications of each detection with and ASCII list. This is the ASSOC mode and it is very useful for extracting the same objects in different filters, for example. In our case, the extraction of the galaxies was performed in the $r-$ images, as they are deeper than the $B-$ band images. The photometry of the galaxies in the $B-$band was obtained using the ASSOC mode of SExtractor.

2.1.6 Photometric corrections

Although SExtractor produces the photometry of the objects in the image, those magnitudes need to be corrected of at least two effects: the **k -correction effect** and the **galactic extinction**. The k-correction is defined as the corrective term that needs to be applied to the observed magnitude in a certain band due to the effect of redshift (Oke & Sandage, 1968; Pence, 1976; Poggianti, 1997).

The k-correction effect was then applied to the SExtractor magnitudes of the galaxies in both filters. For the B-band filter we used the k-correction given by Pence (1976), being $k_B = 4.4225z + 0.0294$. The fit was taken from Varela (2004), and it is valid for data between redshift 0.08 and 0.24. The magnitudes of the $r-$ filter were corrected by using the approximations $k_r = 2.5\ log(1 + z)$ (Jorgensen, Franx & Kjaergaard, 1992), due to the flat spectral shape of elliptical in this wavelength range. The galactic extinctions in both filters were derived from Schlegel, Finkbeiner & Davis (1998).

Hence, the corrections for the SExtractor magnitudes were transformed to reliable magnitudes, using the Bouger equation and the color correction, in the following way:

$$\begin{cases} m_r = m_{SEx,r} + Z_{c,r} + k_{n,r}X_r + C_{c,r}(B-r) - A_r - k_r \\ m_B = m_{SEx,B} + Z_{c,B} + k_{n,B}X_B + C_{c,B}(B-r) - A_B - k_B \end{cases} \tag{2.1}$$

The true color (B-r) can be easily evaluated solving Equation 2.1:

$$(B-r) = \frac{Z_{c,B} - Z_{c,r} + k_{n,B}X_B - k_{n,r}X_r + m_{SEx,B} - m_{SEx,r}}{1 - C_{c,B} + C_{c,r}}$$

Tab 2.4 shows the errors provided by SExtractor for the two different magnitudes measured in Gunn-r. The last column shows the errors in colour obtained as the quadratic sum of the errors of the fixed-aperture magnitude in the two filters B and r. As we see, the errors are in all cases not affecting the final results.

Table 2.4: Errors Measurements in NOT sample

Name	Err Aper	Err Best	Err Col
A 1643	0.005	0.006	0.033
A 1878	0.007	0.008	0.052
A 1952	0.006	0.007	0.040
A 2111	0.007	0.009	0.045
A 2658	0.007	0.008	0.028

After extracting all the objects, we checked if there were some part of the frames overlapped and consequently, some of the objects were measured twice. There were two cases: A2111 and A1952. As a way of control, we checked that their magnitudes were consistent between them. In Figures 2.1, we show their absolute magnitudes versus their magnitude differences. The solid line, shows the mean value of the difference (0.012 for A1952 and 0.026 for A2111), while the dotted lines show the standard deviation of the difference (0.052 for A1952 and 0.034 for A2111).

We see that the mean differences are less than 0.028 and the standard deviation for the galaxies brighter than $M_r \geq -19.5$ are of the same order of magnitude than the calibration errors. The larger differences of A1952 rather than A2111, can be explained as it is the only cluster with a relevant difference in seeing (from 0.5 to 0.8) between the different frames. However, that fact does not affect our results.

We finally obtained a first catalogue of 488 detected objects, including stars and galaxies. The final galaxy catalogue was formed by 456 detected galaxies. We also obtained 27 stars and 5 doubt objects.

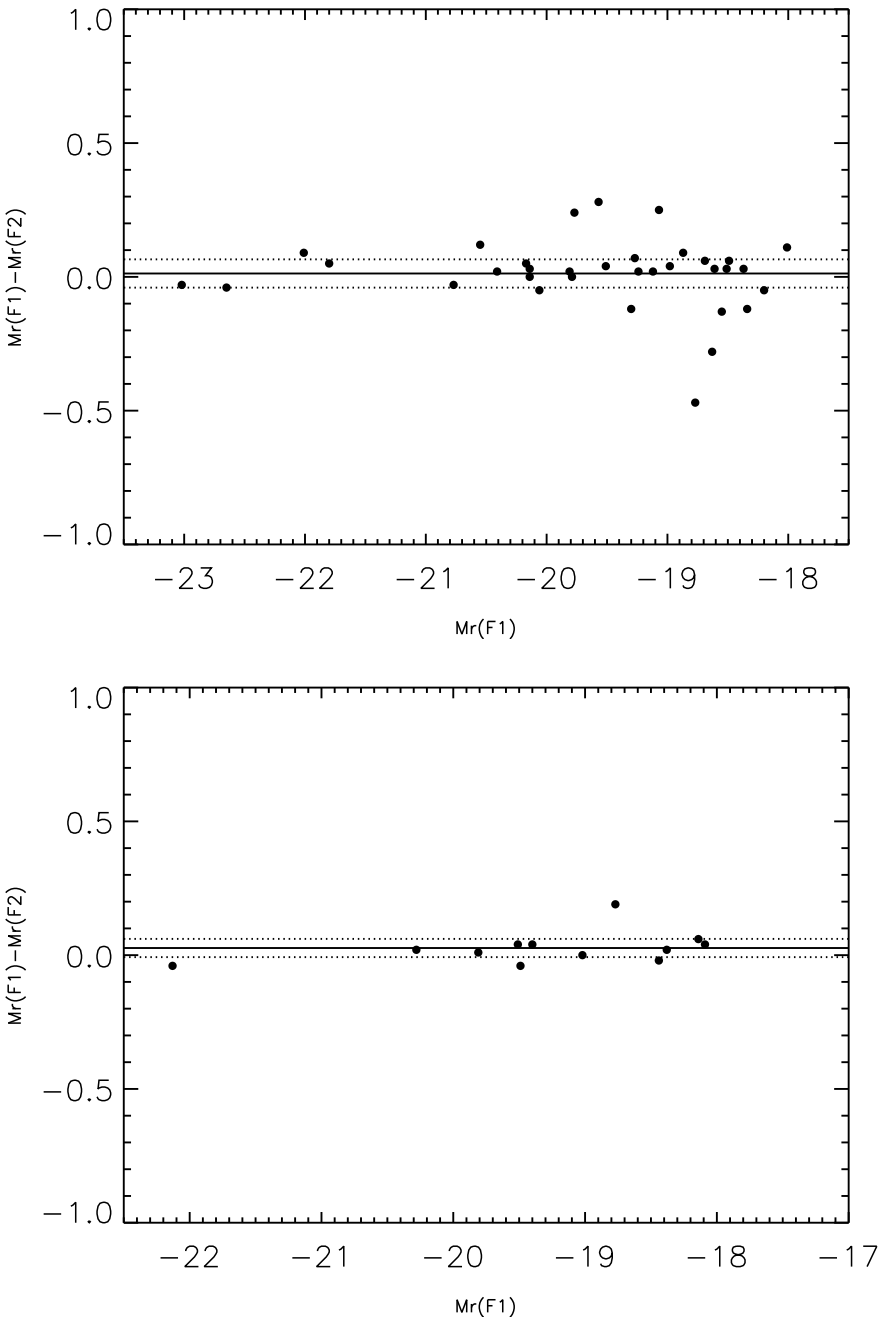

Figure 2.1: Magnitude difference for galaxies in different frames for A1952 and A2111. The solid line indicates the mean value of the difference and the dashed line refers to the standard deviation of the difference.

2.2 Advanced Camera for Surveys Clusters

The other half of the sample at medium redshift consists on five multi-band clusters imaged with the Wide Field Camera (WFC) of the Advanced Camera for Surveys (ACS) in the Hubble Space Telescope (HST) in the same range of redshift.

The CCD of ACS has a field of view of $202'' \times 202''$ and plate scale of $0.05''$/pix. The clusters have been imaged in the full spectral range of the Advanced Camera. In total, twenty orbits were imaged for A1689 in four filters, twenty for A1703, CL0024+1654 and MS1358.4+6245 in six filters and sixteen for A2218 in six filters. The quality of those images is unprecedented due to their depth, wavelength coverage and exceptional resolution from the space.

That main characteristics of the sample are collected in Table 2.5: name of the cluster, the centers obtained by NED, the redshift, the Bautz-Morgan Type, and the richness class. The Bautz-Morgan type and Richness Class corresponding to the cluster CL0024+1654 has not been found in the literature.

Table 2.5: ACS Cluster Global Sample

Name	$\alpha(2000)$			$\delta(2000)$			z	BM type	RC
A 1689	13	11	29	−01	20	17	0.1832	II − III	4
A 1703	13	15	00	+51	49	10	0.2836	II	4
A 2218	16	35	54	+66	13	00	0.1756	II	4
CL0024 + 1654	00	26	36	+17	08	36	0.3900		
MS1358.4 + 6245	13	59	54	+62	30	36	0.3280	I	≥ 4

In Table 2.6, the main information for the observations in F475W band (SDSS-r) and F625W band (SDSS-g) of the five ACS clusters is set. Those bands were selected from the whole multi-band set as being the more similar to the NOT sample bands. Although the SDSS-g band is centered at wavelength 4800 Å and the Bessel -B band at 4290 Å, the difference in not too significative.

Table 2.6: ACS WFC Clusters Observations

Name	Area(Mpc) ^{2}	Exp Time(r) (s)	Exp Time(B) (s)	seeing ($''$)
A 1689	0.615	9500	9500	0.105
A 1703	0.801	5664	9834	0.105
A 2218	0.594	5640	8386	0.105
CL0024 + 1654	1.062	5072	8971	0.105
MS1358.4 + 6245	0.949	5470	9196	0.105

2.2.1 Comments on the sample

Contrary to the NOT sample, the ACS clusters sample has been largely explored and they have a great amount of literature. In this section, we have summarized some of the main results regarding those clusters.

A1689. This cluster is one of the best studied in the literature. The Sunyaev-Zeldovich effect (Sunyaev & Zeldovich, 1970, 1972), has been detected and computed in this cluster (Bonamente et al., 2006). It also presents many gravitational arcs associated with 30 systems or sources with redshift in the range $1 < z < 6$ (Diego et al., 2005).

Several studies have analyzed its mass profile by estimating its dark matter halo with different methods such as gravitational lenses (Tyson & Fischer, 1995; Taylor et al., 1998; Broadhurst et al., 2005a; Diego et al., 2005; Zekser et al., 2006; Halkola, Seitz & Pannella, 2006, 2007), galaxy kinematics (Łokas et al., 2006), or X-ray imaging (Xue & Wu, 2002; Demarco et al., 2003; Andersson & Madejski, 2004; Bonamente et al., 2006).

Although the lensing techniques tend to agree in the calculation of the mass of this cluster, providing a value around $(0.1 - 0.5)10^{15}h^{-1}M_{\odot}$ for the mass contained in a radius of 51 to 110 arcsecs, a systematic discrepancy of about two is found with the estimations provided by X-ray data.

The redshift of this cluster (z=0.1832) was given originally by the work by Teague, Carter & Gray (1990), who obtained sixty-six spectra of the field of each cluster providing a wide coverage of the bright galaxy population. Later on, Duc et al. (2002) gave positions and redshift for all cluster members with magnitude R<18 and within $2''$ of the brightest central galaxy. The X-ray center has been set as prescribed in Bonamente et al. (2006) using Chandra X-ray measurements at the position, $\alpha(J2000)$ =+13d 11m 29.5s, $\delta(J2000)$ = -01h 20m 28.2s. That center has been found to be in agreement with the peak of the mass distribution (Diego et al., 2005), which falls very close to the central dominant galaxy.

Molinari, Buzzoni & Chincarini (1996) performed an study of the ground-based photometry of this cluster in Gunn g, r and i bands, discussing the r versus $g-r$ color diagram, concluding that a ridge line for the elliptical galaxies clearly appeared for this compact cluster. Additionally, De Propris et al. (2003b), analyzed the Butcher-Oemler Effect in the K-band for this cluster, finding a blue-fraction of 0.046 ± 0.038 in the K-band and 0.029 ± 0.025 in the optical within a 0.5 Mpc aperture.

A1703. This cluster is a massive X-ray cluster that contains a large number of gravitational arcs (Limousin et al., 2008). In particular, this cluster exhibits an outstanding bright 'ring' formed by galaxies at z=0.888 located very close to the brightest cluster galaxy.

The redshift of A1703 (z=0.2836) is given in a work by Allen et al. (1992) who identified the redshift of the two brightest X-ray members of the cluster.

The coordinates provided by NED for the center of the cluster are $\alpha(J2000)$ =+13h 15m 00.7s, $\delta(J2000)$= +51d 49m 10s, extracted from the Abell optical Catalogue (Abell, Corwin & Olowin, 1989). Later works by Crawford et al. (1999); Limousin et al. (2008), based on the ROSAT Brightest Cluster Sample, set the center of the cluster as the coordinates provided by the dominant galaxy in X-ray, $\alpha(J2000)$=+13h 15m 05.27s, $\delta(J2000)$= +51d 49m 02.85s.

A2218. A2218 is one of the richest clusters in the Abell catalogue. That cluster is 'famous' due to its ring around its brightest cluster galaxy (Kassiola & Kovner, 1993). Numerous gravitational lenses studies came after the discovery of that 'ring' (Kneib et al., 1996; Soucail, Kneib & Golse, 2004; Kneib et al., 2004), suggesting that the multiple lens system arises from a high-redshift (z>6) source.

Additionally, many attempts to determine the dynamical state of the cluster by studying its X-ray emission have been performed (Neumann & Böhringer, 1999; Cannon, Ponman & Hobbs, 1999; Machacek et al., 2002; Pratt, Böhringer & Finoguenov, 2005), even with the analysis of the Sunyaev-Zeldovich effect (Uyaniker et al., 1997; Tsuboi et al., 1998; Lieu, Mittaz & Zhang, 2006; Morandi, Ettori & Moscardini, 2007). A discrepancy between mass estimates from X-ray and strong lensing analyses is evident (Miralda-Escude & Babul, 1995; Pratt, Böhringer & Finoguenov, 2005). More complete X-ray studies with ROSAT (Markevitch, 1997; Neumann & Böhringer, 1999) or Chandra (Machacek et al., 2002), revealed a complicated X-ray structure near the core, suggesting that the cluster is dynamically active. The most likely explanation is the merger status of A2218. The clumpy X-ray emission appears as a direct consequence of the ongoing merging of the two sub-units (Kneib et al., 1995).

The redshift of this cluster ($z = 0.17$) is provided by Kristian, Sandage & Westphal (1978); Le Borgne, Pelló & Sanahuja (1992). The coordinates given by NED, $\alpha(J2000)$=+16h35m54.0s, $\delta(J2000)$= +66d13m00s, were extracted from the Abell catalogue (Abell, Corwin & Olowin, 1989). However, the peak of the X-ray surface brightness distribution is coincident with the location of the brightest cluster galaxy, $\alpha(J2000)$=+16h35m48.9s, $\delta(J2000)$= +66d12m42s (McHardy et al., 1990). The photometric and spectroscopic study of the clusters center suggest that the cluster consist in fact of two galaxy concentrations, of which one is centered about the brightest cluster galaxy.

Besides, a number of photometrical studies has been performed in that cluster. Butcher & Oemler (1984) gave a concentration parameter of C=0.59, one of the largest in their sample. Jørgensen et al. (1999), extracted the photometry for a magnitude-limited sample, deriving the corresponding Fundamental Plane, adding important knowledge about the properties of E and S0 galaxies. Also, Rakos, Dominis & Steindling (2001); Rakos & Schombert (2005), completed a four color intermediate-band photometry of the cluster population, finding an unusually low fraction of blue galaxies and a large fraction of E/S0 galaxies. They also analyzed the B-r color-magnitude relation finding a slope of 0.068 ± 0.032. Complementary, a quantitative morphological study in the core of that

cluster has been recently performed by Sánchez et al. (2007).

Furthermore, Pracy et al. (2005) studied the luminosity function in that cluster. They find that the total projected luminosity distribution within 1 Mpc of the cluster centre can be well represented by a single Schechter function with moderately flat faint-end slopes: $\alpha = -1.14$, also finding that the brightest galaxies in that cluster exhibit a more compact spatial distribution.

CL0024+1654. This cluster, hereafter CL0024, is the more distant from all the clusters analyzed in this thesis with a redshift of z=0.39. It has a velocity dispersion of $\sigma_v = 1200 km\, s^{-1}$ (Dressler & Gunn, 1992), and an X-ray luminosity of $L_x = 3.7 \times 10^{44} ergs\, s^{-1}$ (Soucail et al., 2000). A single background galaxy is multiply imaged (Colley, Tyson & Turner, 1996; Tyson, Kochanski & dell'Antonio, 1998; Böhringer et al., 2000; Broadhurst et al., 2000; Rögnvaldsson et al., 2001; Kneib et al., 2003). Several analysis with X-ray data have been performed (Kodama et al., 2004; Zhang, Han & Jiang, 2005; Kotov & Vikhlinin, 2005), finding a complex structure in the core region. Evidence of the Sunyaev-Zel'dovich effect (Zemcov et al., 2007), has also been found.

The original redshift was obtained by Gunn & Oke (1975). The position listed in NED comes from the Catalogue by Zwicky et al. (1961) and is set at $\alpha(J2000)$= 00h 26m 36s, $\delta(J2000)$=+17d 08m 36s. However, the X-ray center (Soucail et al., 2000; Treu et al., 2003), is determined to be at $\alpha(J2000)$=00h 26m 36.3s, $\delta(J2000)$=+17d 09m 46s, which is very close to the position of the brightest cluster galaxy, $\alpha(J2000)$=00h 26m 35.7s, $\delta(J2000)$= +17d 09m 43s (Treu et al., 2003).

In addition, Czoske et al. (2001); Alexov, Silva & Pierce (2003), provided this cluster with a wide-field spectroscopic survey of 618 spectra. The morphological distribution has been analyzed to 5 Mpc radius by Treu et al. (2003) up to I=22.5. Also, the original value of the blue fraction given by Butcher & Oemler (1984) is 0.16 ± 0.02 and later on, De Propris et al. (2003a) estimated this to be 0.153 ± 0.068 in the central 0.5 Mpc and 0.200 ± 0.068 in the central 0.7 Mpc.

Additional works have performed deep analysis of different properties such as the Fundamental Plane (van Dokkum & Franx, 1996), the Tully-Fisher relation in that cluster (Metevier et al., 2006) or the nature of strong emission-line galaxies in that cluster (Koo et al., 1997). Also the concentration parameter has been estimated by Dressler et al. (1997) to be 0.53.

MS1358.4+6245. This cluster , hereafter MS1358, is an X-ray, extremely rich cluster, with a compact, concentrated core of galaxies. The Sunyaev-Zeldovich effect has been widely explored on it (LaRoque et al., 2006; Morandi, Ettori & Moscardini, 2007; Hashimoto et al., 2007). It also has weak gravitational lensing of faint distant background objects (Hoekstra et al., 1998).

The redshift (z=0.328) and position of this cluster $\alpha(J2000)$= 13h 59m 54.3s, $\delta(J2000)$= +62d 30m 36s, is set from a work based on Einstein Observatory extended Medium-Sensitivity Survey by Stocke et al. (1991). However, most works have adopted the brightest cluster galaxy set as $\alpha(J2000)$=13h 59m 50.5s,

$\delta(J2000)$=+ 62d 31m 05s (Fisher et al., 1998; van Dokkum et al., 1998; Fabricant, Franx & van Dokkum, 2000)

Likewise, Yee et al. (1998) created a redshift catalogue of the galaxies in the field of this cluster in a wide area ranging in magnitude from $r = 20$ to $r = 22$ and Fisher et al. (1998) added more spectroscopic information in the central 3.5 Mpc. The morphological composition of a sample of galaxies in the central 53 arc minutes have been carried out by Fabricant, Franx & van Dokkum (2000).

In addition, Luppino et al. (1991) presented an analysis of four-color (BVRI) photometry. They included the cluster luminosity function and color-magnitude diagrams and also computed the blue galaxy fraction finding it be $0.10 < f_b < 0.18$ depending on the background galaxy correction. Similarly, Fabricant, McClintock & Bautz (1991) obtained V,R and I photometry of the galaxy population in the cluster center complete to rest band $M_V = -19.5$ and spectra of 70 galaxies within 2 arc minutes. They also estimated the concentration parameter finding a value of 0.49.

The B-V color-magnitude relation was analyzed by van Dokkum et al. (1998) finding a slope of -0.012 $\pm$ 0.003. Also, Kelson et al. (2000) performed an study based on the surface photometry and structural parameters for 55 galaxies in this cluster.

In Chapter 6, we will set and discuss the determination of the center of the cluster. The final center coordinates are provided in Table 6.4.

2.2.2 Reduction and Calibration of the frames

The ACS images were previously reduced using Apsis, the automatic image processing pipeline for the ACS GTO (ACS Guaranteed Time Observations) (Blakeslee et al., 2003). Apsis is able to rotate, align, cosmic-ray-reject, and drizzle the imaging observations together.

Likewise, the images were astrometrizated and calibrated taking advantage of the 2002 February 25 CALACS zero points (Hack, 1999), offset by small amounts necessary for the errors present in this calibration.

2.2.3 Extraction of the sources

The sources in this sample were detected by using SExtractor. The procedure is the same already explained in the last section referring to the NOT sample. In this subsection, we only remark the most relevant parameters, specifying this relation with the parameters set from the NOT sample.

- Extraction Parameters

  We have set the $DETECT\_THRESH$=1.5σ, detecting galaxies that arrived to r isophote of 27.8. Also, we have opted for a $DETECT\_MINAREA$

value of 150 pixels, corresponding to galaxies with radius at least of 7 pixels, which is ≈ three times the medium FWHM for our images.

Concerning the deblending parameters, we have set *DEBLEND_NTHRESH* = 32 and *DEBLEND_MINCONT*=0.005 as the result of different tests to achieve the best accuracy of the deblending image.

- Photometry Parameters

  As in the NOT sample, we have used the *MAG_APER* with an aperture of five kpc, useful for the color determination and the *MAG_BEST* for the computation of the magnitudes.

- Star/Galaxy Separation Parameters

  The stellar index has been considered in the same way as the NOT sample. A value less or equal than 0.2 is chosen to consider an object a galaxy while a stellar index value larger than 0.8 is considered as a star. The rest of the objects are considered doubt objects.

- Background Parameters

  We have taken the value sof *BACK_SIZE* and *BACK_FILTERSIZE* parameters to have enough statistics to have a good estimation of the background. We have then set *BACK_SIZE* = 128 and *BACK_FILTERSIZE*= 3.

The extraction of the galaxies was performed in the r images, to be comparable with the NOT sample. The photometry of the galaxies in the g-band was obtained using the ASSOC mode of SExtractor.

2.2.4 Photometric corrections

We have k-corrected the SExtractor magnitudes of the galaxies in both filters. For the g-band filter we have used an interpolation of the k-correction given by Poggianti (1997) for the Gunn-g band in the range 0.16 to 0.4, being $k_g = 4.70z + 0.35$. For the r-band filter, we used the same approximation as in the NOT sample, $k_r = 2.5\ log(1+z)$ (Jorgensen, Franx & Kjaergaard, 1992). Likewise, the galactic extinctions in both filters have been derived from Schlegel, Finkbeiner & Davis (1998).

We have set in Table 2.7, the errors provided by SExtractor for the two different magnitudes measured in Gunn-r. Also, the last column shows the mean errors in colour obtained as the quadratic sum of the errors of the fixed-aperture magnitude in the two filters, g and r. As we see, the errors are not affecting the final results in all cases.

The final catalogue of detections contains 2341 objects, consisting on 2239 galaxies, 91 stars and 11 doubt objects.

Table 2.7: Errors Measurements in ACS sample

Name	Err Aper	Err Best	Err Col
A 1643	0.003	0.003	0.007
A 1878	0.002	0.002	0.007
A 1952	0.003	0.002	0.008
A 2111	0.002	0.006	0.009
A 2658	0.002	0.002	0.007

Part II

Characterization of the bright central galaxy population in Clusters

Chapter 3

Color-Magnitude Relation

Puedo escribir los versos más tristes esta noche.
Escribir, por ejemplo,: 'La noche está estrellada,
y tiritan, azules, los astros, a lo lejos.'

Pablo Neruda, 'Veinte poemas de amor y una canción desesperada.'

The existence of the **Color-Magnitude Relation (CMR)** for elliptical galaxies was first pointed out by Baum (1959). He noted that the colors of field elliptical galaxies become redder as the galaxies become brighter. Locally, the elliptical galaxies in individual clusters form a red sequence with a well-defined slope and small scatter (Bower, Lucey & Ellis, 1992a,b). A simple straight line fit can describe the CMR for elliptical galaxies in an interval of about eight magnitudes in local clusters such as Virgo (Sandage, 1972b) or Coma (Rood, 1969; Thompson & Gregory, 1993; López-Cruz et al., 1997; Secker, Harris & Plummer, 1997). The large coverage in luminosity, suggests that within this range galaxies have shared a similar evolutionary process.

Later on, in the seventies and eighties, a number of works by Visvanathan & Sandage (1977); Visvanathan & Griersmith (1977); Sandage & Visvanathan (1978); Griersmith (1980); Visvanathan (1981) concluded on the universality of the so called CMR for early type galaxies and even early spiral galaxies, depending on the bands used (Tully, Mould & Aaronson, 1982; Mobasher, Ellis & Sharples, 1986).

The physical origin of the CMR seems to be a consequence of the formation process of the galaxies in clusters. The most massive galaxies are able to retain largest quantities of enriched gas from the supernova explosions in the maximum of the stellar formation activity (Arimoto & Yoshii, 1987). Two main scenarios for the formation of clusters of galaxies still remain in the literature. On one hand, we have the monolithic scenario in which the clusters were formed first (Bower, Kodama & Terlevich, 1998), and on the other, we have the hierarchical

scenario (Kauffmann, Guiderdoni & White, 1994; Kauffmann, 1996; De Lucia & Blaizot, 2007b), in which the galaxies were formed at the outset.

The evolution of the slope of the color-magnitude relation with redshift in clusters of galaxies has been widely explored (van Dokkum & Franx, 1996; Kelson et al., 1997; Ellis et al., 1997; Andreon, Davoust & Heim, 1997; Bender et al., 1998; López-Cruz, Barkhouse & Yee, 2004; Mei et al., 2006; Driver et al., 2006; De Lucia et al., 2007a) and it seems to be an agreement on its constancy up to redshift z $\sim$1. Recent results from the Hubble Space Telescope (HST) demonstrate the existence in clusters at redshift up to z $\sim$ 1 of a tight red sequence, comparable in scatter and slope to that observed in the red sequence of the Coma Cluster (Ellis et al., 1997; Stanford, Eisenhardt & Dickinson, 1998; Mei et al., 2006). This result suggests that the bulk of the stellar population in early-type galaxies in clusters has been formed before z=1 and has passively evolved since then.

Not only the CMR has been used to restrict the formation and evolution of the galaxy population but it also has been applied to many other practical issues such as the background galaxies identification (Fasano et al., 2002; Barkhouse, Yee & López-Cruz, 2007), the determination of distances between clusters (Visvanathan & Griersmith, 1977; Bower, Lucey & Ellis, 1992a) or the detection of clusters of galaxies (Yee, Gladders & López-Cruz, 1999; López-Cruz, Barkhouse & Yee, 2004).

Another interesting feature related to the galaxy colors is the **Butcher-Oemler effect** (Butcher & Oemler, 1984). In this pioneering work, they studied 33 clusters of galaxies up to redshift 0.54 and found an increasing fraction of blue galaxies at progressively higher redshift, in particular from z $\geq$ 0.1. Many works have tried since then to quantify and explain this blue galaxy fraction increment at low redshift (Garilli et al., 1995, 1996; Margoniner & de Carvalho, 2000; Margoniner et al., 2001; Goto et al., 2003; De Propris et al., 2004; Aguerri, Sánchez-Janssen & Muñoz-Tuñón, 2007) and high redshift (Rakos & Schombert, 1995; De Lucia et al., 2007a). For example, Rakos & Schombert (1995) concluded that the galaxy blue fraction increases and they quantified it from a 20 % at z =0.4 to 80% at z =0.9, suggesting that the evolution in clusters is even stronger than previously thought. Also, Margoniner & de Carvalho (2000) completed an study of 48 clusters in the low-medium redshift range 0.03 <z< 0.38 obtaining similar results. However, many works have found no signs of evolution. Thus, Garilli et al. (1995, 1996), who observed and studied a sample of clusters in the redshift range 0.05 $\leq$ z $\leq$ 0.25 found no signs of evolution; De Propris et al. (2004) who computed the blue fractions from 60 clusters at z<0.11 from the 2dF Galaxy Cluster Survey, also conclude that there is no evolutionary trend. Finally, Aguerri, Sánchez-Janssen & Muñoz-Tuñón (2007), who analyzed a large sample of SDSS clusters up to redshift z $\leq$ 0.1, arrived at the same conclusion. Actually, nearly all the works up to date have reported a wide range of blue fraction values at fixed redshift with some trend with the redshift.

Additionally, the blue fraction of galaxies has been found to depend on the cluster richness, in the sense that richer clusters have smaller blue fractions. It also depends on the area surveyed, with the trend of larger blue fractions at larger radii, in agreement with the idea of Butcher & Oemler (1984) that the fraction of blue galaxies increases in the outer parts of the cluster and it depends as well, on the interval of the luminosity function used to compute the blue fraction, obtaining larger blue fractions as fainter objects are included (Margoniner & de Carvalho, 2000; Margoniner et al., 2001). The last authors claimed that all this dependences causes a large scatter in the blue fraction - redshift diagram. Therefore, it is extremely interesting to explore an origin of the scatter in the blue fraction beyond any possible tendency with the redshift.

In this Chapter, we present the study of the CMR and blue fraction for the galaxies found in our cluster samples, (see also Ascaso et al. (2008a)). Throughout this Chapter, the BEST SExtractor magnitudes has been used and the color index B-r and g-r, for the NOT and ACS sample respectively, has been determined by measuring a five kpc aperture as prescribed by Bernardi et al. (2003); Varela (2004), to be able to compare the same regions of the galaxy at different redshift.

3.1 Color-Magnitude Diagram

3.1.1 Completeness Limit

We have computed the magnitude up to which our samples are complete in order to be sure that our results are not biased. To do that, we have plotted in Figure 3.1 and 3.2 the absolute magnitude distribution of the NOT ad ACS sample respectively. The completeness limit has been directly set as the maximum of the histogram. The completeness limit for each cluster and for the whole sample is overplotted in the figures with dotted and dashed lines respectively. The NOT sample appears to be complete up to $M_r \approx$ -19.5, while the ACS sample manifests to be complete up to $M_r \approx$ -17.6. In Figure 3.2, we have overplotted also with a dashed-dotted lined the completeness limit adopted for the NOT sample.

Therefore, to avoid problems due to the discreteness of the bins with the magnitude limit, we have considered only galaxies brighter than M_r=-20 for the analysis of the CMR for the NOT sample and brighter than M_r=-17.8 for the analysis of the CMR for the ACS sample.

3.1.2 Interlopers

A previous remark that we must have into account for the characterization of the cluster population is the identification and exclusion of the possible interlopers that may be found projected in the same field of view. The definitive

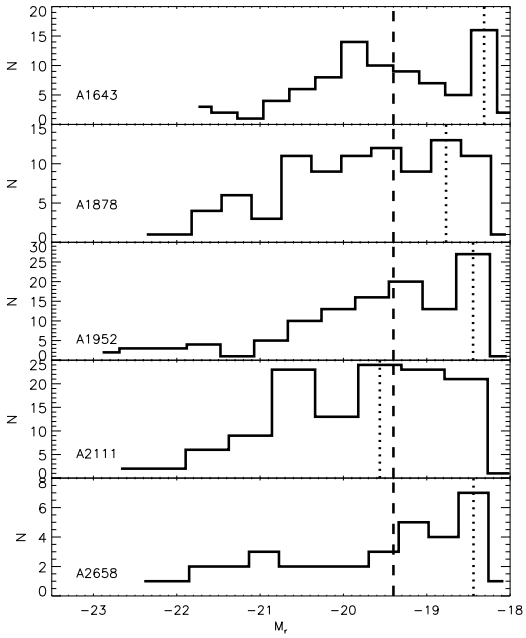

Figure 3.1: Absolute magnitude histogram of the galaxies in the NOT clusters sample. The dotted line shows the completeness magnitude limit for each cluster, whereas the dashed line shows the common magnitude limit we have adopted for the NOT clusters sample.

criterion to find the galaxies that actually belong to a given cluster is the redshift. Unfortunately, the redshift information is in general scant for clusters at redshift ~ 0.2 except for some particular cases. For the NOT sample, we only have found in the literature 22 galaxies in A2111 with redshift data provided by Miller, Oegerle & Hill (2006), whereas for the other clusters there are just one or two redshift entries in the NED.

The panorama changes for the ACS sample, as we have already explained, four out of five clusters observed with the ACS have spectroscopy studies: A1689 (Teague, Carter & Gray, 1990; Duc et al., 2002), with 91 galaxies in the central Mpc and foreground and background estimation up to R<17.5; A2218 (Sánchez et al., 2007), who obtained 31 spectra in the central 200 kpc up to I< 22.5mag; CL0024 (Czoske et al., 2001), who presented 650 identified objects in the central 4 Mpc of the cluster, with a completeness of more than 80% up to V=22 in the central 3 arcmin and also identified an overdensity of galaxies a z ~ 0.18 with no obvious centre and MS1358, with two spectroscopic surveys performed: Fisher et al. (1998), in the central 3.5 Mpc, obtaining 232 cluster members and Yee et al. (1998), who obtained 361 galaxies in the range of Gunn-r from 20 to 22.

In Table 3.1, we have compiled the number of galaxies with redshift obtained

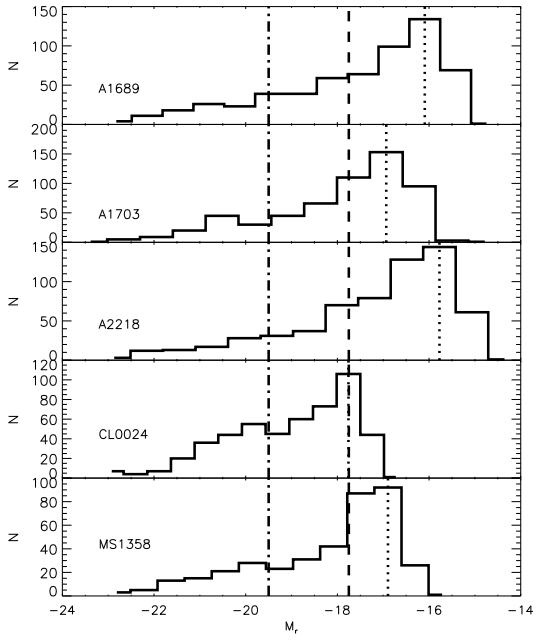

Figure 3.2: Absolute magnitude histogram of the galaxies in the ACS clusters sample. The dotted line shows the completeness magnitude limit for each cluster, the dashed line shows the common magnitude limit for the five ACS clusters and the dashed-dotted line shows the magnitude completeness adopted for the NOT sample.

from the literature. The first column shows the number of detected galaxies in the frames, the second column indicates the number of galaxies that belongs to the cluster, assuming a velocity range of 2400 $km\,s^{-1}$. We have to notice that an important number of galaxies with velocity differences of 4800 $km\,s^{-1}$ has been detected. It is not clear whereas those galaxies belong to the cluster or not. We have not included them in our analysis even if they can not be definitively excluded without an exhaustive dynamical analysis (see, for example, Łokas et al. (2006) for A1689). Those numbers are collected in the third column. Finally, the number of foreground and background galaxies are set in the last two columns.

Of course, those numbers are not complete for our sample. However, through this work we are going to study the galactic population in both samples, up to the NOT completeness limit, which is the most restrictive, except for computing the luminosity function and colour-magnitude diagrams, where we will take benefit of the completeness limit in the ACS sample.

As far as the foreground galaxies are concerned, we can work out the number of field galaxies that are expected in our field of view up to our completeness

Table 3.1: Redshift Information for the ACS Clusters

Name	N_{gal}	$N_{z,cl}$	$N_{z,f,cl}$	$N_{z,f}$	$N_{z,b}$
A 1689	586	34	10	2	62
A 1703	583	2	0	1	1
A 2218	624	58	7	2	22
CL0024	502	83	1	12	21
MS1358	387	54	4	2	5

magnitude limit by integrating the luminosity function of field galaxies in the solid angle corresponding to each of our clusters. The number of foreground galaxies per frame up to magnitude -19.5 that we have obtained for NOT and ACS sample are collected in Tables 3.2 and 3.3.

These estimations are in good agreement with previous findings by Fasano et al. (2000) for the NOT sample and also with the foreground galaxies obtained from the literature for the ACS cluster up to magnitude -19.5. The only case for which the number of foreground galaxies is higher is for CL0024, for which Czoske et al. (2001) identified an overdensity of galaxies a $z \sim 0.18$ with no obvious centre. Consequently, the foreground contamination for our medium-redshift clusters is therefore statistically negligible as they have been already corrected.

Table 3.2: Foreground Galaxies for NOT Clusters Sample

Name	$N_{gal,fg}$/frame	$N_{gal,fg}$/coverage
A 1643	0.52	1.04
A 1878	0.67	1.34
A 1952	0.88	1.45
A 2111	0.73	1.40
A 2658	0.44	0.44

Coming back to the background objects, the CMR provides a robust method (Secker, Harris & Plummer, 1997; Fasano et al., 2002; López-Cruz, Barkhouse & Yee, 2004; Barkhouse, Yee & López-Cruz, 2007), for determining the red early-type background galaxies. We know that the cosmological k-effect (Oke & Sandage, 1968; Pence, 1976; Frei & Gunn, 1994; Poggianti, 1997), makes early-type galaxies look redder as their redshift increases. Then, if we find redder galaxies than those defined to belong to the cluster by the CMR, their distances must be larger than the cluster distance. We have identified background galaxies as those objects that are 0.2 magnitudes redder than the value from the fitted CMR. After applying this criterion, the final number of galaxies retained as

Table 3.3: Foreground Galaxies for ACS Clusters Sample

Name	$N_{gal,fg}$/frame
A 1689	0.65
A 1703	1.76
A 2218	0.59
CL0024	3.35
MS1358	2.39

members of the NOT sample, amounts to 408. They are collected in the Table A.1 presented in the Appendix and they are also available electronically in Ascaso et al. (2008a). The first column of that table gives the name of the cluster. The second and third columns give the coordinates of the galaxy, whereas we give in the fourth column the z information when available. The fifth and sixth columns give the r and B absolute magnitudes of each galaxy, assuming that they are located at the cluster redshift.

Similarly, the same correction have been applied to the g-r diagrams for the ACS clusters. The final number of galaxies is 2239. We do not show these data in this report for economy of space but they will be available electronically in Ascaso et al. (2008c).

3.1.3 Color-Magnitude Fit

The fit to the red sequence of the CMR for each cluster has been determined by carrying out a least absolute deviation regression fit to the observed data (Armstrong & Kung, 1978). For each cluster, it was computed by using an iterative procedure. A first fit was obtained using all the galaxies brighter than $M_r = -19.5$ for a given cluster of the NOT sample and $M_r = -17.8$ for the ACS sample. Then, the distance of each galaxy in B-r and g-r respectively, to the fitted CMR was computed. Those galaxies with a distance larger than three times the *rms* of the fitted relation were rejected, and a new fit to the CMR was done with the remaining ones. This process was repeated until the fit to the CMR did not change anymore. The final fit has been estimated by using a nonparametric bootstrap method (Efron & Tibshirani, 1986), with $n \log^2 n$ resamplings, being n the number of galaxies up to the completeness limit, as prescribed in Babu & Singh (1983). The slope and zero point are the median value of the resampling, while the standard errors have been estimated as the *rms* of the bootstrap samples.

In the left panels of Figures 3.3 and 3.4, we show the colour-magnitude diagrams for all the galaxies in NOT and ACS clusters, together with the fit to the CMR (solid line), showing also the upper 0.2 magnitude limit for considering a galaxy a member cluster (dotted line). The corresponding apparent magnitude to the

M_r=-19.5 and M_r=-17.8 limit respectively, is marked with a vertical line. We have also plotted in the right panel of that figure the histogram of the color differences between the observed and the CMR-fitted values. We give in Tables 3.4 and 3.5 the zero point, a_0, the slope, a_1 and the *rms* of the fitted CMRs for each cluster in NOT and ACS sample.

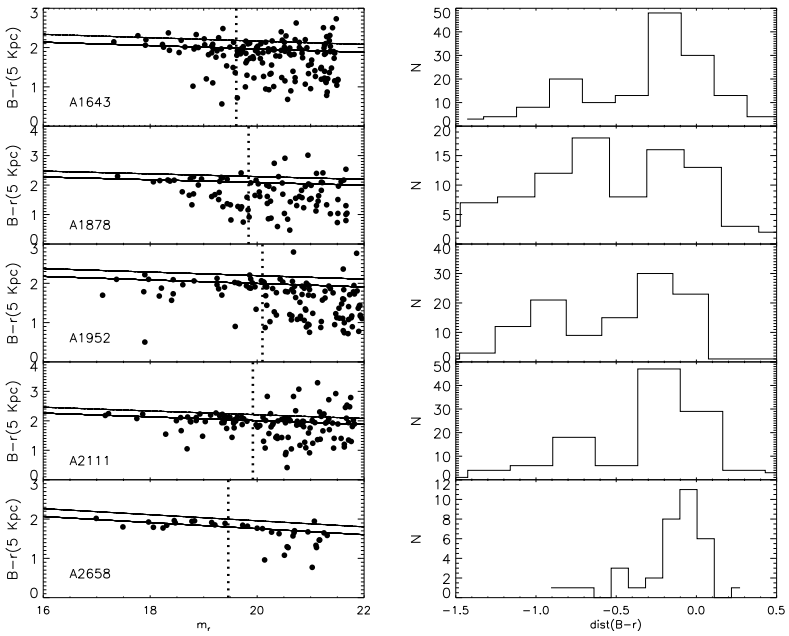

Figure 3.3: Left panels: The color-magnitude diagrams for the NOT clusters. The solid line refers to the fit to the red sequence and the dotted line is the upper 0.2 magnitude limit. The vertical line corresponds to the limit M_r = -20 at the cluster redshift. Right panels: The histograms of the B-r distances of the galaxies to the corresponding red sequence

3.1.4 Color-Morphology

In the left column of Figures 3.5 and 3.6, we have plotted the colour-magnitude diagrams for the galaxy population in the clusters sample and the visual morphology (explained in Chapter 4) has been overplotted with different colors for the NOT and ACS sample. Complementary, in the right hand, we have set the histogram of differences from the CMR for each morphological types.

We can point out several features. A1643 has a very large population of spiral galaxies. That fact is reflected into a high peak into a spiral peak in the color histogram at a mean distance from the CMR of 0.3 extending to distance 0. We note a very concentrated peak of elliptical and lenticular galaxies around

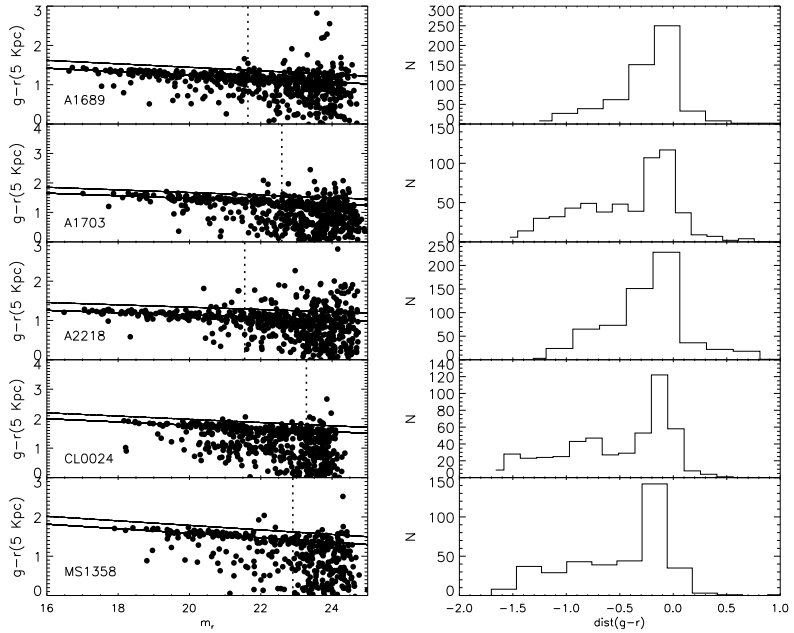

Figure 3.4: Left panels: The color-magnitude diagrams for the ACS clusters. The solid line refers to the fit to the red sequence and the dotted line is the upper 0.2 magnitude limit. The vertical line corresponds to the limit M_r = -17.8 at the cluster redshift. Right panels: The histograms of the B-r distances of the galaxies to the corresponding red sequence

distance 0 which are defining the CMR. It is quite noticeable that the brightest cluster galaxy is a lenticular galaxy, that will be studied in Chapter 8.

A1878 is also a late-type galaxy dominated cluster. At examining the color histograms, we find two main peaks of spiral galaxies, one placed very close the CMR relation and the other at a mean distance of one magnitude from the CMR. This last peak coincides with a peak of irregulars at approximately the same distance. In that case, the BCG is an elliptical galaxy, but the main fraction of galaxies belonging to the CMR are classified as late type galaxies, being probably early spiral galaxies. The ACS sample clusters, A1689, A2218 and MS1358 are also mainly dominated by late-type galaxies, although, the red population dominates in the brightest part of the sequence.

The contrary tendency is found in the rest of the clusters. The CMR is widely populated by early-type galaxies and the BCGs are in all cases elliptical galaxies. At examining the color histograms, we note that the lenticular population is completely dominant for A2111, A1703 and CL0024 and it is skewed towards bluer colours for A1952 and towards redder colors for A2658. Also, for A2111, we find a large blue galaxy population already noticed by several works (Butcher

Table 3.4: CMR parameters in NOT sample

Name	a_0	a_1	rms
A 1643	2.825 ± 0.224	-0.043 ± 0.011	0.035
A 1878	3.022 ± 0.390	-0.046 ± 0.021	0.060
A 1952	2.893 ± 0.257	-0.044 ± 0.013	0.009
A 2111	3.285 ± 0.079	-0.063 ± 0.004	0.053
A 2658	3.301 ± 0.257	-0.077 ± 0.013	0.037

Table 3.5: CMR parameters in ACS sample

Name	a_0	a_1	rms
A 1689	2.131 ± 0.017	-0.044 ± 0.0008	0.003
A 1703	2.367 ± 0.021	-0.044 ± 0.0010	0.006
A 2218	1.736 ± 0.008	-0.029 ± 0.0004	0.004
CL0024	2.878 ± 0.017	-0.054 ± 0.0008	0.006
MS1358	2.740 ± 0.035	-0.057 ± 0.0016	0.004

& Oemler, 1984; Miller, Oegerle & Hill, 2006).

Thus, the red sequence is defined in all the clusters and it is formed mainly by early-type galaxies and in some cases, such as A1643, A1878, A1689, A2218 or MS1358, we also find a substantial population of early-spiral galaxies.

3.1.5 CMR slope versus redshift

In order to compare the results of the fits to the colour-magnitude diagrams with a lower redshift sample, we have plotted in Figure 3.7, the slope values of the fitted CMRs in our clusters at medium redshift together with those obtained by López-Cruz, Barkhouse & Yee (2004) for clusters at $z < 0.15$. As the figure illustrates, there is no clear tendency of the slope of the CMR with the redshift. The mean value of the slope of the CMR for our sample together with López-Cruz, Barkhouse & Yee (2004) is -0.050 ± 0.008. For the NOT sample alone, we obtain -0.055 ± 0.014 and for the ACS sample, -0.046 ± 0.010. The mean value for both samples together is -0.050 ± 0.013, which is the same that the whole mean. In addition, those values are very similar to the slope value found by Mei et al. (2006) for two clusters at z$\sim$1.26.

In other words, the slope values we have found for our clusters at z $\sim$ 0.3 are completely consistent with the values found for lower and much higher redshift values. Moreover, the range of values found at any redshift are also similar. Thus, we find no indication of change of the CMR slope up to z $\sim$ 0.3 and

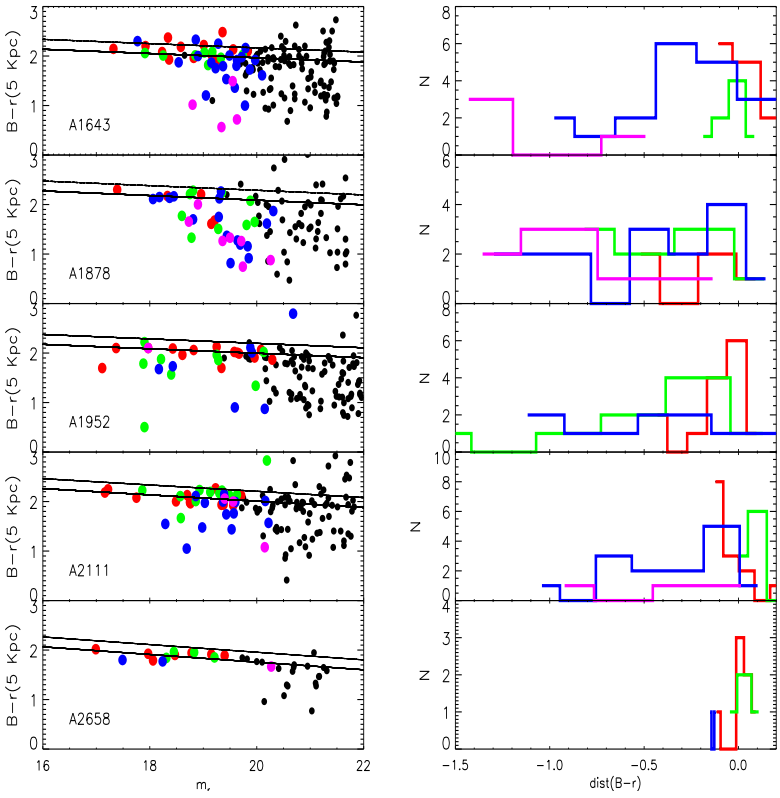

Figure 3.5: Left panels: The color-magnitude diagrams for the NOT clusters galaxy population. The solid line is the fit to the red sequence and the dotted line is the upper 0.2 magnitude limit. Right panels: The histograms of the B-r distance of the galaxies to the corresponding red sequence. Red, Green, Blue and Purple colors refer to galaxies classified as Elliptical, Lenticular, Spiral and Irregular galaxies respectively.

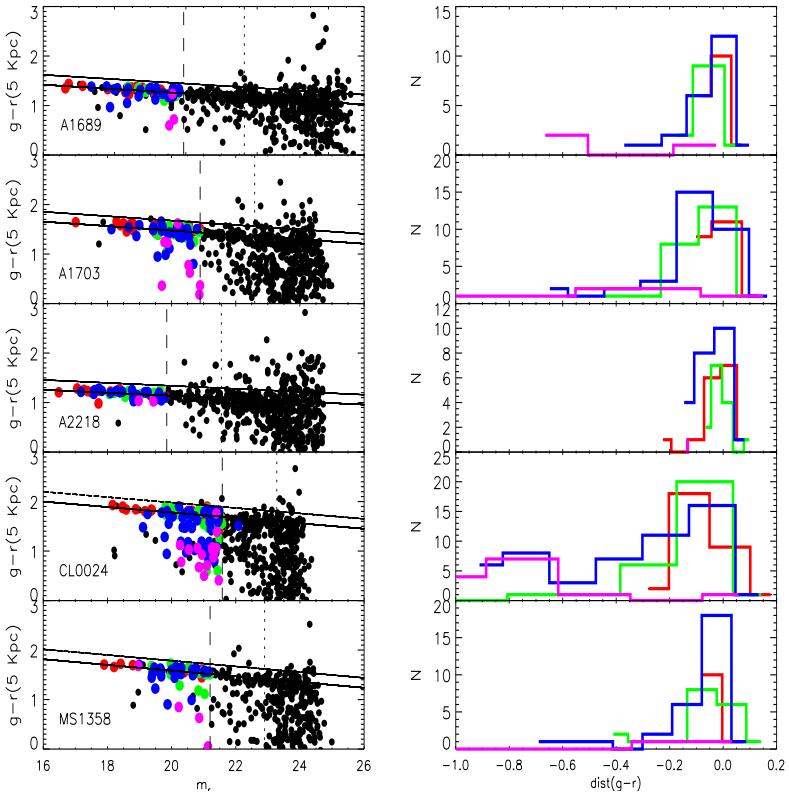

Figure 3.6: Left panels: The color-magnitude diagrams for the ACS clusters galaxy population. The solid line is the fit to the red sequence and the dotted line is the upper 0.2 magnitude limit. Right panels: The histograms of the g-r distance of the galaxies to the corresponding red sequence. Red, Green, Blue and Purple colors refer to galaxies classified as Elliptical, Lenticular, Spiral and Irregular galaxies respectively.

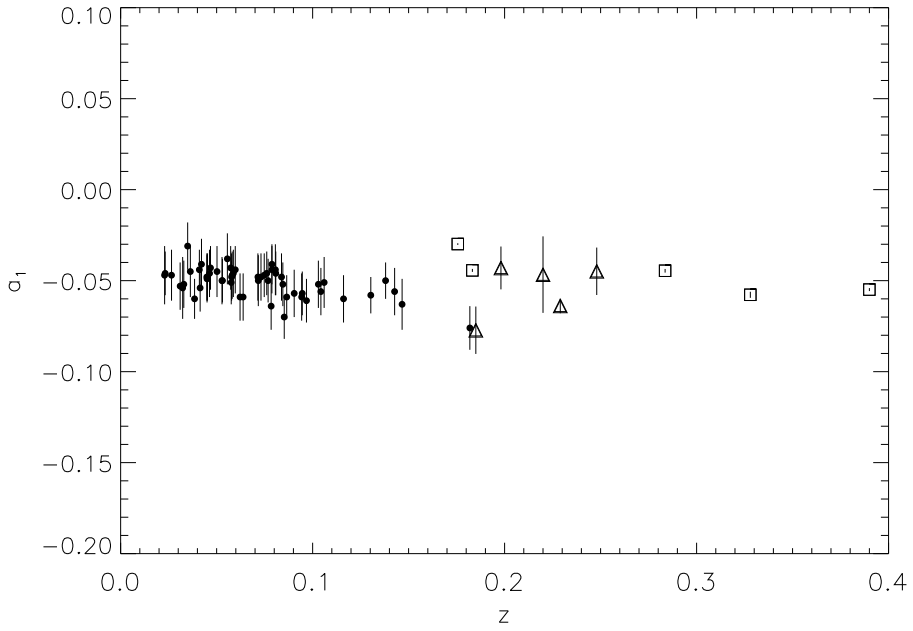

Figure 3.7: Slopes of the CMR for the sample of López-Cruz, Barkhouse & Yee (2004) (black circles), NOT sample (empty triangles) and ACS sample (squares).

even up to z$\sim$1.26. This result would indicate that the stellar populations of the bright, early type galaxies defining the cluster red sequence were settled afterwards the galaxy formation.

3.2 The Butcher-Oemler Effect

As we have previously seen, Butcher & Oemler (1984) found evidence for a possible evolutionary trend of the cluster population: the increasing of the galaxy blue fraction in clusters with redshift, known afterwards as the Butcher-Oemler Effect. Subsequent works (Rakos & Schombert, 1995; Margoniner & de Carvalho, 2000; Margoniner et al., 2001), confirmed that tendency, quantifying also its large dispersion and its dependence with other clusters characteristics. The original analysis of this effect by Butcher & Oemler (1984), defined blue galaxies as those within a radius containing 30 % of the cluster population, which are brighter than M_V=-20 and bluer by 0.2 mag in $B-V$ than the colour-magnitude relation defined by the cluster early-type galaxies.

In this section, we have studied the fraction of blue galaxies, f_b of the bright population, $M_r \leq -20$, for the clusters sample presented in this work. Regarding the NOT sample, we have considered blue galaxies those with $B-r$ color at least 0.26 magnitudes bluer than the red sequence. This color index corresponds to the original Butcher-Oemler definition. The transformations have been performed following the prescriptions by Quintana et al. (2000); Goto et al. (2003); De Propris et al. (2004). For the ACS sample, we have adopted a $g-r$ index of 0.2 as prescribed by Goto et al. (2003). Given the photometric errors and the statistical nature of the k-correction we have just adopted that common value of the color index for all the clusters in spite of their differences in redshift. The results are not substantially affected if individual color values were adopted.

Several authors have noticed that the fraction of blue galaxies strongly depends on the magnitude limit and the cluster-centric distance used (Margoniner & de Carvalho, 2000; Ellingson et al., 2001; Goto et al., 2003; De Propris et al., 2004; Andreon et al., 2006). They observed that f_b grows when the magnitude limit is fainter and the aperture is larger, which reflects the existence of al large fraction of faint blue galaxies in the outer regions of the clusters.

The fraction of blue galaxies has been computed for each cluster using all the surveyed area. In order to compare our results for the different clusters with other studies, we have considered that our results are representative of the area corresponding to a circular aperture that has the same center than the cluster and includes all the area that we have actually covered. For comparison purposes, we have adopted two apertures for the NOT sample, of radius 420 kpc and 735 kpc respectively. For the cluster A2658, only the smaller aperture could be used. For the ACS sample, an aperture of 475 kpc has been selected. In the original definition given by Butcher & Oemler (1984), the fraction was

calculated for an aperture containing 30% of the cluster population (R_{30}). Since only the central parts of our clusters were sampled we could not determine the value of R_{30} for them. The fixed apertures we have used are a substitute of the canonical value. We notice that they are in the range of the expected R_{30} values as given by Butcher & Oemler (1984).

The errors attributed to the measured fractions were computed assuming Poissonian statistics following the prescriptions set in De Propris et al. (2004). In other words, if the blue fraction is defined as the ratio of m blue galaxies observed out of n total galaxies and assuming that m and n obey Poissonian statistic, the blue fraction is

$$f_b = \frac{m}{n}$$

and its likelihood probability function has the following form with n fixed in advance.

$$L \sim f_b^m (1 - f_b)^{n-m}$$

whose maximum is m/n. Let's note that the form of that function is the same for a Poisson or binomial statistics. The variance of the blue fraction can be computed as

$$\sigma^2(f_b) = \begin{cases} \left(\frac{d^2 \ln L}{df_b^2}\right)^{-2} = \frac{m(n-m)}{n^3} & \text{if } n \neq 0 \\ 1/2n & \text{if } n = 0 \end{cases}$$

The value for $m = 0$ is set as $1/2n$ as a reasonable error bar to adopt for the $m = 0$ case (De Propris et al., 2004). The blue fraction values are listed in Tables 3.6 and 3.7 for both samples.

Table 3.6: Blue galaxy fraction of galaxies in NOT sample

Name	$f_b(420kpc)$	$f_b(735kpc)$
A 1643	0.090 ± 0.086	0.090 ± 0.086
A 1878	0.363 ± 0.102	0.517 ± 0.092
A 1952	0.250 ± 0.088	0.285 ± 0.085
A 2111	0.031 ± 0.030	0.125 ± 0.052
A 2658	0.083 ± 0.079	

Regarding the cluster A2111, Butcher & Oemler (1984) obtained a blue fraction of 0.16 ± 0.03 within a r_{30} that, for this cluster, corresponds to 892 kpc. Miller, Oegerle & Hill (2006) obtained, for the same aperture, the values of 0.15 ± 0.03 and 0.23 ± 0.03 using all the photometric data or only galaxies with spectroscopic data, respectively. We have obtained 0.031 ± 0.030 and 0.125 ± 0.052 for our 420 kpc and 735 kpc aperture, a smaller value, in agreement with

Table 3.7: Blue galaxy fraction of galaxies in ACS sample

Name	$f_b(475kpc)$
A 1689	0.048 ± 0.034
A 1703	0.111 ± 0.049
A 2218	0.024 ± 0.024
CL0024	0.315 ± 0.054
MS1358	0.111 ± 0.052

the smaller aperture, even if not significantly different when the errors are taken into account.

De Propris et al. (2003b) computed the blue fractions in a sample of clusters selected in the K-band. Three clusters from the ACS sample are in common with their sample: A1689, CL0024 and MS1358, obtaining blue fraction values of 0.046 ± 0.038, 0.046 ± 0.050 and 0.081 ± 0.044, respectively. Those values were calculated in a 0.5 Mpc aperture and with a cutoff brighter than the original Butcher-Oemler definition. We observe that these values corresponding to K-selected samples are slightly smaller than the values we have obtained in this work optically selected sample in agreement with the results found by De Propris et al. (2003b). Additionally, the blue fraction of MS1358 has been estimated by Luppino et al. (1991) to be $0.10 < f_b < 0.18$ depending on the background correction, which agrees with the range we have obtained in this work.

In Figure 3.8, we show the blue fraction of galaxies in the NOT and ACS clusters as a function of redshift within a radius of 420 and 475 kpc, respectively. Also, in Figure 3.9, the blue fraction for the NOT sample within a radius of 735 kpc is given. We have also plotted for comparison the blue fraction of galaxies obtained from a sample of nearby galaxy clusters by De Propris et al. (2004) within an aperture of $r_{200}/2$. As can be seen in the Figure, our errors bars are very similar to those given by De Propris et al. (2004). In all cases, we have more than 10 galaxies per cluster to compute the blue fraction. The comparison with the data by De Propris et al. (2004), clearly indicate that there is no relation between the value of the blue galaxy fraction and the cluster redshift.

The range of values found is also similar to that found by De Propris et al. (2004) for lower redshift clusters. In particular, the very high blue fraction we obtain for A1878 is found for some lower z clusters in the quoted reference. The central median values we find are $< f_b >$=0.090 ± 0.138 for the 420 kpc and 0.285 ± 0.194 for the 735 kpc aperture in the NOT sample and 0.111 ± 0.114 for the 475 kpc aperture in the ACS sample, in agreement with the median f_b value, 0.162 ± 0.125 of De Propris et al. (2004) for an aperture of $r_{200}/2$.

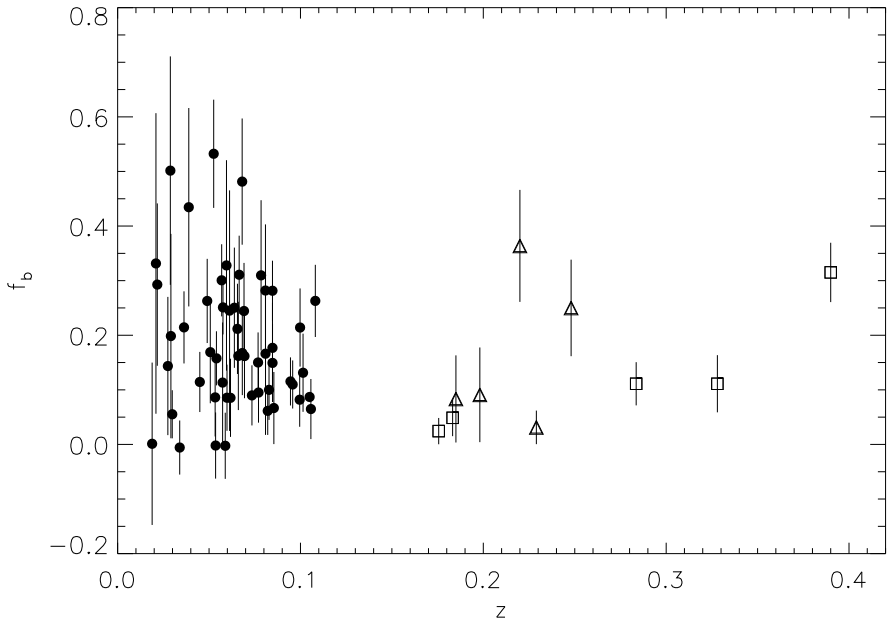

Figure 3.8: Blue fraction of galaxies in NOT (empty triangles) and ACS (empty squares) sample of clusters compared with those obtained by De Propris et al. (2004) (black circles) computed within an aperture of 420 kpc (NOT sample), 475 kpc (ACS sample) and $r_{200}/2$ (De Propris et al., 2004)

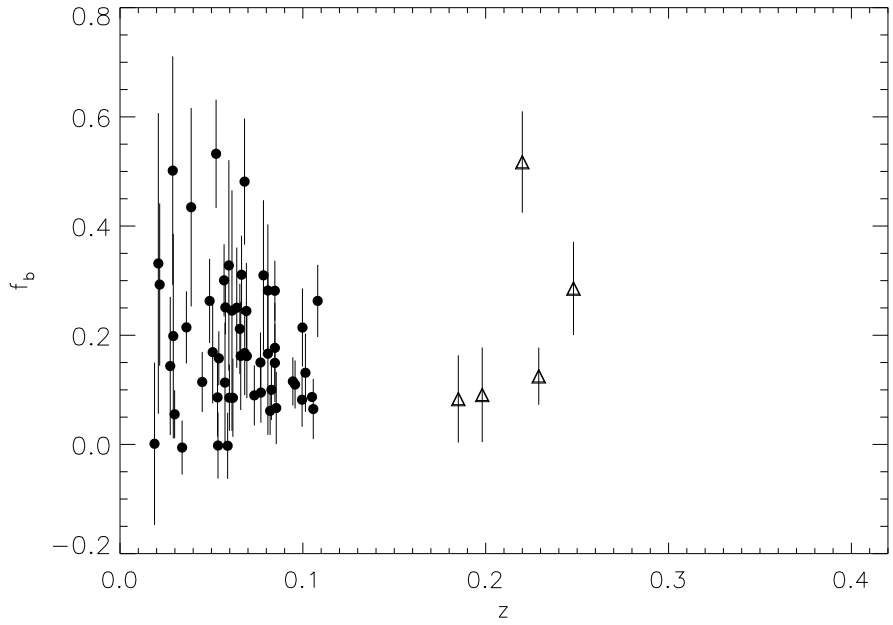

Figure 3.9: Blue fraction of galaxies in NOT sample of clusters (empty triangles) computed within an aperture of 735 kpc, compared with those obtained by De Propris et al. (2004) (black circles) within an aperture of $r_{200}/2$.

We find a nominal difference in the blue fraction as a function of the aperture, in the sense of an increase with the aperture. This is in agreement with the findings by Margoniner & de Carvalho (2000); Goto et al. (2003); De Propris et al. (2004). Unfortunately the statistic errors are too large for the difference to be significant. The apertures used by De Propris et al. (2004) refer to $r_{200}/2$, which is not too different from our 735 kpc aperture.

Chapter 4

Galaxy Morphology

Centellas y meteoros se cruzan con mis gritos
te amo mientras mis pulmones crean la Vía Láctea de nuevo
y el sol vuelve a nacer redondo y amarillo de mi boca
la luna se me suelta de los dedos
Marte, Plutón, Neptuno, Venus, Saturno y sus anillos
las novas, súper novas, los agujeros negros
anillos concéntricos de galaxias innombrables.

Gioconda Belli, 'Nueva teoría sobre el Big Bang'

Since the discovery of the nature of the galaxies, by Edwin Hubble, Hubble (1926), a number of attempts to set a morphological classification for the galaxies has been tried. The most popular classification, given by the same Hubble, was initially developed to classify nearby galaxies in the optical and slightly modified later on by de Vaucouleurs (1959, 1963); van den Bergh (1997). Sandage (1961) illustrated the final Hubble revision. Additional classification systems are, for example, the Yerkes system (Morgan, 1958, 1962) or the luminosity system for spiral galaxies by van den Bergh (1960).

Hubble's classification separated galaxies into two big groups. On one hand, the early type galaxies (elliptical and lenticular galaxies) and on the other hand, late type galaxies (spiral and irregular galaxies). These types were initially thought to form an evolutionary sequence. In particular, the sequence was best defined for spiral galaxies since three classification criteria were available: the relative strength of the bulge, the degree of the resolution of the arms and the openness of the arms.

At present, that system continues being used in many low redshift works, as some physical trends, even with a large dispersion, are associated to each morphological type such as the mean luminosity or the mean colors. For example, early type galaxies possess an older red stellar population, have very little hydrogen and are usually comparatively bright. On the contrary, late type galaxies

have a blue young stellar population, are rich in gas and have generally lower surface brightness than early types. Intermediate types have transitional properties between these extremes.

Furthermore, a number of works have found different correlations between galaxy parameters for a fixed Hubble morphological type. For example, elliptical galaxies present a tight sequence between color index and magnitude, called the Color-Magnitude Relation (Visvanathan & Griersmith, 1977), a relationship between luminosity and central velocity dispersion (Faber & Jackson, 1976), luminosity and metallicity (Terlevich et al., 1981) or between surface brightness, radius and velocity dispersion, more commonly known as the Fundamental Plane (Dressler et al., 1987; Djorgovski & Davis, 1987; Jorgensen, Franx & Kjaergaard, 1992). Likewise, spiral galaxies show correlations between luminosity and rotation velocity (Tully & Fisher, 1977), among others.

However, with the new advances of the technology and the advent of huge telescopes and spatial telescopes, we have been able to observe more and more distant galaxies. What is more, it has been noticed that the morphologies observed for the nearby galaxies as well as the interaction rate of galaxies are changing as the redshift grows (Patton et al., 2000; Conselice, Gallagher & Wyse, 2001; De Propris et al., 2007).

In addition, not only the number of galaxies to process grows exponentially as we arrive deeper in the Universe but the projected size of the galaxy diminishes as they are further away and their morphological details are much more difficult to distinguish with our perception. Therefore, the need of establishing a quantitative morphological classification, without relying on the subjective human eye is more and more compelling. Nevertheless, this aim has not been still solved successfully.

We should not forget that we are dealing with two-dimensional images or in the best of the cases, we may have redshift information provided by spectra. Consequently, we suffer a lack of information at analyzing these data that translates into uncertainty. For example, the high inclination of a galaxy can lead us to completely misinterpret its morphology. Nevertheless, we can not recover this information by quantitative morphologies neither for a particular galaxy and we have to appeal to statistical methods.

In this Chapter, we have classified visually our sample of bright galaxies with the Hubble system into Elliptical, Lenticular, Spiral and Irregular galaxies. This procedure has been possible as the range of redshift is within the limit to allow the human eye to distinguish the morphological signatures of the bright ones, (see, for example Fabricant, Franx & van Dokkum (2000)). Thus, we have explored the differences with other classifications available in the literature. After that, we have computed the concentration parameter of the sample to study correlations with morphology. Finally, the last part of this chapter is dedicated to the study of the degree of interaction in the cluster samples and its relation with the morphology.

4.1 Visual classification

All the galaxies brighter than $M_r = -19.5$ in both samples, were classified visually into four different Hubble types: Elliptical (E), Lenticular (S0), Spiral (Sp) and Irregular (I) galaxies. Finer classifications were found to be much more uncertain. For the NOT sample, we have compared our classification with that reported by Fasano et al. (2000) for the galaxies in common. The morphological classification for that bright subsample is given in the last column of the Table A.1 in the Appendix.

The difficulty of separating E+S0 and Sp has been discussed widely in the literature, (see Smail et al. (1997); Fabricant, Franx & van Dokkum (2000)). Unfortunately, using external information to verify E+S0 versus spiral morphologies is quite difficult. We know that certain properties, such as spectral features or colors correlate with morphology but with a significant scatter. In addition, distinguishing features such as spiral arms, discs, star-forming regions... may be not feasible due to the surface brightness dimming or resolution effects.

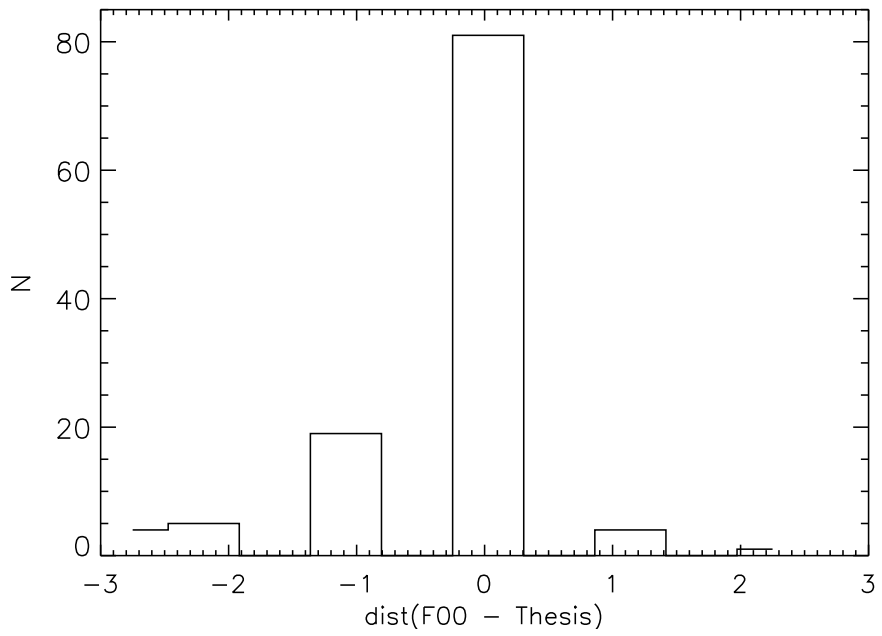

Figure 4.1: Visual classification difference for the galactic population in NOT sample between Fasano et al. (2000) and this work.

In Figure 4.1, we show the result of this comparison. Notice that 70% of the galaxies were classified with the same type, whereas other 20% differ by only one type. Additionally, the distribution of the differences seems to be skewed to negative values. In other words, the classification given by Fasano et al. (2000)

tends to classify more galaxies as early types than in our work. That deviation may be due to the difficulty of distinguishing between lenticular and early spiral galaxies.

Regarding the ACS sample, we have also found visual classifications in the literature for three clusters. For A1689, we have compared our visual classification with the one performed by Teague, Carter & Gray (1990) and Duc et al. (2002). We have obtained few galaxies in common, as their morphological classifications refers mostly to bright objects. The differences have been plotted in Figure 4.2. As we see, there is a good agreement with these authors, obtaining that 75% of the objects have the same type in both classifications. In addition, we have not detected any bias to positive or negative values, which is easily explained as we are comparing the brighter objects, that are easier to assign a morphological type.

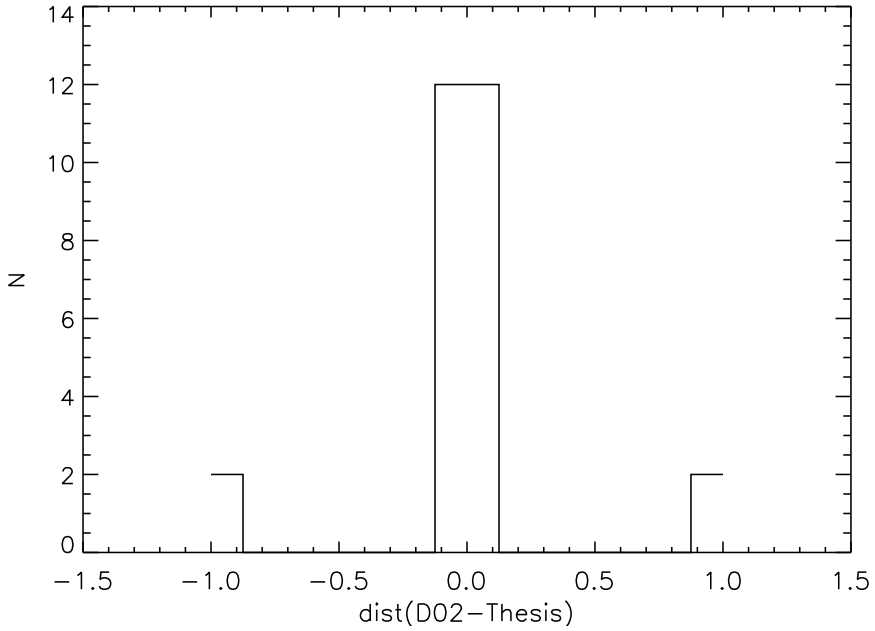

Figure 4.2: Visual classification differences in A1689 between Duc et al. (2002) and this work.

CL0024 is the cluster from the ACS sample, which has the largest number of galaxies visually classified in common. The classification is given by Treu et al. (2003), and achieves similar magnitude limits than us. We have identified 86 galaxies in common, with a very good agreement: 76.74 % of them has been classified with the same morphological type, as it is shown in Figure 4.3. It is noticeable that the distribution is skewed to negative values, as in the case of the galaxies in NOT sample.

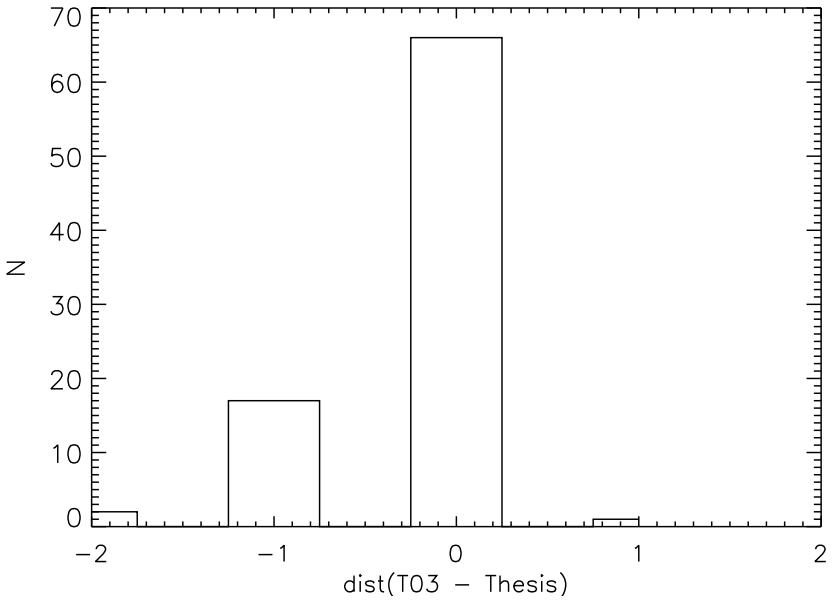

Figure 4.3: Visual classification differences in CL0024 between Treu et al. (2003) and this work.

Finally, Fabricant, Franx & van Dokkum (2000) have performed a visual classification of the galactic population in MS1358, finding only nine galaxies in common, six of which, are of the same type, achieving a coincidence of 66.6%. The difference distribution has been plotted in Figure 4.4. Again, as we are comparing bright objects, the distribution is not skewed to positive or negative values.

Therefore, we can conclude that an overall good agreement between different authors is achieved regarding visual morphological classification. It is also true that the coincidence is always below 80% due to known problems to separate Eliptical galaxies from Lenticular galaxies or even from Early Spiral types.

In Table 4.1 we show the percentages of the different galaxy types in the central part of each cluster in the NOT sample. Similarly, in Table 4.2, the percentages of the different galaxy types in the central part of each cluster of the ACS are collected. Notice that A1643 has a large number of spiral galaxies (around 57%). On the other hand, A1878 contains also a great proportion of late-type galaxies (62-67%), including a large fraction of irregular galaxies (19-26%). Also MS1358, has 49% of late-type galaxies and CL0024 51 %, including 12% of irregular galaxies.

The largest fraction of elliptical galaxies in the ACS sample is 31 %, while we have two cluster in NOT sample, A1952 and A2658 with an elliptical morphology of more than 50% of the population. A diversity is clear as far as morphological

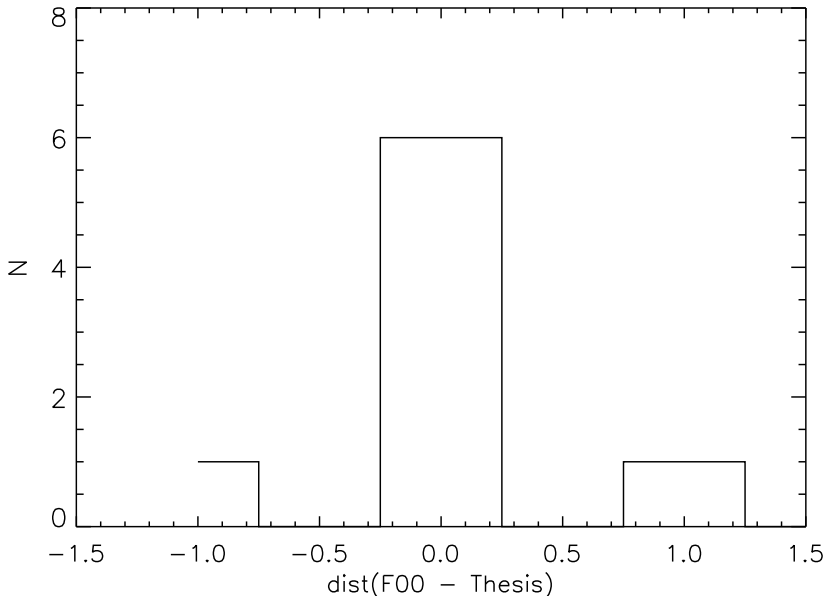

Figure 4.4: Visual classification differences in MS1358 between Fabricant, Franx & van Dokkum (2000) and this work.

populations is concerned.

Within that diversity, it is relevant the fact that the fraction of lenticular galaxies is similar in all clusters (within a 10% of variation). This is an important aspect to consider when analyzing the evolution of the morphological content in clusters.

4.2 The Concentration Parameter

The Concentration Parameter was introduced by Butcher & Oemler (1978) as a measurement of the degree of regularity of the morphological content in each cluster. It was defined as:

$$C = \log(R_{60}/R_{20})$$

where R_{60} and R_{20} are the radii containing 60% and 20% of the cluster populations. Ideally, we should measure the galaxy density in all the cluster area to determine the radius. As the whole cluster population is very difficult to establish, we have tried to estimate that the area covered in our sample is well in the range of the values given by Butcher & Oemler (1978). Comparing to their data, we see that this is a remarkable value to compute the concentration

Table 4.1: Fraction of Morphological Types in NOT sample

Name	420kpc				735kpc			
	E	S0	S	I	E	S0	S	I
A 1643	0.22	0.22	0.56	0.00	0.24	0.19	0.57	0.00
A 1878	0.11	0.22	0.41	0.26	0.14	0.24	0.43	0.19
A 1952	0.52	0.28	0.20	0.00	0.45	0.31	0.24	0.00
A 2111	0.38	0.28	0.28	0.00	0.35	0.28	0.30	0.08
A 2658	0.54	0.31	0.15	0.00				

Table 4.2: Fraction of Morphological Types in ACS sample

Name	475kpc			
	E	S0	S	I
A 1689	0.31	0.22	0.42	0.05
A 1703	0.24	0.28	0.38	0.09
A 2218	0.29	0.25	0.42	0.04
CL0024	0.24	0.25	0.39	0.12
MS1358	0.20	0.31	0.44	0.05

parameter as it would correspond to the mean aperture where more of the 80% of the population is found. In any case, we caution that the apertures used to determine the concentration parameter might be not completely appropriate.

We have calculated the concentration parameter of our clusters in the central 735 kpc. Only the four clusters from the NOT sample were analyzed as the rest of the clusters were not covering enough area to compute that quantity. For the rest of the clusters we have used the concentration value extracted from the literature if available.

The concentration values we have found for the NOT sample are collected in Table 4.3. Butcher & Oemler (1984) computed the concentration values for A2111, A1689, A2218 and CL0024, being 0.40, 0.55, 0.59 and 0.53 respectively, while Fabricant, McClintock & Bautz (1991) estimated the concentration value of MS1358 to be 0.49. The value obtained for A2111 is quite similar to the value we find, and for the rest, we notice that the values we obtain are higher than the NOT sample, which indicates that the ACS clusters are more concentrated than the NOT sample, as we will see in Chapter 6.

We have plotted these values in Figure 4.5, together with the values for lower redshift clusters, as given by Butcher & Oemler (1978) and for a higher redshift sample presented in Dressler et al. (1997). As can be seen in the Figure, our concentration values span the full range of the values measured for lower redshfit

Table 4.3: Concentration Parameter in NOT Clusters

Name	C
A 1643	0.311
A 1878	0.389
A 1952	0.696
A 2111	0.329
A 2658	

clusters. Moreover, this range encompasses also that of the higher redshift clusters concentration values. It does not seem therefore, that there is any clear tendency of the concentration parameter with redshift or morphological types. The NOT sample tends to progressively populate the lower half of the plane when the redshift increases, while ACS clusters are placed in the higher half of the plane, indicating that clusters in ACS sample are richer and more compact than those in NOT sample. Again, these results must be taken with caution.

Likewise, Butcher & Oemler (1978); Dressler et al. (1997) suggested that the more irregular, less concentrated clusters would be preferentially populated by late type galaxies. In that sense, we notice that A1643, the cluster with the largest global fraction of late-type galaxies, presents the lowest value of the concentration parameter. Moreover, A1878, another cluster with a low concentration index presents also a rather high fraction of late type and irregular galaxies and, in fact, is dominated by this population. However, A2111, our third cluster with a low concentration, is dominated by an early-type population. All in all, although there is an indication for the higher fraction of irregular clusters with increasing redshift, the small statistics prevent us to extract a firm conclusion.

4.3 Interaction systems

Other interesting feature that could deserve consideration in clusters at this range of redshift is the proportion of interacting systems compared to lower redshift clusters. To do that, we have calculated the distribution of the **perturbation, f-parameter** defined by Varela et al. (2004) for the galaxies in the final catalogue of cluster galaxies as

$$f = \log(\frac{F_{ext}}{F_{int}}) = 3\log(\frac{R}{D_p}) + 0.4 \times (m_G - m_p) \tag{4.1}$$

where m_G and m_P are the apparent magnitudes of the primary and perturber galaxies respectively, D_p is the projected distance between the galaxy and the perturber, and R is the size of the galaxy. That parameter is a measurement of

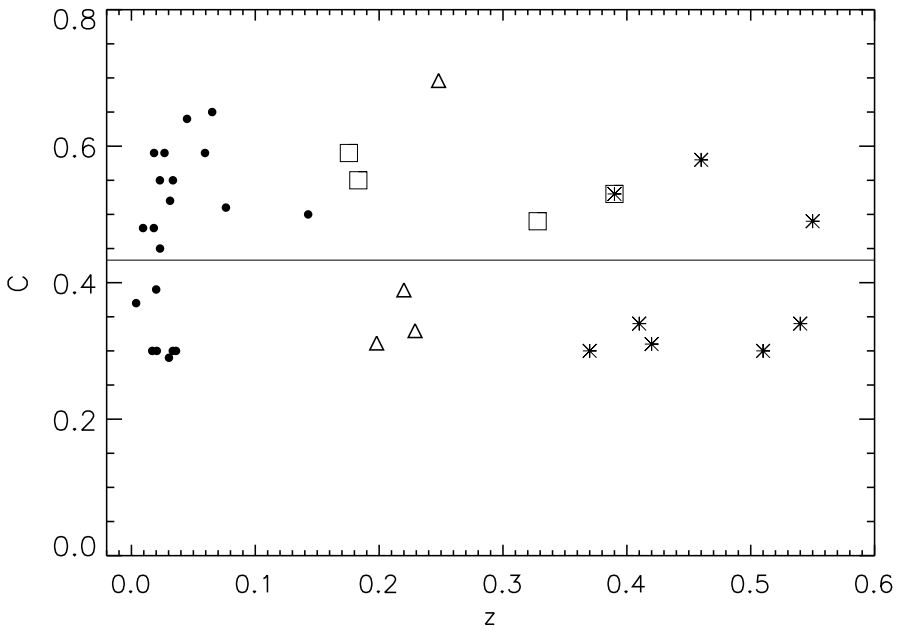

Figure 4.5: Concentration parameter versus redshift for NOT clusters (triangles), a low-redshift compilation (Butcher & Oemler (1978): black points) and a higher redshift sample (Dressler et al. (1997): asteriks). The squares represent the values for the ACS extracted from the literature. The horizontal line is the mean concentration value of our the clusters with enough area coverage

the tidal forces exerted by the perturber, P, on the primary galaxy, G, and the internal force per unit mass in the outer parts of the primary.

The f-parameter gives an account of the relative importance of the tidal forces for every galaxy. The results we found are plotted in Figure 4.6 and 4.7 for the NOT and ACS sample respectively. The median value of the distribution is -1.85 for the NOT sample and -1.76 for the ACS sample, whereas the median value found for the Coma Cluster amounts to -2.7 (Varela et al., 2004). Moreover, we find that 63.97% of the galaxies have a perturbation parameter higher than -2 for the NOT sample and 60.05% of the galaxies for the ACS sample. This is the value chosen by Varela et al. (2004) to select truly interacting systems. These results are suggestive of the presence of a higher fraction of interacting systems in our sample, compared to Coma.

A particular view at the situation in each cluster is collected in Tables 4.4 and 4.5 for both samples. Those tables show the median f-values. We note that A1643 from the NOT sample and CL0024 and MS1358 from the ACS sample, have perturbation parameters which are very close to -2, while they drop to more positive values for A1878, A1952, A2111 and A2658 (NOT sample) and

A1689, A1703 and A2218 (ACS sample) pointing to a more disturbed population than Coma cluster. Nevertheless, more clusters at different redshift need to be explored to extract significant results.

Table 4.4: Median Perturbation f-Parameter for NOT Clusters Sample

Name	f
A 1643	−1.92
A 1878	−1.60
A 1952	−1.29
A 2111	−1.67
A 2658	−1.39

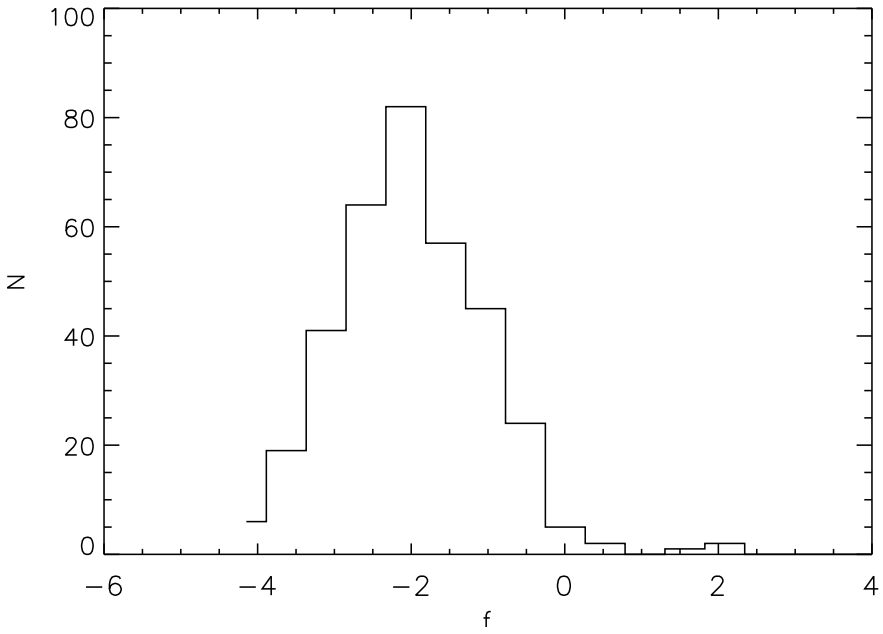

Figure 4.6: Histogram of the f-parameter values for the galaxies belonging to NOT sample.

Table 4.5: Median Perturbation f-Parameter for ACS Clusters Sample

Name	f
A 1689	−1.68
A 1703	−1.67
A 2218	−1.56
CL0024	−1.94
MS1358	−2.08

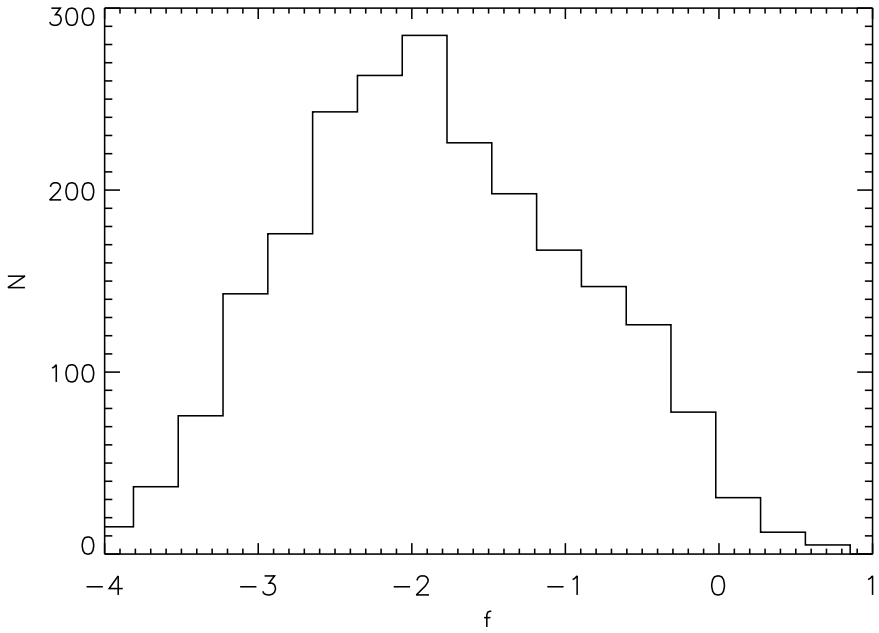

Figure 4.7: Histogram of the f-parameter values for the galaxies belonging to ACS sample.

Chapter 5

Galaxy Surface Brightness Analysis

L'ordinador simula el naixement dels estels
L'ordre matemàtic simula el món real,
crea un altre món -de càlcul, i mental-
regit per lleis exactes, hipòtesis, models:
en un ordinador reneixen els estels
com fa tants anys nasqueren, en brous primordials.
I som com creadors!: veiem a la pantalla
Un món tot just nascut. Una galàxia qualla.
Es formen els estels -i tot sota control!
I regulem el temps i dominem el Sol,
i musiquem i tot la còsmica rondalla!
-fins que el flux elèctric, de cop i volta, es talla.

David Jou, 'El color de la ciència'

The first observations of galaxies provided evidence about the radial symmetry of the galaxies and consequently, a number of pioneering works attempted to describe the light distribution in galaxies taking advantage of that fact. For example, Reynolds (1913) proposed a variation of luminosity in the central region of M31 (without the spiral arms) with the following form:

$$\frac{constant}{(x+1)^2}$$

where x is the projected distance to the centre.

Some years later, in 1930, Hubble introduced an analytical mathematical ex-

pression to fit the light distribution of the galaxies:

$$\frac{I_0}{(\frac{r}{a}+1)^2}$$

where I is the **surface brightness**, (that is, the energy flux per surface unit) at a distance r from the center of the galaxy, I_0 is the central surface brightness and a is a parameter depending on each galaxy.

It was, however, nearly two decades later, when de Vaucouleurs (1948), introduced one of the most popular, obtained empirically, model for describing the light distribution in elliptical galaxies. It is the **de Vaucouleurs Law**, also called the $r^{1/4}$ **law** due to its mathematical form:

$$\log I = \log I_e - 3.33[(r/r_e)^{1/4} - 1] \tag{5.1}$$

where, again I is the surface brightness at a distance r from the center of the galaxy, r_e is the **effective radius** or the radius enclosing half of the total luminosity of the galaxy and I_e is the surface brightness at a distance r_e from the center of the galaxy.

Regarding to more complex morphological profiles, e.g. lenticular or spiral galaxies, two main components have to be differenced: the bulge and the disc. Bulges usually are described by a $r^{1/4}$ profile. On the contrary, discs are better approximated by an **exponential law**, which was introduced by Freeman (1970)

$$I(r) = I_0 e^{-r_d/h} \tag{5.2}$$

where I_0 and h are the central intensity and disc scale length, respectively. The exponential law has been extensively used in the literature to model the surface brightness profile of the discs showed by spiral galaxies, (e.g. Trujillo et al. (2001c); Aguerri et al. (2005); Allen et al. (2006)).

Equations 5.1 and 5.2 are particular cases of a more general form of representing the galaxy surface brightness, introduced by Sersic (1968), the **Sersic law**. The radial variation of the intensity of this law is given by:

$$I(r) = I_e 10^{-b_n[(r/r_e)^{1/n}-1]} \tag{5.3}$$

where r_e is the effective radius, I_e is the intensity at r_e and n is the **shape parameter**, which regulates the steepness of the light profile in the model. Finally, b_n is coupled to n and it is obtained from solving the equation

$$\Gamma(2n) = 2\gamma(2n, b_n)$$

in which Γ and γ represent the mathematical function gamma and incomplete gamma, respectively. That equation can be approximated by $b_n = 0.868n - 0.142$ so that half of the total luminosity is within r_e (see Caon, Capaccioli & D'Onofrio

(1993); Trujillo et al. (2001c)). The Sersic law has been extensively used in the literature to model the surface brightness of elliptical galaxies (Graham & Guzmán, 2003), bulges of early and late-type galaxies (Andredakis, Peletier & Balcells, 1995; Prieto et al., 2001; Aguerri et al., 2004; Möllenhoff, 2004), the low surface brightness of blue compact galaxies (Caon et al., 2005; Amorín et al., 2007), or dwarf elliptical galaxies (Binggeli & Jerjen, 1998; Graham & Guzmán, 2003; Aguerri et al., 2005), among others.

The Sersic model was initially conceived to be able to fit any morphological type with the flexible shape parameter n. For $n = 0.5$ a Sersic model becomes a gaussian profile, for $n = 1$, it turns into a pure exponential, while for $n = 4$, it reduces to a classical de Vaucouleurs profile.

All of those profiles are uni-dimensional. In other words, the fit is doing throughout an axis that crosses the galaxy or with an azimuthal average of the bi-dimensional surface brightness distribution. Therefore, they do not take into account some two dimensional features such as for example, the position angle of the bulge and disk component (Trujillo et al., 2001c), or the intrinsic shapes (Prieto et al., 2001), leading frequently to systematic errors in the results of the fit (Byun & Freeman, 1995).

Many tools have been developed in the last years in order to provide two-dimensional parametric bulge-disk decomposition of the galaxies surface brightness profiles. To quote some of them, GIM2D (Galaxy IMage 2D; Simard (1998)), GALFIT (Peng et al., 2002), BUDDA (Bulge/Disk Decomposition Analysis; de Souza, Gadotti & dos Anjos (2004)), GASPHOT (Galaxy Automatic Surface PHOTometry; Pignatelli, Fasano & Cassata (2006)) or GASP-2D (GALaxy Surface Photometry 2 Dimensional Decomposition; Méndez-Abreu et al. (2008)).

These methods were developed to solve different problems of galaxy decomposition when fiting the two-dimensional galaxy surface-brightness distribution. They use different minimizations routines to perform the fit and different functions to parametrize the galaxy components.

In the present work, the fits have been carried out using the automatic fitting routine, GASP-2D, developed and successfully validated by Méndez-Abreu et al. (2008). A number of reasons can be given for the selection of this routine. The algorithm is quasi-authomatical, what is very useful at dealing with a large number of galaxies. It is also very feasible and minimizes the interaction with the user. In addition, the computational time is not very high as it uses the robust Levenberg-Marquardt algorithm to fit the two-dimensional surface-brightness distribution of the galaxy (Press et al., 1992). In addition, it has the capability of searching for accurate initial trials before the fitting procedure to ensure a good convergence of the fit.

5.1 Two dimensional surface brightness fit

5.1.1 GASP-2D

The GASP-2D routine (Méndez-Abreu et al., 2008), performs a fully two-dimensional fit to the surface brightness of a galaxy. The photometrical galaxy components were characterized by elliptical and concentric isophotes with constant (but possibly different) ellipticity and position angle. We have assumed a cartesian coordinates system (x, y, z) with origin in the galaxy center, the x-axis parallel to the direction of the right ascension and pointing westward, the y-axis parallel to the direction of declination and pointing northward, and the z-axis along the line-of-sight and pointing toward the observer. The plane of the sky is confined to the (x, y) plane, and the galaxy center is located at the position $(x_o,\ y_o)$.

The isophotes of the Sersic models are concentric ellipses centred at (x_o, y_o) with constant position angle PA_b and constant ellipticity $\epsilon_b = 1 - q_b$. Thus, the radius r_b is given by:

$$\begin{aligned} r_b &= [(-(x-x_o)sinPA_b + (y-y_o)cosPA_b)^2 \\ &\quad -((x-x_o)cosPA_b + (y-y_o)sinPA_b)^2/q_b^2]^{1/2} \end{aligned}$$

We have called *bulge*, the photometric galaxy component fitted by a Sersic law in those galaxies fitted with two components. Similarly, we have considered that the disc isophotes are ellipses centered at the galaxy center (x_o, y_o) with constant position angle PA_d and constant ellipticity $\epsilon_d = 1 - q_d$, given by the galaxy inclination $i = arcos(q_d)$. Thus, the radius r_d is given by:

$$\begin{aligned} r_d &= [(-(x-x_o)sinPA_d + (y-y_o)cosPA_d)^2 \\ &\quad -((x-x_o)cosPA_d + (y-y_o)sinPA_d)^2/q_d^2]^{1/2} \end{aligned}$$

During each iteration of the fitted algorithm, the seeing effect has been taken into account by convolving the model image with a circular point spread function (PSF) extracted from the images using the fast Fourier transform (FFT) algorithm (Press et al., 1992), in the Fourier domain. Many works have widely discussed the seeing effect on the scale parameters of Sersic surface brightness profile, (e.g. Trujillo et al. (2001a,b)).

The routine fits all free parameters iteratively using a non-linear least-squares minimization method. It is based on the robust Levenberg-Marquardt method (Press et al., 1992), a wide explanation can be found in Chapter 7). Also, Poissonian and constant weights can be chosen to perform the calculation of the χ^2 and the options for setting boundary constraints or for fixing parameters are available.

One of the most important characteristics of this procedure consists on the adoption of accurate initial trials for the parameters to fit as it ensures the good convergence of the χ^2 distribution.

In a first step, the photometric package SExtractor (Bertin & Arnouts, 1996), measures positions, magnitudes and ellipticities of the sources in the image and afterwards, the elliptically averaged radial profiles of the surface brightness, ellipticity and position angle of the galaxy is derived with the *IRAF* task *ELLIPSE*. The spurious sources are masked automatically with SExtractor and the surface brightness is fitted with ellipses centered on the position of the galaxy center given by (x_0, y_0) in the two-dimensional fit. Also, the program has an option which allows to rotate the image to create the masks. This option is useful for the deblending of galaxies in interaction or very close.

Finally, the trial values are obtained by performing a one dimensional decomposition technique as for example, in Kormendy (1977); Prieto et al. (2001). An exponential law is fitted to the radial surface-brightness profile at large radii, where the light distribution of the galaxy is assumed to be dominated by the disk contribution. Then, the central surface brightness and scale length of the exponential are adopted as initial trials for I_0 and h, respectively. The first estimation of the light distribution of the bulge is given by the residual radial surface-brightness profile, fitted with a Sersic law. Conclusively, the bulge effective radius, effective surface brightness and shape parameter and the disk parameters that provided the best fit are adopted as initial trials for r_e, I_e and n, respectively.

The initial trials for ellipticity and position angles of the disk are found by averaging the values in the outermost portion of the corresponding radial profile. As far as the bulge is concerned, they are estimated by interpolating at r_e the radial profiles of the ellipticity and position angle, respectively.

Once, the trial values are determined, the nonlinear least-squares are initialized with those values, allowing them to vary. A model is considered to be convergent when the χ^2 achieves a minimum and the relative change of the χ^2 between the iterations is less than 10^{-7}. The output of the procedure consists on a model built with the fitted parameters convolved with the adopted circular two dimensional Gaussian PSF and subtracted from the observed image to obtain a residual image.

Two more iterations are performed to ensure the convergence of the algorithm and the no variation of the parameters with all the pixels and regions of the residual image with values greater or less than a fixed threshold, controlled by the user are rejected and initial trials the values obtained in the previous iteration.

We have also tested other packages, such as GALFIT (Peng et al., 2002), to extract structural components from our galaxy images. As GASP-2D, it uses a

Levenberg-Marquardt downhill-gradient method to derive the best fit. However, GALFIT does not search for initial trials, so it often converges on fit solutions, that represent a local minimum instead of giving the global minimum.

The surface brightness of the galaxies in our medium redshift NOT clusters were modelled using one or two photometrical components, depending on the morphological type of the galaxy (Ascaso et al., 2008b). The surface brightness profile of those galaxies modelled with only one component was described by a Sersic law while the surface brightness of those galaxies fitted with two photometrical components were described by a Sersic law plus an exponential one.

5.1.2 Simulations

One of the advantages of the quantitative morphology is that the accuracy of the obtained results can be tested by simulating artificial galaxies similar to the real ones. We have created a large number of artificial galaxies with one and two galactic components described by the mentioned previous equation. These modeled galaxies are similar to the galaxies observed in our medium redshift galaxy clusters.

We have generated 5000 images of galaxies with a Sersic component. The total magnitud, effective radius, shape Sersic parameter, and ellipticity of the simulated galaxies were similar to the observed in the real ones. They were asigned randomly to the models, and their values were in the ranges:

$$18 \leq m_r \leq 21; \quad 0.5\,kpc \leq r_e \leq 4\,kpc; \quad 0.5 \leq n \leq 6; \quad 0.7 \leq \epsilon_b \leq 1 \qquad (5.4)$$

We have also generated 5000 galaxies with two photometric components: Sersic plus exponential. These artificial galaxies have a central photometric *bulge* component, modeled by a Sersic law, and an external *disc* component, modeled by an exponential law. The total magnitud of these galaxies spans a range of $18 \leq m_r \leq 21$. The contribution to the total light from the bulge and disc components is given by the bulge-to-total light ratio. This parameter spreads over the range $0 \leq B/T \leq 1$. The bulge parameters of the simulated galaxies were:

$$0.5\,kpc \leq r_e \leq 4\,kpc; \quad 0.5 \leq n \leq 6; \quad 0.2 \leq \epsilon_b \leq 1 \qquad (5.5)$$

Finally, the disc free parameters of the galaxies were distributed in the ranges:

$$1.75\,kpc \leq h \leq 4.7\,kpc; \quad 0.2 \leq \epsilon_b \leq 1 \qquad (5.6)$$

In order to mimic the same instrumental setup, we have added a background level and photon noise to these artificial images similar to the observed images.

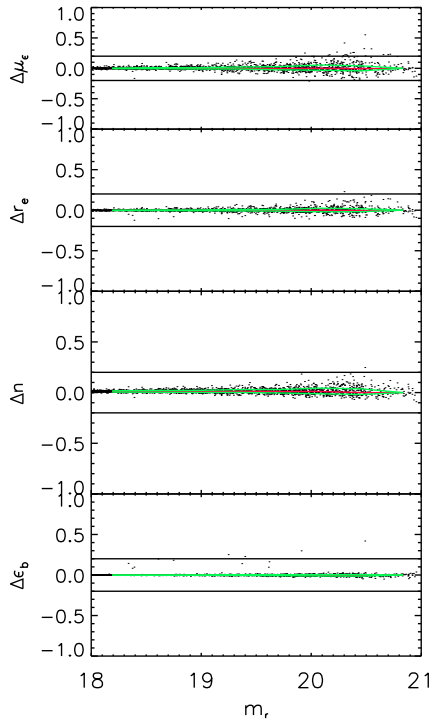

Figure 5.1: Plots of the magnitudes versus parameters of the Sersic profile. The horizontal lines in each panel are the 20% of the error. The green and red lines are the quartile (25%) and median of the error respectively in bins

They were also convolved with a PSF, simulating the seeing that we have in our observations. Finally, these simulated galaxies were fitted using the same procedure as for the real ones.

5.1.3 Galaxies with one photometrical component

In the present subsection, the results of the simulations for one Sersic component are examined. In Figure 5.1, we show the relative errors of the free parameters recovered from the simulated galaxies with only one component as a function of their magnitude. A galaxy is considered to be adequately fitted when all the free parameters are recovered with relative errors less than 20%.

We have previously explored the minimum conditions for the fits to extract reliable results, without depending on the image conditions. The conclusion is that the goodness of the fits depends on the number of pixels (area) used by the

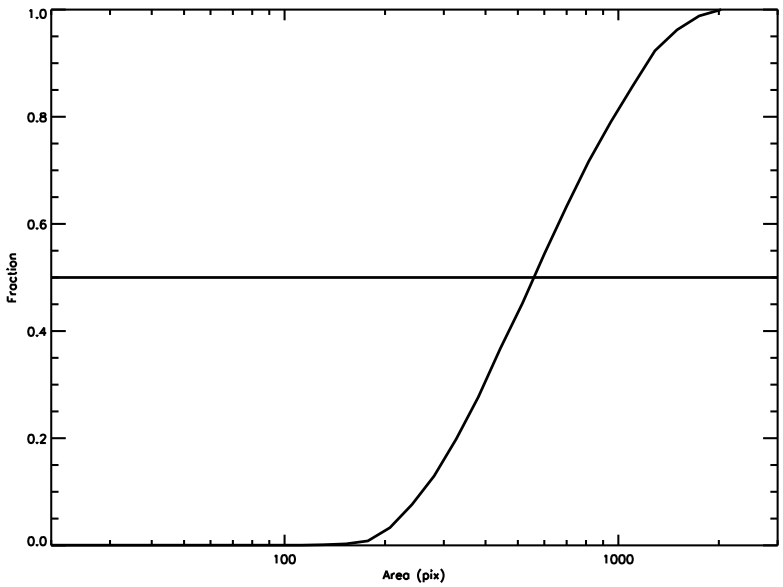

Figure 5.2: Cumulative distribution of the simulations which have an error within 20% versus area for the Sersic Profile. The horizontal line marks the 50% of the distribution.

fitting routine. The recovered fitted parameters have very large errors for areas below a minimum one. This area depends on the number of free parameters used in the fits, the seeing of the images and the S/N of the fitted galaxies.

In Figure 5.2, the fraction of simulated galaxies with one Sersic component for which their parameters were recovered with relative errors smaller than 20% is shown. We have defined the minimum area of the galaxies for which the image conditions were not affecting the goodness of the fit as the value where all the fits for which the recovery of all the parameters are below 20% of error, achieves the 50 % of the cumulative distribution. Below this limit, more than 50% of the Sersic profile galaxies is retrieved with an error of more than 20 %. This minimum value amounts to 550 pixels for the galaxies modeled with only one Sersic component.

The area of a galaxy is also broadly correlated with its total magnitude which means that imposing a minimum area in our fits is similar to imposing a limiting magnitude. In Figure 5.3, we have plotted the correlation between absolute magnitude and area of the galaxies. We obtain that the mean value of 550 pixels, correspond to $M_r \approx -19.8$.

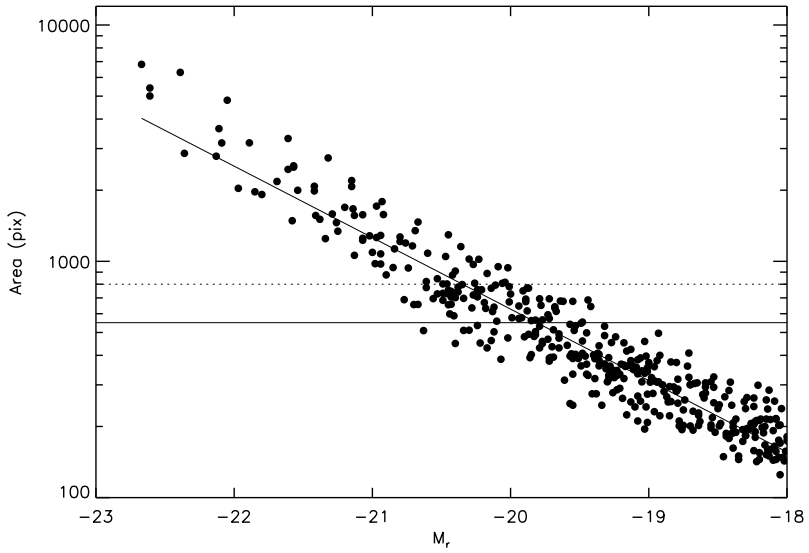

Figure 5.3: Area versus absolute Gunn-r magnitude for the galaxy population in the NOT sample. The solid and dotted horizontal lines show the limit of 550 and 800 pixels, respectively. A fit to the correlation is overplotted.

5.1.4 Galaxies with two photometrical components

This subsection is devoted to the analysis of the results of the simulations when two photometrical components are used. Regarding the minimum area for the fit to be reliable in two components, we have adopted the same procedure that for one photometrical component with the particularity that in this case, the area at which 50% of the population is well fitted depends on their B/T values. Figure 5.4 shows the fraction of simulated galaxies which their free parameters are recovered within relative errors of 20% separated in three ranges of B/T 's. We have adopted as the minimum area needed for a two-component fit, a compromise value between the minimum areas for each B/T range. In our case, the minimum area adopted is then 800 pixels.

For all the artificial galaxies with areas larger than 800 pixels, we have plotted in Figure 5.5, the relative errors of the fitted free parameters of the simulated galaxies with bulge and disc components.

Notice that in general the disc parameters are better fitted than the bulge ones. This is expected since the seeing affects more importantly to the central parameters of the bulge. It is also clear that those galaxies with large B/T show larger errors in the disc parameters than in the bulge ones. In contrast, galaxies with smaller B/T show larger errors in the bulge than in the disc. Let's note that the bulge and disc surface brightness are not well fitted for galaxies fainter

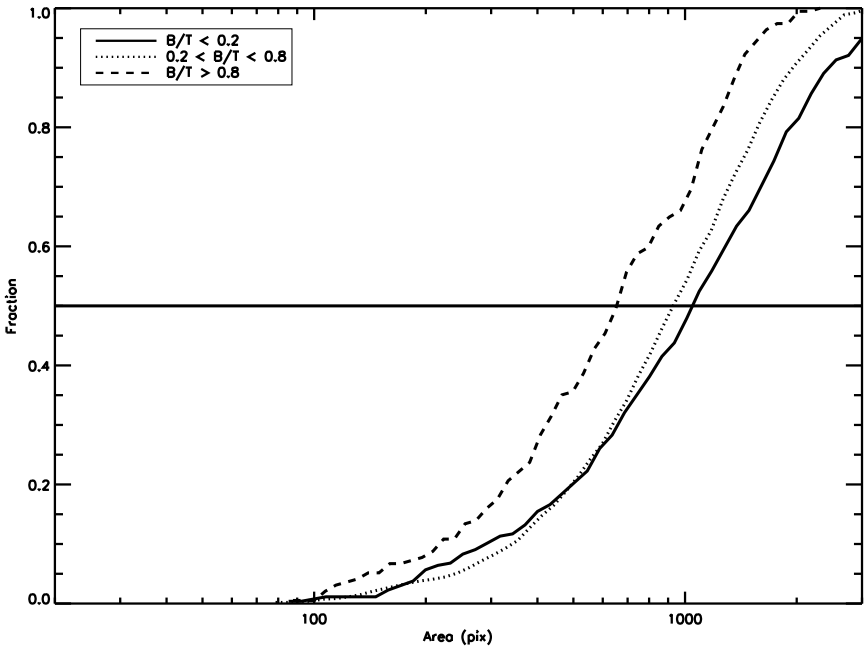

Figure 5.4: Cumulative distribution of the simulations which have an error within 20% versus area for the Sersic+Disc Profile. The horizontal line marks the 50% of the distribution.

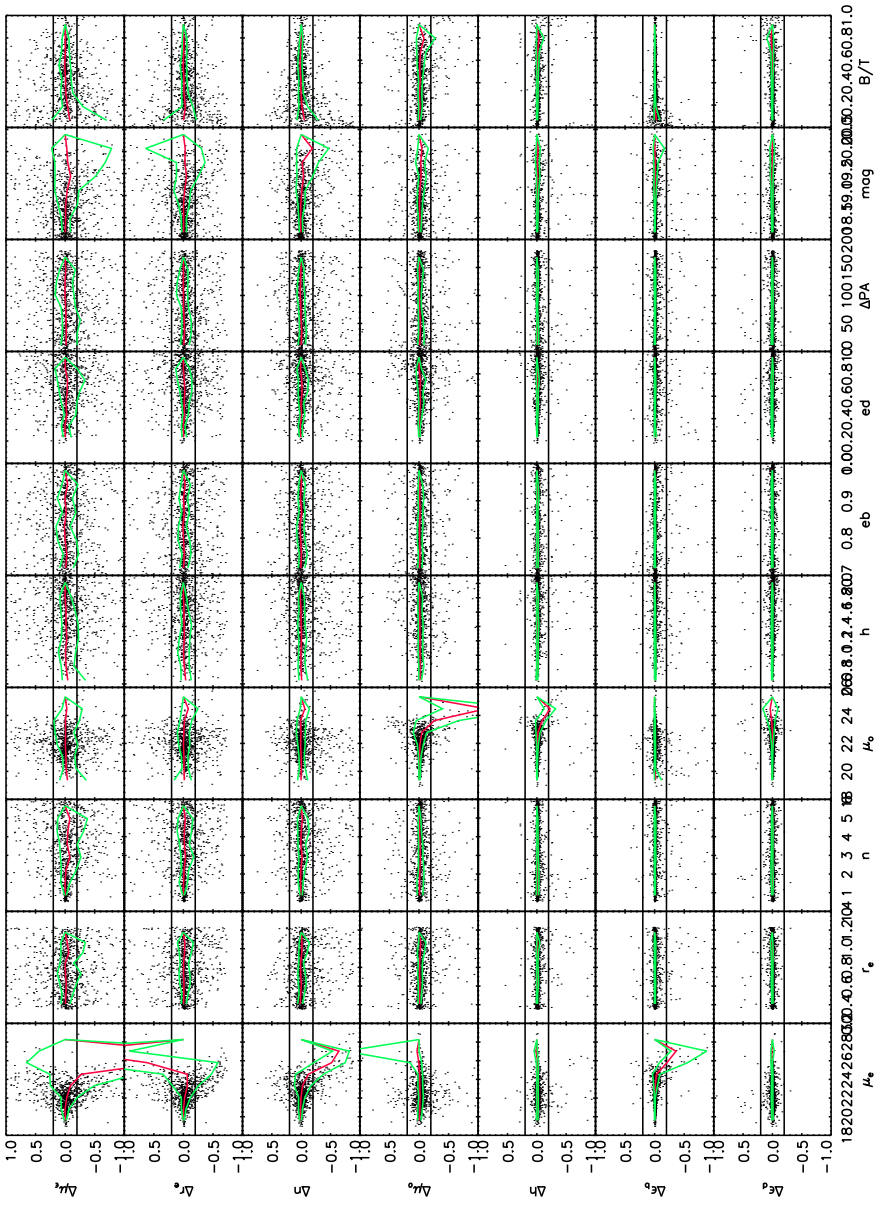

Figure 5.5: Plots of the Sersic+ Disc profile parameters versus their errors for those galaxies with areas larger than 800 pixels. The horizontal lines are the 20% of the error. The green and red lines are the quartile and percentile of the error respectively in bins. (To see landscape)

than magnitude $m_r > 20$ or with bulge surface brightness $\mu_{0,B} > 25.3$ or disc surface brightness $\mu_{O,D} > 25.3$.

We have set those restrictions in our parameter space, as it is shown in Figure 5.6. We do notice that the bulge parameters are the ones with the largest errors. Consequently, we have selected those simulations with B/T ≤ 0.7 from the previous restricted sample as in Figure 5.7. We can conclude that the errors are now within 20%.

5.1.5 Number of components

All the galaxies down to $M_r = -19.8$, that statistically corresponds to 550 pixels limit in area, were fitted with one and two component models. In order to decide the best fitted photometrical model, we have adopted a similar approach as in Allen et al. (2006) for the Millenium Galaxy Catalogue (MGC). This strategy is based on the radial analysis of the surface brightness profiles of the fitted models. Our aim is that those galaxies finally fitted with two components should be *classical* bulge plus disc systems, in other words, that their central regions should be dominated by the bulge, while the disc should dominate at large radial distances from the galaxy center. Galaxies with different light distribution were fitted with only one component.

We have implemented a decision tree algorithm in order to obtain the number of fitted galactic components. The algorithm starts by comparing the magnitude of the galaxy obtained from the two component fit and the magnitude directly measured in the image using SExtractor. If this difference is larger than 0.5 mag then the galaxy is fitted with only one component as it will not be a good fit. In the second step of the algorithm, we have analyzed the bulge-to-total (B/T) ratio given by the two component fit. Those galaxies, clearly dominated by the Sersic component ($B/T >$0.7), were fitted with only one component.

The remaining galaxies were analyzed following a similar procedure as in Allen et al. (2006). We have identify five different types of fitted surface brightness profiles according with the number of intersection between the Sersic and the exponential fitted radial profiles. In Fig 5.8, we have plotted an example of each of those five types. We can identify those with one (Type 1, Type 2 and Type 4), two (Type 3) and zero (Type 5) intersections. Type 1 profiles were considered as *classical* bulge plus disc galaxies. The remaining have bulges dominating the whole galaxy (Type 5), or the disc dominates in the inner regions of the profile (Type 4), or the effective radius of the bulge is larger than the effective radius of the disc (Type 3), or the n Sersic parameter of the bulge has reached the maximum value allowed in the fit (Type 2). Therefore, only the Type 1 profiles were considered faithful two component fits. The remaining were fitted with only one component model.

By using this algorithm, we can ensure that galaxies which have been fitted with a two component model are trustable bulge plus disc galaxies, that is, spiral or lenticular galaxies. For the rest, no clear classical counterpart can be assigned.

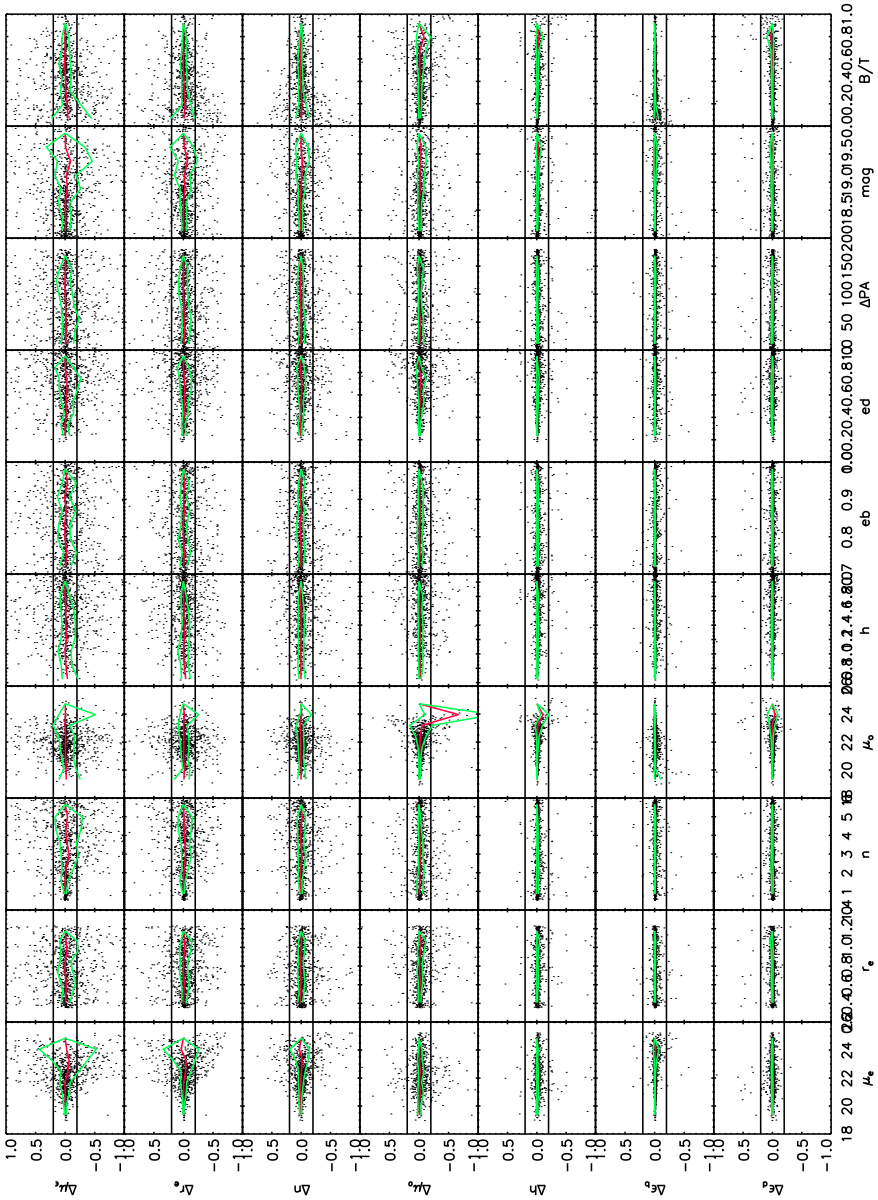

Figure 5.6: Plots of the Sersic+ Disc profile parameters versus its error for $m_r \leq 20$, $\mu_{0,B} \leq 25.3$ and $\mu_{O,D} \leq 25.3$. The green and red lines are the quartile (25%) and median of the error respectively in bins. (To see landscape)

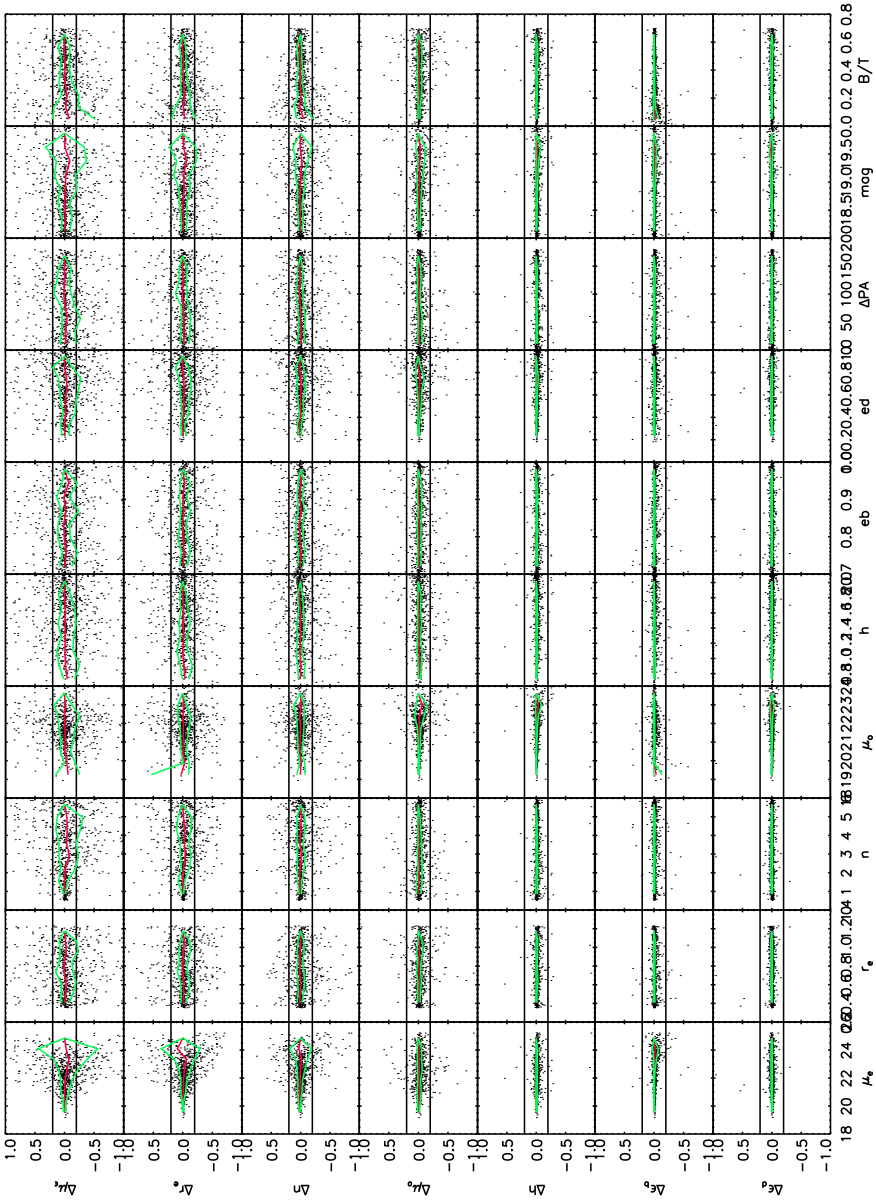

Figure 5.7: Plots of the Sersic+ Disc profile parameters versus its error for $m_r \leq 20$, $\mu_{0,B} \leq 25.3$ and $\mu_{O,D} \leq 25.3$ and B/T ≤ 0.7. The green and red lines are the quartile (25%) and median of the error respectively in bins. (To see landscape)

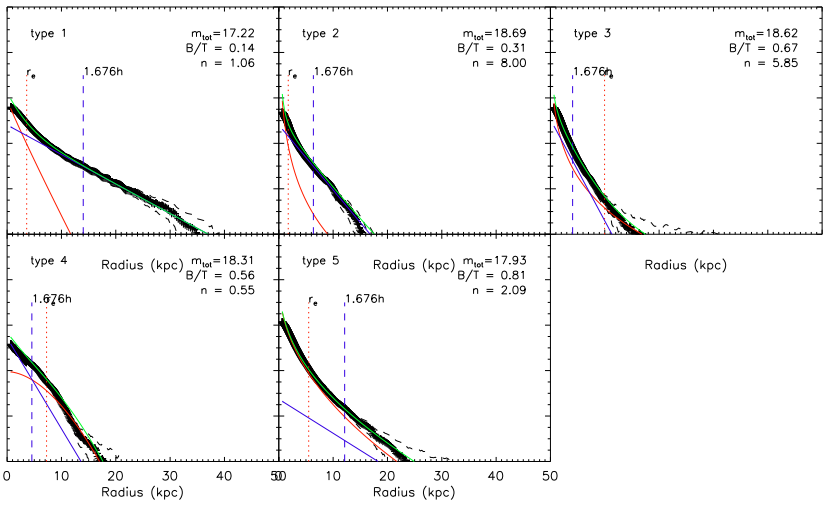

Figure 5.8: Examples of profiles 1 to 5 following the notation of Allen et al. (2006) for the MGC. The black line represents the profile of the galaxy, the red line corresponds to the Sersic profile, the blue line shows the disc profile and the green line designates the sum of both components profile.

In the next section, we will discuss the color information as a complement for determining the morphology quantitatively. For now, the final result is that 47 % of the galaxies with areas larger than 800 pixels are better fitted by a Sersic-one component profile, while for the other 52 %, two components are preferable.

In the Figures B.1 in the Annex, we have plotted the two dimensional images of the galaxies with $M_r \leq -19.8$ including the original galaxy, the symmetric image, the model into one and two components and its corresponding residual image. The last column shows also the surface brightness profiles with the one and two component fit decomposition profiles and its parameters.

5.2 Quantitative Classification

We have reclassified the galaxies in the NOT sample, taking into account the number of fitted photometrical components and their B-r colors. Three diferent galaxy types has been considered as we are interested in studying their structural components: Early-types (E/S0), Early-spiral (Spe) and Late-spiral galaxies (Spl).

The Early-type galaxies were those fitted with one Sersic component and located in the red secuence of the color-magnitud relation of the clusters. Early-type

spiral galaxies were those fitted with two structural components and also close to the red secuence of the CMR. Finally, late-type spiral galaxies were those objects fitted with two components and have at least 0.2 bluer B-r color than the red secuence of the cluster. By construction, early and late spiral galaxies must have a B/T value less than 0.7

This classification results in that 36.20%, 29.31%, and 15.51% of the galaxies were early-type, early-spiral and late-spiral in NOT sample, respectively. The remaining 18.96% of the objects correspond to blue galaxies fitted with only one component. These objects could be a mix of different kind of objects (galaxies with more than two galactic components, blue spiral galaxies not well fitted with two components, irregular galaxies,...).

5.2.1 Qualitative morphology versus Quantitative Classification

We have performed a comparison of the visual morphology classification with our quantitative one. The visual classification is based on the visual characteristic shapes that the eye can distinguish. The quantitative classification tries to get the types from its color and structural components and as it has been repeatedly shown, this classification is not univocal, and the correspondence between both schemes is not completely satisfactory.

We have checked the percentages of the visual morphological types that agree with that quantitative classification. The results are collected in Table 5.1. For galaxies that we have fitted with just one component, we find that a 85.7 % of the galaxies classified as Elliptical and Lenticular galaxies are red and have one component. Also, we find that nearly 90% of the blue galaxies with one component are classified as Late Type galaxies.

The case for the galaxies fitted with two components is somewhat more confusing. We obtain that 41.16% of the galaxies classified as Early spiral are Lenticular or Spiral, while only 22 % of the galaxies with blue colors and two components are classified as Spiral galaxies. Those differences may be due to the difficulty of distinguishing visually arms, bars, discs or similar features in distant galaxies.

To illustrate this, we have compared our visual morphology classification in one of the cluster in ACS sample, A2218, with the quantitative morphology given by Sánchez et al. (2007) in a small area of 200 kpc. They use a quantitatively classification method based on Sersic parameter. We have found that only 47.05% of the galaxies have the same morphological type. Those results indicate that despite the numerous efforts that have been performed to achieve a quantitative description of galaxies, they have not succeed yet in assigning the same type as the visual classification. In any case, our method gives acceptable results for elliptical, lenticular and late type spiral galaxies.

Table 5.1: Visual Morphological Types versus Quantitative Morphological Types for the NOT sample. Columns: quantitative classification. Rows: Visual morphology.

	E	S0	S	I
E/S0	0.57	0.28	0.14	0.00
EarlySp	0.53	0.17	0.23	0.05
LateSp	0.11	0.66	0.22	0.00
Irr	0.10	0.00	0.70	0.20

5.3 Structural parameters

Numerous studies deal with the evidence that field or isolated galaxies have larger discs than galaxies in clusters (de Jong, 1996; Graham, 2001, 2003). Also, the data at high redshift from HST seems to indicate that early-type galaxies have little evolved from redshift ~ 1 to now, while late-type systems seem to change quickly. We have quantified those evidences in our clusters (Ascaso et al., 2008b).

5.3.1 Sersic Parameters

One of the most interesting relations for elliptical galaxies was introduced by Djorgovski & Davis (1987); Dressler et al. (1987). They established that the effective radius, the central velocity dispersion and the mean surface brightness are related for early type galaxies in the logarithmic space with a very low scatter. This relation is commonly known as the **Fundamental Plane (FP)**:

$$\log r_e = \alpha \log \sigma + \beta \log < I >_e + \gamma$$

The existence of the FP can be explained by assuming some well defined M/L relation and that galaxies are in virial equilibrium. The implications of its existence are directly related to the formation and evolution process of the galaxies. Similarly, Dressler et al. (1987) introduced the $D_n - \sigma$ relation, which is directly related to the FP.

The FP provides information on the properties of the early-type galaxies as a class, and may be used for distance determination, evolutionary studies and for cosmological tests (Moles et al., 1998), assuming that the relation is universally valid. That matter is still on debate, in relation with the uncertainty derived from the mislead of the morphologically classification of the galaxies and also with the assumption that the E and S0 galaxies are derived from the same probability function (Jorgensen, Franx & Kjaergaard, 1996).

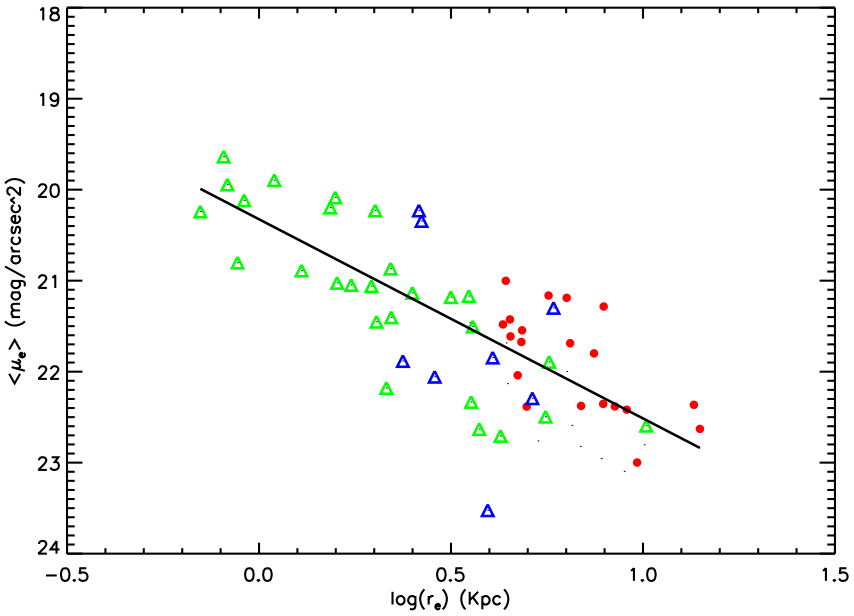

Figure 5.9: Kormendy relation for all the galaxies in the NOT sample. Red points are the E/S0 galaxies, green triangles refer to early-Spiral and Blue triangles account for late-spiral galaxies. The solid line is the fit for the E, S0 and Early Spiral galaxies.

When no information about the velocity dispersion is available, there is another relation, the **Kormendy Relation** (Kormendy, 1977). It illustrates a relation between structural parameters of galaxies. Kormendy (1977) discovered a correlation between the size and the surface brightness of elliptical galaxies. Later on, Binggeli, Sandage & Tarenghi (1984) found that this relationship was only valid for elliptical galaxies brighter than $M_B \leq -20$. For fainter galaxies, the relation does no longer hold.

In Figure 5.9, we have plotted the **Kormendy relation** $<\mu_e>$ -r_e for E/S0 (red points) and the bulges of Early Spiral (green triangles). The Late -Spiral bulges (Blue triangles) are also shown as an illustration. For the E/S0 galaxies and the bulges of Early Spiral, the fit is the following

$$< \mu_e >= (20.32 \pm 0.15) + (2.18 \pm 0.23) \log(r_e) \tag{5.7}$$

while the fit for the bulges of the whole set of galaxies would be

$$< \mu_e >= (20.07 \pm 0.14) + (3.22 \pm 0.21) \log(r_e) \tag{5.8}$$

It is noticeable the much wider dispersion introduced by the bulges of Late

Spirals in the Figure and also reflected in the change of slope in the equations. As expected, we find that E/S0 galaxies can have larger fainter bulges, while the Early Spiral galaxies spread a wider range, including bright, small size bulges.

We have also plotted in Figure 5.10 the relation between effective-radius and shape parameters for red galaxies fitted with one component (red points) and blue galaxies fitted with one component (blue triangles). Clearly, a dichotomy exists. By taking out the obvious outliers, we have obtained the following fits

$$\log n = (0.26 \pm 0.13) + (0.21 \pm 0.17) \log(r_e)$$

and for the blue ones

$$\log n = (-0.04 \pm 0.16) - (0.03 \pm 0.19) \log(r_e)$$

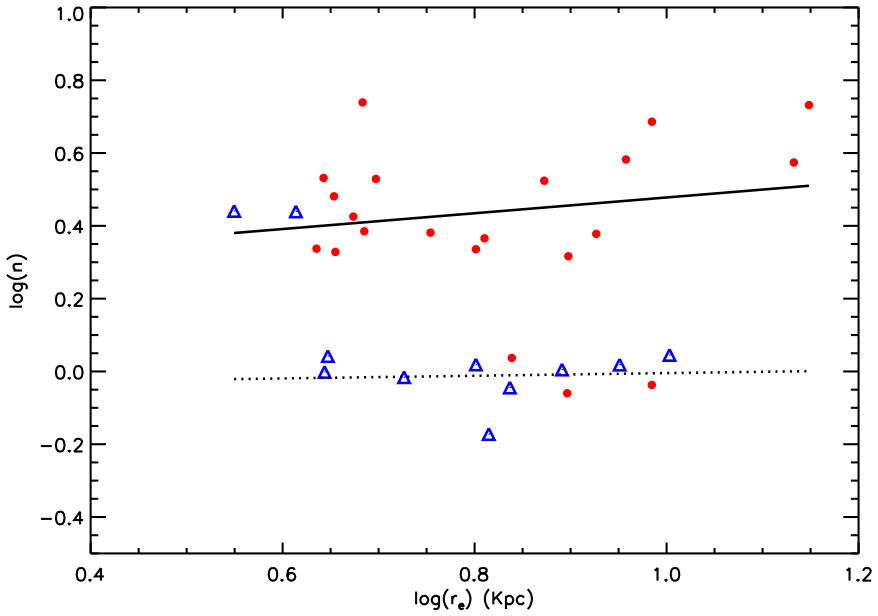

Figure 5.10: Relation between effective ratius and shape parameter for one component galaxies. Red points refer to red-one-component galaxies and blue triangles represent blue-one-component galaxies. Solid and dotted lines are the respective fits

These fits are also shown in the figure. As we see, we find not too different (within errors) slopes for the red and blue population. This result is very interesting as it allows us to difference nearly univocally the early and late type galaxies by identifying the value of their Sersic parameter, and inversely, we can assign a particular shape to a galaxy by determining its color.

As a consequence, we can conclude that the galaxies fitted with one component have a bimodal behavior. The red early-type galaxy population has a n value of $2 \leq n \leq 4$, while the blue late-type galaxy population has a shape parameter, $n \sim 1$.

Furthermore, in the Figure 5.11, we have shown the central surface brightness, the shape parameter and effective radius versus the absolute magnitude for the E/S0 (red points) and the bulges of Early Spiral (green triangles). Again, the bulges of the Late Spiral (blue Triangles) galaxies are shown to illustrate its properties.

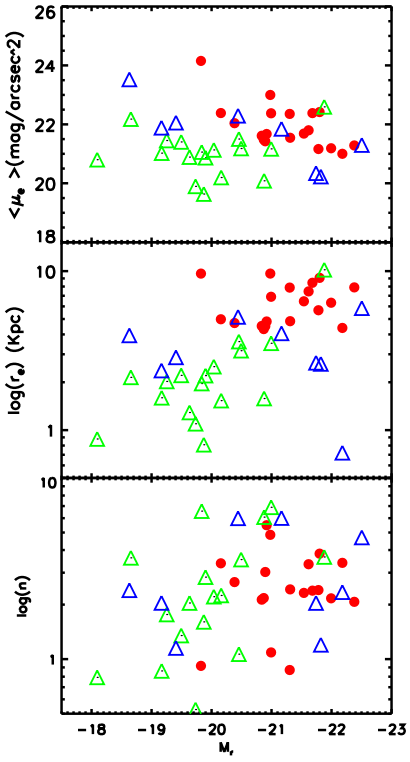

Figure 5.11: Absolute Gunn-r Magnitude versus μ_o, n and B/T for E/S0 (Red points), Early Spiral Bulges (Green Triangles) and Late Spiral Bulges (Blue Triangles).

Clearly, we notice that the bulges of the late spiral galaxies are not following any particular trend. On the contrary, bright E/S0 galaxies ($M_r \geq -20$) are brighter and with fainter surface brightness and they posses larger effective radius while Early Spiral galaxies show much brighter surface brightness and smaller radius, already seen in the analysis of the Kormendy relation. As the Early Spiral galaxies are fitted with two components, we are not able to distinguish any

relevant trends with the shape parameters.

We have also plotted In Figure 5.12, the mean surface brightness, the effective radius and the shape parameter versus B-r color for the E/S0 and the bulges of Early Spiral galaxies. As before, the bulges of the Late Spiral galaxies are also shown to note their dispersion. The symbols are the same as in the previous plot.

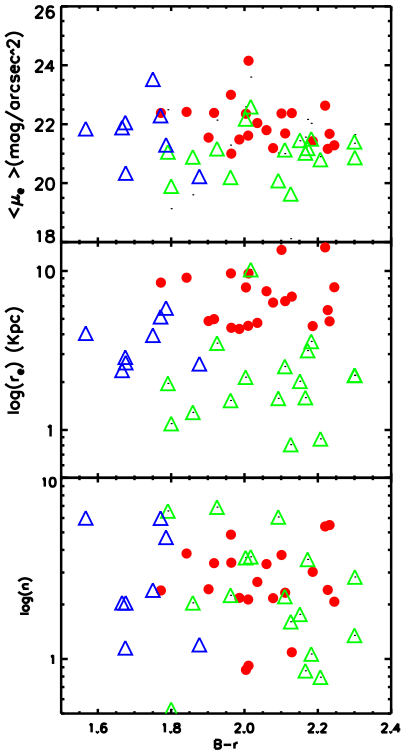

Figure 5.12: B-r color versus μ_o, n and B/T. for E/S0 (Red points), Early Spiral Bulges (Green Triangles) and Late Spiral Bulges (Blue Triangles).

By definition, we can distinguish a clear dichotomy between early and late spiral galaxies. In addition, the same dichotomy in the size of the discs for E/S0 galaxies and Early Spiral galaxies are found. This result is understood in terms of the two component model used to fit Early Spiral galaxies.

Finally, we have compared our bulge scales with the bulge scales of the early type galaxies in the sample of Aguerri et al. (2004). Those galaxies have been selected in the same way as us. The results are plotted in Figure 5.13, the red points indicate the E/S0 galaxies while the blue triangles are the blue galaxies with one component . We see that our sizes are very similar to Coma. We do not find any galaxies in our sample below $\approx$ 2.2 kpc, as that is our seeing

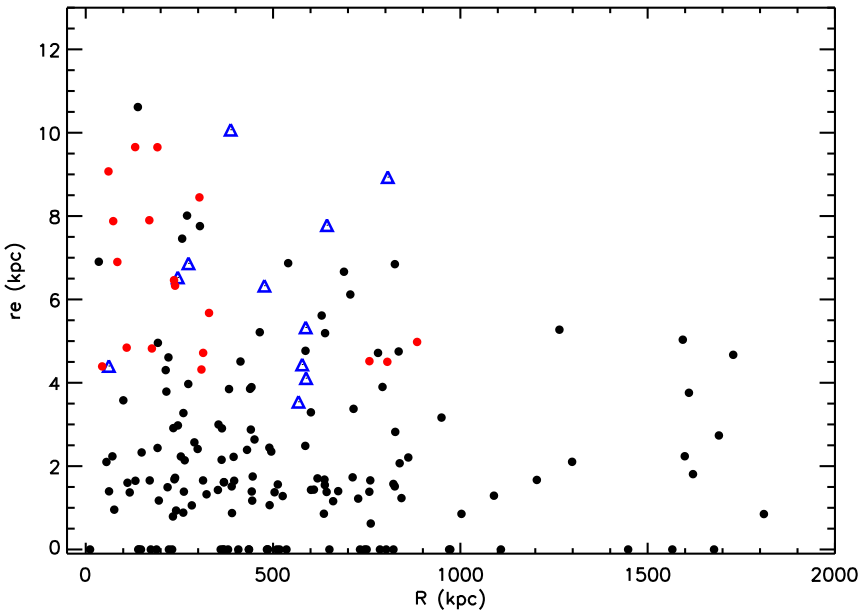

Figure 5.13: Bulge Scales versus radius for Coma Sample, (Aguerri et al. (2004), black points) and NOT sample. The red points refers to red galaxies in one component while blue triangles represent blue galaxies in one component.

limitation to our sample at this distance. It's noticeable that our r_e values are in the same range as those in Coma, as it is shown in Table 5.2. The values for Coma have been computed for those galaxies in the central 735 kpc and effective radius larger than 2.2 kpc.

As far as the shape parameter is concerned, we see in Figure 5.14, that the range of values in NOT sample, expands the range of values of Coma. However, we find a mean value somewhat smaller for NOT sample than for Coma but the values agree within the errors. Therefore, it seems that the bulge sizes are in the same range of magnitude than in Coma Cluster.

Table 5.2: Bulge parameters for Coma and NOT sample

Name	$< r_e >$	$\sigma(r_e)$	$< n >$	$\sigma(n)$	$<$ Dist(kpc) $>$	σ(Dist(kpc))
NOT	6.58	2.38	2.24	1.35	349.72	257.053
Coma	8.73	17.58	3.58	1.54	339.376	180.90

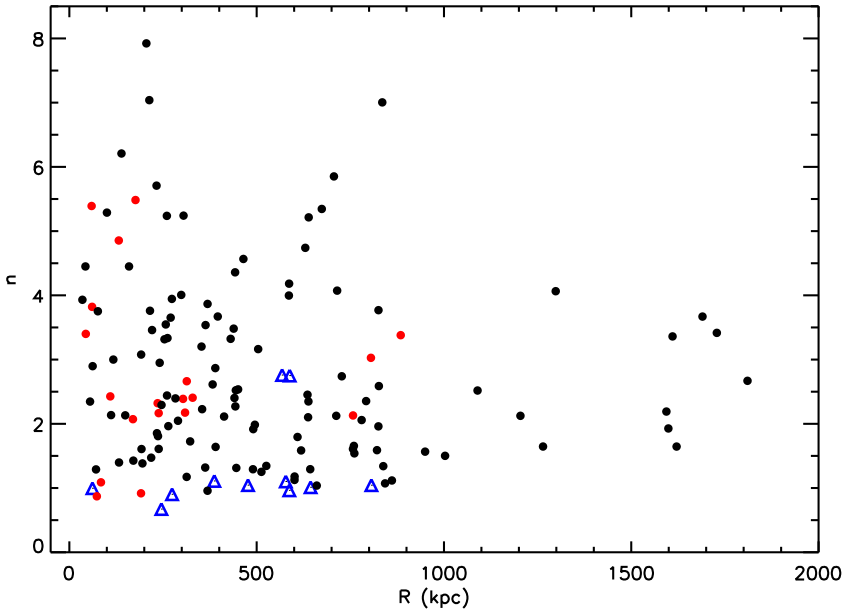

Figure 5.14: Shape parameter versus radius for Coma Sample, (Aguerri et al. (2004), black points) and NOT sample. The red points refers to red galaxies in one component while blue triangles represent blue galaxies in one component.

5.3.2 Disc Parameters

There are several works that have found that early-type galaxies in clusters remain invariant up to redshift at least 1, as a result of the formation of the cluster (Simard et al., 1999; Trujillo & Aguerri, 2004). Thus, any variance in that range in redshift, if it exists, must be in the disk galaxy parameters.

In Figure 5.15, we have plotted the absolute magnitudes of the disks versus their scale parameters. The black points are for the NOT galaxy sample. The blue triangles refer to a sample of field galaxies extracted from the work by Graham (2001) and the red diamonds are the disks from Coma cluster taken from a sample by Aguerri et al. (2004). The horizontal line shows the minimum disc scale we can resolve due to the distance of the clusters.

It is interesting to notice that our disc scales are as large as those of field galaxies, while those discs in Coma represent a minimum percentage. The fit for the Freeman law (Freeman, 1970), for our sample is

$$\log h = (-2.52 \pm 0.57) - (0.152 \pm 0.027) M_r$$

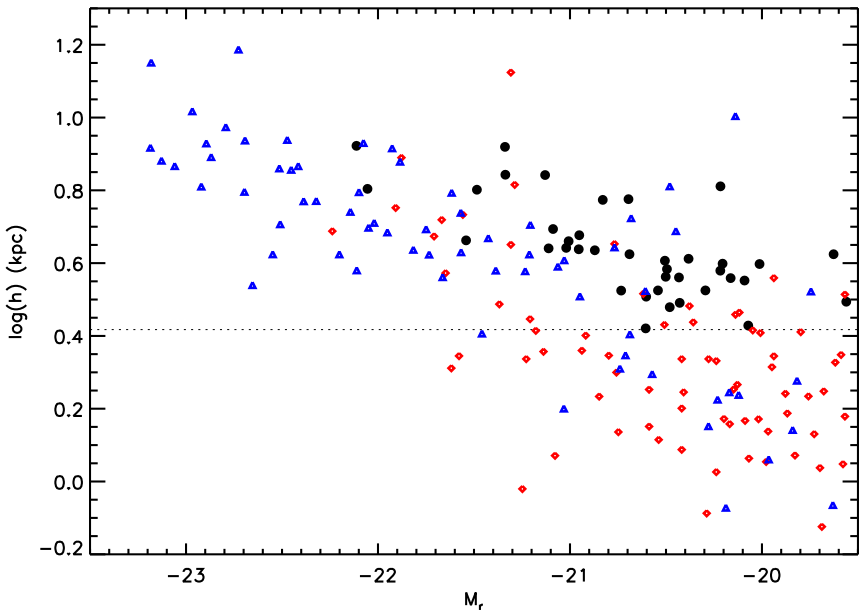

Figure 5.15: Disc scales versus absolute Gunn-r Magnitude for two component galaxies. The blue triangles refer to the field galaxies by Graham (2001), red diamonds are the disks scales for the Coma sample by Aguerri et al. (2004) and black points represent the disc scales in NOT sample. The horizontal line shows the minimum disc size that we can resolve due to the distance of the clusters

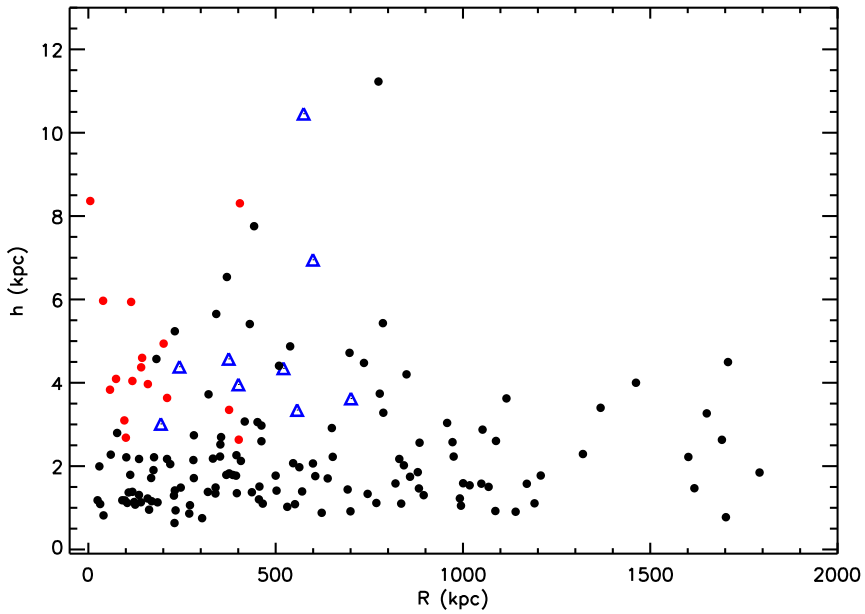

Figure 5.16: Disc Scale versus radius for Coma Sample, (Aguerri et al. (2004), black points) and NOT sample. The red points are red galaxies in two components and the blue triangles are blue galaxies in two components

Regarding to a quantitative description of the disc scales, we have plotted in Figure 5.16, the discs scales in function to the distance to the center of the cluster for the NOT sample and the Coma sample by Aguerri et al. (2004). The black points are the two-component galaxies in Coma, the red points are early spiral galaxies and the blue triangles refer to late spiral galaxies. We find larger discs (a factor of two) in our sample than in Coma as collected in Table 5.3. Those results agree with the idea of evolution from this redshift to local clusters, in the disc scales of the late type galaxy population in clusters.

We have performed statistical tests to check if the disc scales in NOT sample are significantly different to disc scales at lower redshift or disc scales from isolated

Table 5.3: Disc parameters for Coma and NOT sample

Name	$< h >$	σ(h)	$<$ Dist(kpc) $>$	σ(Dist(kpc))
NOT	4.738	1.941	272.16	202.10
Coma	2.47	21.48	524.383	359.080

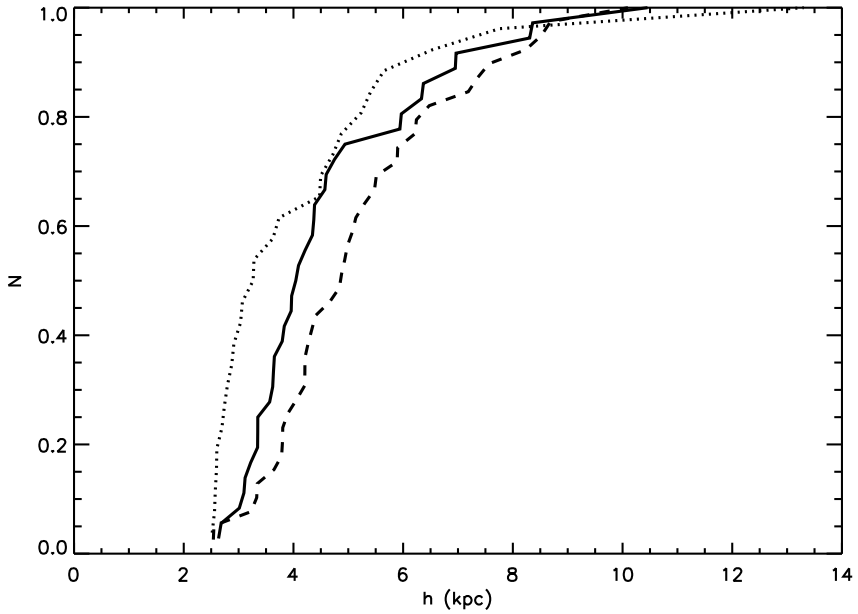

Figure 5.17: Cumulative function of disc scales for the NOT sample (solid line), Aguerri et al. (2004) Coma Cluster (dotted line) and Graham (2001) isolated sample (dashed line)

galaxies. With that purpose, we have applied the Kolmogorov-Smirnov test between the cumulative function of the discs from the clusters in NOT sample, the Coma sample and the sample of isolated galaxies from Graham (2001). Their cumulative functions are shown in Figure 5.17.

The results of the test show that the disc scales in Coma are significantly different from the disc scales in our sample and the disc scales corresponding to the isolated lower redshift Graham (2001) sample. The test does not return significant results for the disc scale distributions for the isolated sample from Graham (2001) and the NOT sample.

We can conclude that the cumulative functions for our disc scales in NOT clusters is different from Coma Cluster and may be similar to local field galaxies. Therefore, we have discs as large as those from field galaxies, which are quantitatively different from Coma.

This result is extremely interesting as it shows an evolution with redshift in the disc scales of the galaxies from lower redshift (Coma) to $z \sim 0.2$. Not only that, but the disc scales in our medium redshift range, could be similar to field galaxies at low redshift, finding an environmental evolution in local clusters respect to $z \sim 0.2$ clusters.

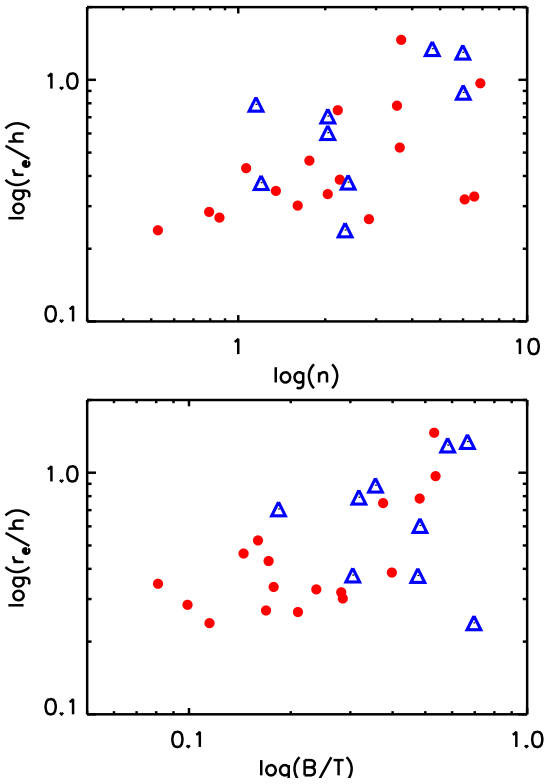

Figure 5.18: Adimensional parameters. n versus r_e/h and B/T versus r_e/h. Red points refer to red two-component galaxies and blue triangles to blue two-component galaxies in NOT sample

5.3.3 Bulge and disc parameters

In Figure 5.18, we have plotted the ratio r_e/h versus shape parameter and bulge-to-total ratio for the two-component galaxies. We find a clear correlation between B/T and r_e/h for the early-spiral galaxies, as exists for local field galaxies (Andredakis, Peletier & Balcells, 1995; Graham & de Blok, 2001), and a much wider dispersion fror the late-spiral galaxies as expected.

These trends suggest a different behavior between Early and Late Type Spiral galaxies. For Early Spiral galaxies, we find an increment of their shape parameter and their bulge sizes with respect to their disc sizes as the galaxies become more spheroidal. On the contrary, Late Spiral galaxies does not seem to show any significant trend with the proportion of the bulge and disk and the shape parameter.

A different way to look at this is analyze the Figure 5.19, where we have plotted the scale of discs versus the effective radius for the early and late spiral galaxies.

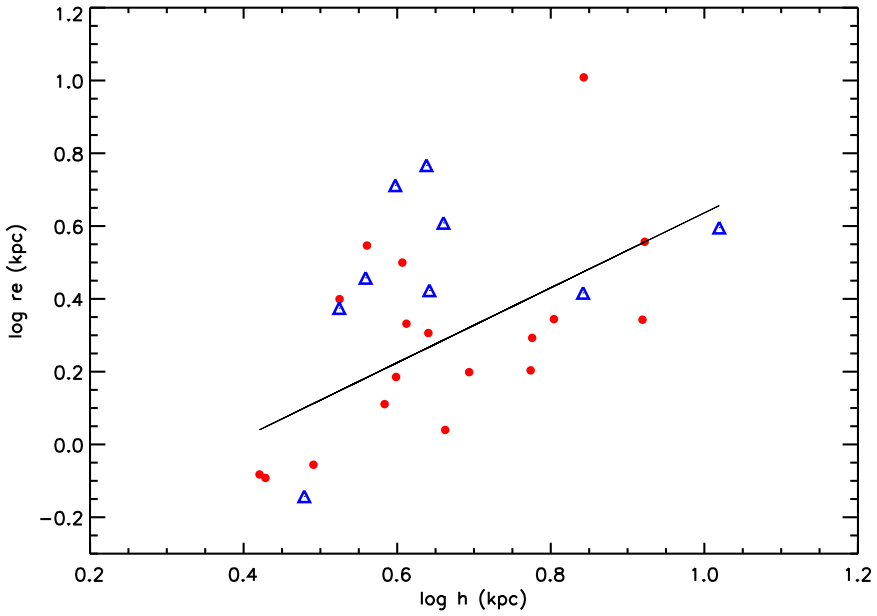

Figure 5.19: Relation between effective ratius and disc scales. Red points refer to the red two-component galaxies and blue triangles to the blue two-component galaxies. The solid line represents the red component fit.

The increase of the effective radius with the disc scale for the early spiral galaxies appears clearly, as it is shown in the following fit

$$\log r_e = -0.39 + 1.02 \log(h)$$

For the late spiral galaxies, the dispersion of r_e values for a small range of h values is too large to define a relation with any degree of significance.

To conclude, early spiral galaxies have larger discs with larger bulge effective radius. Thus, more massive galaxies. That tendency was also noticed by MacArthur, Courteau & Holtzmann (2003). For the late spiral galaxies, the tendency does not seem to exist.

Chapter 6

Spatial Distribution

Les gens ont des étoiles qui ne sont pas les mêmes.
Pour les uns, qui voyagent, les étoiles sont des guides.
Pour d'autres elles ne sont rien que de petites lumières.
Pour d'autres, qui sont savants, elles sont des problèmes.

Antoine de Saint-Exupéry. "Le petit prince"

The spatial distribution in clusters of galaxies is a valuable piece of the puzzle. By studying the location of the galaxies in the cluster, we are able to detect important cluster properties such as the presence of substructures, their dynamical state, etc.

A particular galaxy can be described with three spatial coordinates, (x, y, z) and three velocity coordinates (v_x, v_y, v_z). We usually know two spatial coordinates (x, y), as we are seeing the galaxy projected in the sky. In addition, if we know the redshift of the galaxy, we have also information about one velocity component, v_z.

Even so, that situation is not very frequent. Taking out some some cluster surveys such as ENACS (Mazure et al., 1995), or very well-known studied clusters such as Coma (Struble & Rood, 1991; Jorgensen, Franx & Kjaergaard, 1992; Wegner et al., 1999; Smith et al., 2004; Aguerri et al., 2004), Virgo (Binggeli, Tammann & Sandage, 1987; Ferrarese et al., 2006)), Hercules (Struble & Rood, 1991; Jarrett et al., 1998; Wegner et al., 1999; Sánchez-Janssen et al., 2004; Smith et al., 2004; Crawford, 2005; Estrada et al., 2007), at low redshift and some more at medium redshift, some in our ACS sample, like A1689 (Teague, Carter & Gray, 1990; Duc et al., 2002; Łokas et al., 2006), A2218 (Kristian, Sandage & Westphal, 1978; Le Borgne, Pelló & Sanahuja, 1992; Sánchez et al., 2007), CL0024 (Czoske et al., 2001; Alexov, Silva & Pierce, 2003), MS1358 (Fisher et al., 1998; van Dokkum et al., 1998; Yee et al., 1998; Fabricant, Franx & van Dokkum, 2000), the redshift values per cluster are only known for a small

fraction of the galaxies. Therefore, we have to estimate membership of the cluster by using different techniques such as the CMR (studied in the Chapter 3 (Yee, Gladders & López-Cruz, 1999; López-Cruz, Barkhouse & Yee, 2004)) or other statistical approaches.

The spatial distribution of galaxies of different types in a cluster is considered to be the consequence of the initial conditions of formation and evolution for the galaxies in the clusters, as well as the interaction with the environment. It could also depend on the conditions of the formation of the cluster itself.

A cluster is said to contain substructures when its surface density is characterized by multiple, statistically significant peaks on scales larger than the typical galaxy size (Buote, 2002; Ramella et al., 2007). Numerous works have been devoted also to the study of the statistical determination of substructures in clusters of galaxies, providing different tests (Perea, del Olmo & Moles, 1986; Fitchett, 1988; Pinkney et al., 1996).

Additionally, a relation based on the spatial distribution of the cluster has been widely explored: **the Morphology-Density relation**. Observational evidence about the presence of more early-type galaxies in denser environments was originally noticed by Curtis (1918); Hubble & Humason (1931); Oemler (1974). Later on, Melnick & Sargent (1977) showed that the fraction of lenticular and spiral galaxies depends on the distance from the cluster centre and Dressler (1980) concluded with the morphology - local density relation. That relation refers to the presence of a higher fraction of elliptical galaxies as we approach to the center of the cluster and a higher fraction of spiral galaxies as we abandon the center of the cluster.

Dressler (1980) found this relation for a sample of low redshift clusters. Almost two decades later, Dressler et al. (1997), reanalyzed this relation for a sample of clusters at redshift ~ 0.5, finding this relation only for compact-regular clusters. Besides, Postman et al. (2005) analyzed a sample of high redshift clusters ($z\sim1$) imaged with the Advanced Camera for Surveys (ACS), observing the same tendency than Dressler (1980); Dressler et al. (1997), but with the density of elliptical galaxies five times smaller than in low redshift clusters. On the other hand, several authors (Sanroma & Salvador-Sole, 1990; Whitmore & Gilmore, 1991; Whitmore, Gilmore & Jones, 1993), argued a correlation between morphology and global cluster properties, as for example, the clustercentric distance instead.

The study of the spatial distribution is able to provide useful information in two dimensions (studying the relation of the different properties to the local density) and in a radial dimension, (studying the global relation between ratius and a particular scheme). This information has been analyzed throughout this Chapter.

6.1 Galaxy Density

Density maps are useful tools for studying the cluster dependence with different parameters. However, galaxies have a discrete nature so, limitations in area or depth make difficult the process of determining the density. In our case, as we are studying the central bright galaxy population of the cluster, our limitations are related to the field size as well as to the observational depth.

6.1.1 Density Estimation

The density can be estimated by two different methods. The more common is considering different fixed apertures, *ap*, in the cluster and computing the number of galaxies, n_{gal}, that we have on it. The **local density** in the cluster is obtained with the following equation

$$\rho_{local}(ap) = \frac{n_{gal}(ap)}{\pi(ap)^2}$$

However, that method has the inconvenient that the density is a discrete variable, as it depends on the aperture we have used. Thus, we have used a different method, which consists on considering a fixed number of galaxies, n_{gal} and computing then the minimum area that contains that number, obtaining the density with the following equation

$$\rho_{local}(n_{gal}) = \frac{n_{gal}}{\pi r(n_{gal})^2}$$

where $r(n_{gal})$ is the minimum radius that contain n_{gal} neighbors. This method has been applied in different works (Dressler, 1980; Trevese et al., 1992; Dressler et al., 1997; Fasano et al., 2000; Varela, 2004). The main advantage of that method is that the radius is a continuous variable, so it allows to obtain continuous values of the density function.

We need to fix then the number of galaxies n_{gal} as a compromise between the possibility of detecting peaks corresponding to substructures in the density diagrams and the limited area of the images. We have decided to take n_{gal}=10, as it is able to provide substructures larger than this number, and therefore, dynamically important and it small enough for the area of the cluster to be contained in the image.

In Figure 6.1 and 6.2, we have plotted the logarithm densities distribution for the NOT and ACS sample, respectively. For the ACS sample, we have previously selected the galaxies brighter than $M_r \leq -19.5$. The corresponding mean values are collected in Tables 6.1 and 6.2. It is noticeable that four of the clusters in the ACS sample are much more dense than those in the NOT sample, which may be explained in terms of selection criteria, particularly the richness class. In fact, the richness class for the clusters in the NOT sample is ≤ 3, while the

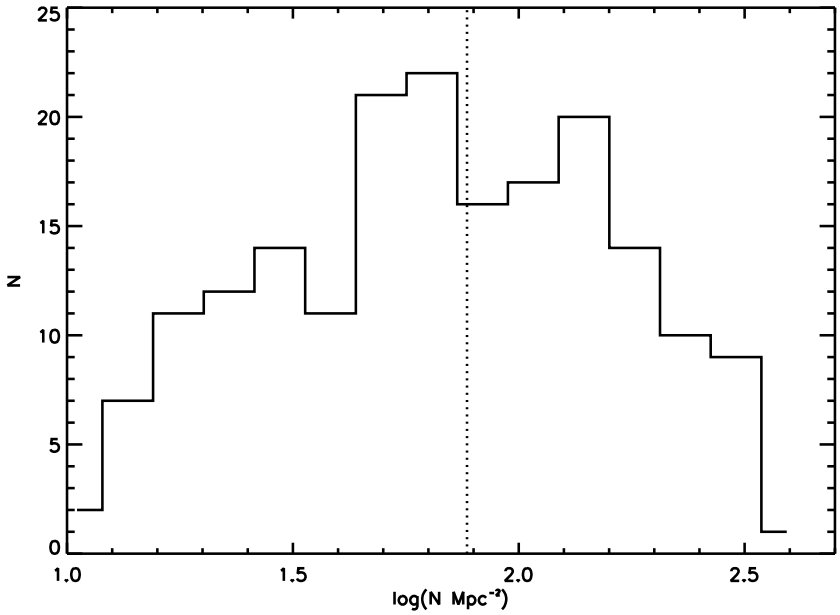

Figure 6.1: Distribution of the local density for the whole NOT sample. The vertical line shows the mean value of the density.

richness class for the ACS sample is above 4. Moreover, all the clusters in ACS sample have been detected in X-ray, being therefore, more massive than NOT sample clusters, from which only A2111 has X-ray data.

In Figure 6.3 and 6.4, the logarithm densities distribution for each cluster in the NOT and ACS sample are presented respectively and the values are collected in Tables 6.1 and 6.2 and showed with vertical lines in the Figures.

Let's note that two out of five clusters in NOT sample, A1878 and A2111 are denser statistically than the whole sample. It's interesting also that A1643, A1952 and A2111 present a second peak of lower density which might be related with the presence of subestructure. As far as the ACS sample is concerned, we see that nearly all the clusters have a density higher than 200 gal/Mpc^2, except MS1358, which is somewhat less dens, even if denser than the NOT sample. We also find some peaks in less dense regions of the clusters in A1703 or A2218, that could correspond to possible substructures.

6.1.2 Morphology-Density Relation

Dressler (1980) found a smooth, monotonic relation, of the presence of spiral, lenticular and elliptical fractions with the local surface density of galaxies, com-

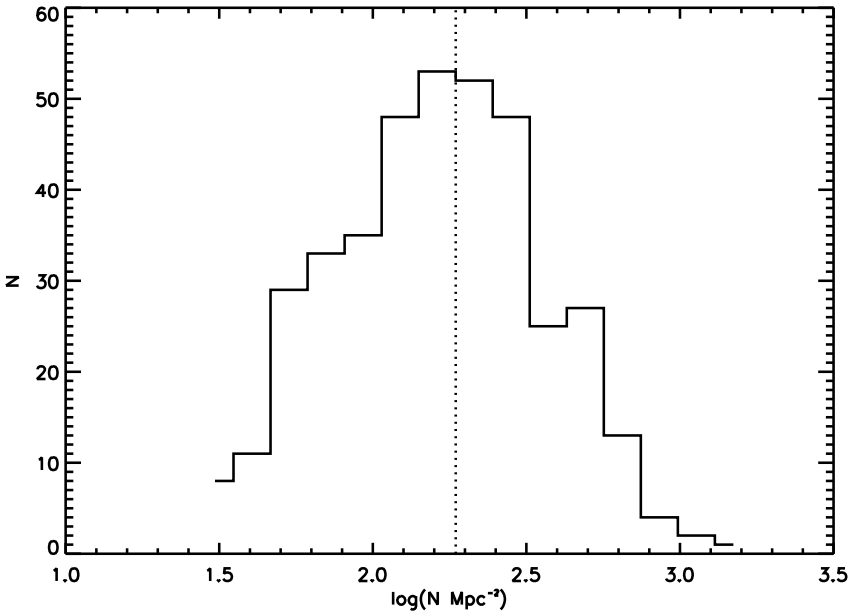

Figure 6.2: Distribution of the local density for the whole ACS sample. Vertical line show the mean value of the density in each cluster.

Table 6.1: Mean Densities for NOT Clusters

Name	$<\rho>$ (N/Mpc^2)	$\sigma(\rho)$ (N/Mpc^2)
A 1643	83.16	62.25
A 1878	140.15	106.30
A 1952	100.29	84.58
A 2111	116.83	94.29
A 2658	67.42	23.13
Sample	108.25	88.58

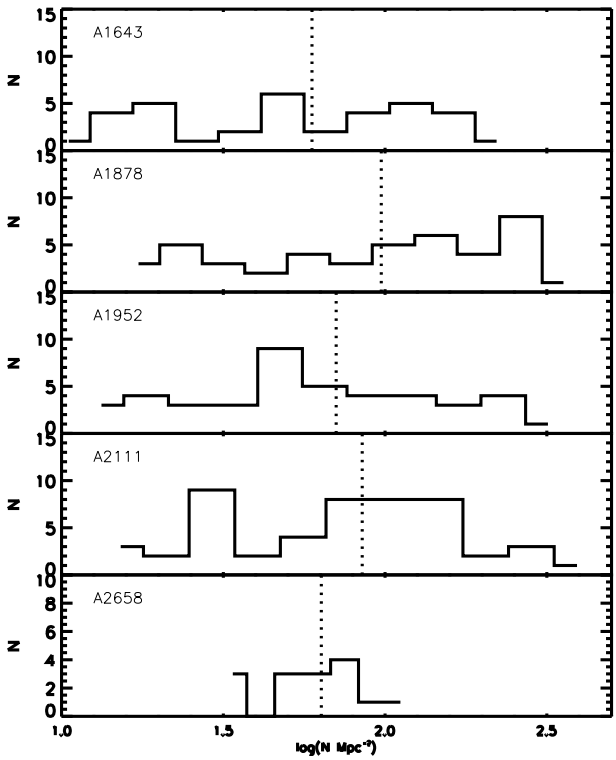

Figure 6.3: Distribution of the local density for each cluster in NOT sample. Vertical lines show the mean value of the density in each cluster.

Table 6.2: Mean Densities for ACS Clusters

Name	$<\rho>$ (N/Mpc^2)	$\sigma(\rho)$ (N/Mpc^2)
A 1689	271.37	182.13
A 1703	232.19	155.47
A 2218	200.81	132.11
CL0024	313.32	274.65
MS1358	175.65	168.71
Sample	250.58	210.50

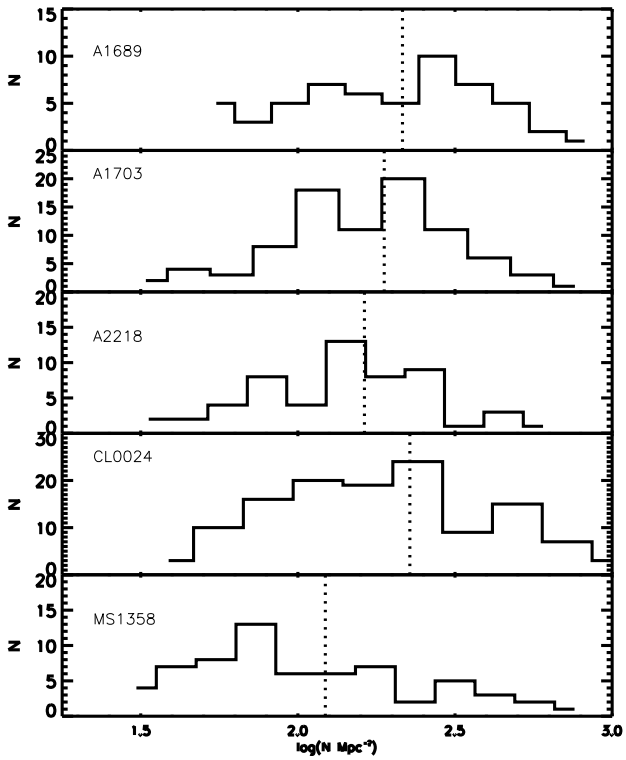

Figure 6.4: Distribution of the local density for each cluster in ACS sample. Vertical lines shows the mean value of the density of each cluster.

monly known as the **Morphology - Density relation**. He concluded that, from a sample of 55 low-redshift rich clusters sample, this relation is universal and representative of every cluster. Later on, Dressler et al. (1997) revisited that work by making a field correction which depends on the morphological type and field contamination in ten clusters at z $\sim$ 0.5. They found the same kind of relation for centrally concentrated 'regular' clusters, but not for clusters that are less concentrated and irregular, in contrast to the situation for low-redshift clusters. Some years later, Postman et al. (2005) studied a sample of seven clusters at higher redshift (z $\sim$1), concluding on the existence of the relation. They detected a change in the morphology-density relation between 0.8 <z<1.2 and that observed at z $\sim$ 0, with the result that the density of E+S0 in the core of clusters was five times smaller.

We have performed a study of this relation in our medium redshift sample. In Figures 6.5 and 6.6, we have plotted the logarithm densities distribution for the whole sample splitting them up into three morphological types. The vertical lines show the mean value for each sample.

Interestingly, we see that for both samples, the mean value for the Elliptical galaxies is higher than the mean value for Lenticular galaxies and Late-type galaxies (Spiral and Irregular). However, for the NOT sample, we obtain a mean value for Late-type galaxies larger than for Lenticular while the contrary is observed for the ACS sample. In addition, for the NOT sample, the elliptical galaxies distribution is somewhat skewed to higher densities and Lenticular galaxies are skewed to lower densities.

These facts, even if agreeing with the work by Dressler (1980) about the larger fraction of Elliptical galaxies in denser areas of the cluster, show a tendency for the lenticular galaxies to populate less dense areas in the cluster than Late-Type galaxies for the NOT sample and the contrary for the ACS sample. These trends could be related with the results found by Dressler et al. (1997) at medium redshift, who argued that the morphology-density relation exits for regular concentrated clusters. Also, Fasano et al. (2002) found an increase of the lenticular population for higher redshift clusters.

Looking at each cluster individually, we have plotted in Figure 6.7 and 6.8 the density function for each cluster separated into three morphological types. Although we have few galaxies to have good resolution, the results could be significant. Thus, we see that A1643 has some early-type galaxies in the densest areas but the late-type galaxy population is completely dominating the rest of the the core of this cluster. We also see that A1878 has a strong gradient of late-type-galaxies which increases to less dense areas. On the other hand, A1952, A2111 and A2658 are 'clasical' clusters as they have a dense elliptical -dominated core and a late type galaxy fraction increasing in the less dense areas.

Regarding to the ACS sample, late-type galaxies dominate all the clusters, although the fraction increase in less dense areas. Only for the cases of CL0024 and MS1358, we have found elliptical galaxies dominating the core. We also note a

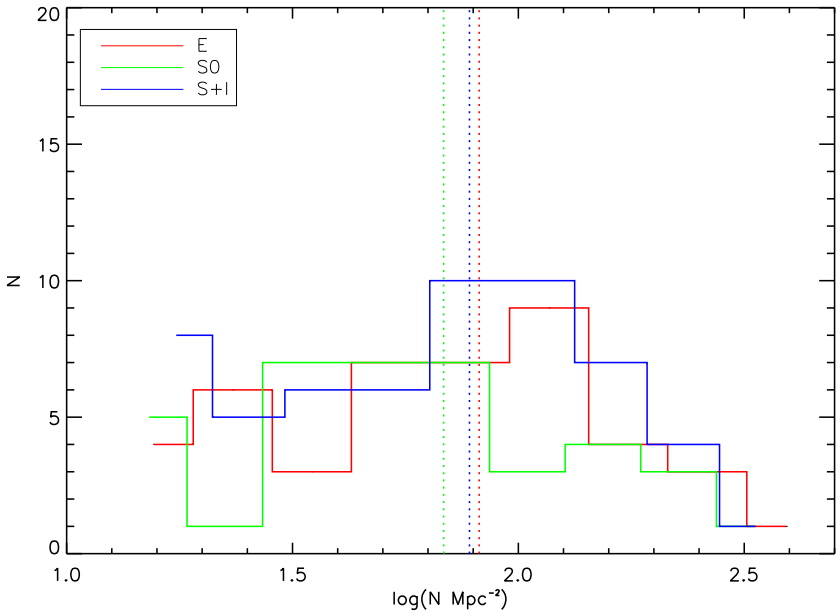

Figure 6.5: Distribution of the local density for three morphological types for the whole NOT sample. Red, Green and Blue lines refer to Eliptical, Lenticular and Late-Type galaxies respectively. Vertical lines shows the mean value of the density for each type.

strong gradient of elliptical galaxies in A2218 corresponding to the merger cluster reported and identified by (Kneib et al., 1995; Markevitch, 1997; Neumann & Böhringer, 1999; Machacek et al., 2002).

6.1.3 Luminosity-Density Relation

We have also studied the relation between density and luminosity. With that purpose, we have plotted in Figures 6.9 and 6.10, the local density versus absolute r magnitude for the whole NOT and ACS sample, separated into three morphological types.

Apparently, we see a mixture of the morphological types. However, we see a region corresponding to the BCGs, (explored in Chapter 8). They are the brightest galaxies ($M_r \leq -22.5$), which are elliptical and are placed in the densest regions ($\rho \geq 100\, gal/Mpc^2$). As far as the Lenticular and Spiral Galaxies we do not distinguish any visible difference in NOT sample, but for the ACS sample, some spiral galaxies appear to be brighter than the brightest lenticular galaxies even if located in areas with similar density.

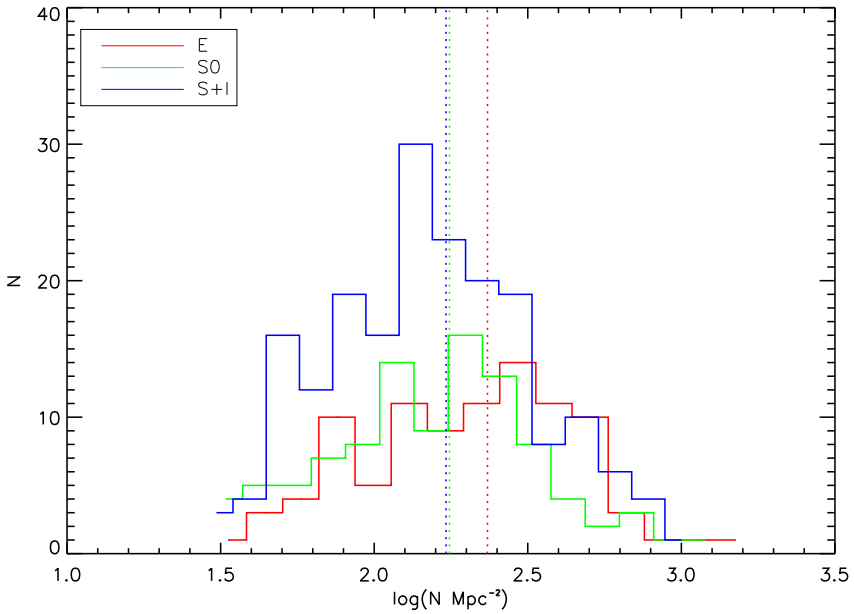

Figure 6.6: Distribution of the local density for three morphological types for the whole ACS sample. Red, Green and Blue lines refer to Eliptical, Lenticular and Late-Type galaxies respectively. Vertical lines shows the mean value of the density for each type.

Let's note the absence of bright galaxies in low density environments. As numerous studies have confirmed (Sandage, 1972a; Gunn & Oke, 1975; Jones & Forman, 1984; Hoessel & Schneider, 1985; Postman & Lauer, 1995; Smith et al., 2005), in clusters of galaxies, we do not find bright galaxies in low density environments. And, as it is also well known, the brightest cluster galaxies are always placed at the center and denser areas of the cluster.

In Figures 6.11 and 6.12, we have shown the luminosity-density relation for the individual clusters, in NOT and ACS sample respectively. It's remarkable the fact that A1878 has a blue bright highly concentrated population, as well as A1643, which presents also a high fraction of blue fainter galaxies, as it was shown in the Chapter 3 and its brightest cluster galaxy is a lenticular galaxy. Also, A1952 has a group of very bright lenticular galaxies in dense environments, which can be a related to a possible substructure as explained in the Chapter 2. Also, A2111 presents a number of spiral galaxies in the dense areas, which may be related with the nature of merger of this cluster.

For the ACS sample, we see as that the elliptical galaxy population occupy the brightest and densest part of the clusters, while the lenticular and spiral galaxy population are also placed in dense areas but with fainter magnitudes ($M_r \lesssim$

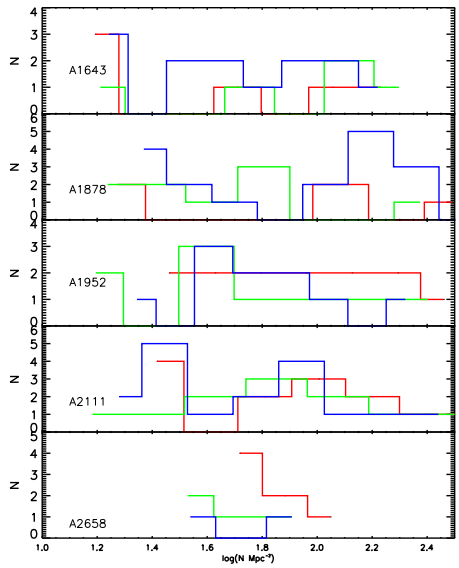

Figure 6.7: Distribution of the local density for three morphological types for individual clusters in NOT sample. Red, Green and Blue lines refer to Eliptical, Lenticular and Late-Type galaxies respectively.

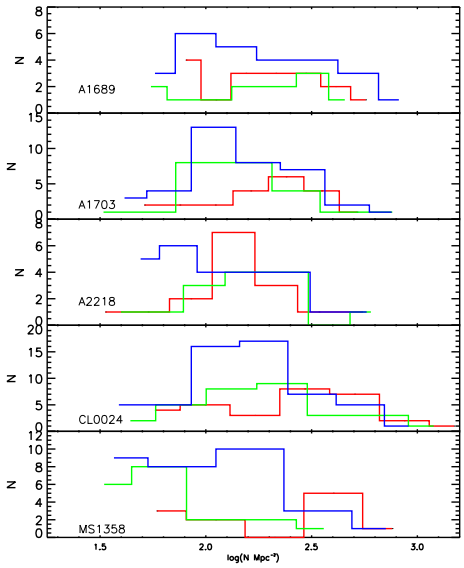

Figure 6.8: Distribution of the local density for three morphological types for individual clusters in ACS sample. Red, Green and Blue lines refer to Eliptical, Lenticular and Late-Type galaxies respectively.

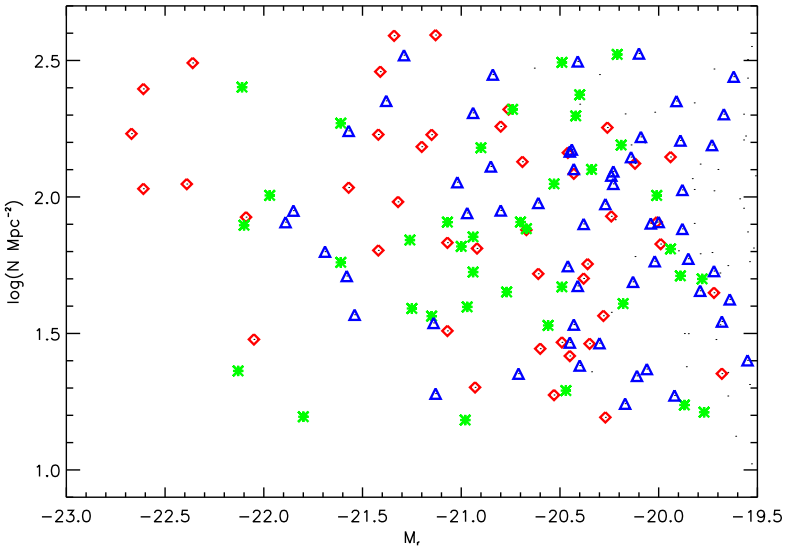

Figure 6.9: Absolute Gunn-r magnitude versus local density into three morphological types for the whole NOT sample. Red diamonds, green asterisks and blue triangles are the Elliptical, Lenticular and Spiral galaxies, respectively.

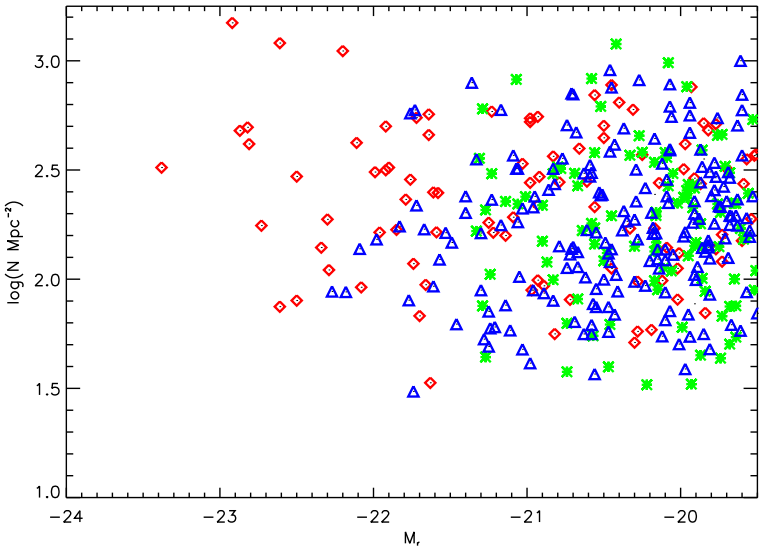

Figure 6.10: Absolute Gunn-r magnitude versus local density into three morphological types for the whole ACS sample. Red diamonds, green asterisks and blue triangles are the Elliptical, Lenticular and Spiral galaxies, respectively.

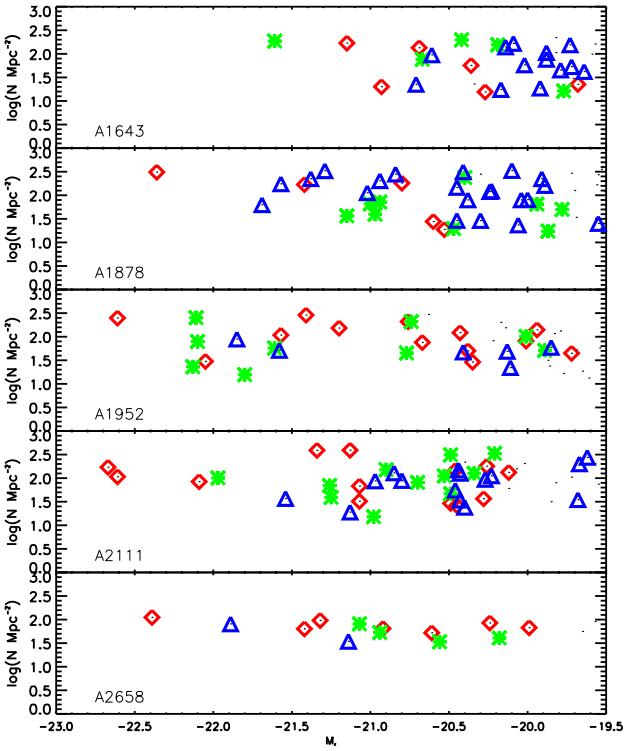

Figure 6.11: Local density versus absolute Gunn-r magnitude into three morphological types for the individual clusters in NOT sample. Red diamonds, green asteriks and blue triangles are the Eliptical, Lenticular and Spiral galaxies, respectively.

-22). In all clusters the brightest galaxies are elliptical galaxies. We note the presence of a bright spiral galaxy placed in the lower density area in the core of A1703. Probably, this galaxy is a foreground galaxy.

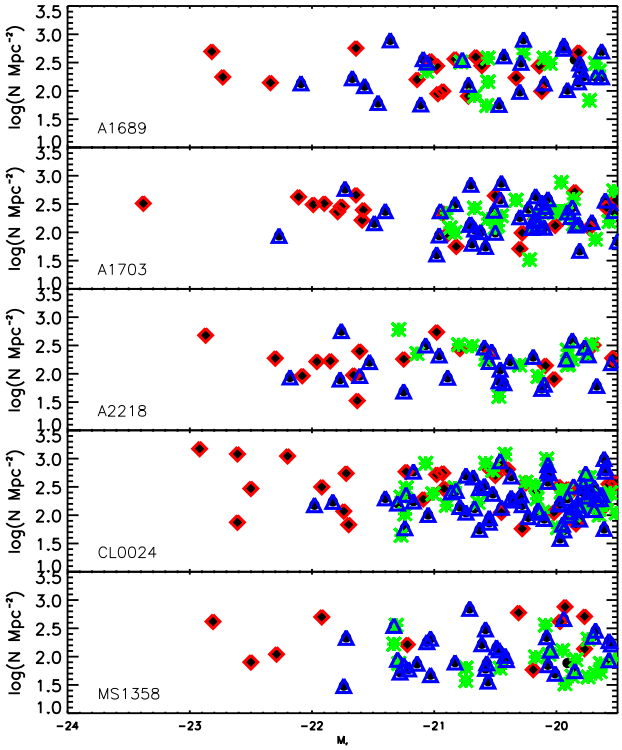

Figure 6.12: Local density versus absolute Gunn-r magnitude into three morphological types for the individual clusters in ACS sample. Red diamonds, green asteriks and blue triangles are the Eliptical, lenticular and Spiral galaxies, respectively.

6.2 The Radial Distribution of Galaxies

6.2.1 Center of the cluster

The center of the cluster is defined to be the point placed at the minimum of the cluster gravitational potential (Sandage, 1972a; Gunn & Oke, 1975; Postman & Lauer, 1995). In the practice, there are several methods to determine the center of the cluster.

- **X-ray distribution**

  Clusters of galaxies have a great proportion of hot gas or plasma at about 10^7 K. The intensity of the X-ray emission is directly related to the depth of the cluster gravitational potential well. In addition, as the X-ray is proportional to the square of the gas density, it is little affected by projection effects in comparison to those arising in optical cluster selection (Romer et al., 1994; van Haarlem, Frenk & White, 1997). Unfortunately, only the more massive clusters can be detected in X-rays, particularly for z >0.1.

- **Brightest Cluster Galaxy (BCG)**

  The Brightest Cluster Galaxies are the galaxies which represent the brightest end of the luminosity function. Not only that, but they have particular properties, different from the rest of the whole sample. That subject will be treated in detail in Chapter 8. Numerous works have determined that they are positioned at the centre of the cluster gravitational potential as they lie close to the peaks of the X-ray emission in concentrated X-ray bright clusters (Jones & Forman, 1984; Rhee & Latour, 1991; Brough et al., 2002).

  According to the theoretical hierarchical scenario (Aragon-Salamanca, Baugh & Kauffmann, 1998; Dubinski, 1998; De Lucia & Blaizot, 2007b), these galaxies could have been originated by the cooling of the gas from the surrounding hot halo medium, together with the accretion of small galaxies falling to the cluster centre as result of dynamical friction and then merge. Other theories (Merritt, 1985; Bird, 1994), suggest that BCGs were formed during or before the cluster collapse and they fell by dynamical friction to the center of the cluster faster than less massive galaxies.

- **Luminosity Barycenter**

  A different approach for locating the center of the cluster is assuming that the luminous mass distribution is tracing the non-luminous mass distribution. The center of the luminosity distribution will be given then by the barycenter coordinates:

$$(X, Y) = (\frac{\sum_i I_i x_i}{\sum_i I_i}, \frac{\sum_i I_i y_i}{\sum_i I_i})$$

Table 6.3: Adopted center position for the NOT Clusters

Name	α(2000)			δ(2000)		
A 1643	12	55	54.00	+44	05	12.40
A 1878	14	12	52.18	+29	14	28.40
A 1952	14	41	03.57	+28	37	00.30
A 2111	15	39	40.60	+34	25	27.00
A 2658	23	44	49.80	−12	17	39.50

where I_i is the luminosity intensity for each galaxy and (x_i, y_i) are the spatial coordinates of the galaxy.

That determination can be problematic due to the limit spatial coverage and their possible biases. Also, the interloper contamination can also affect the results. In addition, the dark matter distribution may behave in a different way from the luminous matter.

- **Dark Matter Center**

  Lensing techniques (Tyson & Fischer, 1995; Kneib et al., 1996; Taylor et al., 1998; Kneib et al., 2004; Broadhurst et al., 2005a; Diego et al., 2005; Zekser et al., 2006), are used to determine the mass of the cluster. The mass is estimated from its dark matter halo profile and consequently, the mass centroid.

- **Density Maximum**

  Assuming the same hypothesis as in the case of the luminosity barycenter that the luminous mass distribution governs the non-luminous mass distribution, we can determine also the center of the cluster finding the peak of the maximum density. That supposition assumes that the center of the cluster must be placed where the largest fraction of luminous matter is concentrated. Again, this approach is valid if the dark matter distribution follows the luminous matter distribution.

We have adopted as the center of the cluster that of the X-ray distribution when known. For the rest, we have established the BCGs coordinates as the center, (see for example, Lin & Mohr (2004)). The center coordinates are collected in Tables 6.3 and 6.4.

The BCG in A2111 is only 5.04 kpc from the X-ray center, while in the ACS sample, we find small distances for A1689 (23.02 kpc), A1703 (7.98 kpc), A2218 (6.15 kpc), and higher differences for CL0024 (99.28 kpc) and MS1358 (195.301 kpc). That fact should be kept in mind in the analysis of the population, as the misalignment of the BCG with the X-ray center could indicate a on-relaxed situation.

Table 6.4: Adopted center position for the ACS Clusters

Name	α(2000)			δ(2000)		
A 1689	13	11	29.5	−01	20	28.2
A 1703	13	15	05.2	+51	49	02.8
A 2218	16	35	48.9	+66	12	42.0
CL0024	00	26	36.3	+17	09	46.0
MS1358	13	59	54.3	+62	30	36.0

6.2.2 Radius-Density Relation

We have studied the radial local density of the galaxies, as it is shown in Figures 6.13 and 6.14 for the NOT and ACS sample respectively. The dotted line refers to a second degree interpolation of this relation.

All the clusters show a smooth decreasing profile as we move towards the outskirts of the cluster, with the exception of A1643, for which the peak found is due to a discontinuity in the area surveyed. For A2658, for which we only cover the inner 420 kpc, we do not have enough area to note any significant tendency.

By comparing these profiles with those showed in Figure 1 of the work by Butcher & Oemler (1978) or the Figure 1 in the work by Butcher & Oemler (1984), we directly see that these profiles are directly related to the concentration of the clusters and therefore with their richness. We observe as the less dense clusters in the NOT sample would be corresponding to b) profiles (Figure 1, in Butcher & Oemler (1978)), corresponding to low concentration values, while for the more dense ACS clusters, our profiles would correspond with d) profiles (Figure 1, Butcher & Oemler (1978)), that is, richer, more concentrated clusters. As we have previously examined in Chapter 4, the concentration values that we have obtained for the NOT sample together with the concentration values extracted from the literature for the ACS clusters give support to these conclusions.

6.2.3 Radius-Morphology Relation

As we have said before, it is well known from the pioneering work by Dressler (1980), that early-type galaxies in clusters at low redshift are located in denser regions and closer to the center of the cluster rather than than late-type galaxies. We want now to investigate the way that those clusters at medium redshift are populated. With that purpose, we have plotted in Figures 6.15 and 6.16 the radius-density relation for each cluster in NOT and ACS sample for early and late morphological types separately.

It's clear that the main population in the central part of A1952, A2111 and A2658 consist on early type galaxies and that these fraction are decreasing as

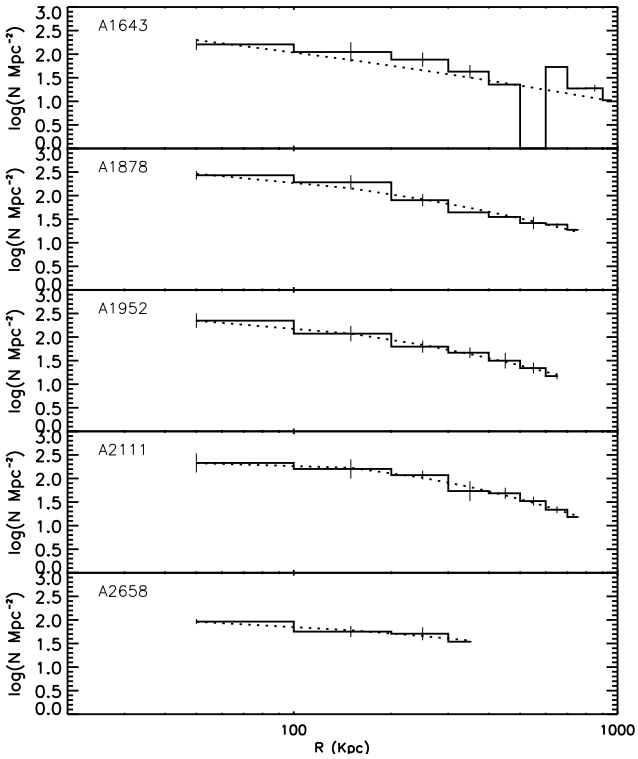

Figure 6.13: Radius-Density Relation for NOT sample

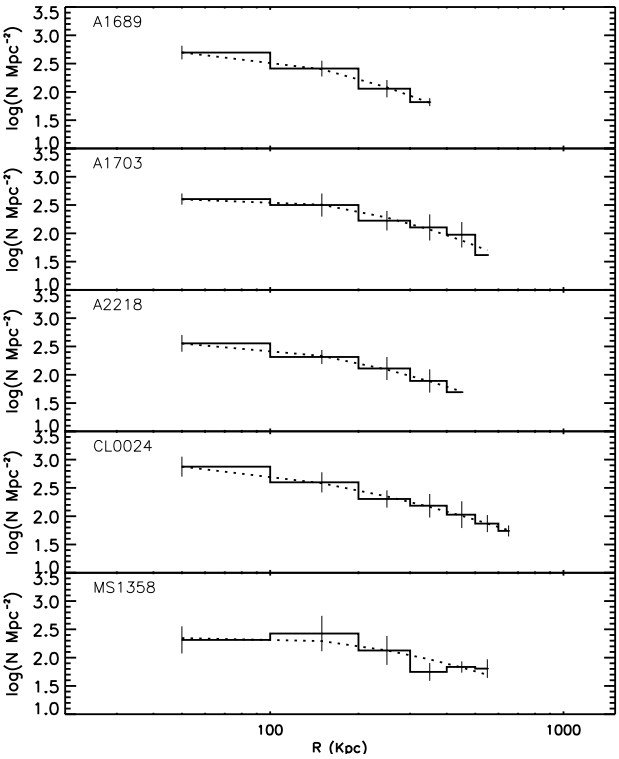

Figure 6.14: Radius-Density Relation for ACS sample

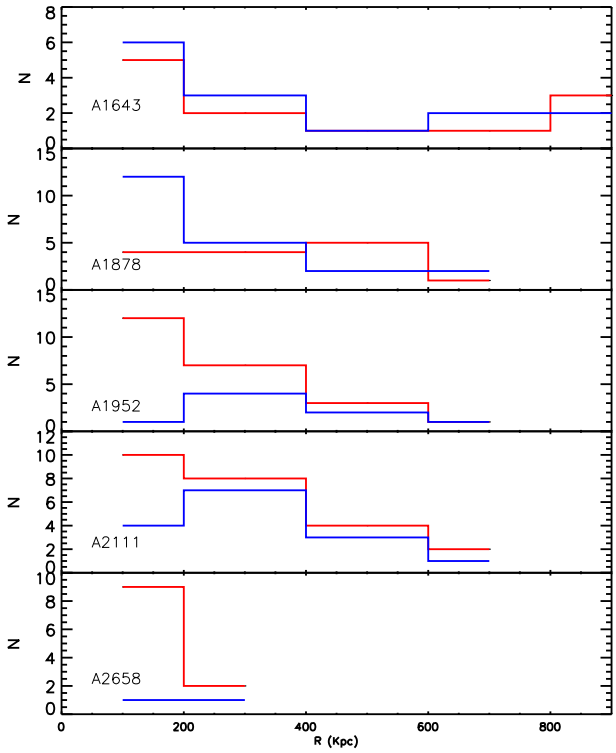

Figure 6.15: Radius-Morphology Relation by morphological types in NOT sample clusters. Red and Blue lines refer to Early and Late Type Galaxy Population.

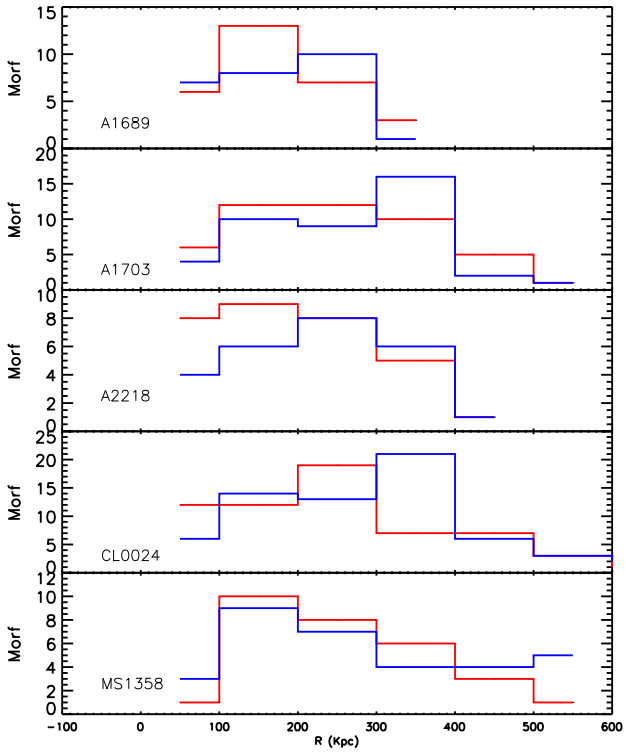

Figure 6.16: Radius-Morphology Relation by morphological types in ACS sample clusters. Red and Blue lines refer to Early and Late Type Galaxy Population.

the distance to the center increases. We find a late-type galaxies peak in A2111, that may be a contribution by the second merging cluster. On the other hand, we find that A1643 and A1878 have a large fraction of late-type galaxies in the central part of the cluster which decreases at larger radios, while the early-type population remains constant, for A1878 and shows a decreasing trend for A1643.

Regarding to the ACS sample, we note a decreasing tendency of the early type population in nearly all clusters, with the exception of the inner 100 kpc, where the tendency is decreasing. The late-type population shows a variety of behaviours. MS1358 shows the same decreasing trend for late types than early types. A1703 and CL0024 seem to have a peak of late type galaxies at about $\sim$ 300 kpc, while A1689 and A2218 shows a late type galaxy maximum at $\sim$ 200 kpc.

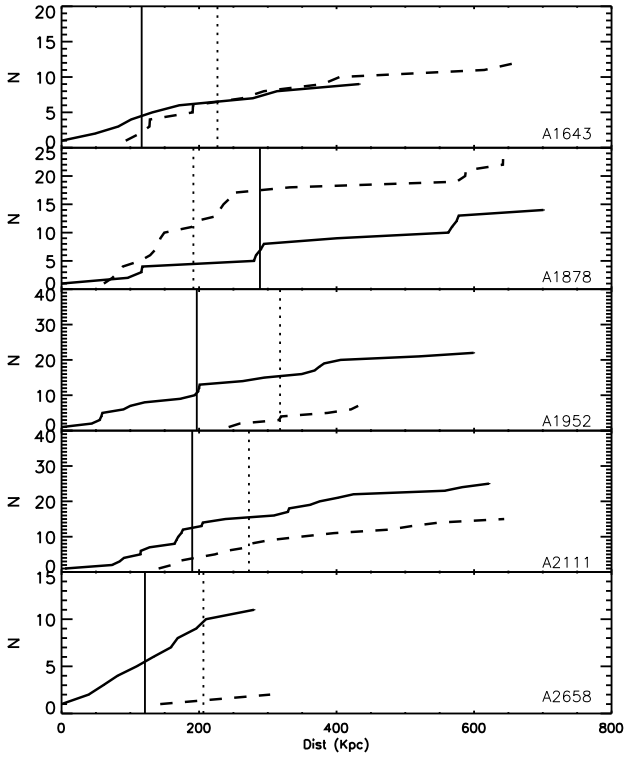

Figure 6.17: Cumulative functions of the different morphological types as a function of the projected radius to the center of the cluster for the NOT sample. Early types: solid lines; late types: dotted lines. The vertical lines indicate the radius where the distributions reach the 50% level.

In Figure 6.17 and 6.18, we have plotted the cumulative functions of the different types of galaxies versus projected distance of each galaxy to the center of the

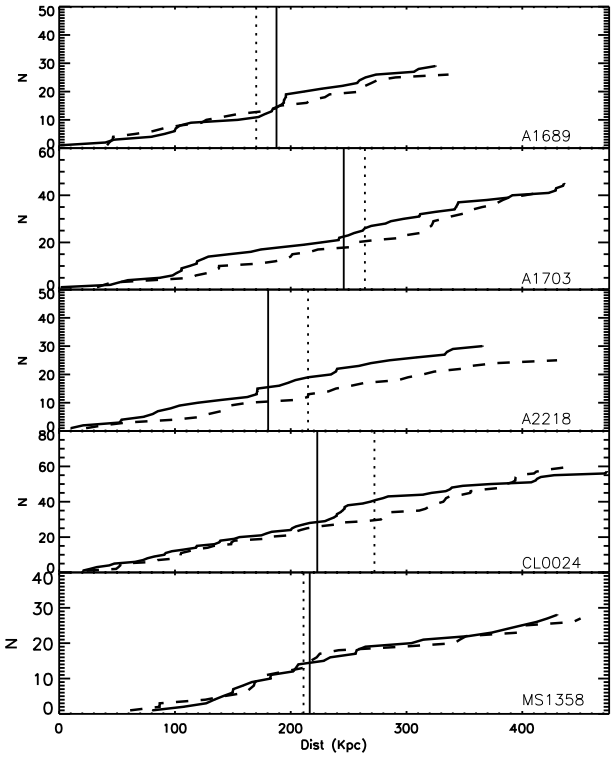

Figure 6.18: Cumulative functions of the different morphological types as a function of the projected radius to the center of the cluster for the ACS sample. Early types: solid lines; late types: dotted lines. The vertical lines indicate the radius where the distributions reach the 50% level.

cluster for both samples. The solid lines represent the cumulative distribution of early-type galaxies, elliptical and lenticular, whereas the dotted lines correspond to the cumulative distribution of late-type galaxies, spiral and irregular. The vertical lines indicate the radius where the cumulative distributions reach the 50% of the distributions.

Regarding to the NOT sample, we see that all the clusters are dominated in their central regions by early type galaxies except A1878, that has a sizable fraction of late-type galaxies, including irregular galaxies. A fact that explains its high (central) fraction of blue galaxies. This is however, not unique since similar cases can also be found at lower redshift (see for example Varela (2004)). A1643 has also a large global fraction of late-type, spiral galaxies, but they do not dominate the core of the cluster. The rest of the clusters are also centrally dominated by a population of elliptical galaxies, with an overall population with a smaller fraction of late-type galaxies.

As far as the ACS sample is concerned, we find one cluster, MS1358 that has a very similar morphological distribution, That is, the two morphological population are not quantitatively different. Also, we find three clusters dominated by an early type population, A1703, A2218 and CL0024 and finally, A1689, which presents a dominating late-type galaxy population in its core.

To test whether the distribution of early and late type galaxies are similar, we have performed a Kolmogorov-Smirnov test. Excluding A2658, for which there are not enough points to extract significant results, we find that the two populations follow significantly different distributions in all clusters except in A1878 and A1952, while for the whole ACS sample, together with A2111 and A1643, the test does not verify the hypothesis. Interestingly, Adami, Biviano & Mazure (1998) found evidence for morphological segregation in low redshift clusters. In our case, we can only say the same for two out of nine clusters in our sample.

In conclusion, we find seven clusters out of ten dominated by an early-type population, two more clusters with the late-type population dominating in their core and one cluster with similar populations. We also find two clusters out of nine (one with an early and late type population dominating respectively) which contain a significantly different morphological population. Those clusters show a situation that agrees with the results found by Adami, Biviano & Mazure (1998) about the morphological segregation at low redshift. However, the other seven clusters does not allow to discern evidence of the morphological segregation found at lower redshift.

The main result that emerges from the discussion is that there are no clear trends regarding the distribution of galaxies of different types in clusters. Diversity appears to be the key word to describe the situation, indicating that the variance of such properties at a given z is very important as to overrun for the tendencies with z. An aspect to be carefully analyzed in any evolutionary study.

Chapter 7

Luminosity Function

Eres, serás, fuiste el Universo encarnado...
Para tí se encenderán las galaxias y se incendiará el sol...
Para que tú ames y vivas y seas...
Para que tú encuentres el secreto y mueras sin poder participarlo,
porque sólo lo poseerás cuando tus ojos se cierren para siempre...

Carlos Fuentes, 'La muerte de Artemio Cruz.'

The **Luminosity Function** (LF) is defined as the number of galaxies per unit volume in a magnitude interval M to M+dM. It can be considered as a probability distribution $\phi(M)$ over absolute magnitude for an individual sample of galaxies. $\phi(M)$ is usually called the **Differential Luminosity Function**, in order to distinguish it from $\Phi(M)$, the **Integrated Luminosity Function**, defined as:

$$\Phi(M) = \int_{-\infty}^{M} \phi(M^{'})dM^{'}$$

The LF has been used to study the way the galaxies form and evolve, Dressler (1984). If we assume that the galaxy mass-to-light ratios are nearly constant, $M/L \approx const$, for the different types of galaxies, the LF can set constraints in the initial mass function and the distribution of density perturbations that are expected to originate the galaxies (Press & Schechter, 1974). Likewise, it can be used as a diagnostic for the changes in the galaxy population due to, for example, the influence of the cluster environment.

Numerous studies to date have noted the difference between the luminosity function for field galaxies and for cluster of galaxies (Hubble & Humason, 1931; Abell, 1965; Oemler, 1974; Binggeli, Sandage & Tammann, 1988; Andreon, 2004), directly related with the luminosity-density analyzed in the previous

Chapter. Lin et al. (1999) presented some evidence for an evolution of M^* for a sample of field galaxies in the redshift range $0.12 < z < 0.55$, of about 0.3 mag in the rest-frame R. Additionally, Blanton et al. (2003), analyzed a larger SDSS data set of field galaxies in the redshift range $0.02 < z < 0.22$ finding a similar variation for M^*. These two works presents therefore evidence for evolution, even if they assume no differential luminosity evolution between bright and faint galaxies.

Regarding to the LF in clusters of galaxies, few signs of evolution have been evidenced up to now. Garilli, Maccagni & Andreon (1999) analyzed the composite luminosity function for a sample of 65 clusters in the redshift range 0.05 $<$ z $<$0.25, finding no evidence of evolution. Likewise, de Propris et al. (1999) found evolution on M^* in the K band in a wide redshift range 0.2$<$ z $<$ 0.9, but only with the assumption of the non evolution of α with redshift.

Also, Gaidos (1997) computed the galaxy composite LF from R imaging of 20 Abell clusters within a redshift range 0.06 $<$z$<$ 0.25, finding that it is well described by a Schechter function with parameters $M_R^* = -20.63 \pm 0.11$ and $\alpha = -1.09 \pm 0.08$ in the magnitude range -24.91 $< M_R <$ -18.91. In this case, the slope they found is similar to the field LF recovered by Lin et al. (1996) from the Las Campanas Redshift Survey, even if the value of M^* is almost one magnitude brighter.

As a consequence, although a number of efforts have been devoted to show the possible evolution of the slope or M^* of the LF from cluster to cluster or from field to cluster, no significant results have been extracted as the LF does not appear to be universal. However, many trends related to the LF for red and blue galaxies seem to provide more information about possible differences in field and clusters. For example, the galaxy clusters LFs seem to be steeper for blue than for red galaxies and their characteristic magnitudes are brighter than in the field, by approximately one magnitude in the red, (see for example, Lin et al. (1996); Gaidos (1997)), and by approximately half a magnitude in the blue (Lumsden et al., 1997; Valotto et al., 1997; Zucca et al., 1997).

In this chapter, we have determined the Schechter parameters for the LF in our ten clusters, medium redshift, sample, by studying their individual and composite luminosity function and analyzing their corresponding morphological and color LFs.

7.1 Background Contamination Estimation

In Chapter 3, we have fitted the Color-Magnitude Relation and dropped out from the cluster all the galaxies whose color was 0.2 magnitude redder than the fit, as background objects are reddened by the cosmological k-effect (Oke & Sandage, 1968; Pence, 1976; Poggianti, 1997). We also ensured by integrating the field luminosity function for field galaxies that the foreground contamination was practically inexistent.

There are at least two more ways for determining the contamination. The most common way of estimating the background contamination is studying the luminosity distribution in the close regions of the cluster (Oemler, 1974). The distance to the field must be enough to be placed outside the cluster and not too large in order to sample the local background. Then, the galaxy counts in the reference field direction are modeled (see Andreon (2004); Andreon, Punzi & Grado (2005)). After that, the difference in the number of counts in each magnitude interval is said to be due to the galaxies from the cluster. Unfortunately, there is no guarantee on the adequacy of the observed background to fit the actual cluster background and the results can not be but statistical in nature.

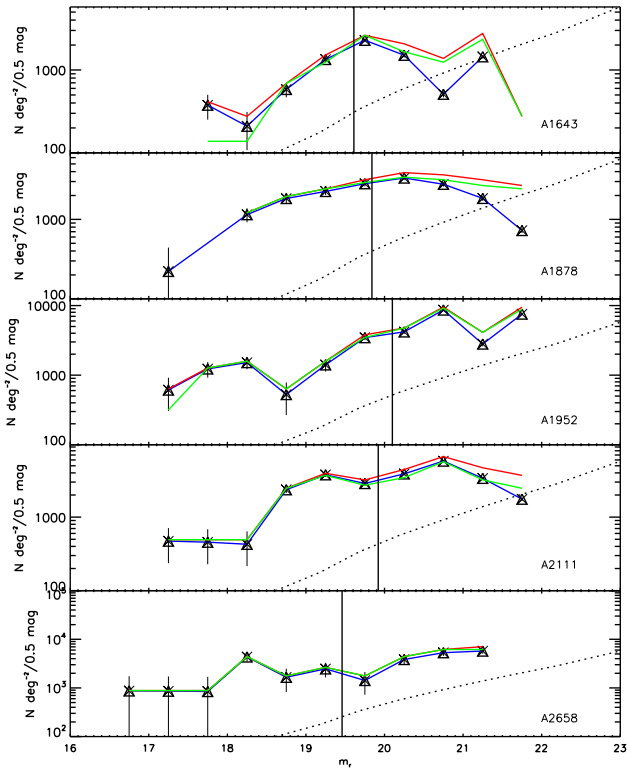

Figure 7.1: Number of galaxies per square degree and 0.5 magnitude bin versus apparent magnitude for all the galaxies detected in NOT sample (red line), without background contamination from McLeod et al. (1995) (blue line) and without background contamination from CMR (green line). The dotted line represents the background contamination given by McLeod et al. (1995). The vertical line shows the completeness limit for each cluster of the sample.

Different measurements provided by a number of authors exist in the literature. We should control that the difference in the instrumentation, methodology and observation conditions are similar to our observations. For our r-band, we have several works that give us the number of galaxies per relative magnitude bin (McLeod et al., 1995; Metcalfe et al., 2001; Yasuda et al., 2001). We have selected the Table 3 from McLeod et al. (1995) as their apparent magnitude range include ours. Metcalfe et al. (2001) give an approximation for galaxies with HST with $m_r > 21$ and Yasuda et al. (2001) arrive to magnitudes $m_r < 21.5$. Several authors (Liske et al., 2003; Berta et al., 2006), provide also reliable galaxy number counts, but unfortunately, in other filters.

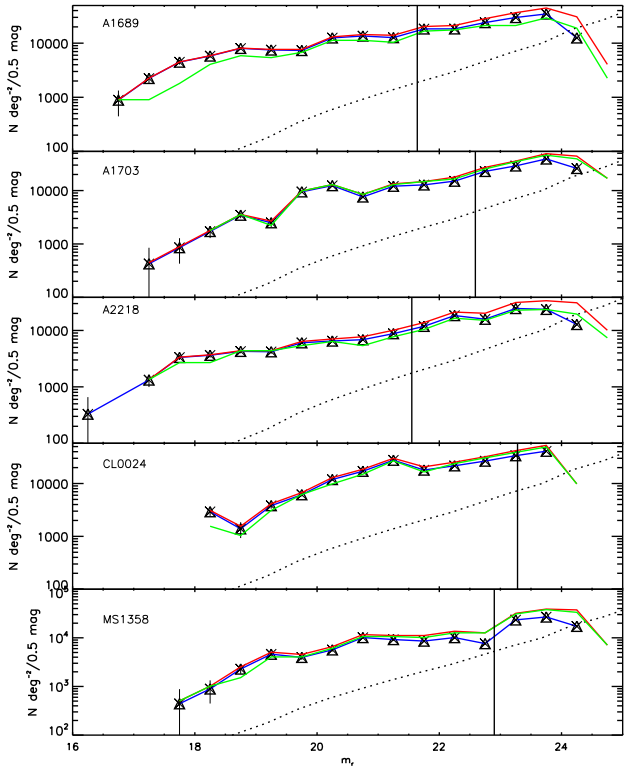

Figure 7.2: Number of galaxies per square degree and 0.5 magnitude bin versus apparent magnitude for all the galaxies detected in ACS sample(red line), without background contamination from McLeod et al. (1995) (blue line) and without background contamination from CMR (green line). The dotted line represents the background contamination given by McLeod et al. (1995). The vertical line shows the completeness limit for each cluster of the sample

In Figures 7.1 and 7.2, we have plotted the points corresponding to the number of galaxies per 0.5 magnitude bin square degree versus magnitude. The dotted line shows a linear spline of the background contamination given by McLeod et al. (1995) and the red line refers to the linear spline of the magnitude distribution for all the galaxies detected without performing the subtraction in the Chapter 3. The blue line corresponds to the count differences from these distributions and finally, the green lines are the galaxy distribution excluding the galaxies by the CMR procedures explained in Chapter 3. The vertical line represents the completeness limit for the sample.

Referring to NOT sample, we only find a slight difference for A1643 and A1878 between the background corrected counts using McLeod et al. (1995) (blue line) and excluding galaxies redder than the CMR (green line) for magnitudes brighter than 19.5. For the rest, the difference of the distributions begins to be noticeable for fainter magnitudes than 20, which is very close to the completeness magnitude limit for the NOT sample, as was set in Figure 3.1. It's noticeable that for A2111, which is the cluster for which we had some redshift information has a nearly coincident background subtraction from McLeod et al. (1995) and the CMR. As we have already seen, the population in A1643 is rather faint, in comparison with the rest of the clusters in the samples. This fact will be translated into a bad fit of the LF as we will see later.

For the ACS sample, A1703, for which we do not have redshift information in literature and MS1358, for which we have very few redshift are the clusters are the clusters that have a largest difference between the subtraction provided by McLeod et al. (1995) and the subtraction provided by the CMR. On the contrary, A1689, A2218 or CL0024 provide an excellent agreement for both distributions up to magnitude $m_r = 22$ at least. Therefore, we will consider the subtraction given by McLeod et al. (1995) as the real galaxy population for computing the luminosity function.

7.2 The Composite Luminosity Function

Since we do not have enough galaxies per magnitude bin in the individual LF, especially, in the NOT sample, we are going to consider the **Composite Luminosity Function** defined by Colless (1989). A number of works in the literature have used it, providing many reliable results (Lumsden et al., 1997; De Propris et al., 2003a; Barkhouse, Yee & López-Cruz, 2007). It has been built by summing up galaxies in absolute magnitude bins and scaling them by the richness of their parent cluster. Specifically, the following summation was carried out

$$N_{c,j} = \frac{R_c}{n_{clus,j}} \sum_i \frac{N_{i,j}}{R_i}$$

where $N_{c,j}$ is the number of galaxies in the jth absolute magnitude bin of the composite LF, $N_{i,j}$ is the number in the jth bin of the ith cluster LF, $n_{clus,j}$ is

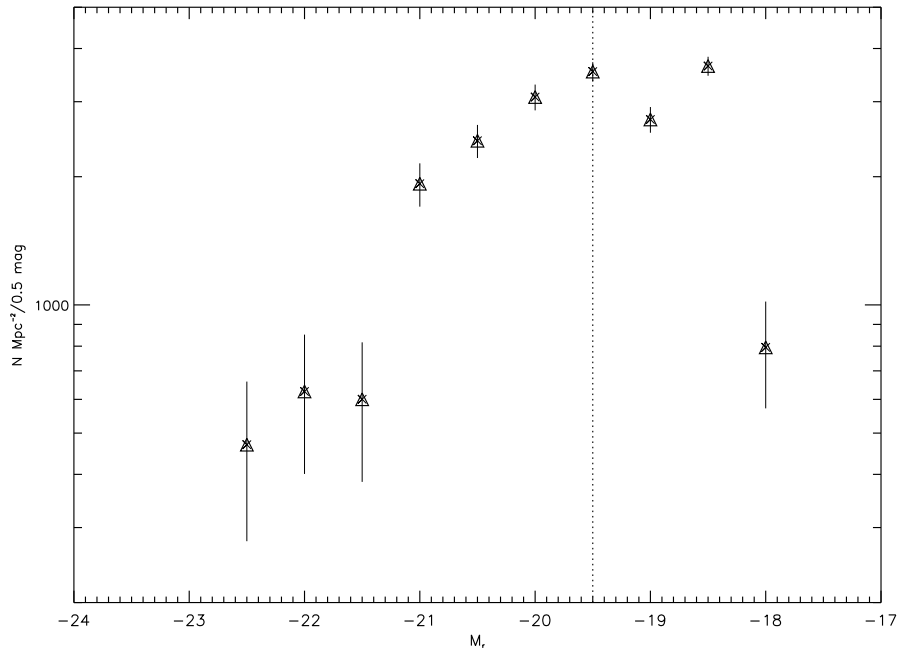

Figure 7.3: Composite Luminosity Function for NOT sample. The vertical line shows the completeness limit of the sample.

the number of clusters contributing to the jth bin, R_i is the normalization used for the it cluster LF and R_c is the sum of all the normalizations:

$$R_c = \sum_i R_i$$

Following Lumsden et al. (1997), we have used a different definition of R_i from the one given in Colless (1989). He used the total number of galaxies brighter than $M = -19$ and we have use the background -corrected number of cluster galaxies brighter than $M = -19.5$, as M_r=-19 is beyond our chosen completeness limit for the NOT sample. For typical values for the LF, the relationship between our definition of richness and that of Colless is $R_i(Colless) \sim 1.34$ $R_i(thesis)$. In Figure 7.3 and 7.4, we have plotted the resulted composite Function for our cluster sample.

The formal errors in $N_{c,j}$ are computed according to

$$\delta N_{c,j} = \frac{R_c}{n_{clus,j}} \left[\sum_i \left(\frac{\delta N_{i,j}}{R_i} \right)^2 \right]^{1/2}$$

where $\delta N_{c,j}$ and $\delta N_{i,j}$ are the formal errors in the jth LF bin for the composite and ith cluster respectively.

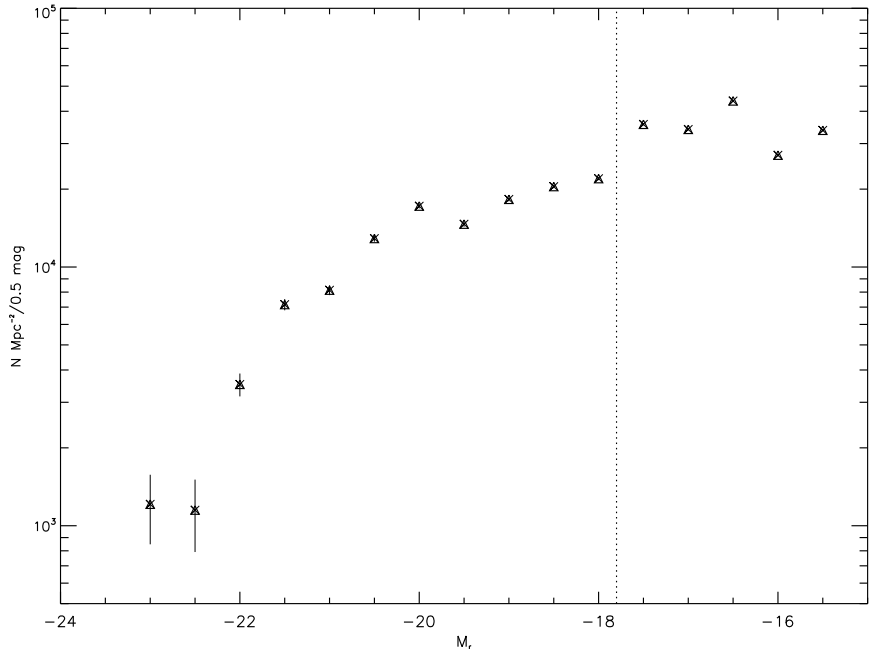

Figure 7.4: Composite Luminosity Function for ACS sample. The vertical line shows the completeness limit of the sample.

7.3 Luminosity Function Fit

The first attempts to study and fit the Luminosity Function were done by Hubble & Humason (1931). They tried to fit their data by a gaussian function. Some decades later, the first clusters compilations were performed by Abell (1958) and Zwicky et al. (1961), who realized that the number of faint galaxies had been underestimated. Abell (1964, 1972), described then two asymptotic behaviors of $\phi(M)$ at the bright and faint end, separated by a 'break point', M* as follows

$$\begin{cases} \log N(\leq m) = K_1 + s_1 m & \text{if } m < m^* \\ \log N(\leq m) = K_2 + s_2 m & \text{if } m \geq m^* \end{cases}$$

where $N(m)$ is the number of galaxies per square degree brighter than m. Zwicky et al. (1961), proposed the following analytical function

$$< n_{cl} > (\Delta m) = k(10^{\Delta m/5} - 1)$$

where $< n_{cl} >$ is the mean number of galaxies in the magnitude range Δm between the magnitude of the brightest galaxy and m.

However, although these estimations were very accurate for the data available, Schechter (1976) proposed an analytical distribution of the luminosity of the galaxies in the following way:

$$\phi_c(L)dL = n^*(L/L^*)^\alpha e^{-L/L^*} d(L/L^*)$$

where ϕ_c is the number of galaxies contained in a volume and in the luminosity range L to $L + dL$ and L^* is the characteristic luminosity corresponding to the 'break point' or *knee* where the slope changes, α is the slope of the luminosity function at low magnitudes and n^* is the constant, which normalizes to the density of galaxies. The whole luminosity of the cluster can be found by integrating the last expression:

$$L_{cluster} = \int_0^\infty L n_c(L) dL = n^* \Gamma(\alpha + 2) L^*$$

where here, Γ represents the mathematical function *Gamma*,

$$\Gamma(a) = \int_0^\infty e^{-t} t^{a-1} dt$$

The analogous Schechter function can be expressed in terms of absolute magnitudes by making the variable change $L/L^* = 10^{(M^*-M)/2.5}$, obtaining the following expression:

$$\phi_c(M)dM = 0.4 \ln(10) \phi^* 10^{0.4(M^*-M)(1+\alpha)} e^{-10^{0.4(M^*-M)}} dM$$

where $\phi_c(M)$ is the number of galaxies per volume unit and magnitude unit, $M^* = 10^{-0.4M^*}$ is the characteristic magnitude where the slope of the LF changes and ϕ^* represent the normalization constant to the galaxy density.

Some authors (Driver et al., 1994; Hilker, Mieske & Infante, 2003; González et al., 2006; Popesso et al., 2006; Barkhouse, Yee & López-Cruz, 2007), have argued that the sum of two Schechter functions provides a more adequate fit to the cluster LF than a single Schechter function. This fact is due to the emergence of a rising faint end (M_r >-19), even though the bright end of the LF appeared to be well fitted by a Schechter function. Alternative LF fitting functions include a Gaussian and a single Schechter function for the bright and faint end respectively (Thompson & Gregory, 1993; Biviano et al., 1995; Parolin, Molinari & Chincarini, 2003), a single power-law fit to the faint end (Trentham et al., 2001; Boué et al., 2008) or an Erlang plus a Schechter function (Biviano et al., 1995).

In our case, we have fitted the LF by a single Schechter function, as we are working in the bright end. We have discussed the influence of including the Brightest Cluster Galaxy in the fit as, in general, the presence of these galaxies is easily noticed by their effect on the brightest magnitude bin, whose value is usually offset from the best-fit Schechter function. Schechter (1976); Sandage (1976); Dressler (1978); Loh & Strauss (2006), remarked that BCGs do not seem to be a natural extension of the cluster LF.

We have explored in the following subsections, different ways of fitting the Luminosity Function, to find the most accurate.

7.3.1 Chi-Square fitting

On account of the differential character of the luminosity function, our abscissas in the fit must be magnitude bins, as their corresponding function values are the number of galaxies in a volume within a magnitude bin. As we do not have too many galaxies, we have obtained few bins, with a moderate number of galaxies.

In order to fit the luminosity function to the Schechter Function, we have minimized the chi-square residuals by using the Levenberg-Marquardt method (LM).

Levenberg-Marquardt Method

Let's call $y = y(x; \overrightarrow{a})$, the function we want to fit, in our case the Schechter function, where $\overrightarrow{a}$ is the set of n-parameters we want to determine. Then, the χ^2 function is defined as

$$\chi^2(\overrightarrow{a}) = \sum_{i=1}^{N} [\frac{y_i - y(x_i, \overrightarrow{a})}{\sigma_i}]^2 \tag{7.1}$$

where x_i and y_i are the set of points that we want to fit and σ_i is standard deviation in each point and N is the number of points where we have a value for the function.

When the solution is close enough to the minimum, the χ^2 can be approximated by a quadratic form:

$$\chi^2(\vec{a}) \approx \gamma - d.\vec{a} + \frac{1}{2}\vec{a}\mathbf{D}\vec{a} \tag{7.2}$$

where $\vec{d}$ is a vector with the same number of components as $\vec{a}$, n and $\mathbf{D}$ is the $n \times n$ Hessian matrix.

If the approximation is good enough, we will jump from the present solution $\vec{a}_{act}$ to the following that minimizes the χ^2 function $\vec{a}_{min}$ as follows:

$$\vec{a}_{min} = \vec{a}_{act} + \mathbf{D}^{-1}[-\nabla\chi^2(\vec{a}_{act})] \tag{7.3}$$

In case the approximation is not good, we will go back with the gradient like that:

$$\vec{a}_{sig} = \vec{a}_{act} - constant[\nabla\chi^2(\vec{a}_{act})] \tag{7.4}$$

where the constant must be small enough not to leave the present descends direction.

To be able to use equation 7.3 and 7.4, we need to compute the gradient of the χ^2 for any set or parameters $\vec{a}$, as well as the Hessian matrix of χ^2.

The χ^2 gradient respect the M parameters that form $\vec{a}$ has the following form:

$$\frac{\partial\chi^2}{\partial a_k} = -2\sum_{i=1}^{N}[\frac{y_i - y(x_i, \vec{a})}{\sigma_i^2}]\frac{\partial y(x_i, \vec{a})}{\partial a_k} \qquad k = 1, 2, \ldots, M \tag{7.5}$$

and deriving again:

$$\frac{\partial^2\chi^2}{\partial a_k \partial a_l} = 2\sum_{i=1}^{N}\frac{1}{\sigma_i^2}[\frac{\partial y(x_i, \vec{a})}{\partial a_k}\frac{\partial y(x_i, \vec{a})}{\partial a_l}] - [y_i - y(x_i, \vec{a})]\frac{(\partial y(x_i, \vec{a}))^2}{\partial a_k \partial a_l} \tag{7.6}$$

Let's note that in that equation, we can ignore the second derivative term as it is negligible when comparing with the first derivative term. In addition, the factor which is multiplying is the error in each point, and therefore, it tends to cancel out when we sum over all i. So, equations 7.5 and 7.6 have the following form:

$$\beta_k = \frac{-1}{2}\frac{\partial\chi^2}{\partial a_k} \tag{7.7}$$

and

$$\alpha_{kl} = \frac{1}{2}\mathbf{D} = \sum_{i=1}^{N} \frac{1}{\sigma_i^2}[\frac{\partial y(x_i, \vec{a})}{\partial a_k}\frac{\partial y(x_i, \vec{a})}{\partial a_l}] \tag{7.8}$$

and, therefore, equation 7.3 can be rewritten as

$$\sum_{l=1}^{M} \alpha_{kl}\delta a_l = \beta_k \tag{7.9}$$

and equation 7.4 as

$$\delta a_l = constant \times \beta_l \tag{7.10}$$

where δa_l denotes the increments that added to the present approximation are the following($\delta a_l = \vec{a}_{min} - \vec{a}_{act}$) for equation 7.3 or ($\delta a_l = \vec{a}_{sig} - \vec{a}_{act}$) for equation 7.4.

Therefore, the condition of χ^2 being a minimum, is that $\beta_k = 0$ for any k (i.e: the gradient is null) and it is independent of the way α is defined.

LM method uses the fact that Hessian Matrix could give us information about the order of magnitude of the constant. If we compare the units in equation 7.10, we have that the constant must have dimensions of $1/\alpha_{kk}$. The authors divided the constant by an addimensional factor λ so that the constant is not too large. We have the possibility of setting $\lambda \gg 1$ for stopping the process. That is, they replace equation 7.10 by

$$\delta a_l = \frac{1}{\lambda\alpha_{ll}}\beta_l \quad \text{or similarly} \quad \lambda\alpha_{ll}\delta a_l = \beta_l \tag{7.11}$$

where α_{ll} is positive by definition in equation 7.8.

Then, LM method introduces a new matrix α' defined as

$$\alpha'_{jk} \equiv \begin{cases} (1+\lambda)\alpha_{jk} & \text{if } j = k \\ \alpha_{jk} & \text{if } j \neq k \end{cases}$$

and, finally, we can replace equations 7.9 and 7.11 by

$$\sum_{l=1}^{M} \alpha'_{kl}\delta a_l = \beta_k \tag{7.12}$$

Notice that when λ is too large, α' sets into a dominant diagonal matrix, so equation 7.12 tends to be identical to equation 7.11, and if λ tends to zero, the equation 7.12 approximates to equation 7.9.

The LM method can very sensitive to the initial conditions. For example, it can find a local minimum (if we are not close enough) or a 'valley' (depending on the problem geometry). To avoid those problems, we have created a grid with initial conditions for the method and selected the one which provides the smallest χ^2 value. The values for the grid have been set to vary in the following ranges

$$-2.5 \leq \alpha \leq -0.5 \quad \text{and} - 19.5 \leq \mathrm{M}^* \leq -22.5$$

with a step of 0.1. We have obtained the same optimal parameters if we set our parameters at random or with the grid, which suggest that the minimum is isolated inside that range.

In Figures 7.5 and 7.6, we have plotted the Schechter fit to the Composite Luminosity Function for the NOT and ACS samples. The solid line shows the fit excluding the BCGs and the dotted lined refers to the fit considering the brightest cluster galaxy in the fit. The results of the fit are

$$\alpha = -0.95 \pm 0.22\,,\; M_r^* = -20.93 \pm 0.37$$

and

$$\alpha = -1.15 \pm 0.18\,,\; M_r^* = -21.38 \pm 0.41$$

with the exclusion and inclusion of the BCG respectively, for the NOT sample.

$$\alpha = -1.11 \pm 0.16\,,\; M_r^* = -21.65 \pm 0.86$$

and

$$\alpha = -1.11 \pm 0.15\,,\; M_r^* = -21.64 \pm 0.75$$

with the exclusion and inclusion of the BCG respectively, for the ACS sample. We have considered in each case, the range of completeness for the fit for every sample.

Although the difference between including or not the BCG in the ACS luminosity composite function fit does not affect the fit, we have noted a different LF for the NOT sample. By excluding the BCG, we see how the fit is weighted by the fainter points, while if we consider the whole range of magnitude, the brighter points make the faint end appear steeper. This is due to the fact that for the NOT clusters, the LF does not extend to faint magnitudes as it does for ACS clusters. The higher weight of the faint end in the ACS clusters makes the influence of including or not the BCG less important.

We can conclude that the values provided for the Composite Function for the ACS sample are representative of the LF at redshift $\sim$ 0.2- 0.4 with an slope of $\alpha = -1.11 \pm 0.15$ and $M_r^* = -21.64 \pm 0.75$

It is noticeable that at the faint end of the LF for the ACS sample, the tendency seems to be ascending, as not fittable by a single Schechter as several authors have already noted (Biviano et al., 1995; Parolin, Molinari & Chincarini, 2003; Boué et al., 2008).

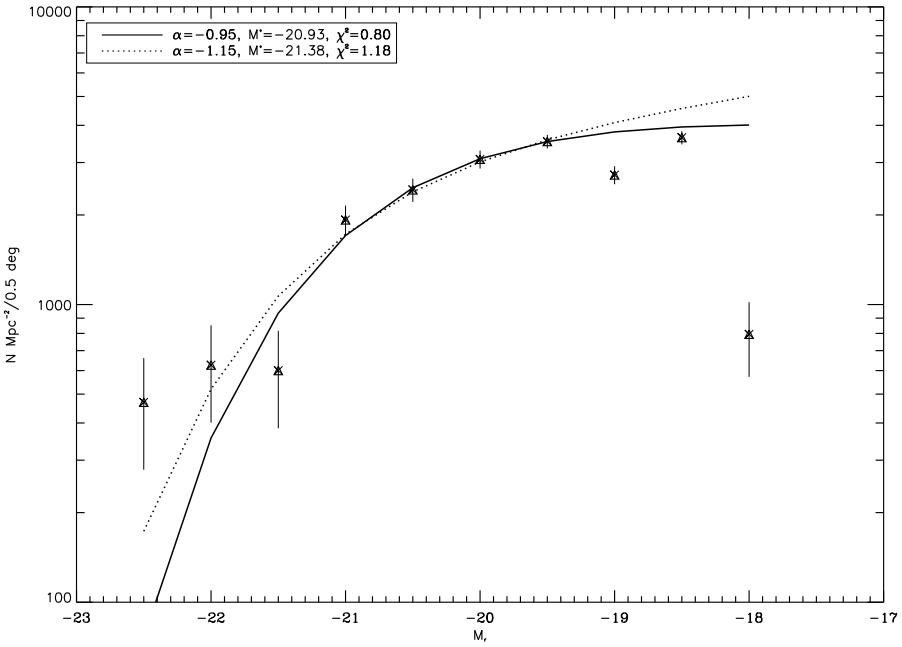

Figure 7.5: Best Schechter fit of the Composite LF for the NOT sample. The solid line refers to the fit excluding the BCGs and the dotted line is referring to the fit including the BCG

In Figure 7.7, we have plotted the Schechter function with the best parameters given by the Levenberg-Marquardt method for each individual cluster in the NOT sample, up to the complete magnitude limit ($M_r = -19.5$). The results of the fit are also collected in Table 7.1. The fits give a median value for the slope of -0.93 and -0.86, considering or not the BCG. A1878 and A2111 appear to have the 'typical LF shape', while for the rest of the cluster in the sample, the bins carry large errors to find a good fit. In particular, A1643 shows a significant difference at considering the BCG or not, which is understandable as it does not show as the typical luminosity function.

For the ACS sample, the situation is completely different. In Figure 7.8, we have plotted the Schechter function with the best parameters given by the Levenberg-Marquardt method, up to the completeness limit, ($M_r = -17.8$). The parameters obtained in the fit are also collected in Table 7.2.

The fit for the ACS sample is considerably different from the NOT sample, as

Table 7.1: Best Schechter Parameters of the Luminosity Function with and without the BCG for the NOT sample

	With BCG			Without BCG		
Name	α	M*	χ^2	α	M*	χ^2
A 1643	-2.00 ± 0.82	-21.53 ± 0.38	1.18	-1.26 ± 0.82	-20.21 ± 0.79	0.02
A 1878	-0.93 ± 0.22	-21.08 ± 0.39	0.72	-0.86 ± 0.24	-20.94 ± 0.38	0.84
A 1952	-1.70 ± 0.10	-22.50 ± 0.00	4.47	-1.70 ± 0.10	-22.50 ± 0.00	4.64
A 2111	-0.50 ± 0.00	-20.63 ± 0.07	4.79	-0.50 ± 0.00	-20.64 ± 0.07	4.60
A 2658	-0.50 ± 0.00	-21.58 ± 0.37	1.26	-0.50 ± 0.00	-21.49 ± 0.41	1.45
Composite	-1.15 ± 0.18	-21.38 ± 0.41	1.18	-0.95 ± 0.22	-20.93 ± 0.37	0.80

Table 7.2: Best Schechter Parameters of the Luminosity Function with and without the BCG for the ACS sample

	With BCG			Without BCG		
Name	α	M*	χ^2	α	M*	χ^2
A 1689	-1.19 ± 0.03	-22.18 ± 0.19	6.93	-1.20 ± 0.03	-22.30 ± 0.25	7.35
A 1703	-1.12 ± 0.03	-21.51 ± 0.14	17.78	-1.10 ± 0.03	-21.46 ± 0.14	18.41
A 2218	-1.22 ± 0.03	-22.23 ± 0.24	2.58	-1.22 ± 0.03	-22.21 ± 0.26	2.81
CL0024	-1.17 ± 0.01	-21.53 ± 0.08	53.79	-1.14 ± 0.01	-21.41 ± 0.07	54.95
MS1358	-0.82 ± 0.03	-20.98 ± 0.12	6.91	-0.85 ± 0.04	-21.06 ± 0.12	6.97
Composite	-1.11 ± 0.15	-21.64 ± 0.75	10.92	-1.11 ± 0.16	-21.65 ± 0.86	12.66

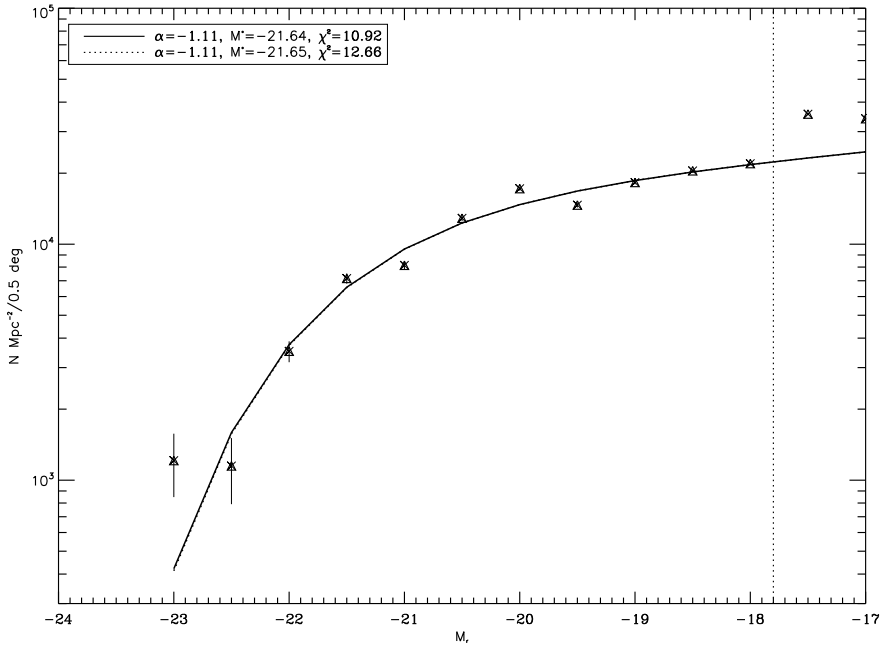

Figure 7.6: Best Schechter fit of the Composite LF for the ACS sample. The solid line refers to the fit excluding the BCGs and the dotted line is referring to the fit including the BCG

the extent in magnitude is much larger. Although we do not cover a large area, the results are much more reliable than in NOT sample. We find a median value for the slope of -1.17 and -1.14, considering or not the BCG, which are considerably higher than the values of NOT sample. For the reasons given before, the differences between including or not the BCG are not relevant in any case.

The value we have obtained for the slope in A2218 agrees with the value reported by Pracy et al. (2005). They studied the projected luminosity function in the inner Mpc in the V-band, by fitting a single Schechter function to the LF. They found a slope of $\alpha = -1.14^{+0.08}_{-0.07}$, reporting also a more compact distribution of the brightest cluster galaxy as it is noticeable in the Figure 7.8. That fact will be analyzed in Chapter 8.

As noted by Barkhouse, Yee & López-Cruz (2007), the results of that fit for two free parameters are not too reliable as there are few bins. Taking this into account, we have refitted the FL but this time fixing the slope at the faint end $\alpha = -1.15$, the value found for the Composite Luminosity Function, which is well in the range of values extracted from the individual clusters from the ACS sample.

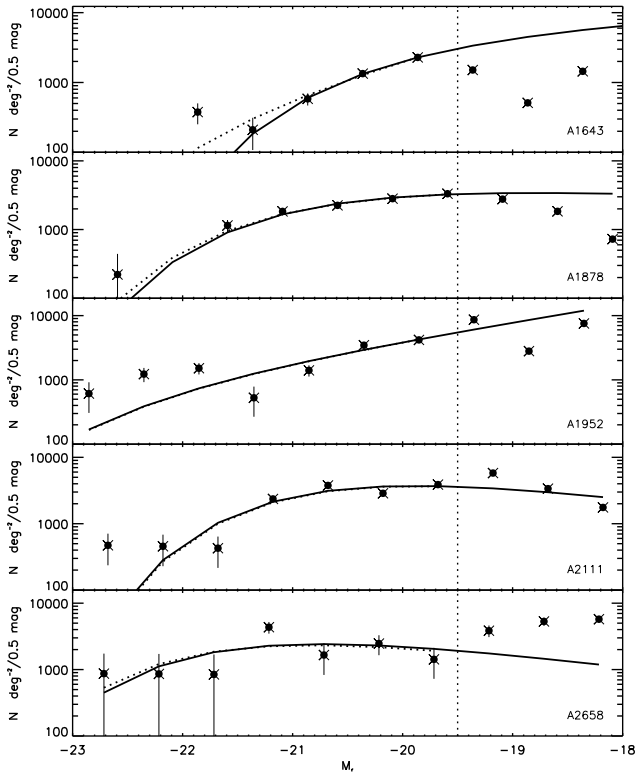

Figure 7.7: Best fit of the differential LF for the NOT sample. The vertical line shows the limit where the sample is complete. The solid line refers to the fit excluding the BCGs and the dotted line is referring to the fit including the BCG

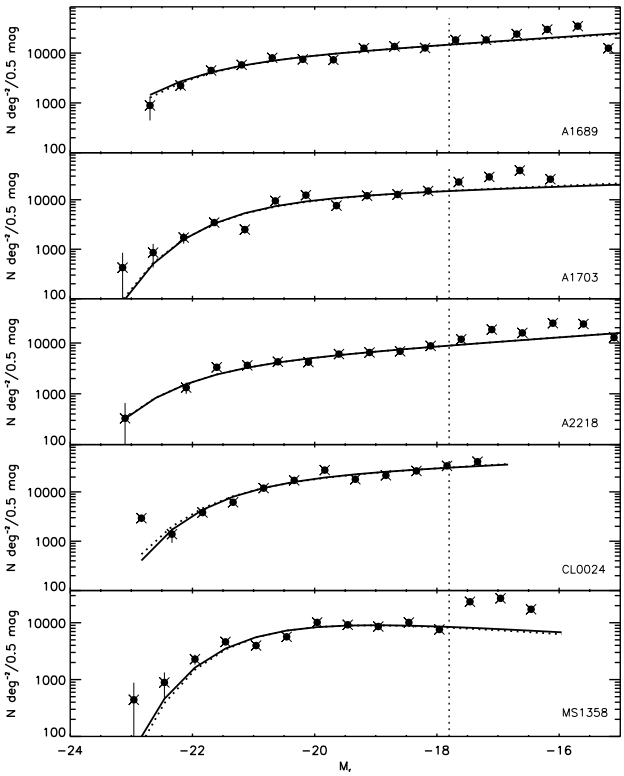

Figure 7.8: Best fit of the differential LF for the ACS sample. The vertical line shows the limit where the sample is complete. The solid line refers to the fit excluding the BCGs and the dotted line is referring to the fit including the BCG

Table 7.3: Best Schechter Parameters of the Luminosity Function with α=-1.15 for the NOT sample

Name	With BCG M*	χ^2	Without BCG M*	χ^2
A 1643	-20.17 ± 0.13	1.57	-20.11 ± 0.13	0.02
A 1878	-21.46 ± 0.17	0.87	-21.41 ± 0.18	1.13
A 1952	-20.80 ± 0.17	5.96	-20.85 ± 0.18	6.23
A 2111	-21.56 ± 0.14	6.49	-21.57 ± 0.15	7.02
A 2658	-22.50 ± 0.00	1.83	-22.50 ± 0.00	2.08

Table 7.4: Best Schechter Parameters of the Luminosity Function with α=-1.15 for the ACS sample

Name	With BCG M*	χ^2	Without BCG M*	χ^2
A 1689	-22.00 ± 0.09	7.08	-22.02 ± 0.10	7.60
A 1703	-21.62 ± 0.07	17.83	-21.64 ± 0.08	18.59
A 2218	-21.91 ± 0.18	2.91	-21.91 ± 0.11	3.13
CL0024	-21.47 ± 0.04	53.87	-21.45 ± 0.04	54.98
MS1358	-22.31 ± 0.13	14.17	-22.25 ± 0.13	12.89

In Figure 7.9 and 7.10, we show the results of the individual Schechter fit for the clusters in NOT and ACS sample, respectively, with the slope $\alpha = -1.15$. The results for M^* are shown in Tables 7.3 and 7.4.

As expected, the fits for the ACS sample are always very good. However, the results differ from the values found for the ACS sample with two free parameters, which seems to indicate that the whole luminosity function can not be properly fit by a single Schechter Function with only one parameter. It is very clear now that the faint end of the Luminosity Function ($M_r \geq -18$) has a rising trend.

The LF fits in the NOT sample have smaller χ^2 than a single luminosity function with two free parameters, but for the cases noted before (A1643 or A2658), the LF seems to be disturbed obtaining a non-reliable fit. It is remarkable the case of A1952, where the first three brightest bins are brighter than the luminosity prescribed by the Schechter fit, indicating the presence of a more luminous group of galaxies.

As many authors have already noted (see Sandage, Tammann & Yahil (1979); Popesso et al. (2004); Andreon (2004); Andreon, Punzi & Grado (2005), the fit of the Luminosity Function by binning the data, allows a quick analysis of the data and it's very 'visual' to see how data is distributed. However, continuity is

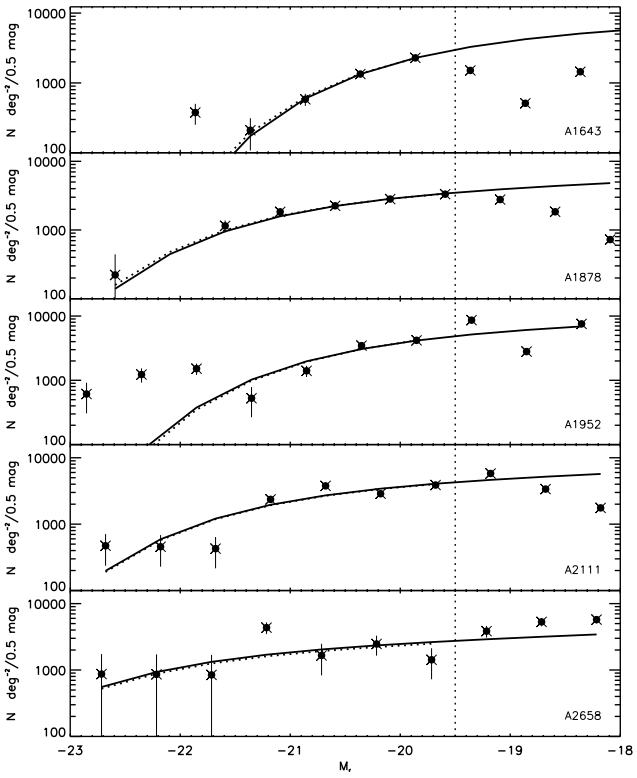

Figure 7.9: Best fit of the differential LF with α=-1.15 for the NOT sample. The vertical line shows the limit where the sample is complete. The solid line refers to the fit excluding the BCGs and the dotted line is referring to the fit including the BCG

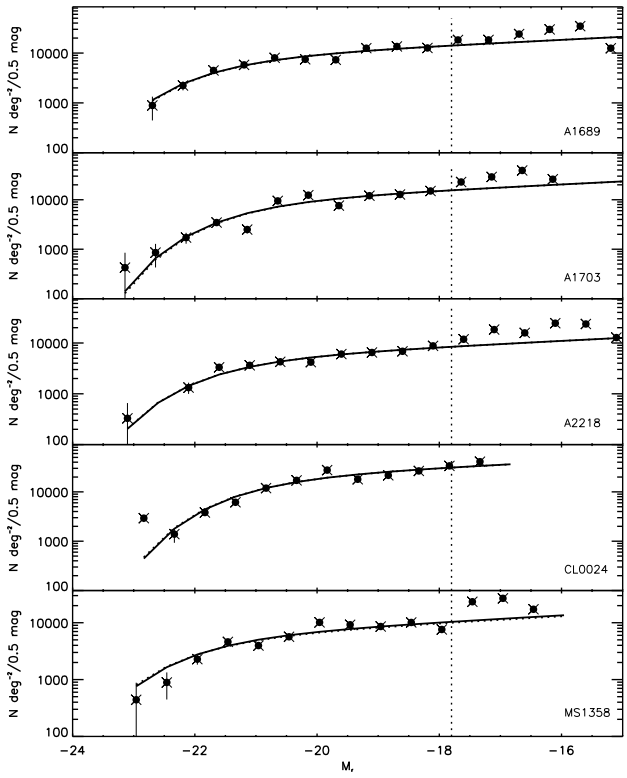

Figure 7.10: Best fit of the differential LF with α=-1.15 for the ACS sample .The vertical line shows the limit where the sample is complete. The solid line refers to the fit excluding the BCGs and the dotted line is referring to the fit including the BCG

lost in binning and therefore, information. In our case, it is very clear that the results of the fit for the NOT sample are too poor for giving reliable information. Even though, three clusters in NOT sample, A1878, A1952 and A2111, together with the whole ACS sample, provide reliable good fits. In the next sections, we are going to investigate alternative fitting methods.

7.3.2 Chi-Square integral fitting

One way to avoid dealing with the magnitude binning, is fitting the integral of the luminosity function. We have used the χ^2 Levenberg-Marquard minimization method explained in the last section. As explored before, we need to get the partial derivatives of the integral function.

Let's work now with the LF expressed in function of the Luminosity instead of absolute magnitude, (see equation 7.3), for the simplicity of the calculus. If we set, $S = L/L^*$ and, therefore, $S_{max} = L_{max}/L^*$, we must calculate the following equation:

$$L(\geq L_i, \leq L_{max}) = \int_{S_i}^{S_{max}} n^* S^\alpha e^{-S} dS = n^*[\gamma(\alpha+1, S_i) - \gamma(\alpha+1, S_{max})]$$

where in this case, γ represents the incomplete mathematical function *gamma*,

$$\gamma(a, x) = \int_x^\infty e^{-t} t^{a-1} dt$$

We need to set the analytical derivates in order to use the Levenberg-Marquardt method.

$$\frac{\partial L}{\partial n^*} = \gamma(\alpha+1, S_i) - \gamma(\alpha+1, S_{max}) = \gamma(\alpha+1, L_i/L^*) - \gamma(\alpha+1, L_{max}/L^*)$$

$$\begin{aligned} \frac{\partial L}{\partial L^*} &= \frac{\partial L}{\partial S}\frac{\partial S}{\partial L^*} = -n^* S^{\alpha+1} e^{-S}/L^*|_{S_i}^{S_{max}} + \frac{\partial S_{max}}{\partial L^*} F(S_{max}) - \frac{\partial S_i}{\partial L^*} F(S_i) \\ &= 2\frac{n^*}{L^*}\left[(L_i/L^*)^{\alpha+1} e^{-L_i/L^*} - (L_{max}/L^*)^{\alpha+1} e^{-L_{max}/L^*}\right] \end{aligned}$$

where F is the integrand, $F(S) = n^* S^\alpha e^{-S}$. We have used the Chain Rule, the Fundamental Calculus Theorem in the second and third step and the in the last equality, we have undone the variable change.

$$\frac{\partial L}{\partial \alpha} = \int_{S_i}^{S_{max}} n^* S^\alpha e^{-S} \ln(S) dS$$

In this equation, we have used that the Leibniz's rule considering that the integrand, F and $\partial F/\partial\alpha$ are continuous in the integration range. We obtain

that integral now, which can not be solved analytically. We can express it by changing variables

$$\left\{ \begin{array}{ll} u = ln(S) & du = 1/SdS \\ dv = S^{\alpha}e^{-S}dS & v = \gamma(\alpha+1,S_i) - \gamma(\alpha+1,S_{max}) \end{array} \right.$$

in the following form

$$\begin{aligned} \frac{\partial L}{\partial \alpha} &= \gamma(\alpha+1,S_i) - \gamma(\alpha+1,S_{max})\Big[\ln(S)\Big]|_{S_i}^{S_{max}} - \\ &\int_{S_i}^{S_{max}} \Big[\gamma(\alpha+1,S_i) - \gamma(\alpha+1,S_{max})\Big]/SdS = \\ &\gamma(\alpha+1,S_i)\Big[\ln(S)\Big]|_{S_i}^{S_{max}} - \int_{S_i}^{S_{max}} \gamma(\alpha+1,S_i)/SdS \end{aligned}$$

In order to solve the integral term of the last equation, we're going to use that the integrand is continuous in the measurable integration range, as the integration limits are always positive.

$$\begin{aligned} \int_{S_i}^{S_{max}} \gamma(\alpha+1,S_i)/SdS &= \int_{S_i}^{S_{max}} 1/S^{'}dS^{'} \int_{S_i}^{\infty} S^{\alpha}e^{-S}dS = \\ \int_{S_i}^{S_{max}} \int_{S_i}^{\infty} S^{\alpha-1}e^{-S}dSdS &= \int_{S_i}^{S_{max}} \gamma(\alpha,S_i)dS = (S_{max}-S_i)\gamma(\alpha,S_i) \end{aligned}$$

Finally the α-derivative has the following form

$$\begin{aligned} \frac{\partial L}{\partial \alpha} &= \gamma(\alpha+1,S_i)(\ln(S_{max}) - \ln(S_i)) - (S_{max}-S_i)\gamma(\alpha,S_i) = \\ &\gamma(\alpha+1,\frac{L_i}{L^*})(\ln(\frac{L_{max}}{L^*}) - \ln(\frac{L_i}{L^*}) - (\frac{L_{max}-L_i}{L^*})\gamma(\alpha,\frac{L_i}{L^*}) \end{aligned}$$

In Figures 7.11 and 7.12, the results of the cumulative Schechter Function are plotted for the NOT and ACS samples, respectively. The fit parameters are given in Tables 7.5 and 7.6. We have applied the decontamination of the background counts by interpolating the counts given by McLeod et al. (1995). Then, we have integrated this interpolation and we have subtracted to our accumulated counts.

Let's note that although the fits are good, the function 'has lost information' as any changes in the slope of the differential LF will be reflected in a much weaker variation in the slope of the cumulative LF. Mathematically, the integral of a continuous function is smoother than the own function, as it is derivable. That's the reason why nearly all the fits have an α parameter very close to -1 and the value of M* tends to achieve the extremes of the boundary extremes. We will have to take that results with caution.

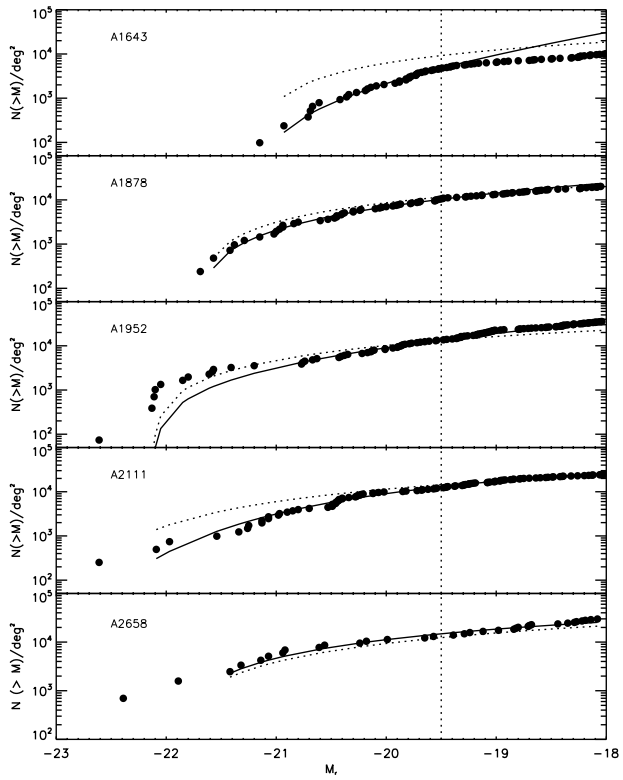

Figure 7.11: Best fit of the cumulative LF for the NOT sample. The vertical line shows the limit where the sample is complete.

Table 7.5: Best Schechter Parameters of the Integral Luminosity Function for the NOT sample

	With BCG			Without BCG		
Name	α	M^*	χ^2	α	M^*	χ^2
A 1643	-1.98 ± 0.36	-20.61 ± 0.52	1.25	-1.99 ± 0.43	-20.95 ± 0.93	1.54
A 1878	-1.01 ± 0.13	-20.97 ± 0.17	1.12	-1.27 ± 0.19	-22.08 ± 0.78	1.07
A 1952	-1.56 ± 0.02	-22.50 ± 0.00	3.80	-1.49 ± 0.03	-22.50 ± 0.00	6.39
A 2111	-1.01 ± 0.07	-21.20 ± 0.09	7.57	-1.01 ± 0.07	-21.20 ± 0.09	7.68
A 2658	-1.00 ± 0.11	-22.50 ± 0.00	0.51	-1.00 ± 0.12	-22.50 ± 0.00	1.35

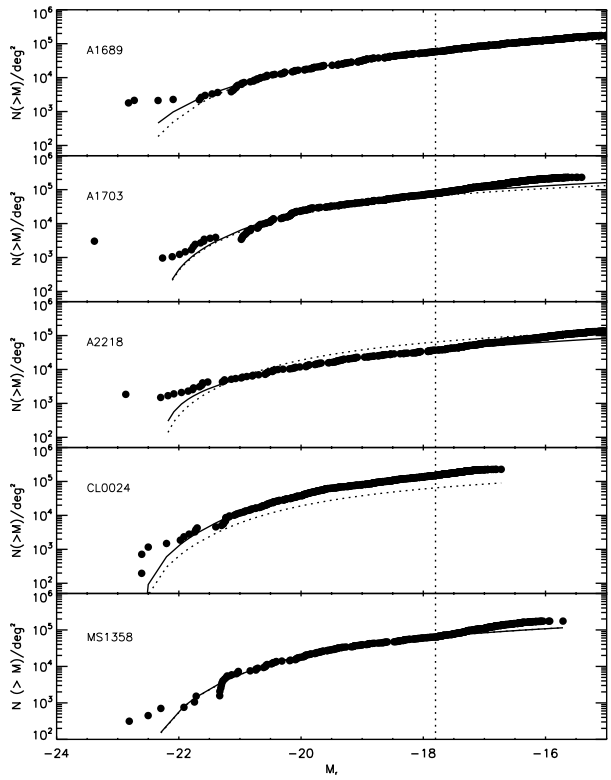

Figure 7.12: Best fit of the cumulative LF for the ACS sample. The vertical line shows the limit where the sample is complete.

Table 7.6: Best Schechter Parameters of the Integral Luminosity Function for the ACS sample

	With BCG			Without BCG		
Name	α	M*	χ^2	α	M*	χ^2
A 1689	-1.25 ± 0.01	-21.76 ± 0.04	3.88	-1.25 ± 0.01	-21.77 ± 0.04	3.84
A 1703	-1.03 ± 0.01	-20.98 ± 0.01	21.01	-1.04 ± 0.01	-21.04 ± 0.01	20.80
A 2218	-1.14 ± 0.01	-21.91 ± 0.04	4.89	-1.16 ± 0.01	-22.22 ± 0.08	5.49
CL0024	-1.09 ± 0.01	-21.07 ± 0.01	5.40	-1.10 ± 0.01	-21.08 ± 0.01	12.83
MS1358	-1.00 ± 0.01	-21.03 ± 0.02	5.40	-1.00 ± 0.01	-21.04 ± 0.02	5.39

7.3.3 Maximum Likelihood Method

The **Maximum Likelihood Method (MLM)** was introduced in Astronomy by Schechter & Press (1976); Sandage, Tammann & Yahil (1979); Sarazin (1980); Efstathiou, Ellis & Peterson (1988). It has a great advantage: the bin dependence is eliminated and in addition, the density parameter ϕ^* drops out as we're going to see in that section.

Consider a galaxy i observed at a redshift z_i, in a flux-limited survey. Let $m_{min,i}$ and $m_{max,i}$ denote the apparent magnitude limits of the field in which galaxy i is located. The probability that this galaxy i has absolute magnitude M_i is given by

$$p_i = p(M_i|z_i) = \phi(M_i) / \int_{M_{min}(z_i)}^{M_{max}(z_i)} \phi(M) dM$$

The likelihood function L of a set of N galaxies, with respective absolute magnitudes M_i are the product of the probabilities p_i

$$L = p(M_1, ..., M_N|z_1, ..., z_N) = \prod_{i=1}^{N} p_i$$

If we apply logarithms, we can express it in the following form:

$$\ln L = \sum_{i=1}^{N} \left[\ln \phi(M_i) - \ln \int_{M_{min}(z_i)}^{M_{max}(z_i)} \phi(M) dM \right]$$

Let's note that for clusters of galaxies, the redshift can be considered as constant, so the likelihood can be expressed as

$$\ln L = \sum_{i=1}^{N} \left[\ln \phi(M_i) \right] - (N-1) \ln \int_{M_{min}}^{M_{max}} \phi(M) dM$$

The method consist on assuming a parametric model for $\phi(M)$ and obtaining the parameters of $\phi(M)$ by maximizing the likelihood L (or $\ln L$) with respect to those parameters. Sandage, Tammann & Yahil (1979) described the so called **STY method** by fitting the Schechter function (equation 7.3) with the Likelihood method. Let's note that this method does not need to bin the data. On the contrary it takes information of each galaxy magnitude. Another convenience of this method is that the normalization ϕ^* drops out in equation 7.3.3 reducing the parameter space to two. It can be determined by

$$\phi^* = \frac{\bar{\rho}}{\int_{M_{min}}^{M_{max}} \phi'(M) dM}$$

where ϕ' is the Schechter function with ϕ^* set to 1 and $\bar{\rho}$ is the mean galaxy density.

As many authors have already noted (Press et al., 1992; Andreon, 2004; Popesso et al., 2004; Andreon, Punzi & Grado, 2005), it is necessary to use a robust minimizator as the desired global maximum may be often found hidden among many poorer, local maxima in high dimensional spaces or in flat 'valleys'.

We have tried different methods for maximizing (or minimizing) the likelihood function: the *Downhill Simplex Minimization Method* (Nelder & Mead, 1965); the *Powell Minimization Method* (Acton, 1970) and the *Davidson-Fletcher-Powell* (see Press et al. (1992)). From those methods, we have obtained the best results from the third method.

Davidson-Fletcher-Powell Method

This algorithm belongs to the so called, *variable metric* or *quasi-Newton* methods. The variable metric methods differ from the conjugate gradient ones in the way that they store and update the information that is accumulated. The former requires a matrix of size $N \times N$ while the later only need intermediate storage on the order of N.

Given an arbitrary function $f(x)$, it can be locally approximated by the quadratic form of equation.

$$f(x) \approx c - bx + \frac{1}{2}xAx$$

The variable metric methods build up iteratively a good approximation to the inverse Hessian matrix A^{-1}, that is, it constructs a sequence of matrix H_i, accomplishing,

$$\lim_{i \to \infty} H_i = A^{-1}$$

Those methods are sometimes called *quasi-Newton* methods. Let's consider finding a minimum to search for a zero of the gradient of the function by using Newton's method . Near the current point x_i, we have the second order

$$f(x) = f(x_i) + (x - x_i)\nabla f(x_i) + \frac{1}{2}(x - x_i)A(x - x_i)$$

which can be expressed as

$$\nabla f(x) = \nabla f(x_i) + A(x - x_i)$$

In Newton's method, we set $\nabla f(x) = 0$ to determine the next iteration point:

$$x - x_i = -A^{-1}\nabla f(x_i)$$

and we have that the left-hand term is the finite step needed for getting to the exact minimum and the right-hand term is known once we have computed an accurate $H \approx A^{-1}$. The word 'quasi' is referred to the fact that we do not use the actual Hessian matrix of f, but instead we use an approximation, which allows the matrix to be a positive definite, symmetric Hessian matrix.

Table 7.7: Best Schechter Parameters of the Luminosity Function using the Maximum Likelihood method with $\alpha = -1.15$ for the NOT sample

Name	M*	χ^2
A 1643	-19.64 ± 0.00	47.42
A 1878	-21.12 ± 0.01	47.19
A 1952	-21.75 ± 0.16	42.32
A 2111	-21.25 ± 0.22	49.63
A 2658	-21.86 ± 0.02	17.11

Table 7.8: Best Schechter Parameters of the Luminosity Function using the Maximum Likelihood method with $\alpha = -1.15$ for the ACS sample

Name	M*	χ^2
A 1689	-21.26 ± 0.01	55.39
A 1703	-21.25 ± 0.11	86.96
A 2218	-21.99 ± 0.01	52.13
CL0024	-21.09 ± 0.01	125.85
MS1358	-21.21 ± 0.34	62.97

This method is implemented in a CERN routine called MINUIT 94.1 (James & Roos, 1975). MINUIT allows the user to set the initial value, the resolution, and the upper and lower limits of any parameter in the function to be minimized. Values of one or more parameters can be kept fixed during a run. MINUIT can use several strategies to perform the minimization. Our choice is MIGRAD (Fletchter, 1970), a stable variation of the *Davidon-Fletcher-Powell* variable metric algorithm for the convergence at the minimum, and the MINOS routine to estimate the error parameters in case of non-linearities. We also have placed constraints on the values of M^* and α that the fitting routine can accept, to avoid being trapped in a false minimum (M^* in the range between -18 and -22 mag and α between 0 and -2.5 (Lumsden et al., 1997; Popesso et al., 2004).

The problem with that maximum likelihood method is that the Gamma Function, $\Gamma(\alpha)$, is undefined for constant values of α. Therefore, the fit tends to converge to those false minima. Therefore, we have decided to perform the fit of Luminosity Function using the Maximum Likelihood with a fixed $\alpha = -1.15$ for both samples. In Table 7.7 and 7.8, we have set the results of the fit.

As we see, the slope at the faint end, fixing $\alpha = -1.15$, M^* varies between $-21.$ to -21.75, with the exception of A1643, that we have previously seen that

its shape does not correspond with the usual LF of a typical cluster. We see also some differences between that fit, and the LM fit with α fixed. The values obtained for M^* here are fainter than those obtained by LM, in particular for three clusters, A2658, A1689 and MS1358. However, the dispersion in the M^* is much smaller with MINUIT than the obtained with that Levenberg-Marquardt method.

After considering the advantages and drawbacks for each method, we conclude that the best fits for the whole ten clusters are provided by their Composite Luminosity Functions. However, the fits provided by the ACS sample are good enough to be considered alone with the chi^2 method.

We have compared these values with a lower redshift sample by López-Cruz et al. (1997). In Figure 7.13, we have plotted the results of the fit for the Schechter Luminosity Function for our sample (black points, ACS sample; triangles, NOT sample) compared to the results found by López-Cruz et al. (1997) in R magnitude at low redshift. We find that the values for the ACS sample for the α parameter are in complete agreement with those found by López-Cruz et al. (1997) at low redshift. However, the values obtained for the NOT sample, spread a much wider range than the rest. Only two clusters in NOT sample showed a smooth LF to show significant results. In particular, A1643 has a quite distorted shape, showing the more deviant values in the Figure.

Regarding to the M^* parameter, the same wide dispersion for three clusters in NOT sample is evident. However, if we consider the ACS sample together with the fits for A1878 and A2111, we note slightly fainter values of M^* as the redsdhift increases, but if we take into account the errors, no variation is obtained.

To conclude, the ACS sample shows a robust value for the Schechter parameter with and without considering the BCGs galaxies

$$\alpha = -1.11 \pm 0.15\,,\; M_r^* = -21.64 \pm 0.75$$

while the NOT sample shows a significant difference between including or not the BCG in the fit as we have fewer bins and therefore the points are much more weighted by the brightest bin. The results we have obtained for the NOT sample are

$$\alpha = -0.95 \pm 0.22\,,\; M_r^* = -20.93 \pm 0.37$$

and

$$\alpha = -1.15 \pm 0.18\,,\; M_r^* = -21.38 \pm 0.41$$

with the exclusion and inclusion of the BCG respectively, for the NOT sample. These Schechter parameters are quite similar to the parameters obtained at

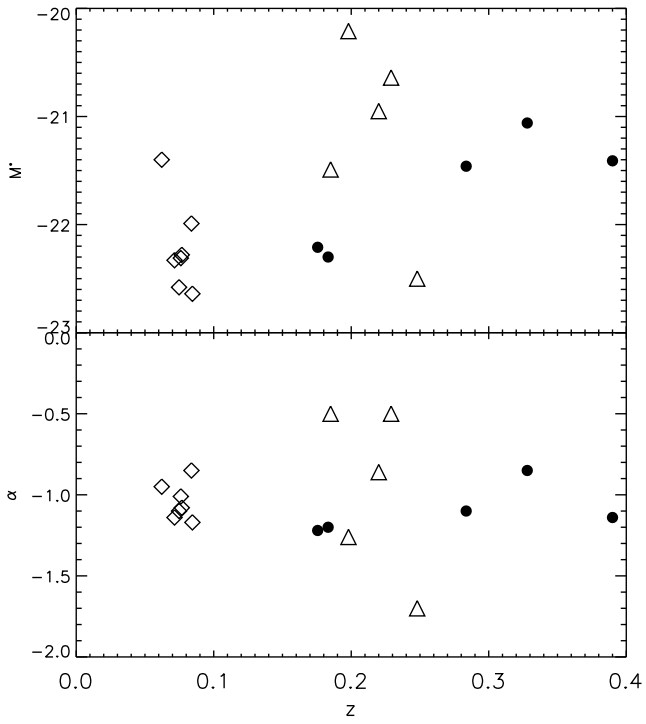

Figure 7.13: Top panel: Schechter M^* parameter versus redshift. Bottom panel: Schechter α parameter versus redshift for NOT sample (triangles), ACS sample (black points), compared with López-Cruz et al. (1997) sample (diamonds).

lower redshift even if we find slightly fainter values of M^* than lower redshift sample. This result goes in the sense of a fainter young population in clusters at z $\sim$ 0.2

7.4 Luminosity - Morphology relation

As we will discuss later, many authors have claimed for the non-universality of the LF. One of the main arguments that supports this assert is the different behavior of the LF referring to morphological types. In that section, we have studied the Luminosity Function by separating them into different morphological types. In Figures 7.14 and 7.15, the luminosity distribution for early and late type galaxy population are shown for the NOT sample, while in Figures 7.16 and 7.17 the corresponding distributions for the ACS sample are displayed.

Even if we have few galaxies to find a reliable fit for the luminosity function, we are able to distinguish some trends. For example, we note a nearly constant trend of the early type galaxy population for nearly all clusters, with the exception of A1643, A2111 and A1689, where we find a larger number of faint early type galaxies than bright. As far as the late type population is concerned, we note an ascending tendency in a great proportion of clusters, finding a larger number of galaxies at fainter magnitudes. However, that tendency seems to be the opposite in A1878, A2111 and MS1358. As it is noticeable in the Figures, we have few galaxies and large errors in this distribution so we can not extract any reliable conclusions.

However, as we saw in the last section, the whole population in clusters with small area coverage and restrictions in magnitude is much better described by the Composite Luminosity Function. We have computed the Composite Luminosity Function for early types (Figures 7.18 and 7.20) and for late types (Figures 7.19 and 7.21) for the NOT and ACS sample respectively. The values given by the Schechter fit are collected in Tables 7.9 and 7.10.

Table 7.9: Best Schechter Parameters of the Cumulative Luminosity Function for Early and Late Types for the NOT sample

	With BCG			Without BCG		
Name	α	M*	χ^2	α	M*	χ^2
Early	-0.50	-22.50	13.89	-0.50	-22.50	12.18
Late				-0.50	-22.50	14.36

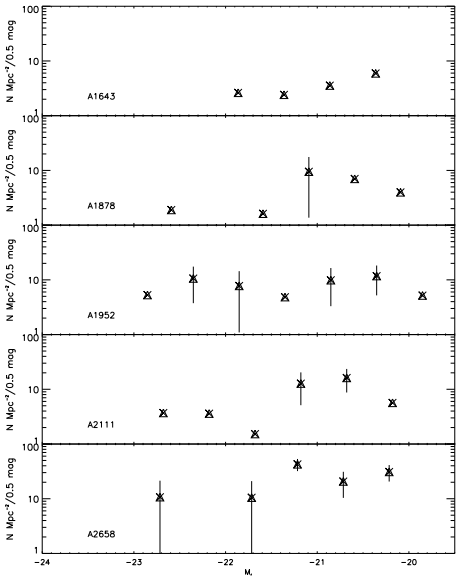

Figure 7.14: LF for Early Type galaxies NOT sample clusters

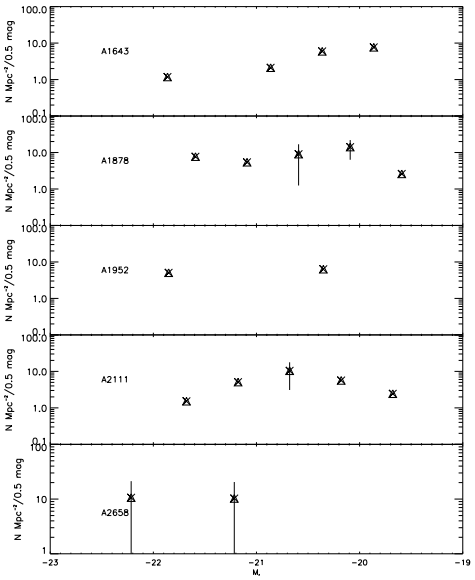

Figure 7.15: LF for Late Type galaxies NOT sample clusters

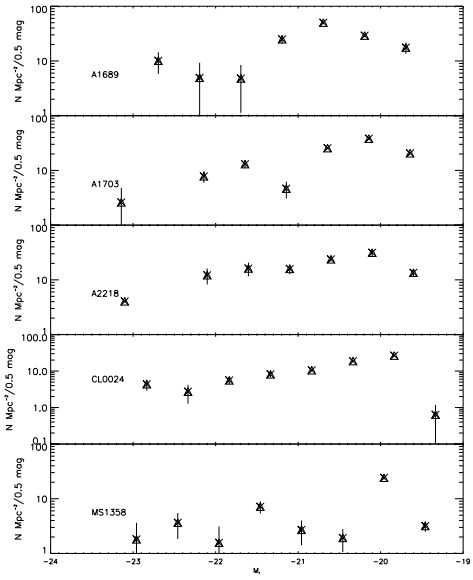

Figure 7.16: LF for Early Type galaxies in ACS sample clusters.

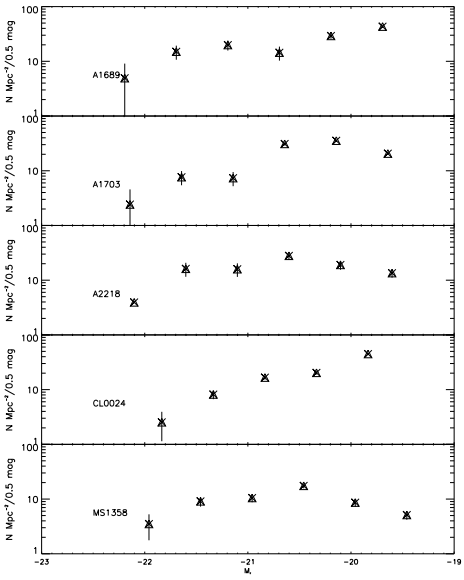

Figure 7.17: LF for Late Type galaxies in ACS sample clusters.

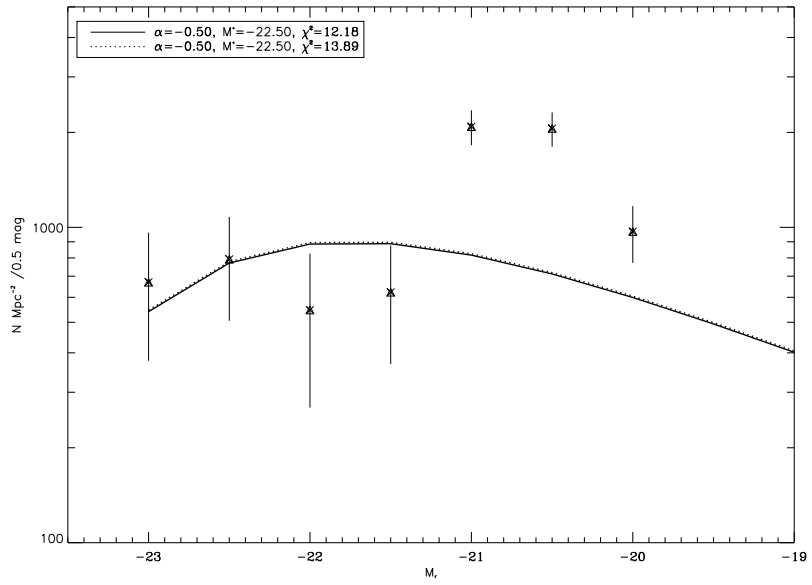

Figure 7.18: Composite LF for Early Type galaxies in NOT sample.

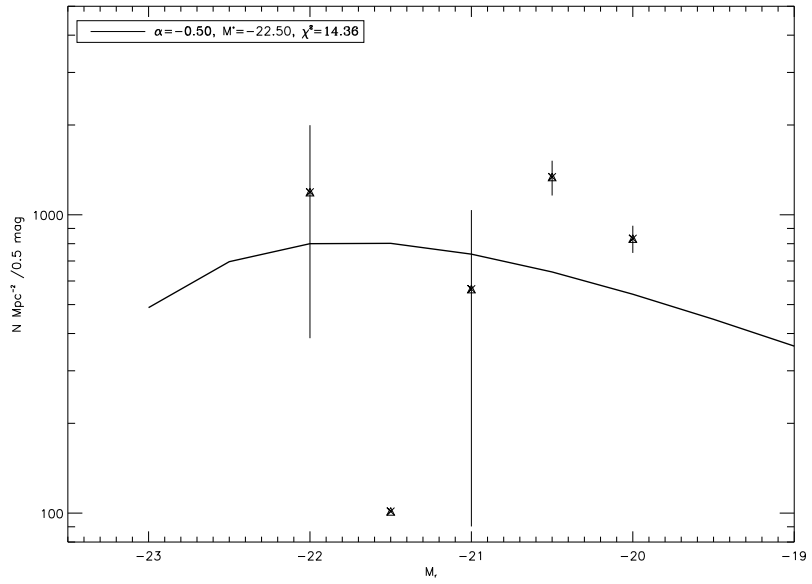

Figure 7.19: Composite LF for Late Type galaxies in NOT sample.

Table 7.10: Best Schechter Parameters of the Cumulative Luminosity Function for Early and Late Types for the ACS sample

	With BCG			Without BCG		
Name	α	M*	χ^2	α	M*	χ^2
Early	-0.50	-20.95	20.27	-0.50	-20.94	22.28
Late				-0.50	-20.96	7.54

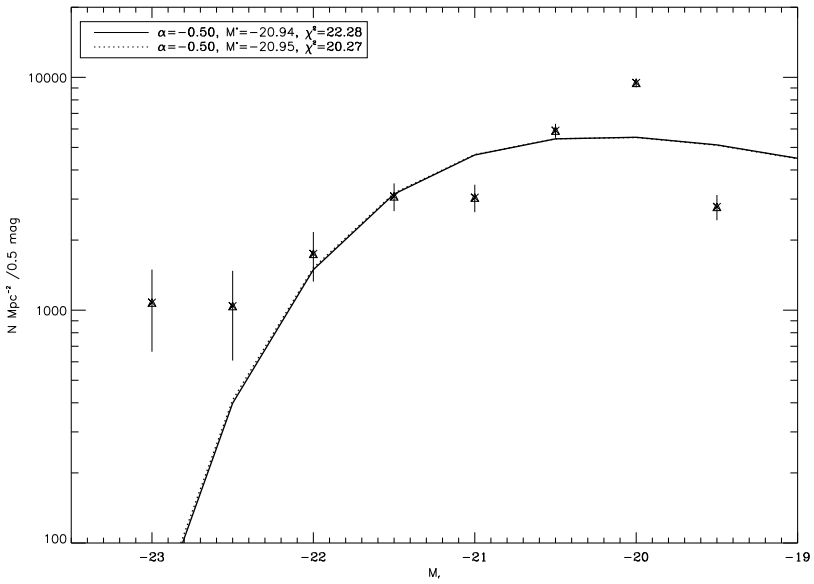

Figure 7.20: Composite LF for Early Type galaxies in ACS sample.

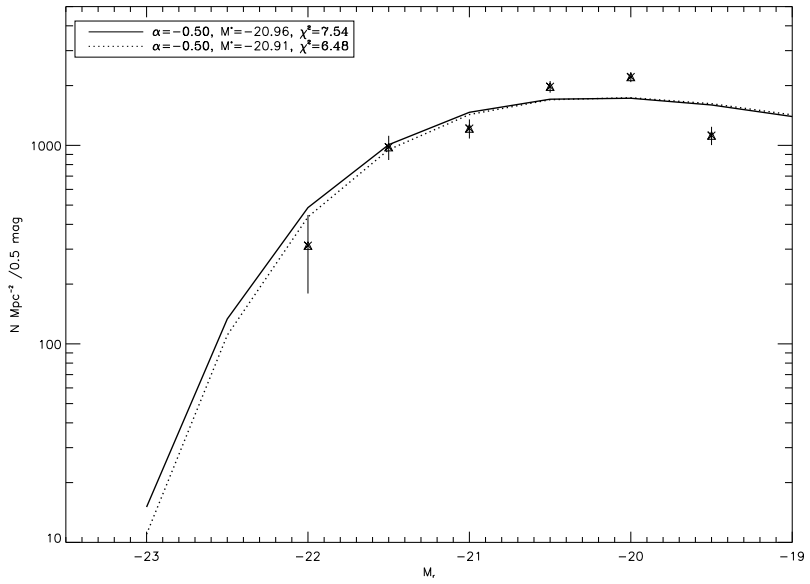

Figure 7.21: Composite LF for Late Type galaxies in ACS sample.

As we have seen, the fits are not reliable for none of both samples. This fact could be due to the large errors due to poor sampling and the limitations in magnitude, but also for the impossibility of fitting the morphological population with a Schechter function. At the view of that results, we can not extract significant results about the behavior of the LF for morphological types.

7.5 Luminosity - Color relation

We have computed the Luminosity Function for different galaxy population colors. Contrary to the Luminosity-Morphology relation, we have information enough to consider the whole completeness luminosity range for the fit. The results are shown in Figures 7.22, 7.23 for NOT clusters and in Figures 7.24 and 7.25 for the ACS clusters, for the red and blue galaxy population respectively. At first sight, we observe flatter slopes for the red population than for the blue. Specifically, for the ACS sample, where we have a deeper completeness limit.

Similarly to the previous section, we have computed the Composite Luminosity Function for red and blue galaxy population (Figures 7.26 and 7.27) for the NOT sample, while the results for the red and blue galaxy population for the ACS sample are set in Figures 7.28 and 7.29. The results of the fit are collected in Tables 7.11 and 7.12 respectively.

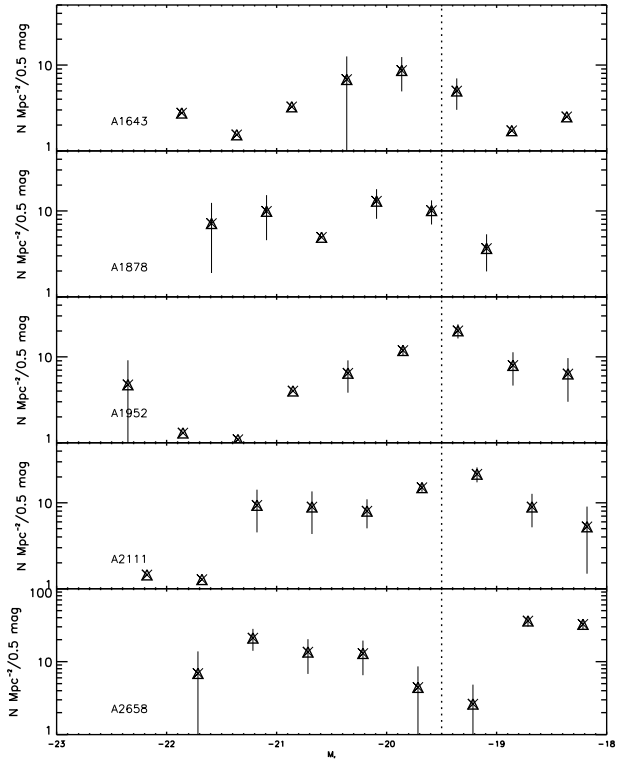

Figure 7.22: LF for Red galaxies NOT sample clusters

The main conclusion that is extracted from the Luminosity-Color functions are that the slope values given for the red population in both samples (without considering the brightest bin in the fit) are much flatter than the blue galaxy population. Additionally, we obtain brighter M^* values for the red than for the blue galaxy population.

Those results are in agreement with the results found in Barkhouse, Yee & López-Cruz (2007). They found that the red LF is generally flat for $-22 \leq M_R \leq -18$. On the contrary, as the blue LF contains a larger contribution from faint galaxies than the red LF, the blue LF has a rising faint- end component. However, Barkhouse, Yee & López-Cruz (2007) found a steeper value of α (≈ -1.7) for $M_R > -21$. That fact can be explained as they explored a large radius than as (r_{200}) and steeper slopes have been noted for larger radius.

However, regarding to the M^* parameter, Barkhouse, Yee & López-Cruz (2007) found a brighter value for the blue LF than for the red. We have found here the opposite behaviour. Nevertheless, those results are not directly comparable as they fit two Schechter function to the blue and red LF.

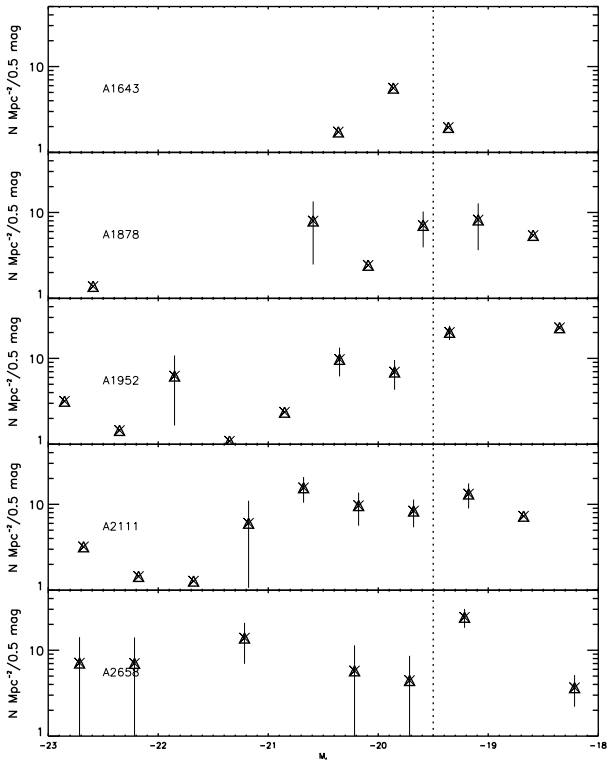

Figure 7.23: LF for Blue galaxies NOT sample clusters

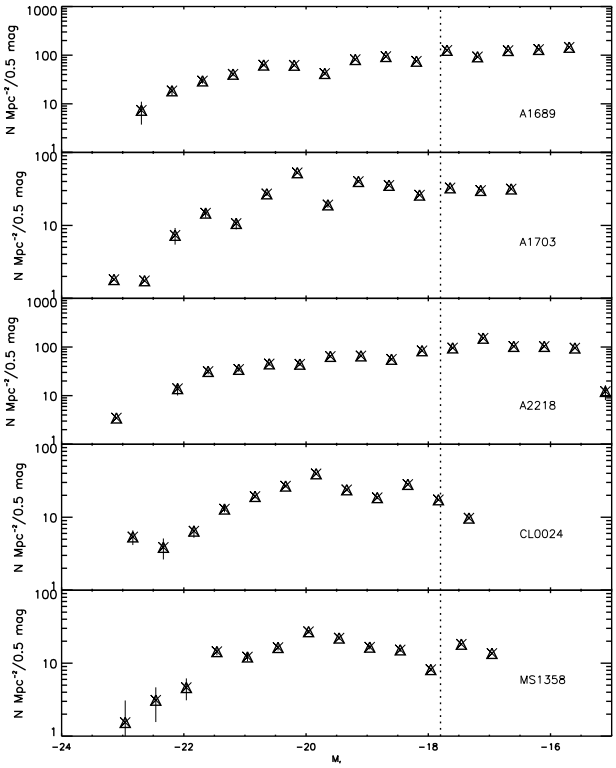

Figure 7.24: LF for Red galaxies ACS sample clusters

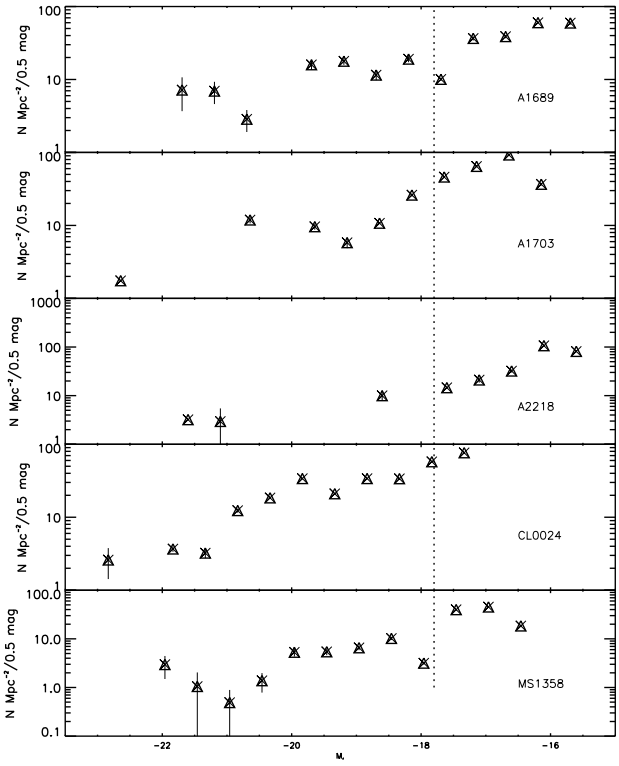

Figure 7.25: LF for Blue galaxies ACS sample clusters

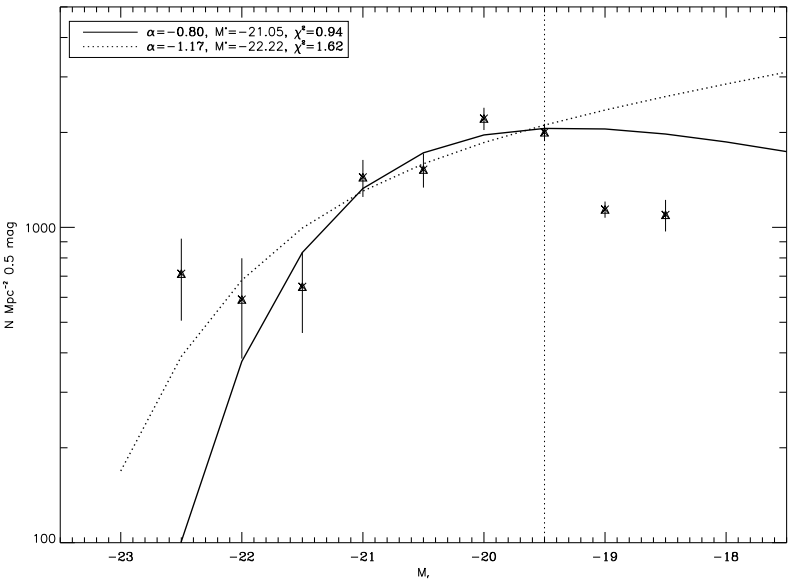

Figure 7.26: Composite LF for Red galaxies in NOT sample.

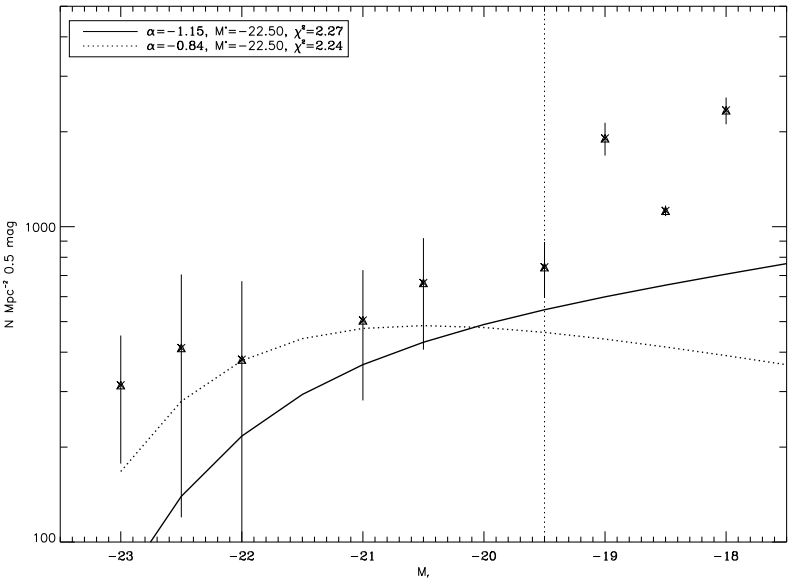

Figure 7.27: Composite LF for Blue galaxies in NOT sample.

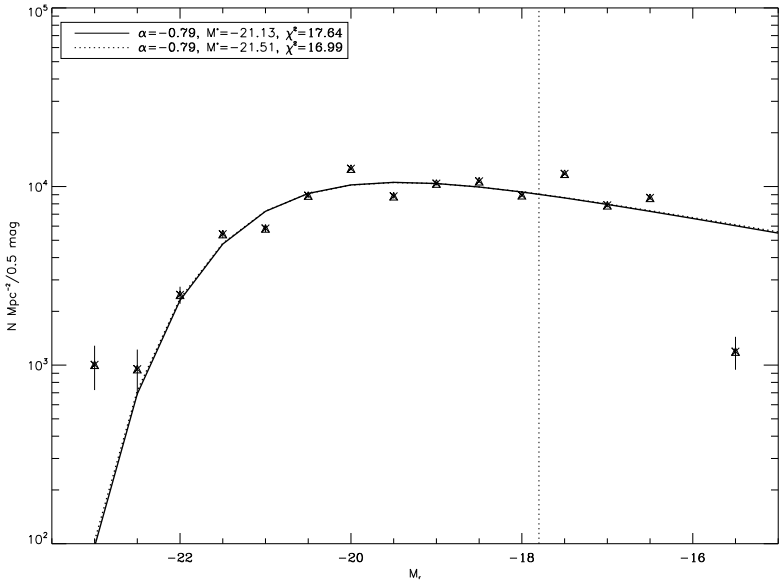

Figure 7.28: Composite LF for Red galaxies in ACS sample.

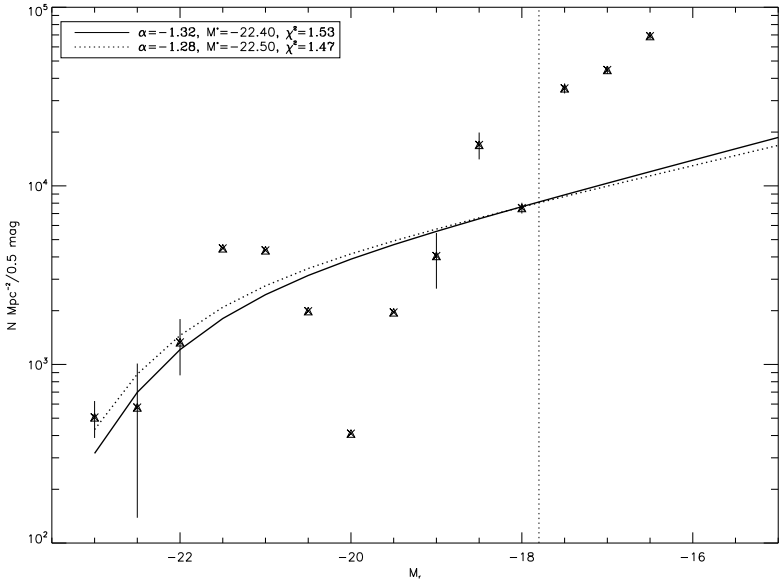

Figure 7.29: Composite LF for Blue galaxies in ACS sample.

Table 7.11: Best Schechter Parameters of the Cumulative Luminosity Function for Red and Blue Galaxies for the NOT sample

	With BCG			Without BCG		
Name	α	M*	χ^2	α	M*	χ^2
Red	-1.17 ± 0.16	-22.23 ± 0.68	1.62	-0.80 ± 0.24	-21.05 ± 0.42	0.94
Blue	-0.84 ± 0.19	-22.50 ± 0.00	2.24	-1.15 ± 0.30	-22.50 ± 0.00	2.27

Table 7.12: Best Schechter Parameters of the Cumulative Luminosity Function for Red and Blue Galaxies for the ACS sample

	With BCG			Without BCG		
Name	α	M*	χ^2	α	M*	χ^2
Red	-0.79 ± 0.02	-21.15 ± 0.06	16.99	-0.79 ± 0.02	-21.13 ± 0.06	17.64
Blue	-1.28 ± 0.04	-22.50 ± 0.00	1.47	-1.32 ± 0.02	-22.40 ± 1.31	1.53

7.6 Universality

A central subject in the early studies (Hubble, 1936; Abell, 1962; Oemler, 1974), of the galaxy cluster LF has been to determine whether the LF is universal in shape. Schechter (1976) suggested that the cluster LF is universal in shape and can be characterized with a turnover of $M_B^* = -20.6 + 5 \log h_{50}$ and a faint-end slope of $\alpha = -1.25$.

Further support for a universal LF has been provided by several studies: Dressler (1978); Lugger (1986); Colless (1989); Gaidos (1997); Yagi et al. (2002); De Propris et al. (2003a). They studied samples of several clusters samples concluding with the good agreement of the parameters.

In contrast, a number of studies have also discussed that the shape of the cluster LF is not universal (see (Godwin & Peach, 1977; Dressler, 1978; Binggeli, Sandage & Tammann, 1988; Piranomonte et al., 2001; Hansen et al., 2005; Popesso et al., 2006; Barkhouse, Yee & López-Cruz, 2007)). Some of them have argued that the results found by Dressler (1978) did not consider a consistent cluster radius or limiting absolute magnitude in comparing different clusters.

However, as many authors have shown (Binggeli, Sandage & Tammann, 1988; Varela, 2004; Barkhouse, Yee & López-Cruz, 2007), the luminosity function is different for different morphological types, so it seems evident that it can not be Universal. However, some of them claim about the universality of the luminosity function for different morphological types.

The results found in the last subsection give support to this conclusion. Different trends in the slope parameter α are distinguished for blue (steeper slopes) and red galaxies (flatter slopes), in agreement with the results obtained by Barkhouse, Yee & López-Cruz (2007) at lower redshift. We have also found brighter values of M^* for blue than for red population with a contrary tendency than in the work by Barkhouse, Yee & López-Cruz (2007) with two Schechter functions. As a consequence, at the view of these results, we can not conclude that LF is universal for different morphological types but we can conclude that the different galaxy population with red and blue colors follow different LF.

Finally, even if we have limitations in magnitude completeness in the analysis of this range of redshift and area for these samples, we have determined the global parameters of a single Schechter function by fitting the composite Luminosity Function of both NOT and ACS samples. We have found that for fainter magnitude completeness limits, the inclusion of the brightest bins are not affecting the whole fit. We can then conclude with reliable values for the general LF in the redshift range z $\sim$ 0.2-0.4 are $\alpha \approx -1.11$ and $M_r^* \approx -21.6$. These values are in the range of the values found at lower redshift (see López-Cruz et al. (1997)), however we find slightly fainter values of M^* at z $\sim$ 0.2 indicating a possible evolution in the luminosity of the bright galaxies in this range of redshift.

Part III

The Brightest Cluster Galaxies

Chapter 8

The Brightest Cluster Galaxies: BCGs

Avanza envuelta en belleza,
como la noche de regiones sin nubes y cielos estrellados;
y todo lo mejor de lo oscuro y lo brillante,
se une en su rostro y en sus ojos...

Ray Bradbury, 'Crónicas Marcianas.'

The **Brightest Cluster Galaxies (BCG)** are generally giant elliptical galaxies near the spatial and gravitational centre of a galaxy cluster. They are the brightest and most massive stellar systems in the Universe. BCGs are found very close to the centre of the clusters of galaxies determined from X-ray observations or gravitational lensing observations (Jones & Forman, 1984; Smith et al., 2005).

Those objects possess a number of singular properties. Their luminosities are remarkably homogenous, as noticed first by Humason, Mayall & Sandage (1956). A number of works (Sandage, 1972a; Gunn & Oke, 1975; Hoessel & Schneider, 1985; Postman & Lauer, 1995), verified their high luminosities and small scatter in absolute magnitude and consequently, proposed them as 'standard candles' with which to measure cosmological distances. In fact, they were originally used to increase the range of Hubble's redshift - distance law (Sandage, 1972a,c).

Furthermore, there are numerous pieces of evidence, (see for example (Tremaine & Richstone, 1977)), that show that BCGs are not extracted from the same luminosity distribution as the Schechter luminosity function of normal galaxies (Schechter, 1976), and that they are not statistical fluctuations in the luminosity function. We have found similar results, as shown in Chapter 7.

Different theories have been proposed to explain their formation and singular features: the accumulation of tidal stripped debris from clusters of galaxies (Ostriker & Tremaine, 1975; McGlynn & Ostriker, 1980; Malumuth & Richstone,

1984; Merritt, 1985), the rapid merging in the collapse of the cluster core, galactic 'cannibalism' of giant galaxies spiraling into the center of the cluster under the influence of dynamical friction, or the creation by the X-ray emission-driven cooling flows of gas (Fabian, Nulsen & Canizares, 1982).

On a different perspective, considerable observational evidence suggest that giant elliptical galaxies were formed at high redshift, and have been passively evolving to the present day (Bower, Lucey & Ellis, 1992a; Aragon-Salamanca et al., 1993; Stanford, Eisenhardt & Dickinson, 1998; van Dokkum et al., 1998).

The latest hierarchical simulations of BCG formation (De Lucia & Blaizot, 2007b), predict that the stellar components of BCGs were formed very early (50% at z $\sim$ 5 and 80 % at z $\sim$ 3). This star formation occurs in separate subcomponents which then accrete to form the BCG through 'dry' mergers. It is important to note that in these simulations, local BCGs are not directly descended from high-z (z>0.7) BCGs. However, De Lucia & Blaizot (2007b) find little physical difference between the progenitors of local BCGs and high-z BCGs or between the local BCGs and the descendants of the high-z BCGs.

On the other hand, some BCGs show an excess of light, usually called envelopes, over the de Vaucouleur ($r^{1/4}$) profile at large radii (Matthews, Morgan & Schmidt, 1964; Oemler, 1973, 1976; Schombert, 1986, 1987, 1988; Graham et al., 1996). Therefore, a large fraction of these BCGs are termed as cD galaxies (Jordán et al., 2004; Patel et al., 2006). Although the origin of such extended envelopes is still not completely clear, Patel et al. (2006) claimed that the extended stellar haloes of BCGs are likely from BCGs themselves: the intra-cluster light has much lower surface brightness and only dominates at large radii (Zibetti et al., 2005; Bernardi et al., 2007; Lauer et al., 2007)

Also, in the halo of cD galaxies, we can find large numbers of globular clusters, that can provide diagnostics of the cD formation process, assuming that the total luminosities and masses of the cannibalized galaxies should be printed in their metallicities (Brodie & Huchra, 1991; Jordán et al., 2004).

The study of the Brightest Galaxy Clusters (BCGs) from the NOT and ACS samples have been faced in this Chapter. Those BCGs were extracted from the cluster image by developing an algorithm allowing to extract the halo by means of an iterative process and a refinement of the masks for objects located in the galaxy halo (Ascaso et al., 2008c). We have studied the nature of these BCGs and also try to confirm the studies that consider the BCGs as standard candles for cosmological studies of the evolution in the Universe.

Table 8.1: BCGs in NOT Clusters

Name	α(2000)			δ(2000)			z	m_r	M_r	$B-r$	T
A 1643	12	55	54	+44	05	12	0.198*	17.91	−21.61	2.06	$S0$
A 1878	14	12	52	+29	14	28	0.222	17.39	−22.36	2.30	E
A 1952	14	41	03	+28	37	00	0.248*	17.37	−22.61	2.10	E
A 2111	15	39	40	+34	25	27	0.228	17.16	−22.67	2.18	E
A 2658	23	44	49	−12	17	39	0.185*	16.99	−22.39	2.01	E

* Cluster redshift

Table 8.2: BCGs in ACS Clusters

Name	α(2000)			δ(2000)			z	m_r	M_r	$g-r$	T
A 1689	13	11	29	−01	20	27	0.182	16.87	−22.75	1.348	E
A 1703	13	15	05	+51	49	03	0.283	17.34	−23.09	1.643	E
A 2218	16	35	49	+66	12	44	0.180	16.72	−22.79	1.207	E
CL0024	00	26	35	+17	09	43	0.387	18.87	−22.57	1.931	E
MS1358	13	59	50	+62	31	05	0.327	18.29	−22.13	1.707	E

8.1 BCGs population

The BCGs in NOT and ACS sample are shown in Figures 8.1 and 8.2 respectively. At examining the frames, we can see that all the BCGs sample have an extended halo, in which small galaxies are embedded. In Tables 8.1 and 8.2, their main characteristics are collected. The first four columns give the name of the cluster, the coordenates of the BCG and the redshift, if available. The fifth and sixth column also shows the apparent and absolute r magnitude in a 5 kpc aperture. The next column refers to the color (B-r for the NOT sample and g-r for the ACS sample) and finally, the morphological type is listed in the last column.

We can observe an homogeneous range of properties in the BCGs sample. All the galaxies are very bright elliptical red galaxies, with the exception of that in A1643, which is a lenticular galaxy. Some of them have also a visible halo, and they look like cD galaxies (A1952 or A2658 in NOT sample and A2218 or MS1358 in ACS sample).

In some of them, especially in the ACS sample, with better resolution, we can distinguish small globular clusters in the halo. And, in all cases, they are surrounded by a number of small galaxies.

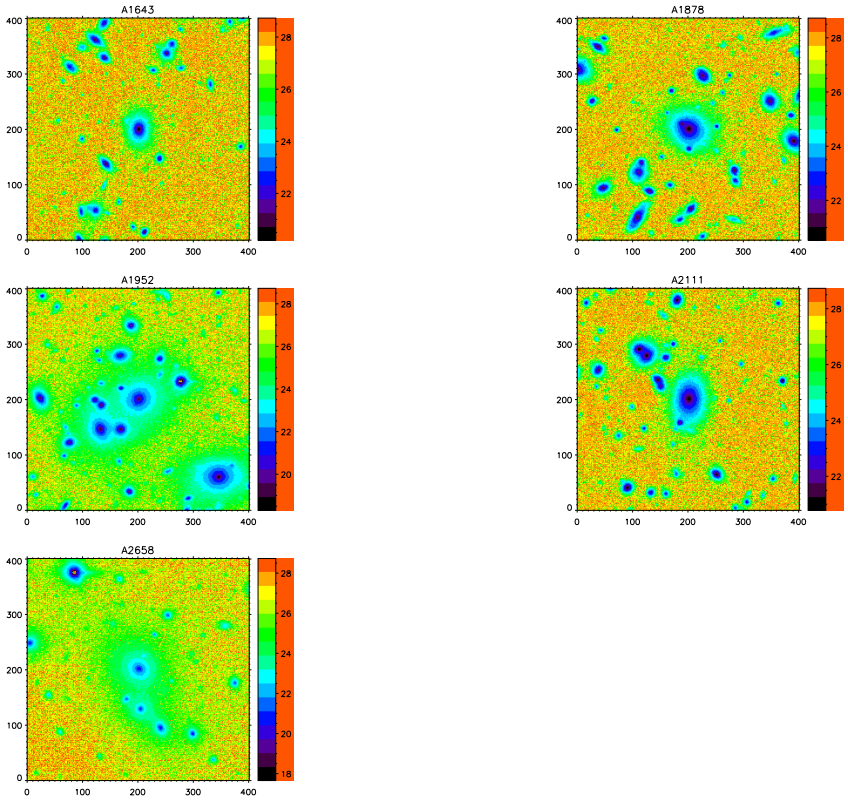

Figure 8.1: BCGs population in NOT sample

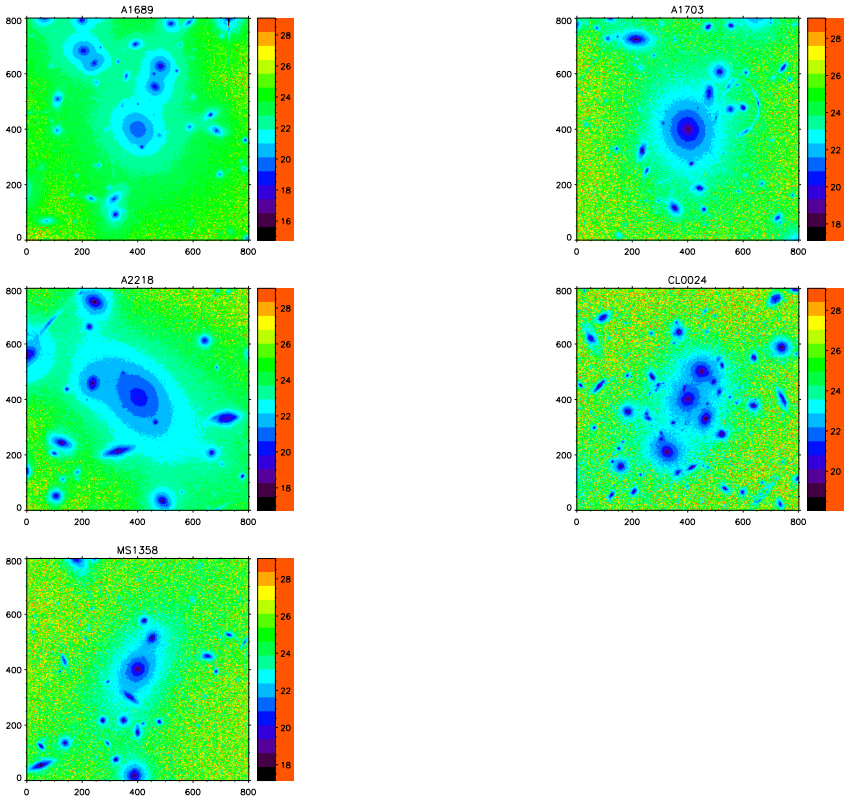

Figure 8.2: BCGs population in ACS sample

8.2 Extraction Algorithm

Background Subtraction Method

One of the most difficult tasks in studying the BCGs is extracting the cD galaxy from the crowed cluster images, as their halos extends much further than the elliptical galaxies. In many clusters, the halo of the cD extends nearly to the whole Abell Radius of the cluster. As an illustration, we have shown in Figure 8.3, two frames from our samples (A1952 from the NOT sample and A1689 from the ACS sample), where we have smoothed the light distribution to improve the perception of the extent of the light.

Therefore, we have investigated in the following questions: How to subtract it without changing the cluster properties? And without changing the light profiles of the rest of the galaxies? This is a difficult subject that has not yet definitively solved although valuable attempts have been carried out (Patel et al., 2006; Seigar, Graham & Jerjen, 2007). We present here a procedure that can achieves good results (Ascaso et al., 2008c).

The initial idea consisted on masking all the galaxies in the frame except the BCG with SExtractor in order to avoid adding light from the sources to the BCG. Then, we fit a model to the cD galaxy with the IRAF tasks ELLIPSE and BMODEL. We subtract then the model to the BCG and estimate the background in that image with SExtractor, subtracting it from the original image. That last step was thought in order to subtract part of the light of the halo at subtracting the background. After that, we iterated this procedure and finally we obtained the model of the BCG and the rest of the galaxies without the BCG.

In order to illustrate the difficulty of this process, we have set in Figure 8.4, two improper subtractions of one of our clusters, A1689. The upper panel shows an underestimation of the light of the halo, while the bottom panel is an overestimation fo the cD halo light.

After examining that results, we realized that the presence of spurious 'arcs' or 'black areas' were due to an inaccurate masking of the objects in the halo of the cD for the case of the underestimation, so we used an IRAF routine[1], which allows to mask any objects in the image by specifying the exact shape of the mask, (e.g. a circle, ellipse, rectangle, etc).

Regarding to the second case, the overestimation of the light, we performed different tests to find out that the SExtractor parameter BACK_SIZE, was crucial for estimating the background and subtracting the right light level, as it has been already noticed by some authors, (e.g., Patel et al. (2006)). We chose then the value of BACK_SIZE as the area corresponding to the measure of the largest galaxy, taking apart the BCG, with enough (≥ 50 %) surrounding background area to be estimated.

[1]This referred IRAF routine was kindly provided by Jesús Varela

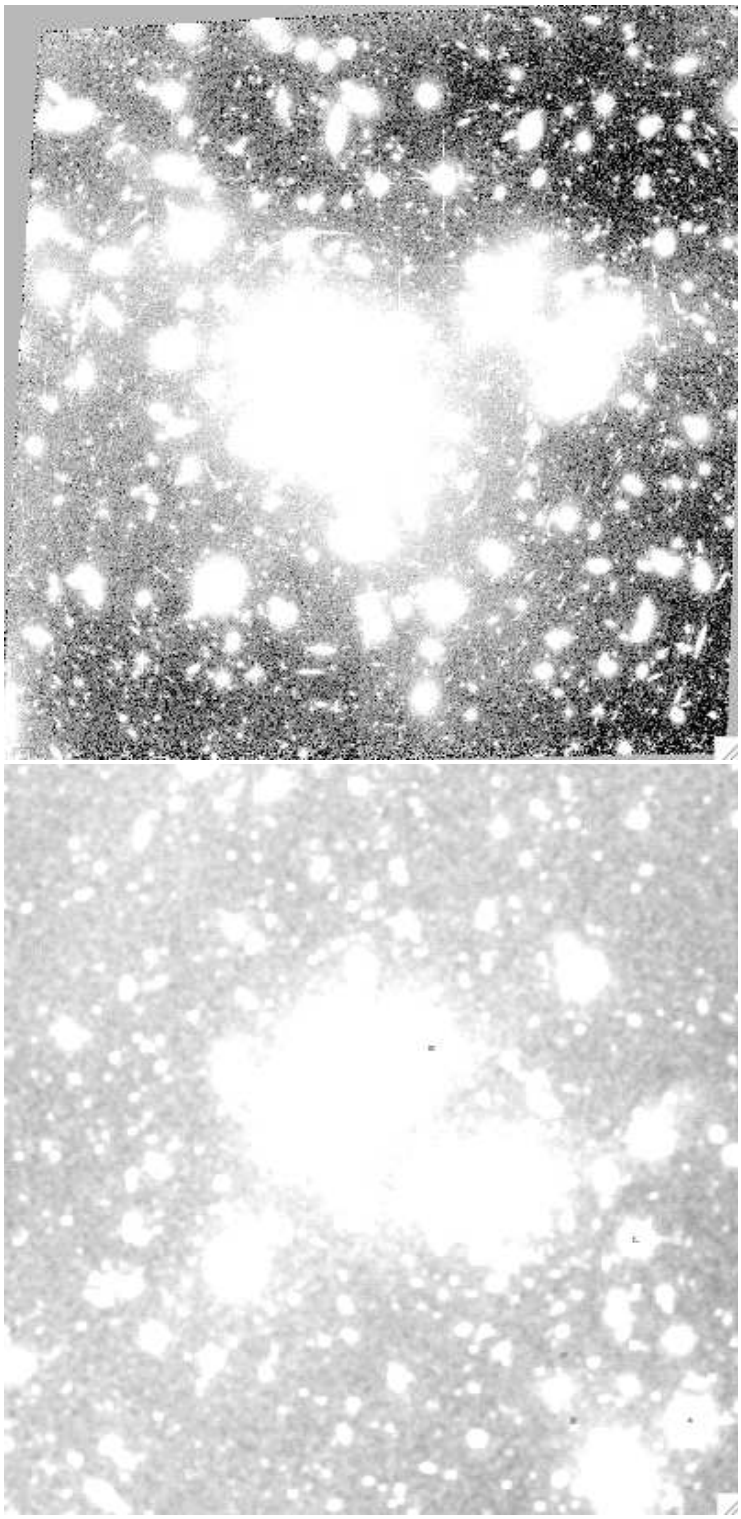

Figure 8.3: A1689 (ACS) and A1952 (NOT) smoothed images

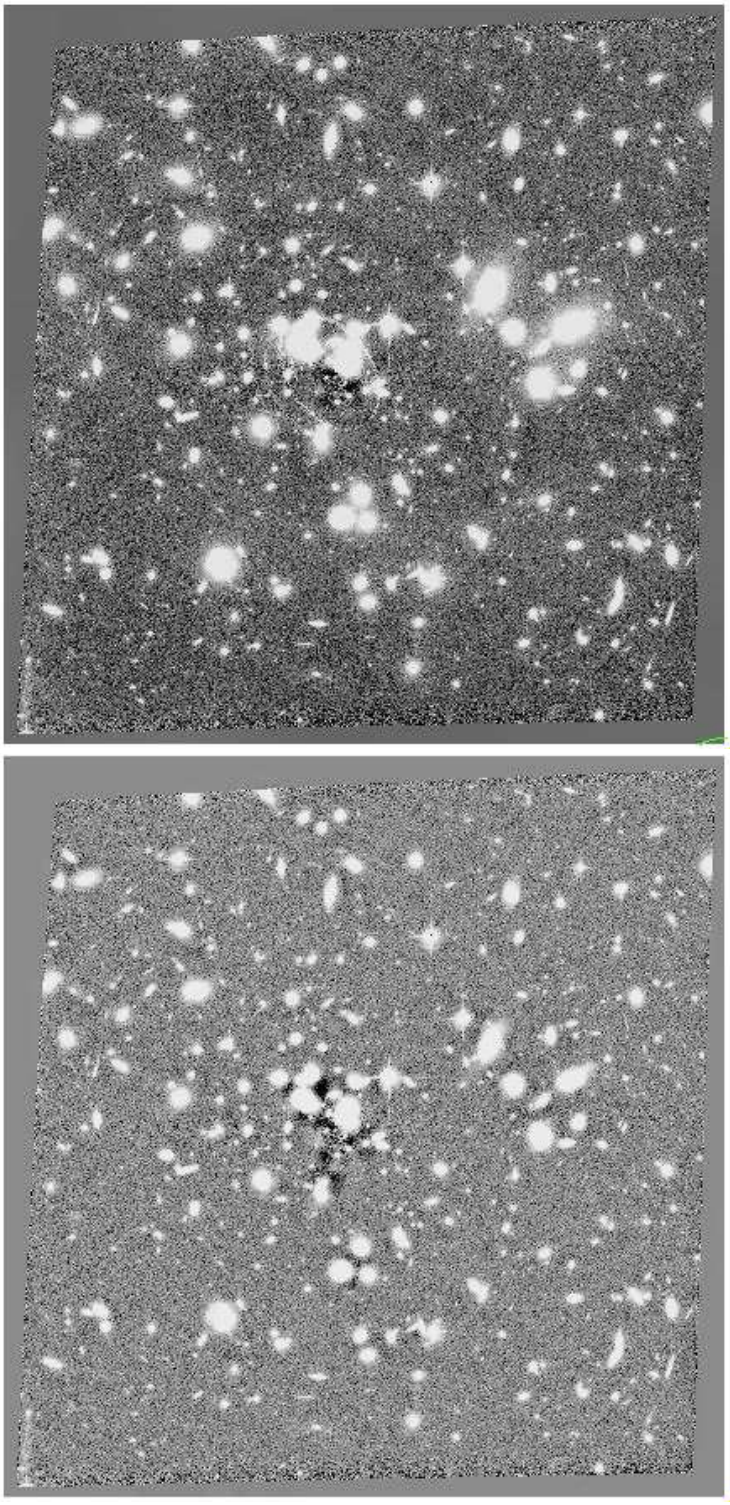

Figure 8.4: A1689 BCGs inadequate subtractions.

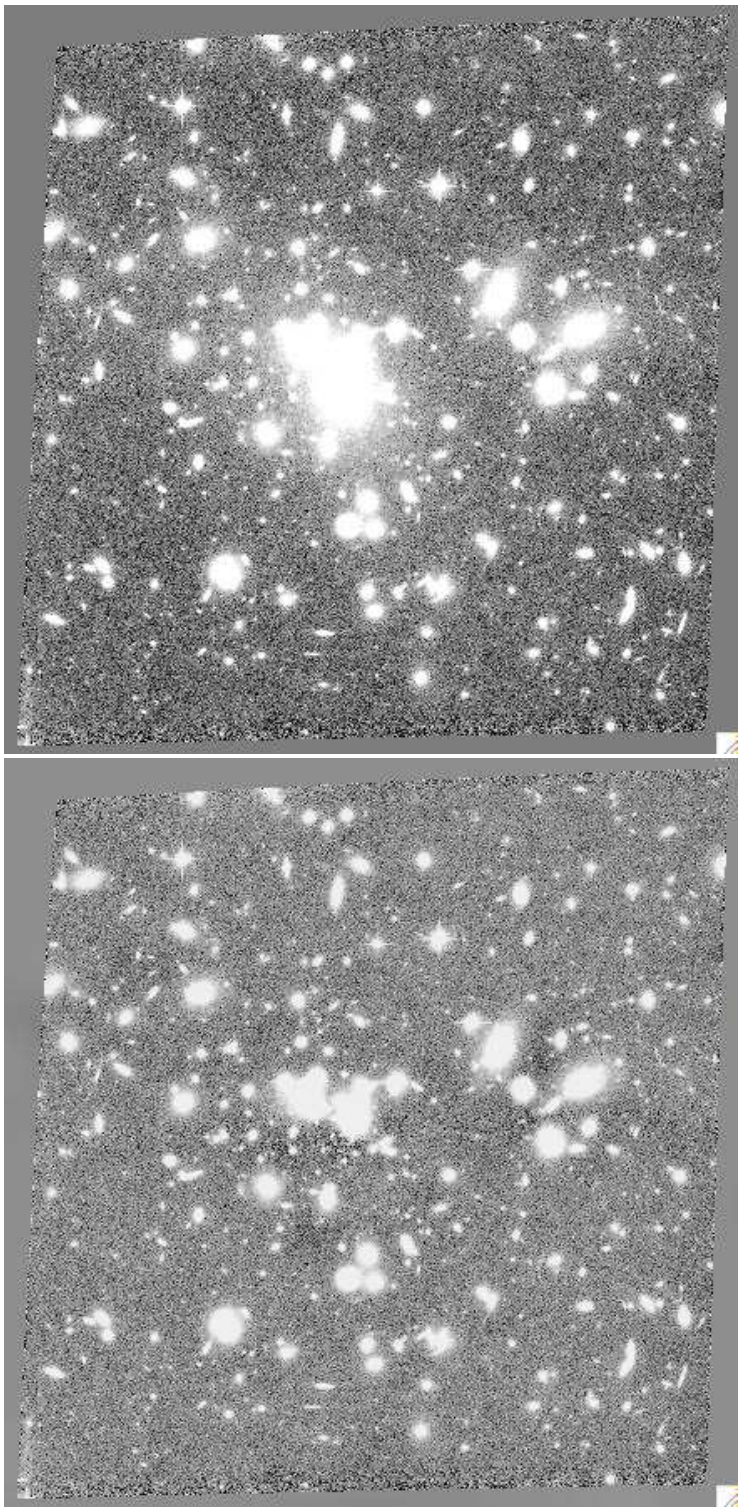

Figure 8.5: A1689 BCGs subtraction.

After applying this correction, we achieved really acceptable results as it is illustrated in Figure 8.5 for the last example, A1689. In this plot, we have shown the original cluster in the upper panel, together with the 'right' subtraction of the BCG after the refinements. The results look now satisfactory.

All the BCGs in the clusters belonging to both samples have been extracted with excellent results. The resulting images are collected in the Appendix sections C and D for the NOT and ACS respectively.

8.3 Analysis

8.3.1 Degree of Dominance

The **Degree of Dominance,** Δm**,** is the quantification of how dominant the BCG is with respect to the rest of the galaxies in the cluster. The definition was given by Kim et al. (2002), as the magnitude difference between the BCG magnitude (m_1) and the average magnitude of the second (m_2) and third (m_3) brightest member. That is:

$$\Delta m = (m_2 + m_3)/2 - m_1$$

The second and third brightest galaxies are selected as the next two brightest galaxies on the cluster red sequence within a radius of 500 kpc of the BCG. Taking the average of the second and third ranked galaxies is slightly more robust to contamination than just using the second. It also removes the weighting from cases where there are two BCG candidates that are far more luminous than the rest of the cluster, as for example in the case of A2218, that has two main bright galaxies.

Some studies in the literature (Kim et al., 2002; Jordán et al., 2004; Stott et al., 2008) have used the Degree of Dominance to study the degree of alignment of the more dominant BCGs with the host cluster and extract therefore conclusions about the BCG and cluster formation. In this work, we only mapped the central region of the clusters, so we have not been able to correlate it with extended properties of the cluster.

In Tables 8.3 and 8.4, we have set the values of the Degree of Dominance in each cluster for the NOT and ACS sample respectively. In the third column, we have also set the difference between the first and second member, (called Δm_2, in this work). We notice that the clusters A2658 and A2218 have a maximum aperture of 420 kpc and 475 kpc respectively. As those apertures are very close to 500 kpc, we will set this value in the analysis, being aware of this fact.

In Figure 8.6, we have compared the Degree of Dominance obtained for our sample with the absolute magnitude of the BCG of the given cluster. No significant tendency seem to be present for the whole sample.

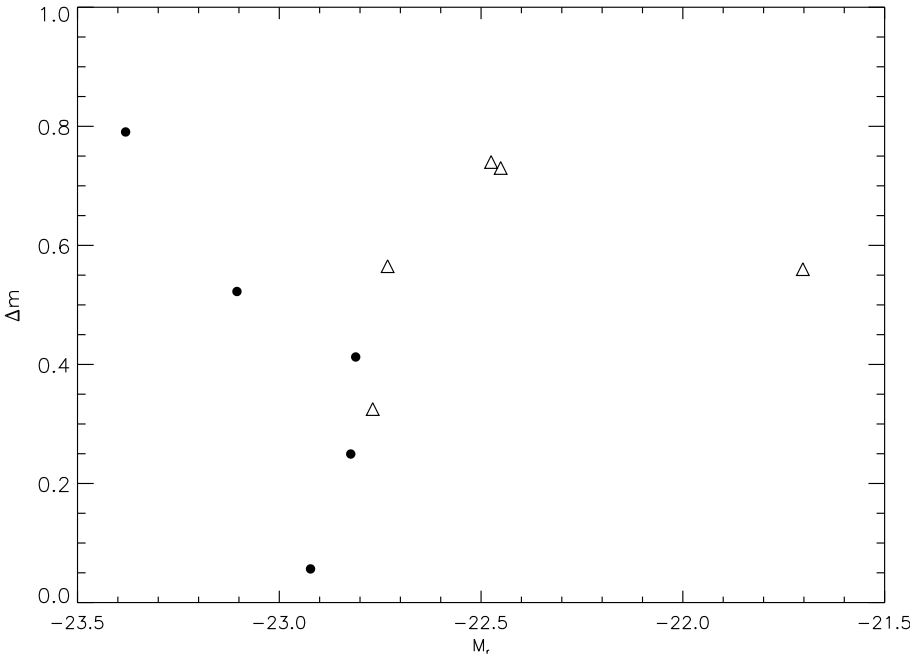

Figure 8.6: Degree of Dominance versus BCG magnitude. Triangles refer to NOT sample while black points refer to ACS sample.

However, we know that X-ray cluster properties are directly related to the cluster mass properties and the depth of the cluster gravitational potential well. As a consequence, being more massive, those clusters could provide information about the evolutionary problems taking place on them and about the way the BCGs were formed (Edge, 1991). So, if we take only the X-ray clusters from the sample, (that is, the entire ACS sample and A2111 from the NOT sample), we observe a decreasing tendency of the degree of dominance with brightness, indicating that the BCG becomes brighter as its predominance in the clusters is higher. That trend goes in the sense of the formation of the cluster through hierarchical models (De Lucia & Blaizot, 2007b). For the less massive clusters in NOT sample, however, we do not find any noticeable tendency.

We find that for three BCGs, (A2111, A2218 and A1689), there is more than a factor of two between Δm and Δm_2, as it is clearly shown in Figure 8.7. As many works have reported (Wang, Ulmer & Lavery, 1997; Henriksen, Wang & Ulmer, 1999; Miller, Oegerle & Hill, 2006; Kneib et al., 1995; Markevitch, 1997; Neumann & Böhringer, 1999; Machacek et al., 2002), A2111 and A2218 are thought to be two cluster mergers which will explain the existence of two large dominant galaxies. For the case of A1689, there is no evidence reported about the possible merging character of this cluster but a factor of two of discrepancy

Table 8.3: Degree of Dominance in NOT BCGs Sample

Name	Δm	Δm_2
A 1643	0.560	0.450
A 1878	0.730	0.670
A 1952	0.565	0.529
A 2111	0.325	0.059
A 2658*	0.740	0.500

* Aperture of 420 kpc

Table 8.4: Degree of Dominance in ACS BCGs Sample

Name	Δm	Δm_2
A 1689	0.249	0.093
A 1703	0.790	0.723
A 2218**	0.522	0.237
CL0024	0.056	0.046
MS1358	0.412	0.309

** Aperture of 475 kpc

between the masses estimated by X-ray and lensing techniques has been reported (Andersson & Madejski, 2004; Diego et al., 2005). Furthermore, A2111 and A1689 have the smallest Δm value after CL0024, which would indicate a very bright dominant population in the cluster.

On the other hand, we find that the values for the Δm and Δm_2 for three BCGs, A1878, A1952 and A1703, remain nearly constant, what would indicate an outstanding BCG compared to the rest of the galaxy population in the cluster. In addition, two clusters out of these three, A1878 and A1703, (and also A2658) have a Degree of Dominance higher than 0.65, the value selected by Kim et al. (2002) to call a dominant BCG. That fact is noticed also in the lower number of iterations needed at extracting the cD galaxy in the last section.

In Figure 8.8, we have plotted the relation of the Degree of Dominance with the redshift for both samples. We see as our cluster at highest redshift, CL0024, is the cluster with the smallest degree of dominance, or the similar range of luminosity in its bright population. However, if we take out that cluster, we do not see any tendency. We only note that at redshift ≈ 0.2, the dispersion seems to be larger than at redshift ≈ 0.25. Larger samples of BCGs would be needed to establish this indication.

We have also looked for any correlations of the degree of dominance with the

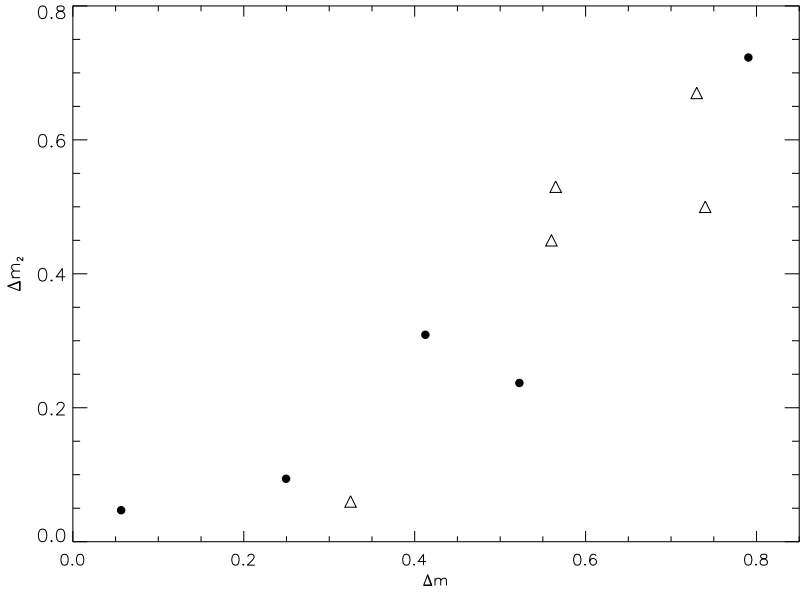

Figure 8.7: Degree of Dominance versus Δm_2. Triangles refer to NOT sample while black points refer to ACS sample.

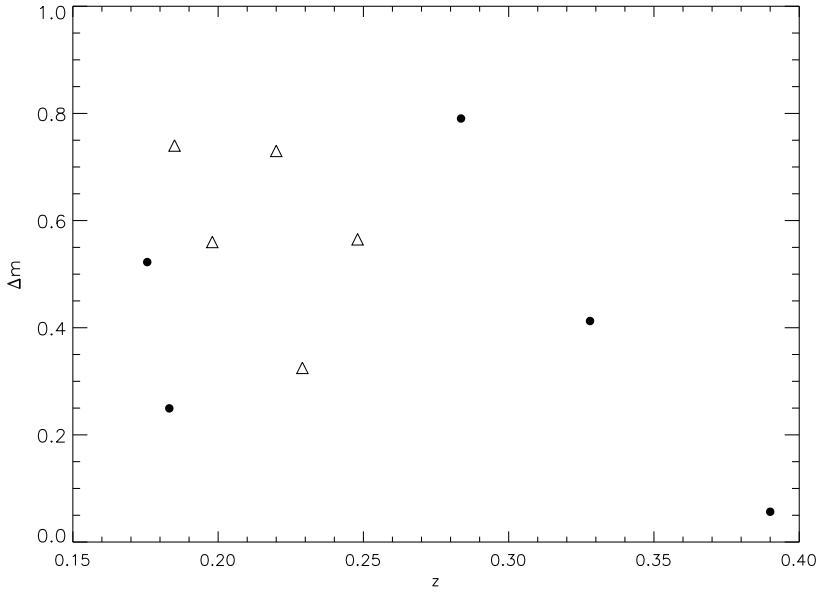

Figure 8.8: Redshift versus Degree of Dominance. Triangles refer to NOT sample while black points refer to ACS sample.

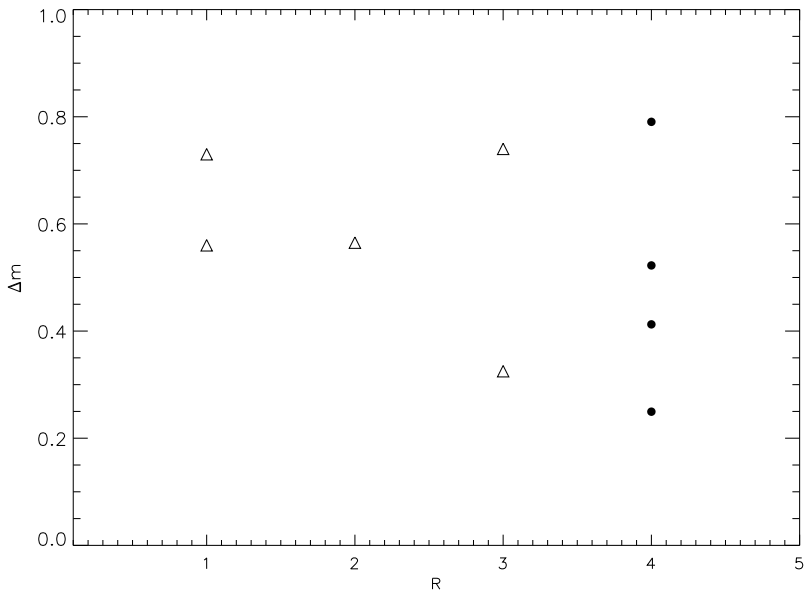

Figure 8.9: Cluster Richness Class versus Degree of Dominance. Triangles refer to NOT sample while black points refer to ACS sample.

cluster richness class. The results are shown in Figure 8.9. Unfortunately, we have not been able to find in the literature the corresponding RC for our most distant cluster. We distinguish a trend with Richness Class, indicating that very rich clusters have a wide range of values of the Degree of Dominance, while, on the contrary, poorer clusters, seem to have larger degree of dominance values, indicating a more homogeneous luminosity between their members. Again, we can not conclude as our sample may be biased to richer clusters.

8.3.2 Morphology

As we have already mentioned, Schombert (1986) conducted an extensive survey of BCG brightness profiles finding that not all BCGs galaxies were cD galaxies. A **cD galaxy** is considered a giant elliptical that has a separate extended low surface brightness envelope, which is evident as an inflection in the brightness profile typically at $\mu_V \sim 24$ or greater (Oemler, 1976; Schombert, 1986; Tonry, 1987; Kormendy & Djorgovski, 1989). That is, cD's are elliptical galaxies with shallower surface brightness profiles than

$$d\log\mu_V/d\log r \approx 2$$

at $\mu_V \sim 24$ mag arcsec^{-2}. Those galaxies exhibit a characteristic 'break' over an $r^{1/4}$ law, and are much brighter than typical elliptical galaxies, with luminosities

of $\sim 10L_*$ (Sandage & Hardy, 1973; Schombert, 1986). The cD classification itself was introduced by Matthews, Morgan & Schmidt (1964) to denote the very large D galaxies that they found in some clusters and the 'c' prefix was taken from the notation for supergiants stars in stellar spectroscopy. Type cD galaxies behave in similar ways as BCGs. They are very generally found in dense regions, and in virtually all cases, they are located near the spatial and kinematical center of their host cluster, or subcluster. A number of theories have been suggested to justify the formation of cD galaxies related to the cluster environment and their close link to their dynamical history.

Many authors have pointed out that the envelopes themselves might be distinct entities from the galaxies themselves for a number of reasons. First of all, the cD envelope luminosity is weakly correlated with some properties of the host cluster, most notably with cluster richness and X-ray luminosity (Schombert, 1988). Secondly, both the position angle and ellipticity of cD galaxy isophotes commonly show discontinuities at r_b, where the envelope begins to dominate the surface brightness profile (Schombert, 1988; Porter, Schneider & Hoessel, 1991). Finally, the envelopes have surface brightness profiles with power-law slopes that are similar to those measured from the surface density profiles of the surrounding cluster galaxies.

We must be cautious with the analysis of the surface brightness of the cD galaxies as a constant power law will rise above an $R^{1/4}$ law at large radii, a cD envelope may be erroneously detected as separate component, even though a single power law could describe the BCG completely.

In Figure 8.10 and 8.11, we have plotted the $r^{1/4}$ profiles versus the surface brightness for the NOT and ACS sample respectively, in order to determine if the BCGs galaxies are also cD galaxies. At the view of these profiles, we can assign a cD halo to A1952 from the NOT sample and A1703, A2218 and MS1358 from the ACS sample, as it can be easily identified the characteristic 'break' from the de Vaucouleurs profile. The rest of the galaxies does not seem to have a different profile from a De Vacouleurs law or, in some cases, steeper than them.

8.3.3 Surface Brightness

Following several works in literature (Schombert, 1986; Jordán et al., 2004; Lin & Mohr, 2004; Seigar, Graham & Jerjen, 2007), we have examined the surface brightness profiles for the BCGs. We have fitted different profiles and examined its parameters. In Figures 8.12 and 8.13, we have plotted different fits to the surface brightness of the BCGs for the NOT and ACS sample respectively. The left upper panel shows the de Vaucouleurs fit, the right upper refers to the Sersic profile, the bottom left shows a Sersic plus Exponential profile and finally the bottom right plot shows a fit with two Sersic's profiles. All of them have been fitted using the same fitting package that we have used in this thesis,

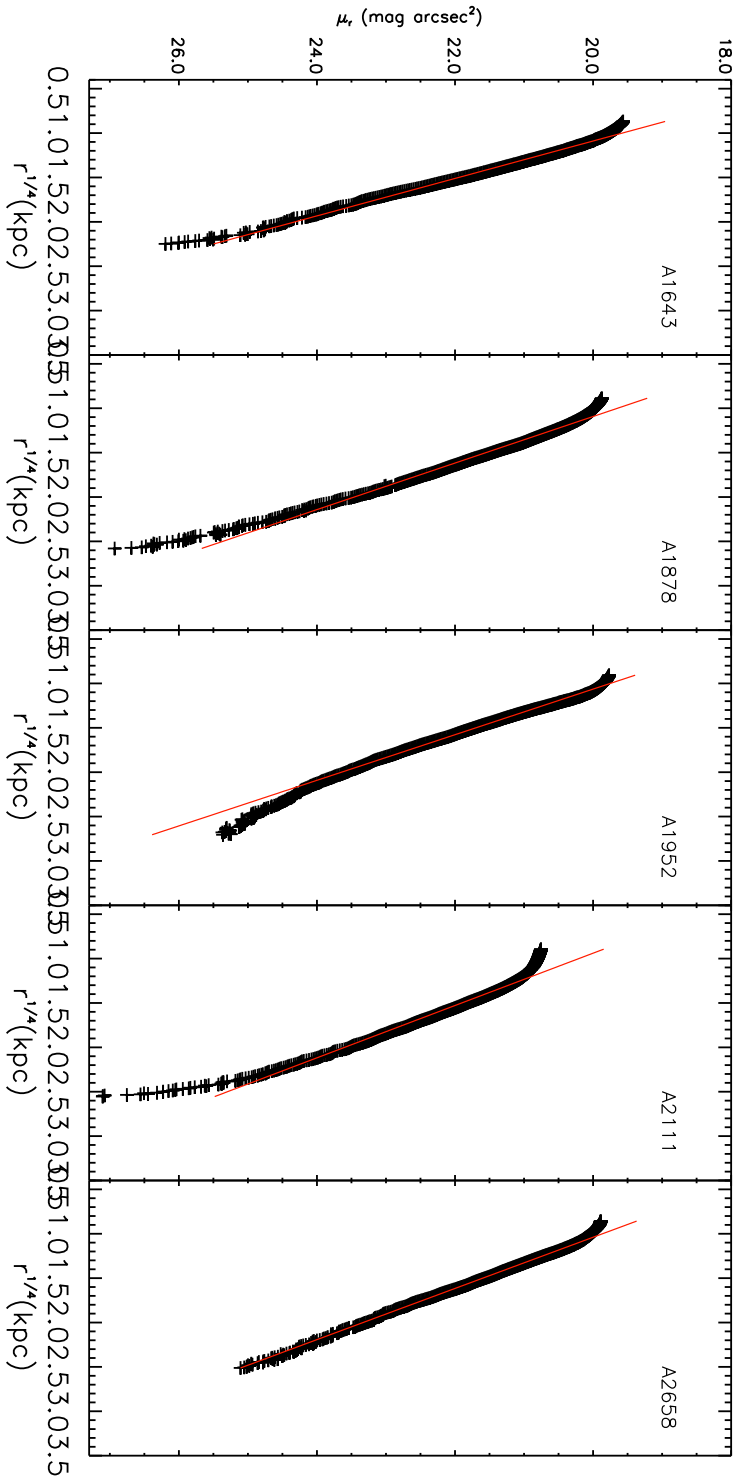

Figure 8.10: Deviation of the surface brightness profiles from the De Vaucouleurs profile for the NOT BCGs. Red line: De Vaucouleus fit. Black line: BCG profile. (To see landscape)

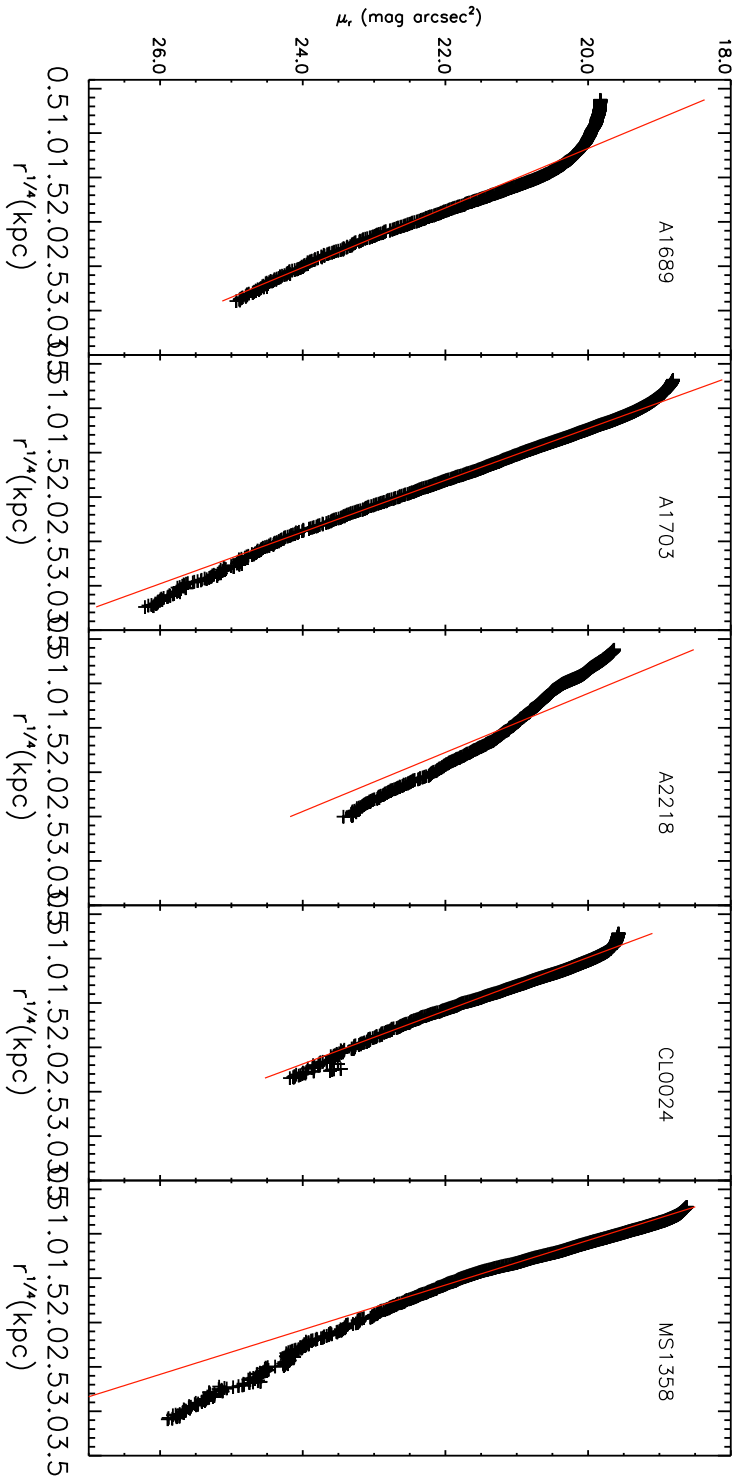

Figure 8.11: Deviation of the surface brightness profiles from the De Vaucouleurs profile for the ACS BCGs. Red line: De Vaucouleus fit. Black line: BCG profile. (To see landscape)

Table 8.5: BCGs de Vaucouleurs fit

	GASP − 2D				GALFIT			
Name	$R_e('')$	ε	PA	χ^2	$R_e('')$	ε	PA	χ^2
A 1643	2.94	0.70	0.28	1.37	3.08	0.72	178.75	11.79
A 1878	6.48	0.86	54.01	2.46	4.95	0.83	63.72	18.69
A 1952	5.45	0.90	134.11	1.94	24.39	0.74	122.57	44.86
A 2111	10.02	0.74	177.60	5.51	6.83	0.61	179.84	16.19
A 2658	10.85	0.84	43.82	2.68	15.56	0.65	26.80	54.62
A 1689	20.03	0.86	38.37	6.01	33.68	0.78	20.68	249.83
A 1703	8.20	0.86	7.90	2.24	12.03	0.77	2.08	59.71
A 2218	20.02	0.84	45.75	30.89	47.49	0.48	49.69	89.48
CL0024	7.43	0.82	5.72	3.18	6.83	0.74	137.52	89.79
MS1358	4.11	0.94	8.24	2.92	15.56	0.49	148.33	77.74

GASP-2D, explained in Chapter 5 and also with GALFIT (Peng et al., 2002), for comparison. The results are collected in Tables 8.5, 8.6 8.7 and 8.8, respectively.

The use of de Vaucouleurs $R^{1/4}$ law (de Vaucouleurs, 1948), to describe BCG surface brightness profiles was proved by Schombert (1986) to offer a poor match, only achieving a good fit over a restricted range of surface brightness. In fact, in the profiles presented in his work many of the BCGs profiles appear to be better fitted by power laws than de Vaucouleurs law. In addition, if the BCG is a cD galaxy, a constant power law will rise above an $R^{1/4}$ law at large radii and the fit will be erroneous. At analyzing the profiles, we note that except the case of the BCG in A2658, where the Gaps-2D fit describes well the whole profile, the rest of the BCGs are not well described at any radii. Let's note the shallower profiles than de Vaucouleurs fit for the cD galaxies in A1952, A1703, A2218 and MS1358.

A single Sersic law (Sersic, 1968), has been used in Graham et al. (1996), achieving very good results due to the flexibility of the n shape parameter, achieving, most of the BCGs larger values of n than 4. All the BCGs in NOT sample, except A1952 (which is a cD galaxy) and CL0024 are very well described by a single Sersic law. Also the BCGs belonging to A1689 and A1703 are well described by a Sersic law with GALFIT but not by GASP-2D. We obtain n values larger than 4 for the BCGs in A1952, A2658, A1703, CL0024 and MS1358, indicating the presence of the cD halo for three of these five clusters.

Table 8.6: BCGs Sersic fit

	GASP − 2D					GALFIT				
Name	$R_e('')$	n	ε	PA	χ^2	$R_e('')$	n	ε	PA	χ^2
A 1643	2.22	3.16	0.70	0.32	0.949	2.07	2.14	0.75	0.41	9.95
A 1878	3.47	2.48	0.86	54.10	0.822	3.39	1.92	0.82	58.03	15.64
A 1952	15.17	6.57	0.90	132.75	0.781	60.61	6.92	0.76	122.14	38.27
A 2111	3.62	1.86	0.75	176.85	1.393	4.02	1.59	0.67	176.32	13.31
A 2658	10.94	4.02	0.84	43.61	2.727	13.20	3.41	0.66	26.37	46.79
A 1689	9.74	2.53	0.84	14.32	4.47	29.60	3.77	0.79	20.67	214.07
A 1703	6.16	3.31	0.84	171.26	1.99	15.33	4.74	0.76	2.41	50.96
A 2218	12.96	1.97	0.62	40.06	1.75	18.65	2.12	0.50	50.40	71.84
CL0024	10.00	4.43	0.83	174.14	3.37	38.53	5.56	0.74	129.88	74.06
MS1358	8.24	5.44	0.91	152.31	2.46	168.70	9.14	0.54	152.18	57.94

Additionally, many works have considered the use of two Sersic laws to measure the surface brightness of very deep exposures of cD galaxies (Seigar, Graham & Jerjen, 2007). As GASP-2D has not the option of fitting two Sersic laws, we have fitted them only with GALFIT. We obtain that two Sersic law are describing quite accurately nearly all BCGs, with the exception of the BCGs in A1703, A2218 or MS1358, (cD galaxies). However, the BCGs belonging to A1703 and A2218 are well described by a Sersic plus an exponential law and the BCG in MS1358 obtains a more reliable fit than two Sersic profiles. Then, two Sersic laws seem to describe very well the shape profiles for many BCGs but not for the cD galaxies.

Let's note that sometimes, at introducing two components, the disc component makes the fit look better but they are not 'physical' as they are very small and contained in the bulge, (see for example the profiles of the BCGs in A1952 or A1689). This second component forces the fit to obtain smaller of the shape parameter, n, for nearly all the profiles. For example, for a Sersic plus Exponential fit, only one case with GASP-2D procedure and two cases with GALFIT show a larger n value than 4 and for two Sersic profiles, only one case shows one component with the shape parameter larger than 4.

We want to emphasize the large extent of these galaxies. In particular, the BCGs in A1952, A1689 or A2218 are really giant systems. Particularly remarkable is the profile of the BCG in A2218, whose extense envelope is only well fitted with a Sersic plus Exponential disc. One possible explanation to the existence of such a galaxy is related to the merger appearance of this cluster, as many authors have suggested (Kneib et al., 1995; Markevitch, 1997; Neumann & Böhringer, 1999; Machacek et al., 2002), and therefore its profile can be disturbed by the environmental influence of the merging cluster.

In general, we obtain much better fits by using GASP-2D than GALFIT. The main and more important difference between these two packages is the ability of GASP-2D to select good initial conditions for the fit. Unfortunately, GASP-2D does not allow to fit different profiles from Sersic, de Vaucouleurs or Exponential fit.

It is relevant that the same kind of objects, apparently very homogeneous, are fitted by different surface brightness profiles. This result suggests that the surface brightness profiles of these objects are not so homogeneous as their luminosity.

Table 8.7: BCGs Sersic plus Exponential fit

	GASP − 2D								GALFIT							
Name	$R_e('')$	n	ε_b	PA_b	$h('')$	ε_d	PA_d	χ^2	$R_e('')$	n	ε_b	PA_b	$h('')$	ε_d	PA_d	χ^2
A 1643	1.73	2.74	0.70	179.95	4.32	0.85	47.63	0.90	0.78	0.99	0.78	177.89	2.09	0.73	2.73	5.11
A 1878	2.48	2, 37	0.89	45.68	2.91	0.73	66.58	0.75	1.52	1.30	0.81	45.85	3.06	0.80	63.18	7.88
A 1952	20.77	8.00	0.89	145.86	15.19	0.25	101.75	0.57	9.21	4.34	0.82	123.25	29.64	0.67	43.42	12.28
A 2111	1.11	1.07	0.90	15.37	2.74	0.66	173.95	0.95	1.42	1.04	0.95	22.86	3.36	0.59	173.44	6.79
A 2658	3.39	2.77	0.84	56.07	6.24	0.71	19.11	2.54	10.65	3.42	0.69	36.52	3.66	0.49	43.50	23.96
A 1689	2.77	1.04	0.83	44.46	10.50	0.84	25.72	2.52	3.44	1.31	0.90	31.12	23.74	0.54	17.91	134.10
A 1703	3.42	2.52	0.87	14.38	17.23	0.44	171.26	1.66	3.59	2.49	0.86	1.78	28.65	0.40	3.60	26.70
A 2218	14.97	2.77	0.73	60.55	5.51	0.47	37.18	1.32	29.93	2.90	0.53	36.70	10.01	0.22	65.32	37.90
CL0024	0.61	1.33	0.78	133.05	2.59	0.87	163.35	1.82	13.59	5.00	0.85	7.54	14.16	0.40	123.72	39.54
MS1358	0.84	2.37	0.91	72.43	4.99	0.44	151.01	1.67	2.43	3.16	0.90	143.47	34.09	0.29	157.5	30.61

Table 8.8: BCGs Sersic plus Sersic fit

	GASP − 2D								
Name	$R_e('')$	n_b	ε_b	PA_b	$R_e('')$	n_d	ε_d	PA_d	χ^2
A 1643	1.04	1.22	0.77	178.72	4.56	0.52	0.72	4.66	4.63
A 1878	2.22	1.50	0.82	50.22	7.01	0.56	0.79	69.19	7.29
A 1952	22.93	1.82	0.89	121.44	1.47	1.75	0.95	142.29	10.77
A 2111	1.87	1.11	0.83	178.80	6.85	0.68	0.59	173.51	6.18
A 2658	3.29	2.23	0.98	158.02	21.59	1.11	0.42	27.42	21.64
A 1689	4.50	1.54	0.84	23.76	28.19	0.43	0.56	16.22	98.29
A 1703	4.29	2.66	0.82	0.61	83.87	0.38	0.16	5.90	23.06
A 2218	28.93	2.85	0.53	41.23	14.20	0.43	0.20	64.75	32.55
CL0024	14.41	4.61	0.84	5.29	17.99	0.30	0.38	123.82	34.13
MS1358	1.43	2.83	0.93	89.62	82.57	3.19	0.40	154.32	30.56

8.3.4 Hubble Diagram

The BCGs have been shown to vary little in luminosity within a fixed metric aperture (Sandage, 1972a,c; Postman et al., 2005) and in the past decade, the near-infrared K-band Hubble diagram has been studied in detail by numerous authors (Aragon-Salamanca, Baugh & Kauffmann, 1998; Brough et al., 2002), up to redshift $z \sim 1$. That band has turned out to be extremely suitable for the study of the BCG evolution because the k-correction remains unchanged by the star formation history of the galaxy, and the extinction is appreciably smaller than at other wavelengths (Charlot, Worthey & Bressan, 1996; Madau, Pozzetti & Dickinson, 1998).

In this section, we have studied the Hubble diagram in the r-band for our clusters sample. Even though this band is more sensitive to the star formation on the galaxies than the K- band, has smaller dispersion than blue bands and smaller extinction.

In Figure 8.14, we have plotted the Hubble Diagram for our sample. We observe that the data in the ACS sample, which are clusters that emit in X-ray describe a very well defined Hubble sequence as it is shown in the fit. For the rest of the clusters, the NOT sample, we do not find a trend in the Hubble Diagram. Regarding to A2111, it is also and X-ray emitter but it is less rich than the the clusters in the ACS sample and does not follow the same trend.

Sandage, Kristian & Westphal (1976); Kristian, Sandage & Westphal (1978) printed out that the BCGs magnitudes need to be corrected by different effects, other than aperture, k-dimming, galactic absorption or richness of the cluster. They proposed to 'normalize' the luminosity to a given richness class and cluster type. In this way, the dispersion we observe in the Hubble diagram could be

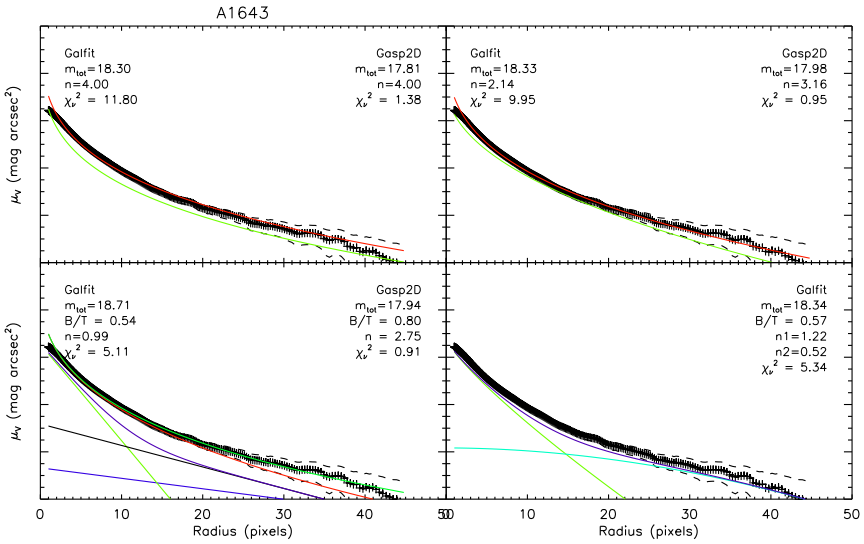
A1643
Galfit
m_tot=18.30
n=4.00
χν² = 11.80
Gasp2D
m_tot=17.81
n=4.00
χν² = 1.38
Galfit
m_tot=18.33
n=2.14
χν² = 9.95
Gasp2D
m_tot=17.98
n=3.16
χν² = 0.95
Galfit
m_tot=18.71
B/T = 0.54
n=0.99
χν² = 5.11
Gasp2D
m_tot=17.94
B/T = 0.80
n = 2.75
χν² = 0.91
Galfit
m_tot=18.34
B/T = 0.57
n1=1.22
n2=0.52
χν² = 5.34
μν (mag arcsec²)
Radius (pixels)

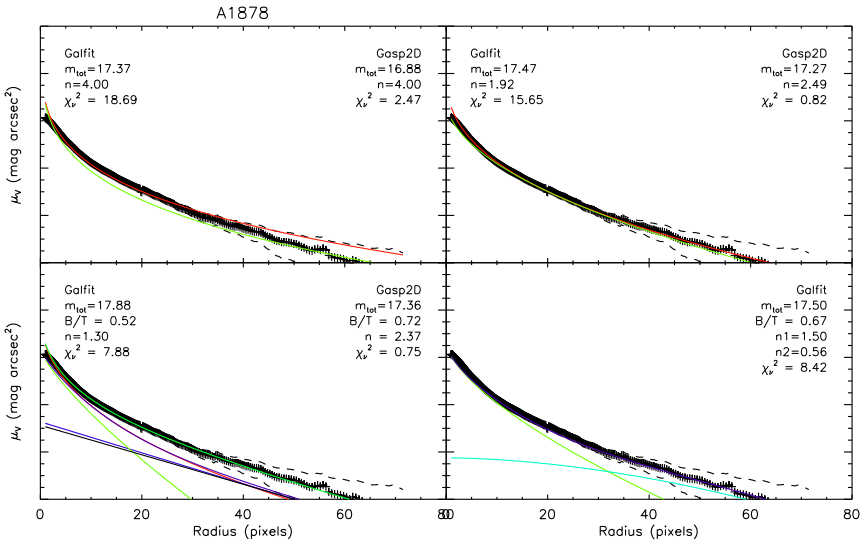
A1878
Galfit
m_tot=17.37
n=4.00
χν² = 18.69
Gasp2D
m_tot=16.88
n=4.00
χν² = 2.47
Galfit
m_tot=17.47
n=1.92
χν² = 15.65
Gasp2D
m_tot=17.27
n=2.49
χν² = 0.82
Galfit
m_tot=17.88
B/T = 0.52
n=1.30
χν² = 7.88
Gasp2D
m_tot=17.36
B/T = 0.72
n = 2.37
χν² = 0.75
Galfit
m_tot=17.50
B/T = 0.67
n1=1.50
n2=0.56
χν² = 8.42
μν (mag arcsec²)
Radius (pixels)

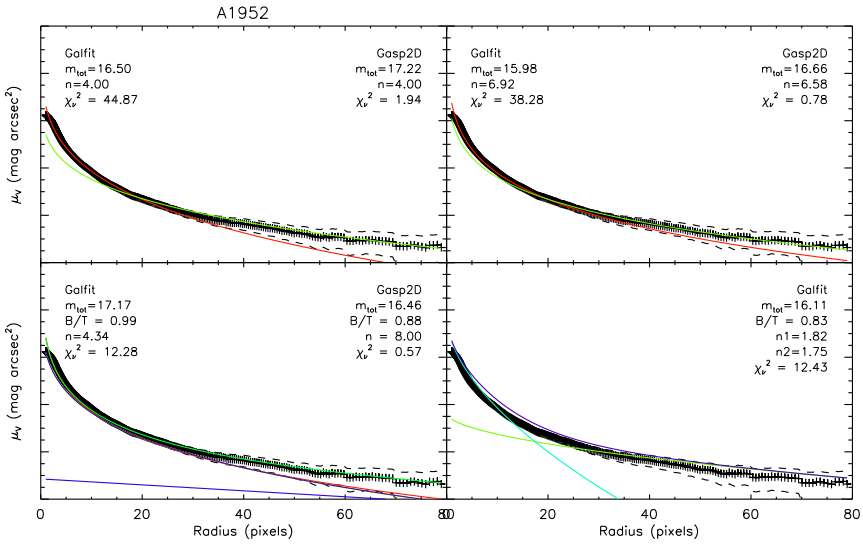
A1952
Galfit
m_tot=16.50
n=4.00
χ_ν² = 44.87
Gasp2D
m_tot=17.22
n=4.00
χ_ν² = 1.94
Galfit
m_tot=15.98
n=6.92
χ_ν² = 38.28
Gasp2D
m_tot=16.66
n=6.58
χ_ν² = 0.78
Galfit
m_tot=17.17
B/T = 0.99
n=4.34
χ_ν² = 12.28
Gasp2D
m_tot=16.46
B/T = 0.88
n = 8.00
χ_ν² = 0.57
Galfit
m_tot=16.11
B/T = 0.83
n1=1.82
n2=1.75
χ_ν² = 12.43
μ_v (mag arcsec²)
Radius (pixels)
0
20
40
60
80

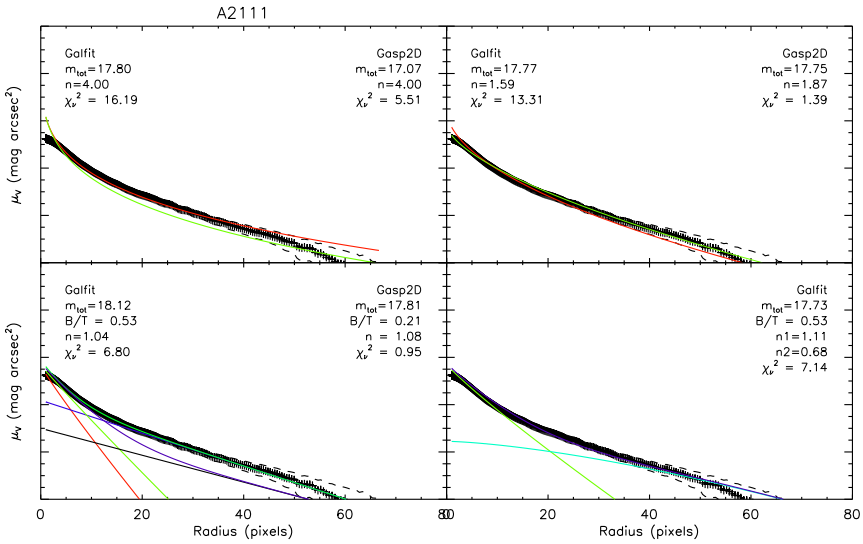
A2111
Galfit
m_tot=17.80
n=4.00
χ_ν² = 16.19
Gasp2D
m_tot=17.07
n=4.00
χ_ν² = 5.51
Galfit
m_tot=17.77
n=1.59
χ_ν² = 13.31
Gasp2D
m_tot=17.75
n=1.87
χ_ν² = 1.39
Galfit
m_tot=18.12
B/T = 0.53
n=1.04
χ_ν² = 6.80
Gasp2D
m_tot=17.81
B/T = 0.21
n = 1.08
χ_ν² = 0.95
Galfit
m_tot=17.73
B/T = 0.53
n1=1.11
n2=0.68
χ_ν² = 7.14
μ_v (mag arcsec²)
Radius (pixels)
0
20
40
60
80

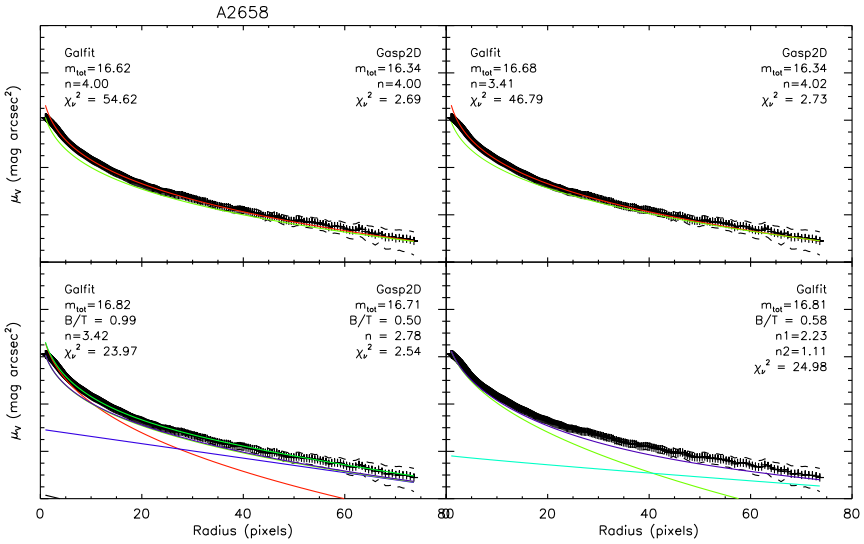

Figure 8.12: Surface brightness profiles for the NOT BCGs. Upper left: De Vaucouleurs fit (Red line, GASP-2D fit, Green Line, GALFIT fit). Upper right: Sersic fit (Red line, GASP-2D fit, Green Line, GALFIT fit). Bottom left: Sersic+Exponential fit, (Red line, GASP-2D Sersic fit, Green Line, GASP-2D Exponential fit, Blue line GASP-2D total fit; Light Green line, GALFIT Sersic fit, Black line, GALFIT Exponential fit, Violet line, GALFIT total fit). Bottom right: Sersic+ Sersic fit, (Red line, GASP-2D First Sersic fit, Green Line, GASP-2D Second Sersic fit, Blue line GASP-2D total fit; Light Green line, GALFIT First Sersic fit, Black line, GALFIT Second Sersic fit, Violet line, GALFIT total fit)

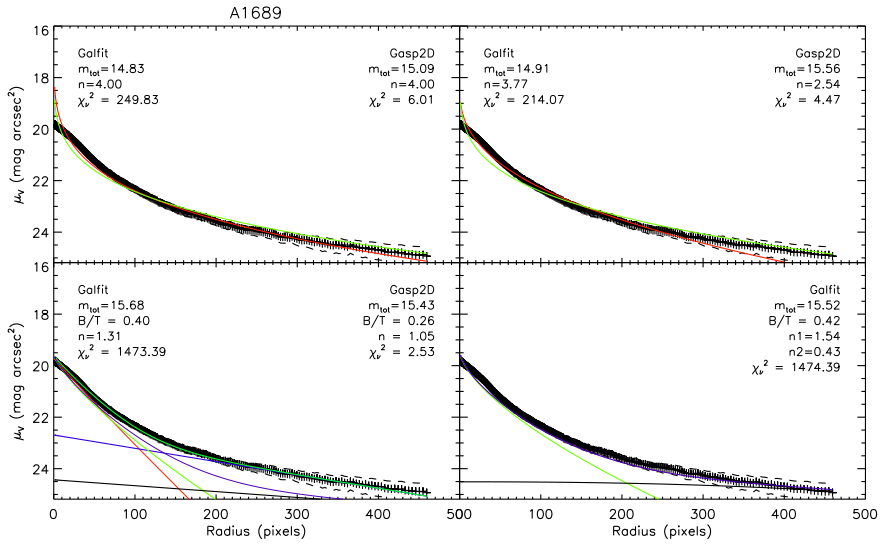
A1689
Galfit
m_tot=14.83
n=4.00
χ_ν² = 249.83
Gasp2D
m_tot=15.09
n=4.00
χ_ν² = 6.01
Galfit
m_tot=14.91
n=3.77
χ_ν² = 214.07
Gasp2D
m_tot=15.56
n=2.54
χ_ν² = 4.47
Galfit
m_tot=15.68
B/T = 0.40
n=1.31
χ_ν² = 1473.39
Gasp2D
m_tot=15.43
B/T = 0.26
n = 1.05
χ_ν² = 2.53
Galfit
m_tot=15.52
B/T = 0.42
n1=1.54
n2=0.43
χ_ν² = 1474.39
μ_v (mag arcsec²)
Radius (pixels)

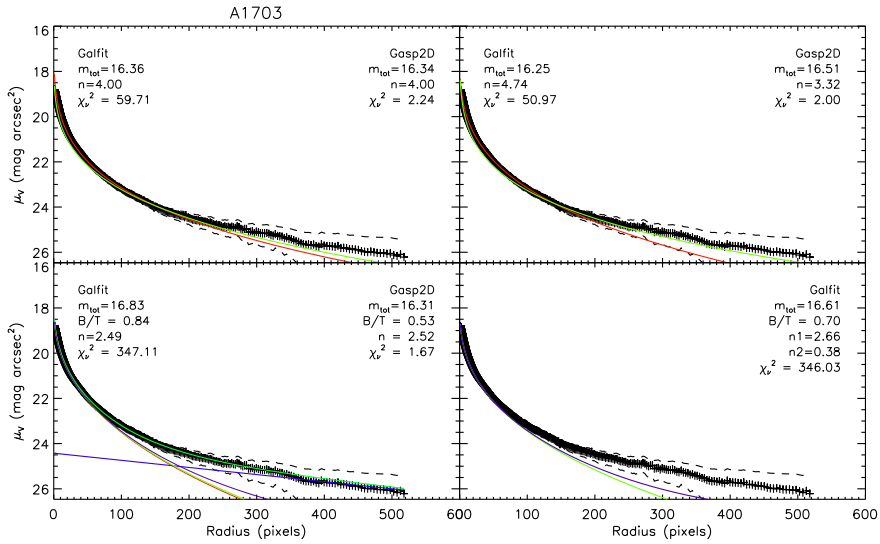
A1703
Galfit
m_tot=16.36
n=4.00
χ_ν² = 59.71
Gasp2D
m_tot=16.34
n=4.00
χ_ν² = 2.24
Galfit
m_tot=16.25
n=4.74
χ_ν² = 50.97
Gasp2D
m_tot=16.51
n=3.32
χ_ν² = 2.00
Galfit
m_tot=16.83
B/T = 0.84
n=2.49
χ_ν² = 347.11
Gasp2D
m_tot=16.31
B/T = 0.53
n = 2.52
χ_ν² = 1.67
Galfit
m_tot=16.61
B/T = 0.70
n1=2.66
n2=0.38
χ_ν² = 346.03
μ_v (mag arcsec²)
Radius (pixels)

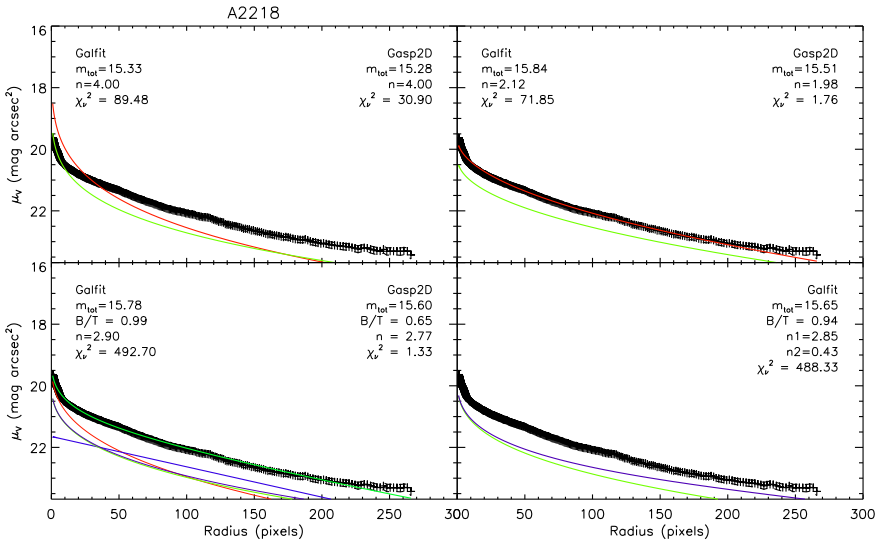
A2218
Galfit
m_tot=15.33
n=4.00
χν² = 89.48
Gasp2D
m_tot=15.28
n=4.00
χν² = 30.90
Galfit
m_tot=15.84
n=2.12
χν² = 71.85
Gasp2D
m_tot=15.51
n=1.98
χν² = 1.76
Galfit
m_tot=15.78
B/T = 0.99
n=2.90
χν² = 492.70
Gasp2D
m_tot=15.60
B/T = 0.65
n = 2.77
χν² = 1.33
Galfit
m_tot=15.65
B/T = 0.94
n1=2.85
n2=0.43
χν² = 488.33
μν (mag arcsec²)
Radius (pixels)

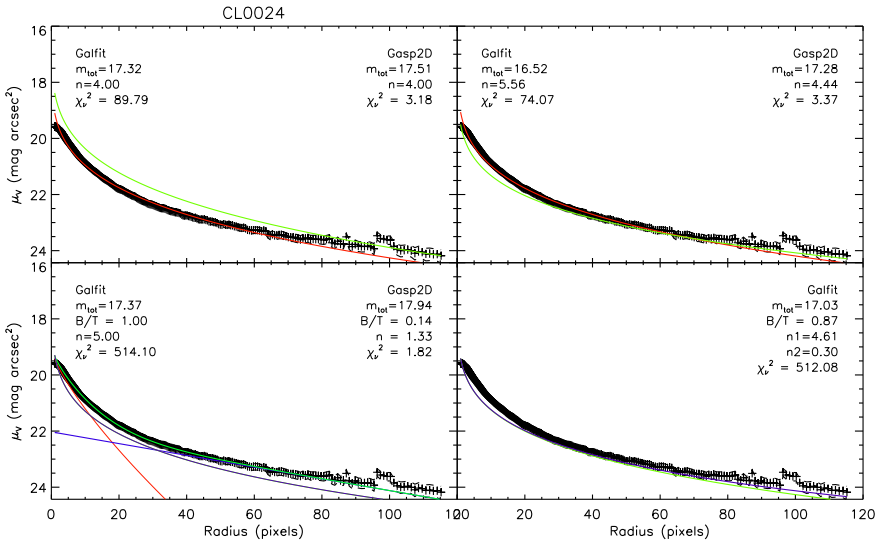
CL0024
Galfit
m_tot=17.32
n=4.00
χν² = 89.79
Gasp2D
m_tot=17.51
n=4.00
χν² = 3.18
Galfit
m_tot=16.52
n=5.56
χν² = 74.07
Gasp2D
m_tot=17.28
n=4.44
χν² = 3.37
Galfit
m_tot=17.37
B/T = 1.00
n=5.00
χν² = 514.10
Gasp2D
m_tot=17.94
B/T = 0.14
n = 1.33
χν² = 1.82
Galfit
m_tot=17.03
B/T = 0.87
n1=4.61
n2=0.30
χν² = 512.08
μν (mag arcsec²)
Radius (pixels)

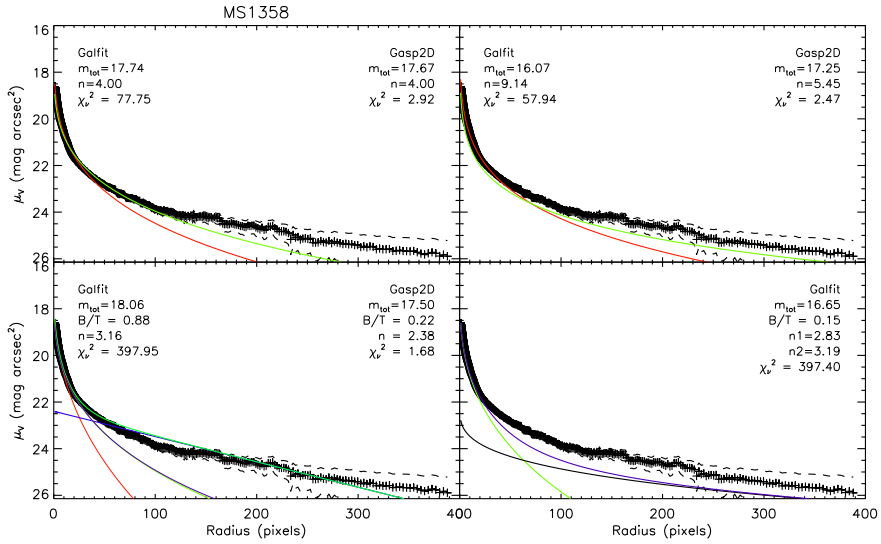

Figure 8.13: Surface brightness profiles for the ACS BCGs. Upper left: De Vaucouleurs fit (Red line, GASP-2D fit, Green Line, GALFIT fit). Upper right: Sersic fit (Red line, GASP-2D fit, Green Line, GALFIT fit). Bottom left: Sersic+Exponential fit, (Red line, GASP-2D Sersic fit, Green Line, GASP-2D Exponential fit, Blue line GASP-2D total fit; Light Green line, GALFIT Sersic fit, Black line, GALFIT Exponential fit, Violet line, GALFIT total fit). Bottom right: Sersic+ Sersic fit, (Red line, GASP-2D First Sersic fit, Green Line, GASP-2D Second Sersic fit, Blue line GASP-2D total fit; Light Green line, GALFIT First Sersic fit, Black line, GALFIT Second Sersic fit, Violet line, GALFIT total fit)

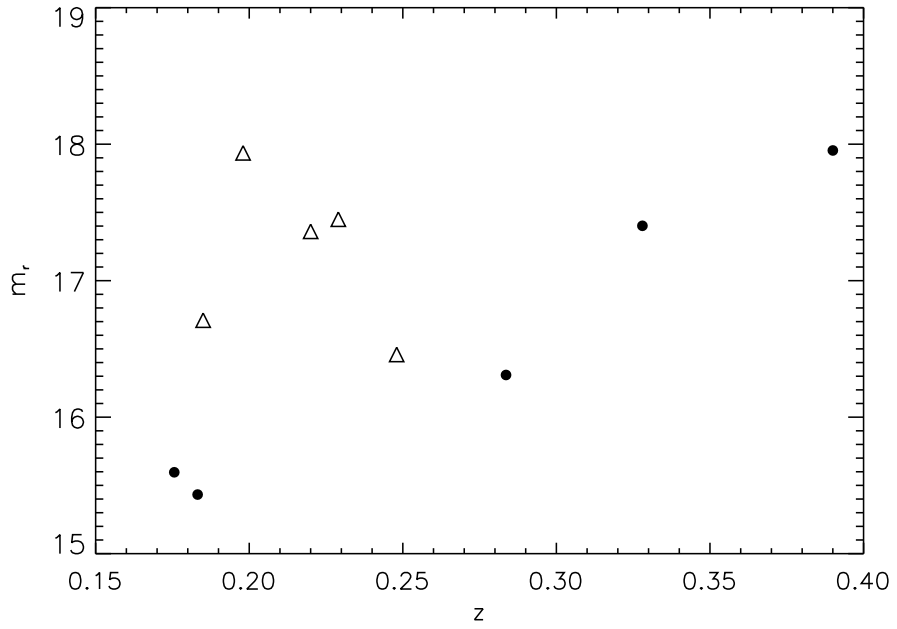

Figure 8.14: Hubble Diagram for the BCGs in NOT (Triangles) and ACS sample (Black Points).

significantly reduced. It is not surprising that selecting clusters by some criteria related to richness can provide very tight $m - z$ relations.

As many authors have noticed (Aragon-Salamanca, Baugh & Kauffmann, 1998; Collins & Mann, 1998; Burke, Collins & Mann, 2000; Brough et al., 2005), the K-band Hubble diagram for BCGs is very well defined up to redshift 1, with a small dispersion (within 0.3 mag). With the purpose of looking into the location of our BCGs sample in the K-band Hubble diagram and as we do not have K magnitudes, we have used a color transformation of R-K=2.6 (Lauer & Postman, 1994), following for example, Aragon-Salamanca, Baugh & Kauffmann (1998) or Burke, Collins & Mann (2000).

Then, in Figure 8.15, we show our BCGs sample (red points and blue triangles refers to the ACS and NOT sample, respectively), together with the 45 BCGs in EMSS (Einstein Medium Sensitivity Survey), X-ray-selected clusters sample at low redshift (Gioia & Luppino, 1994) in K-band, extracted from Collins & Mann (1998), (black points, in the Figure 8.15)

As expected from the previous analysis, the BCGs in the ACS sample, which are found in more massive and luminous X-ray clusters, seem to be well in the range of the values provided by the EMSS clusters, while the BCGs in NOT sample, belonging to less massive, non-X-ray emitters and less rich clusters show

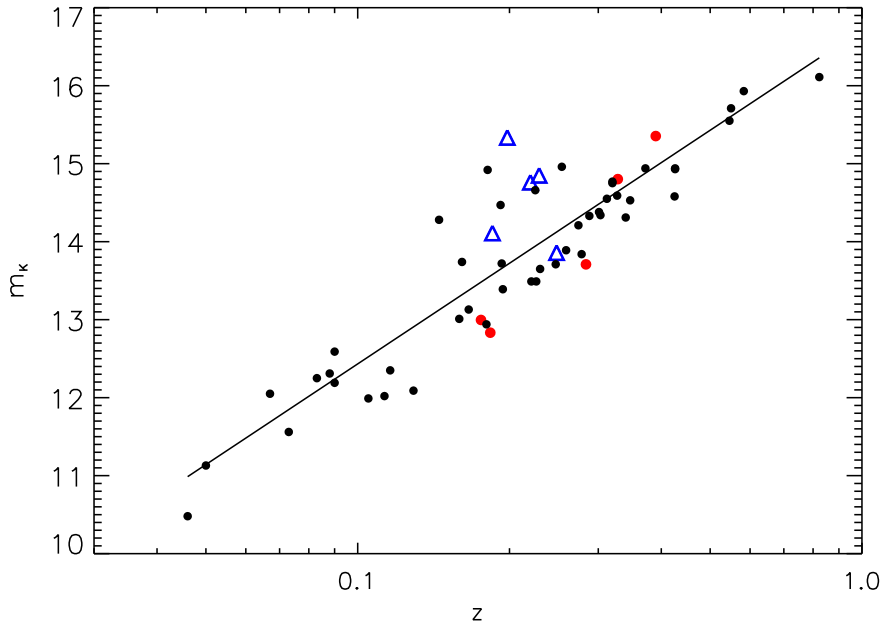

Figure 8.15: K-band Hubble Diagram for the BCGs in NOT (Blue Triangles) and ACS sample (Red Points). The black points are the BCGs in a X-ray selected sample given by Collins & Mann (1998). The solid line is the whole sample linear fit.

a larger dispersion in comparison to the rest of the clusters. Indeed, the largest dispersion is produced by our NOT clusters.

Despite of this fact, the whole sample can be fitted with a moderate dispersion of 0.268. If only the ACS sample together with Collins & Mann (1998) sample is considered, the dispersion is lower, 0.235. Both values are compatible with the dispersion found by Collins & Mann (1998). Clearly, the X-ray ACS sample seems to have a more homogeneous range of properties than the NOT sample. Without going now into the details, it is evident that a richness correction would bring the NOT clusters closer to the fit line, providing a lower dispersion.

As a conclusion, we observe a quite homogeneous range of properties for the BCGs in our sample. In particular, for the ACS sample, that has been selected to have richness class higher than 4 in all cases and higher X-ray luminosities and masses. These results agree with the need of a richness correction in the BCGs magnitudes to consider a small dispersion in the Hubble diagram (?Kristian, Sandage & Westphal, 1978).

8.4 Are they Standard Candles?

Since the first identification of photometric homogeneity of BCGs (Humason, Mayall & Sandage, 1956; Sandage, 1972a,b), the BCGs have been explored in detail in order to demonstrate that they could be treated as 'Standard Candles' for performing cosmological probes.

The main piece of evidence in that sense, was the spectacular small dispersion of 0.25 mag of the luminosities of the BCGs, with an adequate selection of the data in luminosity and cluster morphology.

Lauer & Postman (1994); Postman & Lauer (1995), performed the first studies in large samples of BCGs. They selected 119 BCGs up to redshift ≤ 0.05 from a sample of 153 clusters in the ACO catalogue (Abell, Corwin & Olowin, 1989), basing their exclusions on the redshift, lack of significant overdensity or non-elliptical BCG morphology. They investigated into the relationship between L_m, the metric luminosity within the central 10 h^{-1} kpc of the BCGs and logarithmic slope of the surface brightness profiles α, finding a reduction of the cosmic scatter in L_m and an independence of the color, cluster richness and BCG location within the host cluster, concluding with the following sentence: *BCGs are a highly homogeneous population, making them suitable for statistical studies of galaxy peculiar velocities on large scales.*

In the following years, a large number of works, (e.g. Collins & Mann (1998); Brough et al. (2002)), have been devoted to corroborate the homogeneity of the BCGs. Some of them have established that the dispersion of BCGs in clusters with an X-ray luminosity $L_x \geq 2.3 \times 10^{44} ergs^{-1}$ in the passband $0.3 - 3.5keV$ is about half as large (0.24) as those in less luminous clusters, and their mean absolute magnitude in the raw K-band is 0.5 mag brighter. However, there are still few BCGs with redshift below 0.3 in these analyses so the evolutionary nature of this effect remains unclear.

We have confirmed that trend with our 0.15-0.3 redshift sample. We have found that our richer, more luminous X-ray BCGs sample, achieves a smaller dispersion (of 0.23) in the Hubble Diagram. However, if we consider the rest of the sample that does not emit in X-ray, their dispersion, even if within the results previously found, amounts to 0.28. This fact was already noted by Sandage, Kristian & Westphal (1976); Kristian, Sandage & Westphal (1978), who gave a richness correction to the BCGs magnitudes in order to decrease the dispersion in the Hubble Diagram.

It seems like the homogeneity of the BCGs is patent at considering clusters with the same richness class (the ACS sample). As a conclusion, the use of 'Standard Candles' can be done only for clusters selected with a variety of properties, such as X-ray luminosity, richness class or any other requirements like the ones specified by Sandage (1976); Kristian, Sandage & Westphal (1978); Postman & Lauer (1995).

At present, one of the applications of the BCG characteristics has been the use of their homogeneity for detecting clusters of galaxies in large surveys. In particular, a cluster detection algorithm based on the optical properties of the BCGs, MaxBCG (Koester et al., 2007), have been developed. On one hand, this algorithm takes advantage of the colors of the brightest members and their spatially 'clustering' falling off as $\sim 1/r$ in two dimensions. On the other hand, they combine these information with the existence of the BCG residing at the brightest end of the CMR sequence and its placement at the halo center. As a consequence, they have been able to recover 90% of the clusters at $0.1 < z < 0.3$ with 10 or more red galaxies through large, realistic, mock galaxy catalogues.

Part IV

Conclusions

Chapter 9

Conclusions and Future Prospects

When I heard the learn'd astronomer;
When the proofs, the figures, were ranged in columns before me;
When I was shown the charts and the diagrams,
to add, divide, and measure them;
When I, sitting, heard the astronomer, where he lectured
with much applause in the lecture-room,
How soon, unaccountable, I became tired and sick,
Till rising and gliding out, I wander'd off by myself,
In the mystical moist night-air, and from time to time,
Look'd up in perfect silence at the stars.

Walt Whitman, 'Leaves of grass'

We have analyzed a sample of ten clusters of galaxies at medium redshift ($0.15 \leq z \leq 0.4$), covering a wide range of properties in luminosity, X-ray properties, richness, dynamical states... This sample is mainly subdivided in two subsamples: the NOT sample (five clusters observed from the ground, less massive and rich, with few references available in the literature and with an area coverage slightly larger) and the ACS sample (five more clusters observed from the space with plenty of literature available, rich, massive, X-ray emitters and with a smaller area coverage). A cluster in the NOT sample, A2111 is also a X-ray emitter, so sometimes, it has been analyzed together with the ACS sample in order to compare its X-ray properties.

We have been able to study therefore the degree of cosmic variance from lower and higher redshift samples, as well as single out the main properties of some individual objects. In this chapter, we summarize the main conclusions that have been derived from the results of the analysis of this sample.

9.1 Conclusions

9.1.1 Bright Galaxy Population

- We have found an excellent agreement between the slopes of the Color-Magnitude Relation for our medium redshift sample and a low redshift sample. They are also very similar to the slope values recovered for two clusters at $z \approx 1.26$. This fact supports the no variation of the CMR up to redshift ≈ 0.3 at least and more probably at higher redshift. In other words, the stellar population for the bright early type galaxies was settled just after the galaxy formation.

- The median central values for the galaxy blue fraction values computed in different apertures in our samples achieves a good agreement with those found for lower redshift samples. Diversity seems to be the dominant aspect up to this range of redshift, $z \sim 0.3$.

- The concentration values for our samples have been found to span the full range of the values measured for lower and higher redshift samples.

- We have looked into the rate of interacting systems in our sample. The median values obtained for the perturbation f-parameter are smaller than that for Coma cluster, suggesting the presence of a higher degree of interaction in our clusters samples, with respect to Coma.

- An algorithm to decide whether or not a galaxy should be fitted into one or two components has been developed. The final classification gives us 47% of the galaxies with areas larger than 800 pixels in the NOT sample, are better fitted by a Sersic-one component profile, while the 52% are better fitted by a two components (Sersic+Disc profiles).

- We have found a dichotomy for the red and blue bulges of the galaxies in the NOT sample fitted by one component -Sersic model in the plane $n - r_e$ allowing to distinguish nearly univocally the early ($2 \leq n \leq 4$) and late types ($n \sim 1$).

- The same range of values for the effective radius, r_e and shape parameter, n for the bulge of galaxies in our sample and Coma Cluster has been found, indicating that the bulge of the galaxies in our medium redshift NOT clusters were set at redshift larger than 0.25 at least.

- The disc scales in the NOT sample have been compared with those of lower redshift field galaxies sample and with the disc scales extracted from Coma galaxies. We have found that our disc scales are as large as those of field galaxies, while they are significantly different from disc scales in Coma. This result gives support to an evolution hypothesis in the disc scales of galaxies in clusters from lower redshift samples to redshift ~ 0.2 clusters.

- The analysis of the Morphology - Density for the NOT and ACS samples give similar results with other at lower redshift. Two clusters out of ten show significantly different radial distribution of the early and late type galaxies, indicating a morphological segregation, like clusters at low redshift.

- The Luminosity Function at redshift $\sim$ 0.2- 0.4 is well described by a composite Schechter Function with parameters of $\alpha \sim -1.11$ and $M_r^* \sim 21.64$. These parameters are quite similar to the parameters obtained at lower redshift samples even if we find slightly fainter values of M^*.

- We have found different behavior for the Luminosity Function for blue and red galaxy population. The red galaxy population show a much flatter slope and a brighter value of M^* than the blue galaxy population.

- The Universality of the global Luminosity Function is not supported by our results as we find significant differences from cluster to cluster, even in the ACS sample. However, the same tendencies for red and blue galaxies in both samples are found, which might suggest a Universality of the Luminosity Function regarding to different color population.

9.1.2 Brightest Cluster Galaxies

- An algorithm has been developed for the extraction of the Brightest Cluster Galaxy without changing its properties and the properties of the nearby galaxies.

- The Degree of Dominance of the BCGs does not show any clear correlation with redshift. Richer clusters spread all the ranges of degrees of dominance, while the dispersion seems to be less in poorer clusters. However, this result may be biased as we are not covering homogeneously the richness class range.

- We have tested the nature of cD galaxies from our BCGs sample, finding that four out of ten BCGs at least are cD galaxies.

- The best fit for the surface brightness of the BCGs shows a variety of different profiles. This result indicates that the surface brightness profiles of BCGs are not as homogeneous as their luminosity.

- The Hubble Diagram for the BCGs in our whole sample, together with data at lower and higher redshift shows a global dispersion of 0.268, while if we consider only the BCGs from the ACS sample (X-ray emitters and richer clusters), we find a dispersion of 0.235. An homogeneous range of properties for the BCGs in ACS sample has been noticed, suggesting that a richness correction must be applied to consider these objects as *Standard Candles*.

9.2 Future Prospects

As we have previously seen throughout this thesis, there is a lack of cluster data at medium redshift due to the need to obtain very good seeing conditions from the Ground to obtain quality data or to the difficulty of obtaining observations from the Space covering a large enough areas. Therefore, we want to continue exploiting the excellent data presented in this thesis by focusing on the following points:

- To study the detailed surface brightness from the ACS sample in all the multi-wavelenght range, taking advantage of the already available multi-color observations to analyze the color radial profiles.
- To extend, correct and automatize the algorithm extraction of the BCGs in the multi-wavelenght range.
- To introduce the use of two Sersic components or different functions in the GASP-2D package to be able to fit BCGs galaxies with the quality of this package.
- To develop and apply a richness correction to BCGs in poorer NOT clusters to homogenize their properties with BCGs placed in richer clusters.

Our main interest now refers to the cluster galactic populations properties. One of our priorities is therefore, to expand the size of the cluster sample analyzed in this thesis in order to quantify the degree of variance of their properties in this range of redshift and also to extend this sample to other redshift ranges. Moreover, we have seen in the last part of the thesis that mostly all the observation in K-band that have been performed in large samples of BCGs have been at medium-high redshift. Therefore, larger analysis of BCGs are needed at low-medium redshift to determine their 'Standard Candles' status.

In order to do that, the study and development of different techniques to detect and extract clusters of galaxies is intended to be investigated in the close future in the Deep Lens Survey (DLS; Wittman et al. (2006)), which is a multi-band (B,V,R,z) very deep photometry (up to 29/29/29/28 mag per square arcsecond surface brightness) survey of five 4 square degree fields using the Mosaic CCD imagers at the Blanco and Mayall telescopes. This survey is able to provide information from redshift ~ 1 to the present epoch. Once the largest number of clusters are detected, the main properties of their galactic population and BCGs will be analyzed, providing a much wider range of data to analyze the cosmic variance in clusters of galaxies.

9.3 Conclusiones

Hemos analizado una muestra de diez cúmulos de galaxias a *redshift* medio ($0.15 \leq z \leq 0.4$), cubriendo un amplio rango de propiedades en luminosidades, propiedades en rayos-X, riqueza, estados dinámicos... Esta muestra está principalmente subdividida en dos submuestras: la de NOT (cinco cumulos observados desde tierra, menos masivos y ricos, con poca literatura disponible y con una cobertura en área ligerament mayor) y la de la ACS (cinco cúmulos observados desde el espacio con gran cantidad de literatura disponible, ricos, masivos, emisores en rayos-X y con una cobertura en área menor). Uno de los cúmulos en la muestra del NOT, A2111, emite también en rayos-X, con lo que, en algunos casos, será analizado junto con la muestra del ACS para comparación de sus propiedades-X.

Hemos estudiado, por lo tanto, el grado de varianza cósmica en comparación con muestras a bajo y alto *redshift*, así como el destacamiento de las principales propiedades de algunos objetos individuales. En este capítulo, resumimos las principales conclusiones que se han derivado de los resultados del análisis de esta muestra.

9.3.1 Población Galáctica Brillante

- Hemos encontrado una buena concordancia entre las pendientes de la relación color-magnitud de nuestra muestra a medio *redshift* y una muestra a bajo *redshift*. Estos valores son muy similares a la pendiente encontrada para dos cúmulos a $z \approx 1.26$. Este hecho apoya la no-variación de la CMR hasta *redshift* ≈ 0.3 como mínimo y muy probablemente a mayor *redshift*. En otras palabras, la población estelar para las galaxias tempranas brillantes se formó justo después de la formación de las galaxias.
- Los valores centrales medianos para la fracción de galaxias azules calculada en diferentes aperturas para nuestras muestras alcanza un buen acuerdo con las encontradas en muestras a bajo *redshift*. La diversidad parece ser la tendencia más remarcable hasta este rango de redshift, $z \sim 0.3$.
- Los parámetros de concentración de nuestras muestras barren todo el rango de valores medidos para muestras a *redshift* menores y mayores.
- La tasa de sistemas en interacción en nuestra muestra también se ha tenido en consideración. Lo valores medianos obtenidos para el parámetro de perturbación son menores que los del cúmulo de Coma, sugiriendo la presencia de un grado de interacción más alto en nuestros cúmulos que en Coma.
- Hemos elaborado un algoritmo para decidir si una galaxia determinada debería ser ajustada en una o dos componentes. La clasificación final nos da que un 47% de galaxias con áreas mayores que 800 píxeles que se ajustan mejor por un pérfil de una componente-Sersic, mientras que el 52% se ajusta mejor por dos componentes (perfiles Sersic+Disco).

- Hemos encontrado una dicotomía para los bulbos de las galaxias rojas y azules ajustados por un modelo de una componente en la muestra NOT en el plano $n - r_e$, permitiéndonos distinguir muy claramente entre tipos tempranos ($2 \leq n \leq 4$) y tardíos ($n \sim 1$).

- Se ha obtenido el mismo rango de valores para el radio efectivo, r_e y el parámetro de forma, n para los bulbos de las galaxias de nuestra muestra y las del cúmulo de Coma, indicando que los bulbos de las galaxias en la muestra NOT se formaron a *redshift* mayores que 0.25 como mínimo.

- Las escalas de los discos en la muestra NOT se compararon con las de las galaxias de campo a bajo *redshift* y con las escalas de los discos del cúmulo de Coma. Hemos encontrado que las escalas de nuestros discos son tan grandes como las de las galaxias de campo, mientras que son significantemente diferentes de las escalas de los discos en Coma. Estos resultados estan de acuerdo con una hipótesis de evolución en las escalas de los discos desde muestras a bajo *redshift* hasta cúmulos a *redshift* $\sim$ 0.2.

- La relación Morfología-Densidad para las muestras NOT y ACS dan resultados similares con respecto a muestras a *redshift* menores. Dos cúmulos de diez, muestran distribuciones radiales significantemente diferentes para los tipos tempranos y tardíos, indicando una segregación morfológica, que está patente a bajo *redshift*.

- La Función de Luminosidad a *redshift* $\sim 0.2 - 0.4$ está bien descrita por una Función de Schechter con parámetros de $\alpha \sim -1.11$ y $M_r^* \sim -21.64$. Estos parámetros son bastante similares a los parámetros obtenidos a bajo *redshift*, incluso aunque encontremos valores ligeramente más débiles de M^* que para muestras a menor *redshift*.

- Hemos encontrado different comportamiento de la Función de Luminosidad para poblaciones galácticas rojas y azules. La población galáctica roja muestra una pendiente mucho más plana y un valor más brillante de M^* que los de la población galáctica azul.

- Nuestros resultados no apoyan la universalidad de la función de luminosidad, ya que hemos encontrado diferencias significativas de cúmulo a cúmulo, incluso en la muestra ACS. Sin embargo, se han encontrado las mismas tendecias para las galaxias rojas y azules en ambas muestras, lo que podría sugerir la universalidad de la función de luminosidad respecto a diferentes colores.

9.3.2 Galaxia Más Brillante del Cúmulo

- Se ha desarrollado un algorimo para la extracción de la BCG (Galaxia Más Brillante del Cúmulo, de sus siglas en inglés), sin cambiar sus propiedades y las propiedades de las demás galaxias cercanas.

- El grado de dominancia de las BCGs en el cúmulo no muestra correlaciones claras con el *redshift*. Los cúmulos más ricos despliegan todo el rango de grado de dominancia, mientras que la dispersión parece ser menor in cúmulos más pobres. Sin embargo, este resultado puede estar sesgado ya que no estamos cubriendo homogéneamente el rango de clase de riqueza en nuestra muestra de cúmulos.

- Hemos analizado la naturaleza de galaxias cD de nuestra muestra de BCGs, asegurando que cuatro de diez BCGs al menos son galaxias cD.

- El mejor ajuste para el brillo superficial de las BCGs muestra una variedad de perfiles diferentes. Estos resultados indican que los perfiles de brillo superficial de estos objetos no son tan homogéneos como sus luminosidades.

- El diagrama de Hubble para las BCGs en nuestra muestra global, junto con los datos compilados a menor y mayor *redshift* muestra una dispersión global de 0.268, mientras que si consideramos solo las BCGs de la muestra ACS (cúmulos en rayos-X y más ricos), encontramos una dispersión de 0.235. Es remarcable el grado de homogeneidad de las propiedades de las BCG en la muestra ACS, lo que sugiere que una corrección de riqueza se debe aplicar para considerar estos objetos como 'Candelas Estándares'.

Bibliography

Abell, G. O. 1958, ApJS, 3, 211

Abell, G. O. 1962, Problems of Extra-Galactic Research, 15, 213

Abell, G. O. 1964, ApJ, 140, 1624

Abell, G. O. 1965, ARA&A, 3, 1

Abell, G. O. 1972, External Galaxies and Quasi-Stellar Objects, 44, 341

Abell, G. O., Corwin, H. G., Jr., & Olowin, R. P. 1989, ApJS, 70, 1

Acton F.S, 1970, *Numerical Methods That Work*, 1990, corrected edition, (Washington: Mathematical Association of America), 464

Adami, C., Biviano, A., & Mazure, A. 1998, A&A, 331, 439

Aguerri, J. A. L., Balcells, M., & Peletier, R. F. 2001, A&A, 367, 428

Aguerri, J. A. L., Iglesias-Paramo, J., Vilchez, J. M., & Muñoz-Tuñón, C. 2004, AJ, 127, 134

Aguerri, J. A. L., Iglesias-Páramo, J., Vílchez, J. M., Muñoz-Tuñón, C., & Sánchez-Janssen, R. 2005, AJ, 130, 475

Aguerri, J. A. L., Sánchez-Janssen, R., & Muñoz-Tuñón, C. 2007, A&A, 471, 17

Alexov, A., Silva, D. R., & Pierce, M. J. 2003, AJ, 126, 2644

Allen, S. W., et al. 1992, MNRAS, 259, 67

Allen, P. D., Driver, S. P., Graham, A. W., Cameron, E., Liske, J., & de Propris, R. 2006, MNRAS, 371, 2

Amorín, R. O., Muñoz-Tuñón, C., Aguerri, J. A. L., Cairós, L. M., & Caon, N. 2007, A&A, 467, 541

Andersson, K. E., & Madejski, G. M. 2004, ApJ, 607, 190

Andredakis, Y. C., Peletier, R. F., & Balcells, M. 1995, MNRAS, 275, 8

Andreon, S., Davoust, E., & Heim, T. 1997, A&A, 323, 337

Andreon, S. 2004, A&A, 416, 865

Andreon, S., Punzi, G., & Grado, A. 2005, MNRAS, 360, 727

Andreon, S., Quintana, H., Tajer, M., Galaz, G., & Surdej, J. 2006, MNRAS, 365, 915

Aragon-Salamanca, A., Ellis, R. S., Couch, W. J., & Carter, D. 1993, MNRAS, 262, 764

Aragon-Salamanca, A., Baugh, C. M., & Kauffmann, G. 1998, MNRAS, 297, 427

Arimoto, N., & Yoshii, Y. 1987, A&A, 173, 23

Armstrong R.D. & Kung M.T., 1978, Appl Stat, 27, 363

Ascaso, B. & González-Casado G., 2003, *Estudio comparativo de modelos de distribución de materia en cúmulos de galaxias*, UPC, 1400503621 PT Asc

Ascaso, B. & Moles M., 2007 ApJ, 660L, 89

Ascaso, B., Moles M., Aguerri J.A.L., Sánchez-Janssen R. & Varela J., 2008, A&A, (accepted)

Ascaso, B., Aguerri J.A.L., Moles M. & Sánchez-Janssen R., 2008 (to be submitted)

Ascaso, B., Benitez N., Ford H. & Postman M. , 2008 in preparation

Barkhouse, W. A., Yee, H. K. C., & López-Cruz, O. 2007, ApJ, 671, 1471

Baum, W. A. 1959, PASP, 71, 106

Babu G.J. & Singh K., 1983, *Ann. Stat.*, 11, 999

Bautz, L. P., & Morgan, W. W. 1970, ApJ, 162, L149

Bekki, K., Couch, W. J., & Shioya, Y. 2002, ApJ, 577, 651

Bender, R., Saglia, R. P., Ziegler, B., Belloni, P., Greggio, L., Hopp, U., & Bruzual, G. 1998, ApJ, 493, 529

Benítez, N. 2000, ApJ, 536, 571

Bernardi, M., et al. 2003, AJ, 125, 1882

Bernardi, M., Hyde, J. B., Sheth, R. K., Miller, C. J., & Nichol, R. C. 2007, AJ, 133, 1741

Berta, S., et al. 2006, A&A, 451, 881

Bertin, E., & Arnouts, S. 1996, A&AS, 117, 393

Binggeli, B., Sandage, A., & Tarenghi, M. 1984, AJ, 89, 64

Binggeli, B., Tammann, G. A., & Sandage, A. 1987, AJ, 94, 251

Binggeli, B., Sandage, A., & Tammann, G. A. 1988, ARA&A, 26, 509

Binggeli, B., & Jerjen, H. 1998, A&A, 333, 17

Bird, C. M. 1994, AJ, 107, 1637

Biviano, A., Durret, F., Gerbal, D., Le Fevre, O., Lobo, C., Mazure, A., & Slezak, E. 1995, A&A, 297, 610

Blakeslee, J. P., Anderson, K. R., Meurer, G. R., Benítez, N., & Magee, D., 2003, in ASP Conf. Ser. 295, Astronomical Data Analysis Software and Systems XII, ed. H. E. Payne, R. I. Jedrzejewski, & R. N. Hook (San Francisco: ASP), 12, 257

Blanton, M. R., et al. 2003, ApJ, 594, 186

Böhringer, H., Soucail, G., Mellier, Y., Ikebe, Y., & Schuecker, P. 2000, A&A, 353, 124

Bonamente, M., Joy, M. K., LaRoque, S. J., Carlstrom, J. E., Reese, E. D., & Dawson, K. S. 2006, ApJ, 647, 25

Bonnarel, F., et al. 2000, A&AS, 143, 33

Boué, G., Adami, C., Durret, F., Mamon, G. A., & Cayatte, V. 2008, A&A, 479, 335

Bower, R. G., Lucey, J. R., & Ellis, R. S. 1992, MNRAS, 254, 589

Bower, R. G., Lucey, J. R., & Ellis, R. S. 1992, MNRAS, 254, 601

Bower, R. G., Kodama, T., & Terlevich, A. 1998, MNRAS, 299, 1193

Broadhurst, T., Huang, X., Frye, B., & Ellis, R. 2000, ApJ, 534, L15

Broadhurst, T., Takada, M., Umetsu, K., Kong, X., Arimoto, N., Chiba, M., & Futamase, T. 2005, ApJ, 619, L143

Broadhurst, T., et al. 2005, ApJ, 621, 53

Brodie, J. P., & Huchra, J. P. 1991, ApJ, 379, 157

Brough, S., Collins, C. A., Burke, D. J., Mann, R. G., & Lynam, P. D. 2002, MNRAS, 329, L53

Brough, S., Collins, C. A., Burke, D. J., Lynam, P. D., & Mann, R. G. 2005, MNRAS, 364, 1354

Buote, D. A. 2002, Merging Processes in Galaxy Clusters, 272, 79

Burke, D. J., Collins, C. A., & Mann, R. G. 2000, ApJ, 532, L105

Burkert, A. 1995, ApJ, 447, L25

Butcher, H., & Oemler, A., Jr. 1978, ApJ, 226, 559

Butcher, H., & Oemler, A., Jr. 1984, ApJ, 285, 426

Byun, Y. I., & Freeman, K. C. 1995, ApJ, 448, 563

Cannon, D. B., Ponman, T. J., & Hobbs, I. S. 1999, MNRAS, 302, 9

Caon, N., Capaccioli, M., & D'Onofrio, M. 1993, MNRAS, 265, 1013

Caon, N., Cairós, L. M., Aguerri, J. A. L., & Muñoz-Tuñón, C. 2005, ApJS, 157, 218

Coe, D., Benítez, N., Sánchez, S. F., Jee, M., Bouwens, R., & Ford, H. 2006, AJ, 132, 926

Charlot, S., Worthey, G., & Bressan, A. 1996, ApJ, 457, 625

Colless, M. 1989, MNRAS, 237, 799

Colley, W. N., Tyson, J. A., & Turner, E. L. 1996, ApJ, 461, L83

Collins, C. A., & Mann, R. G. 1998, MNRAS, 297, 128

Conselice, C. J., Gallagher, J. S., III, & Wyse, R. F. G. 2001, ApJ, 559, 791

Crawford, C. S., Allen, S. W., Ebeling, H., Edge, A. C., & Fabian, A. C. 1999, MNRAS, 306, 857

Crawford, K. 2005, S&T, 110, 123

Curtis, H. D. 1918, Publications of Lick Observatory, 13, 55

Czoske, O., Kneib, J.-P., Soucail, G., Bridges, T. J., Mellier, Y., & Cuillandre, J.-C. 2001, A&A, 372, 391

de Jong, R. S. 1996, A&AS, 118, 557

De Lucia, G., et al. 2007, MNRAS, 374, 809

De Lucia, G., & Blaizot, J. 2007, MNRAS, 375, 2

de Propris, R., Stanford, S. A., Eisenhardt, P. R., Dickinson, M., & Elston, R. 1999, AJ, 118, 719

De Propris, R., et al. 2003, MNRAS, 342, 725

De Propris, R., Stanford, S. A., Eisenhardt, P. R., & Dickinson, M. 2003, ApJ, 598, 20

De Propris, R., et al. 2004, MNRAS, 351, 125

De Propris, R., Conselice, C. J., Liske, J., Driver, S. P., Patton, D. R., Graham, A. W., & Allen, P. D. 2007, ApJ, 666, 212

de Souza, R. E., Gadotti, D. A., & dos Anjos, S. 2004, ApJS, 153, 411

de Vaucouleurs, G. 1948, Annales d'Astrophysique, 11, 247

de Vaucouleurs, G. 1959, Handbuch der Physik, 53, 275

de Vaucouleurs, G. 1963, ApJS, 8, 31

Demarco, R., Magnard, F., Durret, F., & Márquez, I. 2003, A&A, 407, 437

Diego, J. M., Sandvik, H. B., Protopapas, P., Tegmark, M., Benítez, N., & Broadhurst, T. 2005, MNRAS, 362, 1247

Djorgovski, S., & Davis, M. 1987, ApJ, 313, 59

Dressler, A. 1978, ApJ, 223, 765

Dressler, A. 1980, ApJ, 236, 351

Dressler, A. 1984, ARA&A, 22, 185

Dressler, A., Lynden-Bell, D., Burstein, D., Davies, R. L., Faber, S. M., Terlevich, R., & Wegner, G. 1987, ApJ, 313, 42

Dressler, A., & Gunn, J. E. 1992, ApJS, 78, 1

Dressler, A., et al. 1997, ApJ, 490, 577

Driver, S. P., Phillipps, S., Davies, J. I., Morgan, I., & Disney, M. J. 1994, MNRAS, 268, 393

Driver, S. P., et al. 2006, MNRAS, 368, 414

Dubinski, J. 1998, ApJ, 502, 141

Duc, P.-A., et al. 2002, A&A, 382, 60

Edge, A. C. 1991, MNRAS, 250, 103

Efron B. & Tibshirani R., 1986, *Stat. Sci.*, 1, 54

Efstathiou, G., Ellis, R. S., & Peterson, B. A. 1988, MNRAS, 232, 431

Eliche-Moral, M. C., Balcells, M., Aguerri, J. A. L., & González-García, A. C. 2006, A&A, 457, 91

Ellingson, E., Lin, H., Yee, H. K. C., & Carlberg, R. G. 2001, ApJ, 547, 609

Ellis, R. S., Smail, I., Dressler, A., Couch, W. J., Oemler, A. J., Butcher, H., & Sharples, R. M. 1997, ApJ, 483, 582

Estrada, J., et al. 2007, ApJ, 660, 1176

Faber, S. M., & Jackson, R. E. 1976, ApJ, 204, 668

Fabian, A. C., Nulsen, P. E. J., & Canizares, C. R. 1982, MNRAS, 201, 933

Fabricant, D. G., McClintock, J. E., & Bautz, M. W. 1991, ApJ, 381, 33

Fabricant, D., Franx, M., & van Dokkum, P. 2000, ApJ, 539, 577

Fasano, G., Poggianti, B. M., Couch, W. J., Bettoni, D., Kjærgaard, P., & Moles, M. 2000, ApJ, 542, 673

Fasano, G., Bettoni, D., D'Onofrio, M., Kjærgaard, P., & Moles, M. 2002, A&A, 387, 26

Fasano, G., et al. 2006, A&A, 445, 805

Fetisova T.S., 1982, *Soviet Astron.*, 25, 647

Ferrarese, L., et al. 2006, ApJS, 164, 334

Fisher, D., Illingworth, G., & Franx, M. 1995, ApJ, 438, 539

Fisher, D., Fabricant, D., Franx, M., & van Dokkum, P. 1998, ApJ, 498, 195

Fitchett, M. 1988, MNRAS, 230, 161

Fletchter R., 1970, *Comput Journal*, 13, 317

Freeman, K. C. 1970, ApJ, 160, 811

Frei, Z., & Gunn, J. E. 1994, AJ, 108, 1476

Gaidos, E. J. 1997, AJ, 113, 117

Gal, R. R., de Carvalho, R. R., Lopes, P. A. A., Djorgovski, S. G., Brunner, R. J., Mahabal, A., & Odewahn, S. C. 2003, AJ, 125, 2064

Garilli, B., Maccagni, D., Carrasco, L., & Recillas, E. 1995, Fresh Views of Elliptical Galaxies, 86, 297

Garilli, B., Bottini, D., Maccagni, D., Carrasco, L., & Recillas, E. 1996, ApJS, 105, 19

Garilli, B., Maccagni, D., & Andreon, S. 1999, A&A, 342, 408

Gerhard, O. E., & Fall, S. M. 1983, MNRAS, 203, 1253

Gioia, I. M., & Luppino, G. A. 1994, ApJS, 94, 583

Godwin, J. G., & Peach, J. V. 1977, MNRAS, 181, 323

González, R. E., Lares, M., Lambas, D. G., & Valotto, C. 2006, A&A, 445, 51

Goto, T., et al. 2003, PASJ, 55, 739

Graham, A., Lauer, T. R., Colless, M., & Postman, M. 1996, ApJ, 465, 534

Graham, A. W. 2001, AJ, 121, 820

Graham, A. W., & de Blok, W. J. G. 2001, ApJ, 556, 177

Graham, A. W., & Guzmán, R. 2003, AJ, 125, 2936

Graham, A. W. 2003, AJ, 125, 3398

Griersmith, D. 1980, AJ, 85, 1295

Gunn, J. E., & Gott, J. R. I. 1972, ApJ, 176, 1

Gunn, J. E., & Oke, J. B. 1975, ApJ, 195, 255

Hack W.J., 1999, CALACS Operation and Implementation, ISR ACS-99-03

Halkola, A., Seitz, S., & Pannella, M. 2006, MNRAS, 372, 1425

Halkola, A., Seitz, S., & Pannella, M. 2007, ApJ, 656, 739

Hansen, S. M., McKay, T. A., Wechsler, R. H., Annis, J., Sheldon, E. S., & Kimball, A. 2005, ApJ, 633, 122

Hashimoto, Y., Böhringer, H., Henry, J. P., Hasinger, G., & Szokoly, G. 2007, A&A, 467, 485

Henriksen, M., Wang, Q. D., & Ulmer, M. 1999, MNRAS, 307, 6

Hilker, M., Mieske, S., & Infante, L. 2003, A&A, 397, L9

Hoekstra, H., Franx, M., Kuijken, K., & Squires, G. 1998, ApJ, 504, 636

Hoessel, J. G., & Schneider, D. P. 1985, AJ, 90, 1648

Hubble, E. P. 1926, ApJ, 64, 321

Hubble, E., & Humason, M. L. 1931, ApJ, 74, 43

Hubble, E. 1936, ApJ, 84, 158

Humason, M. L., Mayall, N. U., & Sandage, A. R. 1956, AJ, 61, 97

James F. & Roos M., 1975, *Minuit: A system for Function Minimizations and Analysis of Parameter Errors and Correlations*, Computer Physics Communications, 10, 343

Jarrett, T. H., Chester, T., Huchra, J., & Schneider, S. 1998, Bulletin of the American Astronomical Society, 30, 901

Jones, C., & Forman, W. 1984, ApJ, 276, 38

Jordán, A., Côté, P., West, M. J., Marzke, R. O., Minniti, D., & Rejkuba, M. 2004, AJ, 127, 24

Jorgensen, I., Franx, M., & Kjaergaard, P. 1992, A&AS, 95, 489

Jorgensen, I. 1994, PASP, 106, 967

Jorgensen, I., Franx, M., & Kjaergaard, P. 1996, MNRAS, 280, 167

Jørgensen, I., Franx, M., Hjorth, J., & van Dokkum, P. G. 1999, MNRAS, 308, 833

Kassiola, A., & Kovner, I. 1993, ApJ, 417, 474

Kauffmann, G., Guiderdoni, B., & White, S. D. M. 1994, MNRAS, 267, 981

Kauffmann, G. 1996, MNRAS, 281, 487

Kelson, D. D., van Dokkum, P. G., Franx, M., Illingworth, G. D., & Fabricant, D. 1997, ApJ, 478, L13

Kelson, D. D., Illingworth, G. D., van Dokkum, P. G., & Franx, M. 2000, ApJ, 531, 159

Kim, R. S. J., Annis, J., Strauss, M. A., & Lupton, R. H. 2002, Tracing Cosmic Evolution with Galaxy Clusters, 268, 395

Kneib, J. P., Mellier, Y., Pello, R., Miralda-Escude, J., Le Borgne, J.-F., Boehringer, H., & Picat, J.-P. 1995, A&A, 303, 27

Kneib, J.-P., Ellis, R. S., Smail, I., Couch, W. J., & Sharples, R. M. 1996, ApJ, 471, 643

Kneib, J.-P., et al. 2003, ApJ, 598, 804

Kneib, J.-P., Ellis, R. S., Santos, M. R., & Richard, J. 2004, ApJ, 607, 697

Kodama, T. 1999, Star Formation in Early Type Galaxies, 163, 250

Kodama, T., Balogh, M. L., Smail, I., Bower, R. G., & Nakata, F. 2004, MNRAS, 354, 1103

Koester, B. P., et al. 2007, ApJ, 660, 221

Koo, D. C., Guzman, R., Gallego, J., & Wirth, G. D. 1997, ApJ, 478, L49

Kormendy, J. 1977, ApJ, 217, 406

Kormendy, J., & Djorgovski, S. 1989, ARA&A, 27, 235

Kotov, O., & Vikhlinin, A. 2005, ApJ, 633, 781

Kristian, J., Sandage, A., & Westphal, J. A. 1978, ApJ, 221, 383

Landolt, A. U. 1992, AJ, 104, 340

LaRoque, S. J., Bonamente, M., Carlstrom, J. E., Joy, M. K., Nagai, D., Reese, E. D., & Dawson, K. S. 2006, ApJ, 652, 917

Lavery, R. J., & Henry, J. P. 1986, ApJ, 304, L5

Lauer, T. R., & Postman, M. 1994, ApJ, 425, 418

Lauer, T. R., et al. 2007, ApJ, 662, 808

Le Borgne, J. F., Pello, R., & Sanahuja, B. 1992, A&AS, 95, 87

Lieu, R., Mittaz, J. P. D., & Zhang, S.-N. 2006, ApJ, 648, 176

Limousin M. et al., 2008, arXiv:0802.4292v1

Lin, H., Kirshner, R. P., Shectman, S. A., Landy, S. D., Oemler, A., Tucker, D. L., & Schechter, P. L. 1996, ApJ, 464, 6

Lin, H., Yee, H. K. C., Carlberg, R. G., Morris, S. L., Sawicki, M., Patton, D. R., Wirth, G., & Shepherd, C. W. 1999, ApJ, 518, 533

Lin, Y.-T., & Mohr, J. J. 2004, ApJ, 617, 879

Liske, J., Lemon, D. J., Driver, S. P., Cross, N. J. G., & Couch, W. J. 2003, MNRAS, 344, 307

Loh, Y.-S., & Strauss, M. A. 2006, MNRAS, 366, 373

Łokas, E. L., & Mamon, G. A. 2001, MNRAS, 321, 155

Łokas, E. L., Prada, F., Wojtak, R., Moles, M., & Gottlöber, S. 2006, MNRAS, 366, L26

López-Cruz O., Yee H.K.C., Brown J.P., Jones C. & Forman W., 1997, ApJ, 475, 97

López-Cruz, O., Barkhouse, W. A., & Yee, H. K. C. 2004, ApJ, 614, 679

Lugger, P. M. 1986, ApJ, 303, 535

Lumsden, S. L., Collins, C. A., Nichol, R. C., Eke, V. R., & Guzzo, L. 1997, MNRAS, 290, 119

Luppino, G. A., Cooke, B. A., McHardy, I. M., & Ricker, G. R. 1991, AJ, 102, 1

MacArthur, L. A., Courteau, S., & Holtzman, J. A. 2003, ApJ, 582, 689

Machacek, M. E., Bautz, M. W., Canizares, C., & Garmire, G. P. 2002, ApJ, 567, 188

Madau, P., Pozzetti, L., & Dickinson, M. 1998, ApJ, 498, 106

Malumuth, E. M., & Richstone, D. O. 1984, ApJ, 276, 413

Margoniner, V. E., & de Carvalho, R. R. 2000, AJ, 119, 1562

Margoniner, V. E., de Carvalho, R. R., Gal, R. R., & Djorgovski, S. G. 2001, ApJ, 548, L143

Markevitch, M. 1997, ApJ, 483, L17

Matthews, T. A., Morgan, W. W., & Schmidt, M. 1964, ApJ, 140, 35

Mazure, A., et al. 1995, Astrophysics, 38, 367

McGlynn, T. A., & Ostriker, J. P. 1980, ApJ, 241, 915

McHardy, I. M., Stewart, G. C., Edge, A. C., Cooke, B., Yamashita, K., & Hatsukade, I. 1990, MNRAS, 242, 215

McLeod, B. A., Bernstein, G. M., Rieke, M. J., Tollestrup, E. V., & Fazio, G. G. 1995, ApJS, 96, 117

Mei, S., et al. 2006, ApJ, 644, 759

Melnick, J., & Sargent, W. L. W. 1977, ApJ, 215, 401

Méndez-Abreu, J., Aguerri, J. A. L., Corsini, E. M., & Simonneau, E. 2008, A&A, 478, 353

Merritt, D. 1984, ApJ, 276, 26

Merritt, D. 1985, ApJ, 289, 18

Metcalfe, N., Shanks, T., Campos, A., McCracken, H. J., & Fong, R. 2001, MNRAS, 323, 795

Metevier, A. J., Koo, D. C., Simard, L., & Phillips, A. C. 2006, ApJ, 643, 764

Miller, N. A., Oegerle, W. R., & Hill, J. M. 2006, AJ, 131, 2426

Miralda-Escude, J., & Babul, A. 1995, ApJ, 449, 18

Mobasher, B., Ellis, R. S., & Sharples, R. M. 1986, MNRAS, 223, 11

Moles, M., Campos, A., Kjaegaard, P., Fasano, G., & Bettoni, D. 1998, ApJ, 495, L31

Moles, M., Bettoni, D., Fasano, G., Kjærgaard, P., Varela, J., & Milvang-Jensen, B. 2004, A&A, 418, 495

Molinari, E., Buzzoni, A., & Chincarini, G. 1996, A&AS, 119, 391

Möllenhoff, C. 2004, A&A, 415, 63

Montogomery, K. A., Marschall, L.A., & Janes, K. A. 1993, AJ, 106, 181

Moore, B., Katz, N., Lake, G., Dressler, A., & Oemler, A. 1996, Nature, 379, 613

Morandi, A., Ettori, S., & Moscardini, L. 2007, MNRAS, 379, 518

Morgan, W. W. 1958, PASP, 70, 364

Morgan, W. W. 1962, ApJ, 135, 1

Navarro, J. F., Frenk, C. S., & White, S. D. M. 1995, MNRAS, 275, 720

Nelder J.A. & Mead R. 1965, *Computer Journal*, 7, 308

Nelson, A. E., Gonzalez, A. H., Zaritsky, D., & Dalcanton, J. J. 2002, ApJ, 566, 103

Neumann, D. M., Böhringer, H. 1999, ApJ, 512, 630

Oemler, A. 1973, ApJ, 180, 11

Oemler, A. J. 1974, ApJ, 194, 1

Oemler, A., Jr. 1976, ApJ, 209, 693

Oke, J. B., & Sandage, A. 1968, ApJ, 154, 21

Ostriker, J. P., & Tremaine, S. D. 1975, ApJ, 202, L113

Parolin, I., Molinari, E., & Chincarini, G. 2003, A&A, 407, 823

Patel, P., Maddox, S., Pearce, F. R., Aragón-Salamanca, A., & Conway, E. 2006, MNRAS, 370, 85

Patton, D. R., Carlberg, R. G., Marzke, R. O., Pritchet, C. J., da Costa, L. N., & Pellegrini, P. S. 2000, ApJ, 536, 153

Pence, W. 1976, ApJ, 203, 39

Peng, C. Y., Ho, L. C., Impey, C. D., & Rix, H.-W. 2002, AJ, 124, 266

Perea, J., del Olmo, A., & Moles, M. 1986, MNRAS, 222, 49

Pignatelli, E., Fasano, G., & Cassata, P. 2006, A&A, 446, 373

Pinkney, J., Roettiger, K., Burns, J. O., & Bird, C. M. 1996, ApJS, 104, 1

Piranomonte, S., Longo, G., Andreon, S., Puddu, E., Paolillo, M., Scaramella, R., Gal, R., & Djorgovski, S. G. 2001, Virtual Observatories of the Future, 225, 73

Poggianti, B. M. 1997, A&AS, 122, 399

Popesso, P., Böhringer, H., Brinkmann, J., Voges, W., & York, D. G. 2004, A&A, 423, 449

Popesso, P., Biviano, A., Böhringer, H., & Romaniello, M. 2006, A&A, 445, 29

Porter, A. C., Schneider, D. P., & Hoessel, J. G. 1991, AJ, 101, 1561

Postman, M., & Lauer, T. R. 1995, ApJ, 440, 28

Postman, M., et al. 2005, ApJ, 623, 721

Pracy, M. B., Driver, S. P., De Propris, R., Couch, W. J., & Nulsen, P. E. J. 2005, MNRAS, 364, 1147

Pratt, G. W., Böhringer, H., & Finoguenov, A. 2005, A&A, 433, 777

Press, W. H., & Schechter, P. 1974, ApJ, 187, 425

Press W. H. et al., 1992, Numerical recipes in FORTRAN: The art of Scientic Computing (Cambridge: Cambridge Univ. Press)

Prieto, M., Aguerri, J. A. L., Varela, A. M., & Muñoz-Tuñón, C. 2001, A&A, 367, 405

Quilis, V., Moore, B., & Bower, R. 2000, Science, 288, 1617

Quintana, H., Infante, L., Fouque, P., Carrasco, E. R., Cuevas, H., Hertling, G., & Nuñez, I. 2000, ApJS, 126, 1

Rakos K.D. & Schombert J.M., 1995, ApJ, 439, 47

Rakos K.D., Dominis D. & Steindling S., 2001, ARA&A, 369, 750

Rakos K.D. & Schombert J.M., 2005, AJ, 130, 1002

Ramella M. et al. 2007, A&A, 470, 39

Reynolds J. H. 1913, MNRAS, 74, 132

Rhee G.F.R.N & Latour H.J., 1991, A&A, 243, 38

Roberts, M. S., & Haynes, M. P. 1994, ARA&A, 32, 115

Romer A.K. et al., 1994, *Nature*, 372, 75

Rögnvaldsson Ö.E. et al., 2001, MNRAS, 332, 131

Rood H.J., 1969, ApJ, 158, 657

Rood H.J. & Sastry G.N., 1971, PASP, 83, 313

Sánchez-Janssen, R., Iglesias-Páramo, J., Muñoz-Tuñón, C., Aguerri, J. A. L., & Vílchez, J. M. 2004, IAU Colloq. 195: Outskirts of Galaxy Clusters: Intense Life in the Suburbs, 438

Sánchez, S. F., Cardiel, N., Verheijen, M. A. W., Pedraz, S., & Covone, G. 2007, MNRAS, 376, 125

Sandage A., 1961, *The Hubble Atlas of Galaxies*, Carnegie Inst. of Wash. Publ. No 618, Washington, D.C.

Sandage, A. 1972a, ApJ, 173, 485

Sandage, A. 1972b, ApJ, 176, 21

Sandage, A. 1972, ApJ, 178, 1

Sandage, A., & Hardy, E. 1973, ApJ, 183, 743

Sandage, A. 1976, ApJ, 205, 6

Sandage, A., Kristian, J., & Westphal, J. A. 1976, ApJ, 205, 688

Sandage, A., & Visvanathan, N. 1978, ApJ, 223, 707

Sandage, A., Tammann, G. A., & Yahil, A. 1979, ApJ, 232, 352

Sanroma, M., & Salvador-Sole, E. 1990, ApJ, 360, 16

Sarazin, C. L. 1980, ApJ, 236, 75

Schechter, P. 1976, ApJ, 203, 297

Schechter, P., & Press, W. H. 1976, ApJ, 203, 557

Schlegel, D. J., Finkbeiner, D. P., & Davis, M. 1998, ApJ, 500, 525

Schombert, J. M. 1986, ApJS, 60, 603

Schombert, J. M. 1987, ApJS, 64, 643

Schombert, J. M. 1988, ApJ, 328, 475

Secker, J., Harris, W. E., & Plummer, J. D. 1997, PASP, 109, 1377

Seigar, M. S., Graham, A. W., & Jerjen, H. 2007, MNRAS, 378, 1575

Sersic J.L., 1968, Atlas de Galaxias Australes (Córdoba: Obs. Astron. Univ. Nac)

Smail, I., Ellis, R. S., Dressler, A., Couch, W. J., Oemler, A. J., Sharples, R. M., & Butcher, H. 1997, ApJ, 479, 70

Smith, R. J., et al. 2004, AJ, 128, 1558

Smith, G. P., Kneib, J.-P., Smail, I., Mazzotta, P., Ebeling, H., & Czoske, O. 2005, MNRAS, 359, 417

Simard, L. 1998, Astronomical Data Analysis Software and Systems VII, 145, 108

Simard, L., et al. 1999, ApJ, 519, 563

Soucail, G., Ota, N., Böhringer, H., Czoske, O., Hattori, M., & Mellier, Y. 2000, A&A, 355, 433

Soucail, G., Kneib, J.-P., & Golse, G. 2004, A&A, 417, L33

Stanford, S. A., Eisenhardt, P. R., & Dickinson, M. 1998, ApJ, 492, 461

Stocke, J. T., Morris, S. L., Gioia, I. M., Maccacaro, T., Schild, R., Wolter, A., Fleming, T. A., & Henry, J. P. 1991, ApJS, 76, 813

Stott, J. P., Edge, A. C., Smith, G. P., Swinbank, A. M., & Ebeling, H. 2008, MNRAS, 384, 1502

Sunyaev, R. A., & Zeldovich, Y. B. 1970, Comments on Astrophysics and Space Physics, 2, 66

Sunyaev, R. A., & Zeldovich, Y. B. 1972, Comments on Astrophysics and Space Physics, 4, 173

Struble, M. F., & Rood, H. J. 1991, ApJS, 77, 363

Taylor, A. N., Dye, S., Broadhurst, T. J., Benitez, N., & van Kampen, E. 1998, ApJ, 501, 539

Teague, P. F., Carter, D., & Gray, P. M. 1990, ApJS, 72, 715

Terlevich, R., Davies, R. L., Faber, S. M., & Burstein, D. 1981, MNRAS, 196, 381

Thompson, L. A., & Gregory, S. A. 1993, AJ, 106, 2197

Tonry, J. L. 1987, Structure and Dynamics of Elliptical Galaxies, 127, 89

Tremaine, S. D., & Richstone, D. O. 1977, ApJ, 212, 311

Trentham, N., Tully, R. B., & Verheijen, M. A. W. 2001, MNRAS, 325, 385

Treu, T., Ellis, R. S., Kneib, J.-P., Dressler, A., Smail, I., Czoske, O., Oemler, A., & Natarajan, P. 2003, ApJ, 591, 53

Trevese, D., Flin, P., Migliori, L., Hickson, P., & Pittella, G. 1992, A&AS, 94, 327

Trujillo, I., Aguerri, J. A. L., Cepa, J., & Gutiérrez, C. M. 2001a, MNRAS, 321, 269

Trujillo, I., Aguerri, J. A. L., Cepa, J., & Gutiérrez, C. M. 2001b, MNRAS, 328, 977

Trujillo, I., Aguerri, J. A. L., Gutiérrez, C. M., & Cepa, J. 2001c, AJ, 122, 38

Trujillo, I., & Aguerri, J. A. L. 2004, MNRAS, 355, 82

Tsuboi, M., Miyazaki, A., Kasuga, T., Matsuo, H., & Kuno, N. 1998, PASJ, 50, 169

Tully, R. B., & Fisher, J. R. 1977, A&A, 54, 661

Tully, R. B., Mould, J. R., & Aaronson, M. 1982, ApJ, 257, 527

Tyson, J. A., & Fischer, P. 1995, ApJ, 446, L55

Tyson, J. A., Kochanski, G. P., & dell'Antonio, I. P. 1998, ApJ, 498, L107

Uyaniker, B., Reich, W., Schlickeiser, R., & Wielebinski, R. 1997, A&A, 325, 516

Valotto, C. A., Nicotra, M. A., Muriel, H., & Lambas, D. G. 1997, ApJ, 479, 90

van den Bergh, S. 1960, Publications of the David Dunlap Observatory, 2, 159

van den Bergh, S. 1997, AJ, 113, 2054

van Dokkum, P. G., & Franx, M. 1996, MNRAS, 281, 985

van Dokkum, P. G., Franx, M., Kelson, D. D., Illingworth, G. D., Fisher, D., & Fabricant, D. 1998, ApJ, 500, 714

van Haarlem, M. P., Frenk, C. S., & White, S. D. M. 1997, MNRAS, 287, 817

Varela J., 2004, Ph.D. Thesis, Universidad Complutense de Madrid

Varela, J., Moles, M., Márquez, I., Galletta, G., Masegosa, J., & Bettoni, D. 2004, A&A, 420, 873

Visvanathan, N., & Griersmith, D. 1977, A&A, 59, 317

Visvanathan, N., & Sandage, A. 1977, ApJ, 216, 214

Visvanathan, N. 1981, A&A, 100, L20

Wang, Q. D., Ulmer, M. P., & Lavery, R. J. 1997, MNRAS, 288, 702

Wegner, G., Colless, M., Saglia, R. P., McMahan, R. K., Davies, R. L., Burstein, D., & Baggley, G. 1999, MNRAS, 305, 259

Whitmore, B. C., & Gilmore, D. M. 1991, ApJ, 367, 64

Whitmore, B. C., Gilmore, D. M., & Jones, C. 1993, ApJ, 407, 489

Wittman, D., Dell'Antonio, I. P., Hughes, J. P., Margoniner, V. E., Tyson, J. A., Cohen, J. G., & Norman, D. 2006, ApJ, 643, 12

Xue, S.-J., & Wu, X.-P. 2002, ApJ, 576, 152

Yagi, M., Kashikawa, N., Sekiguchi, M., Doi, M., Yasuda, N., Shimasaku, K., & Okamura, S. 2002, AJ, 123, 87

Yasuda, N., et al. 2001, AJ, 122, 1104

Yee, H. K. C., Ellingson, E., Morris, S. L., Abraham, R. G., & Carlberg, R. G. 1998, ApJS, 116, 21

Yee, H. K. C., Gladders, M. D., & López-Cruz, O. 1999, Photometric Redshifts and the Detection of High Redshift Galaxies, 191, 166

York, D. G., et al. 2000, AJ, 120, 1579

Zemcov, M., Borys, C., Halpern, M., Mauskopf, P., & Scott, D. 2007, MNRAS, 376, 1073

Zekser, K. C., et al. 2006, ApJ, 640, 639

Zhang, L., Han, Z. X., & Jiang, Z. J. 2005, A&A, 429, 489

Zibetti, S., White, S. D. M., Schneider, D. P., & Brinkmann, J. 2005, MNRAS, 358, 949

Zucca, E., et al. 1997, A&A, 326, 477

Zwicky, F. 1951, PASP, 63, 61

Zwicky F., 1953, *Helvet. phys. acta*, 26, 241

Zwicky F., 1956, *Pro. Third Berkeley Symposium on Mathematical Statistics and Probability*, 3, 113

Zwicky F., Herzog E., Wild P., Karpowick, & Kowal C., 1961-1968, *Catalogue of Galaxies and of Clusters of Galaxies*, Vols 1-6 Pasadena: Calif. Inst. Technol.

Part V

Appendix

Appendix A

Catalogue of galaxies belonging to the NOT sample

Imposible fotografiar el bostezo indolente del Universo

Arturo Pérez-Reverte, 'El pintor de batallas.'

Name	α (J2000)			δ (J2000)			z	M_r	M_B	Morph
A 1643	12h	55m	52.30s	44d	05m	47.30s		-19.88	-20.46	S
A 1643	12h	55m	52.44s	44d	05m	52.70s		-19.52	-20.82	
A 1643	12h	55m	54.14s	44d	05m	52.70s		-19.79	-18.64	
A 1643	12h	55m	59.31s	44d	05m	53.20s		-19.36	-17.98	
A 1643	12h	55m	53.80s	44d	03m	15.20s		-19.79	-18.61	S
A 1643	12h	55m	55.18s	44d	03m	47.50s		-20.67	-19.46	S0
A 1643	12h	55m	49.83s	44d	04m	08.80s		-19.82	-19.24	
A 1643	12h	55m	49.75s	44d	04m	05.50s		-20.61	-19.63	S
A 1643	12h	55m	47.93s	44d	04m	01.20s		-20.36	-19.10	E
A 1643	12h	55m	48.06s	44d	04m	06.70s		-18.24	-17.09	
A 1643	12h	55m	51.98s	44d	04m	05.90s		-18.93	-19.06	
A 1643	12h	55m	59.67s	44d	04m	05.20s		-19.64	-18.62	S
A 1643	12h	55m	53.06s	44d	04m	06.60s		-18.89	-17.82	
A 1643	12h	55m	55.75s	44d	04m	07.30s		-19.39	-18.88	
A 1643	12h	56m	01.43s	44d	04m	07.90s		-19.71	-19.19	
A 1643	12h	55m	53.64s	44d	04m	13.70s		-20.09	-19.36	S
A 1643	12h	55m	50.96s	44d	04m	31.00s		-21.15	-20.05	E
A 1643	12h	55m	59.04s	44d	04m	26.90s		-19.00	-17.81	
A 1643	12h	55m	55.35s	44d	04m	34.40s		-20.69	-20.35	E
A 1643	12h	55m	54.88s	44d	04m	33.90s		-20.14	-19.56	S
A 1643	12h	55m	56.61s	44d	04m	38.20s		-18.70	-20.14	
A 1643	12h	55m	52.33s	44d	04m	46.80s		-18.42	-19.14	

A 1643	12h	55m	52.97s	44d	04m	50.00s		-19.82	-19.09	
A 1643	12h	55m	52.96s	44d	04m	39.20s	0.1978	-19.73	-19.60	S
A 1643	12h	55m	52.70s	44d	04m	44.50s		-20.42	-19.74	S0
A 1643	12h	55m	54.94s	44d	04m	45.60s		-19.29	-19.15	
A 1643	12h	55m	48.16s	44d	04m	49.50s		-19.49	-18.74	
A 1643	12h	55m	47.94s	44d	04m	51.60s		-19.59	-18.95	
A 1643	12h	55m	51.98s	44d	04m	53.10s		-19.57	-19.08	
A 1643	12h	55m	55.21s	44d	04m	53.10s		-18.00	-17.50	
A 1643	12h	55m	54.40s	44d	04m	53.70s		-18.26	-17.50	
A 1643	12h	55m	59.29s	44d	04m	57.10s		-20.02	-18.94	S
A 1643	12h	55m	56.07s	44d	04m	58.00s		-18.49	-17.59	
A 1643	12h	55m	54.00s	44d	05m	12.40s		-21.61	-20.35	S0
A 1643	12h	56m	01.63s	44d	05m	09.10s		-19.45	-18.11	
A 1643	12h	55m	49.61s	44d	05m	09.50s		-18.25	-17.15	
A 1643	12h	55m	47.67s	44d	05m	15.70s		-18.15	-17.15	
A 1643	12h	55m	54.61s	44d	05m	21.40s		-19.23	-17.99	
A 1643	12h	55m	53.05s	44d	05m	23.40s		-20.19	-18.97	S0
A 1643	12h	56m	00.41s	44d	05m	29.90s		-19.20	-18.91	
A 1643	12h	55m	48.02s	44d	05m	35.90s		-19.73	-18.91	
A 1643	12h	55m	52.36s	44d	05m	38.40s		-19.16	-19.35	
A 1643	12h	55m	52.76s	44d	05m	37.90s		-19.88	-19.97	S
A 1643	12h	55m	54.21s	44d	05m	44.70s		-19.41	-18.29	
A 1643	12h	56m	01.53s	44d	03m	29.90s		-18.65	-20.27	
A 1643	12h	55m	50.27s	44d	03m	30.50s		-19.27	-18.68	
A 1643	12h	55m	53.07s	44d	05m	47.80s		-18.67	-17.64	
A 1643	12h	55m	48.08s	44d	05m	51.70s		-18.23	-17.80	
A 1643	12h	55m	34.43s	44d	08m	50.30s		-19.53	-18.37	
A 1643	12h	55m	44.49s	44d	08m	53.60s		-19.09	-18.13	
A 1643	12h	55m	45.49s	44d	06m	39.60s		-18.15	-19.35	
A 1643	12h	55m	44.70s	44d	06m	35.60s		-19.65	-18.94	
A 1643	12h	55m	38.43s	44d	06m	29.90s		-18.50	-17.72	
A 1643	12h	55m	38.94s	44d	06m	35.20s		-18.31	-17.92	
A 1643	12h	55m	45.18s	44d	06m	46.30s		-19.68	-18.40	E
A 1643	12h	55m	32.98s	44d	06m	50.40s		-19.92	-19.46	S
A 1643	12h	55m	33.62s	44d	06m	30.00s		-18.06	-17.72	
A 1643	12h	55m	37.87s	44d	06m	57.10s		-18.59	-17.40	
A 1643	12h	55m	46.43s	44d	06m	58.80s		-18.14	-17.06	
A 1643	12h	55m	33.82s	44d	07m	12.50s		-20.93	-19.67	E
A 1643	12h	55m	36.30s	44d	07m	15.70s		-18.80	-18.47	
A 1643	12h	55m	41.25s	44d	07m	15.00s		-18.32	-17.59	
A 1643	12h	55m	39.33s	44d	07m	21.30s		-19.72	-18.39	S
A 1643	12h	55m	37.74s	44d	07m	23.30s		-18.00	-17.63	
A 1643	12h	55m	38.60s	44d	07m	29.10s		-18.09	-16.93	
A 1643	12h	55m	46.75s	44d	07m	35.40s		-18.99	-17.90	
A 1643	12h	55m	42.78s	44d	07m	48.60s		-18.24	-16.93	
A 1643	12h	55m	36.40s	44d	07m	53.40s		-20.71	-20.57	I

A 1643	12h	55m	36.55s	44d	07m	54.10s		-20.34	-20.10	
A 1643	12h	55m	36.63s	44d	08m	20.30s		-20.17	-20.49	I
A 1643	12h	55m	36.38s	44d	08m	24.40s		-19.77	-19.13	S0
A 1643	12h	55m	36.57s	44d	08m	30.40s		-20.27	-19.84	E
A 1643	12h	55m	43.31s	44d	08m	28.90s		-18.20	-18.04	
A 1643	12h	55m	38.31s	44d	08m	38.70s		-18.02	-17.76	
A 1643	12h	55m	37.59s	44d	06m	21.10s		-19.42	-18.66	S
A 1878	14h	12m	54.12s	29d	16m	16.60s		-18.74	-17.61	
A 1878	14h	12m	49.83s	29d	13m	40.60s		-18.90	-18.43	
A 1878	14h	12m	47.43s	29d	13m	55.50s		-18.53	-20.39	
A 1878	14h	12m	47.82s	29d	13m	53.40s		-21.69	-20.68	S
A 1878	14h	12m	53.32s	29d	13m	47.00s		-18.37	-18.29	
A 1878	14h	12m	54.23s	29d	13m	57.60s		-20.23	-20.50	S
A 1878	14h	12m	50.11s	29d	13m	59.90s		-18.63	-19.32	
A 1878	14h	12m	49.97s	29d	14m	02.60s		-20.45	-19.30	S
A 1878	14h	12m	56.80s	29d	14m	03.60s		-20.38	-20.06	I
A 1878	14h	12m	54.78s	29d	14m	03.90s		-18.55	-17.39	
A 1878	14h	12m	47.17s	29d	14m	05.80s		-20.04	-19.70	I
A 1878	14h	12m	49.47s	29d	14m	09.90s		-21.57	-20.53	S
A 1878	14h	12m	49.03s	29d	14m	07.80s		-18.94	-21.00	
A 1878	14h	12m	52.50s	29d	14m	11.40s		-20.94	-20.28	S
A 1878	14h	12m	54.85s	29d	14m	17.30s		-19.91	-19.67	S
A 1878	14h	12m	54.65s	29d	14m	23.80s		-19.23	-19.19	
A 1878	14h	12m	47.85s	29d	14m	17.10s		-19.70	-18.95	
A 1878	14h	12m	54.15s	29d	14m	19.30s		-20.80	-19.49	E
A 1878	14h	12m	52.75s	29d	14m	20.20s		-18.72	-20.18	
A 1878	14h	12m	52.18s	29d	14m	28.40s	0.2220	-22.36	-21.69	E
A 1878	14h	12m	46.85s	29d	14m	26.40s		-21.02	-20.50	I
A 1878	14h	12m	54.72s	29d	14m	31.90s		-21.42	-20.23	E
A 1878	14h	12m	56.29s	29d	14m	31.40s		-20.24	-19.80	I
A 1878	14h	12m	51.24s	29d	14m	48.20s		-20.10	-20.01	S
A 1878	14h	12m	51.04s	29d	14m	39.30s		-19.72	-20.22	
A 1878	14h	12m	50.98s	29d	14m	42.30s		-20.84	-21.55	I
A 1878	14h	12m	46.74s	29d	14m	40.00s		-18.44	-18.10	
A 1878	14h	12m	53.29s	29d	14m	41.40s		-20.30	-20.22	
A 1878	14h	12m	53.32s	29d	14m	44.60s		-19.55	-21.50	
A 1878	14h	12m	49.12s	29d	14m	42.50s		-21.38	-20.33	S
A 1878	14h	12m	50.12s	29d	14m	47.30s		-20.40	-19.13	S0
A 1878	14h	12m	52.25s	29d	14m	53.70s		-20.41	-20.57	S
A 1878	14h	12m	51.99s	29d	14m	57.10s		-19.53	-19.92	
A 1878	14h	12m	50.96s	29d	14m	56.60s		-21.29	-20.33	S
A 1878	14h	12m	46.14s	29d	14m	55.60s		-19.94	-19.35	S0
A 1878	14h	12m	46.58s	29d	14m	59.10s		-20.94	-19.69	S0
A 1878	14h	12m	53.29s	29d	14m	56.90s		-18.53	-17.55	
A 1878	14h	12m	48.23s	29d	15m	01.10s		-19.28	-18.27	
A 1878	14h	12m	50.01s	29d	15m	05.00s		-18.23	-17.10	

A 1878	14h	12m	56.61s	29d	15m	05.30s	-19.18	-19.30	
A 1878	14h	12m	49.37s	29d	15m	12.10s	-18.79	-17.72	
A 1878	14h	12m	50.60s	29d	15m	13.20s	-18.64	-18.42	
A 1878	14h	12m	49.68s	29d	15m	14.20s	-19.56	-19.22	
A 1878	14h	12m	55.12s	29d	15m	14.70s	-18.85	-17.83	
A 1878	14h	12m	51.24s	29d	15m	22.10s	-19.89	-19.95	S
A 1878	14h	12m	53.39s	29d	15m	22.30s	-19.01	-18.65	
A 1878	14h	12m	51.04s	29d	15m	28.90s	-19.51	-21.46	
A 1878	14h	12m	53.49s	29d	15m	27.70s	-18.76	-18.14	
A 1878	14h	12m	52.60s	29d	15m	41.10s	-18.61	-18.01	
A 1878	14h	12m	52.43s	29d	15m	48.70s	-21.00	-19.79	S0
A 1878	14h	12m	55.73s	29d	15m	56.70s	-18.18	-17.32	
A 1878	14h	12m	53.61s	29d	16m	00.80s	-19.77	-18.60	
A 1878	14h	12m	53.04s	29d	16m	07.40s	-18.86	-21.15	
A 1878	14h	12m	47.96s	29d	16m	09.50s	-19.69	-19.16	
A 1878	14h	13m	00.54s	29d	13m	56.90s	-21.15	-20.41	S0
A 1878	14h	12m	56.76s	29d	14m	03.60s	-20.00	-20.14	I
A 1878	14h	12m	56.78s	29d	12m	00.30s	-19.87	-18.86	S0
A 1878	14h	12m	57.80s	29d	12m	01.60s	-20.47	-19.97	S0
A 1878	14h	12m	59.05s	29d	12m	14.40s	-20.60	-20.01	E
A 1878	14h	12m	59.84s	29d	12m	19.50s	-20.45	-21.96	S
A 1878	14h	13m	00.58s	29d	12m	22.90s	-20.30	-19.90	S
A 1878	14h	13m	01.89s	29d	12m	17.50s	-19.55	-18.93	S
A 1878	14h	13m	05.79s	29d	12m	20.80s	-18.24	-18.48	
A 1878	14h	12m	58.97s	29d	12m	33.00s	-18.13	-17.07	
A 1878	14h	13m	01.29s	29d	12m	36.90s	-20.97	-20.65	S0
A 1878	14h	13m	05.52s	29d	12m	36.60s	-18.59	-18.07	
A 1878	14h	13m	02.23s	29d	12m	40.50s	-18.23	-18.12	
A 1878	14h	13m	05.38s	29d	12m	42.80s	-18.24	-17.75	
A 1878	14h	12m	58.42s	29d	12m	53.60s	-18.05	-19.13	
A 1878	14h	12m	58.26s	29d	12m	54.90s	-19.49	-20.04	
A 1878	14h	13m	05.59s	29d	12m	54.20s	-20.53	-19.81	E
A 1878	14h	13m	04.82s	29d	12m	55.40s	-19.03	-18.41	
A 1878	14h	13m	02.81s	29d	12m	55.70s	-19.44	-18.73	S
A 1878	14h	12m	58.70s	29d	12m	56.60s	-18.92	-18.15	
A 1878	14h	13m	04.41s	29d	13m	00.70s	-20.06	-19.78	S
A 1878	14h	12m	55.45s	29d	13m	04.30s	-19.48	-19.63	I
A 1878	14h	12m	55.11s	29d	13m	09.90s	-19.13	-19.64	
A 1878	14h	12m	57.07s	29d	13m	19.80s	-18.08	-18.08	
A 1878	14h	12m	57.65s	29d	13m	22.20s	-18.09	-17.93	
A 1878	14h	13m	00.40s	29d	13m	37.50s	-19.13	-18.71	
A 1878	14h	12m	57.01s	29d	13m	43.90s	-19.27	-18.62	
A 1878	14h	12m	57.70s	29d	13m	48.90s	-19.78	-19.18	S0
A 1878	14h	13m	03.99s	29d	13m	53.50s	-19.36	-19.74	
A 1878	14h	13m	02.65s	29d	14m	01.20s	-18.08	-18.25	
A 1952	14h	41m	07.84s	28d	38m	29.40s	-22.05	-21.10	E

A 1952	14h	40m	59.08s	28d	38m	35.40s	-20.11	-19.24	S
A 1952	14h	41m	01.82s	28d	35m	57.10s	-20.13	-19.75	S
A 1952	14h	40m	59.60s	28d	36m	07.40s	-19.18	-18.44	
A 1952	14h	41m	02.64s	28d	36m	14.50s	-18.79	-18.40	
A 1952	14h	41m	01.57s	28d	36m	31.50s	-18.30	-18.20	
A 1952	14h	40m	59.42s	28d	36m	42.00s	-19.05	-18.36	
A 1952	14h	41m	04.07s	28d	36m	47.50s	-19.94	-19.04	E
A 1952	14h	41m	04.47s	28d	36m	49.70s	-18.71	-20.59	
A 1952	14h	41m	01.82s	28d	37m	09.60s	-18.17	-20.22	
A 1952	14h	41m	01.92s	28d	37m	14.50s	-20.76	-20.80	E
A 1952	14h	41m	02.66s	28d	37m	10.00s	-22.11	-21.94	S0
A 1952	14h	41m	03.13s	28d	37m	10.10s	-21.41	-20.84	E
A 1952	14h	41m	02.67s	28d	37m	02.40s	-20.63	-19.99	
A 1952	14h	40m	58.41s	28d	36m	52.50s	-19.89	-19.03	S0
A 1952	14h	41m	01.19s	28d	37m	00.50s	-21.20	-20.33	E
A 1952	14h	40m	59.94s	28d	37m	22.10s	-18.59	-17.95	
A 1952	14h	40m	59.55s	28d	37m	34.20s	-18.29	-17.81	
A 1952	14h	41m	01.81s	28d	37m	34.70s	-19.48	-18.91	
A 1952	14h	41m	01.58s	28d	37m	48.30s	-18.21	-20.37	
A 1952	14h	41m	01.32s	28d	37m	43.20s	-21.57	-21.82	E
A 1952	14h	41m	01.53s	28d	37m	44.30s	-19.21	-18.96	
A 1952	14h	40m	59.15s	28d	37m	47.80s	-18.93	-20.67	
A 1952	14h	40m	59.50s	28d	37m	48.80s	-19.90	-19.01	
A 1952	14h	40m	58.98s	28d	37m	51.40s	-18.41	-18.51	
A 1952	14h	41m	03.17s	28d	37m	52.50s	-18.10	-17.71	
A 1952	14h	40m	59.94s	28d	38m	00.10s	-20.38	-19.53	E
A 1952	14h	41m	08.82s	28d	37m	59.00s	-19.72	-19.04	E
A 1952	14h	41m	05.82s	28d	38m	02.20s	-18.68	-17.82	
A 1952	14h	41m	00.90s	28d	38m	04.70s	-19.54	-18.59	
A 1952	14h	41m	04.06s	28d	38m	08.40s	-19.13	-19.23	
A 1952	14h	41m	07.98s	28d	38m	09.40s	-19.08	-18.20	
A 1952	14h	41m	03.17s	28d	38m	21.10s	-18.04	-18.15	
A 1952	14h	41m	05.43s	28d	38m	21.80s	-19.11	-18.99	
A 1952	14h	41m	02.63s	28d	35m	50.80s	-18.52	-18.54	
A 1952	14h	40m	59.43s	28d	38m	27.20s	-19.17	-19.37	
A 1952	14h	41m	01.91s	28d	35m	54.80s	-19.06	-20.83	
A 1952	14h	40m	59.20s	28d	38m	24.20s	-19.32	-18.60	
A 1952	14h	41m	13.59s	28d	37m	29.60s	-22.13	-21.43	S0
A 1952	14h	41m	05.84s	28d	37m	41.60s	-20.22	-19.27	
A 1952	14h	41m	14.94s	28d	37m	42.60s	-21.80	-20.98	S0
A 1952	14h	41m	05.68s	28d	37m	46.70s	-18.22	-18.33	
A 1952	14h	41m	08.53s	28d	37m	49.00s	-19.26	-19.18	
A 1952	14h	41m	03.16s	28d	37m	52.20s	-18.08	-17.86	
A 1952	14h	41m	15.18s	28d	35m	29.10s	-18.16	-20.08	
A 1952	14h	41m	15.04s	28d	35m	21.20s	-19.32	-21.52	
A 1952	14h	41m	15.18s	28d	35m	24.30s	-19.61	-21.59	

A 1952	14h	41m	03.94s	28d	35m	21.30s	-20.35	-19.38	E
A 1952	14h	41m	13.55s	28d	35m	21.80s	-19.77	-19.72	
A 1952	14h	41m	05.92s	28d	35m	29.90s	-20.77	-19.82	S0
A 1952	14h	41m	08.36s	28d	35m	28.50s	-18.46	-18.64	
A 1952	14h	41m	08.59s	28d	35m	30.80s	-19.01	-19.42	
A 1952	14h	41m	08.51s	28d	35m	32.50s	-20.41	-20.52	S
A 1952	14h	41m	04.76s	28d	35m	32.40s	-19.40	-19.16	
A 1952	14h	41m	07.83s	28d	35m	32.30s	-18.39	-20.48	
A 1952	14h	41m	07.59s	28d	35m	35.00s	-21.58	-21.23	S
A 1952	14h	41m	11.01s	28d	35m	33.00s	-19.87	-18.93	
A 1952	14h	41m	10.10s	28d	35m	33.70s	-19.03	-18.15	
A 1952	14h	41m	05.91s	28d	35m	38.50s	-19.36	-18.50	
A 1952	14h	41m	08.19s	28d	35m	44.50s	-21.61	-20.93	S0
A 1952	14h	41m	03.56s	28d	35m	44.20s	-19.69	-19.45	
A 1952	14h	41m	13.72s	28d	35m	54.10s	-18.37	-18.45	
A 1952	14h	41m	13.55s	28d	35m	52.00s	-18.78	-21.38	
A 1952	14h	41m	03.27s	28d	35m	56.30s	-19.34	-18.51	
A 1952	14h	41m	08.00s	28d	36m	03.20s	-18.96	-18.97	
A 1952	14h	41m	09.73s	28d	36m	02.80s	-18.20	-17.44	
A 1952	14h	41m	05.67s	28d	36m	05.30s	-18.64	-17.72	
A 1952	14h	41m	12.15s	28d	36m	07.00s	-19.45	-18.73	
A 1952	14h	41m	10.72s	28d	36m	07.50s	-18.10	-18.28	
A 1952	14h	41m	14.47s	28d	36m	26.20s	-19.86	-19.18	
A 1952	14h	41m	05.45s	28d	36m	26.40s	-18.40	-17.58	
A 1952	14h	41m	04.06s	28d	36m	26.50s	-18.06	-20.09	
A 1952	14h	41m	04.22s	28d	36m	27.80s	-18.35	-19.37	
A 1952	14h	41m	12.94s	28d	36m	27.30s	-19.29	-18.61	
A 1952	14h	41m	06.81s	28d	36m	31.50s	-20.01	-21.90	E
A 1952	14h	41m	07.10s	28d	36m	37.30s	-20.67	-20.27	E
A 1952	14h	41m	07.03s	28d	36m	39.20s	-22.10	-22.55	S0
A 1952	14h	41m	03.36s	28d	36m	37.10s	-20.43	-19.40	E
A 1952	14h	41m	14.04s	28d	36m	40.80s	-18.80	-18.92	
A 1952	14h	41m	03.11s	28d	36m	46.60s	-20.74	-19.93	S0
A 1952	14h	41m	04.07s	28d	36m	52.70s	-19.32	-20.90	
A 1952	14h	41m	03.57s	28d	37m	00.30s	-22.61	-24.23	E
A 1952	14h	41m	03.14s	28d	36m	57.00s	-19.55	-21.16	
A 1952	14h	41m	10.75s	28d	36m	47.30s	-19.16	-21.67	
A 1952	14h	41m	06.34s	28d	37m	01.30s	-18.75	-18.04	
A 1952	14h	41m	06.48s	28d	37m	06.90s	-20.14	-19.23	
A 1952	14h	41m	08.25s	28d	37m	13.80s	-21.85	-21.21	S
A 1952	14h	41m	12.33s	28d	37m	11.00s	-19.03	-19.11	
A 1952	14h	41m	06.26s	28d	37m	12.20s	-18.15	-17.28	
A 1952	14h	41m	09.40s	28d	37m	13.00s	-18.55	-18.59	
A 1952	14h	41m	09.72s	28d	37m	17.80s	-19.85	-20.07	S
A 1952	14h	41m	05.02s	28d	37m	34.90s	-18.05	-20.08	
A 1952	14h	41m	06.27s	28d	37m	27.50s	-20.01	-20.84	S0

A 1952	14h	41m	05.49s	28d	37m	33.90s		-19.02	-21.47	
A 1952	14h	41m	05.32s	28d	37m	35.90s		-19.18	-20.34	
A 1952	14h	41m	04.78s	28d	37m	31.60s		-19.79	-21.64	
A 1952	14h	41m	04.76s	28d	37m	35.50s		-19.83	-19.94	
A 1952	14h	41m	04.77s	28d	35m	05.50s		-18.30	-18.55	
A 1952	14h	41m	06.32s	28d	37m	18.30s		-18.30	-17.78	
A 1952	14h	41m	14.57s	28d	37m	18.70s		-19.65	-19.37	
A 1952	14h	41m	11.82s	28d	37m	19.30s		-18.39	-18.59	
A 1952	14h	41m	07.53s	28d	37m	23.60s		-19.14	-18.20	
A 1952	14h	41m	04.29s	28d	37m	23.00s		-18.54	-18.27	
A 1952	14h	41m	05.23s	28d	35m	06.80s		-19.10	-18.75	
A 1952	14h	41m	03.35s	28d	37m	29.50s		-20.17	-19.26	
A 1952	14h	41m	06.39s	28d	37m	33.60s		-18.12	-17.60	
A 1952	14h	41m	12.23s	28d	35m	06.70s		-19.05	-18.27	
A 1952	14h	41m	08.44s	28d	35m	09.00s		-18.39	-17.78	
A 1952	14h	41m	05.36s	28d	37m	40.50s		-18.42	-17.71	
A 1952	14h	41m	10.78s	28d	35m	12.30s		-18.24	-18.05	
A 1952	14h	41m	13.01s	28d	35m	15.30s		-19.08	-19.23	
A 1952	14h	41m	10.45s	28d	35m	16.60s		-19.36	-19.26	
A 1952	14h	41m	14.88s	28d	35m	29.70s		-18.45	-19.98	
A 2111	15h	39m	35.52s	34d	26m	56.20s		-20.46	-19.56	S
A 2111	15h	39m	37.64s	34d	27m	03.80s	0.2295	-21.26	-20.22	S0
A 2111	15h	39m	31.84s	34d	27m	05.10s		-19.01	-18.09	
A 2111	15h	39m	38.48s	34d	24m	32.40s		-19.37	-18.96	
A 2111	15h	39m	40.16s	34d	24m	18.10s		-19.38	-18.33	
A 2111	15h	39m	39.34s	34d	24m	44.50s		-20.26	-19.31	E
A 2111	15h	39m	38.45s	34d	24m	51.40s		-20.02	-19.08	
A 2111	15h	39m	40.16s	34d	24m	55.70s		-20.49	-19.27	S0
A 2111	15h	39m	42.76s	34d	24m	56.60s		-18.32	-17.38	
A 2111	15h	39m	37.84s	34d	24m	57.00s		-18.55	-17.54	
A 2111	15h	39m	39.81s	34d	25m	00.50s		-18.06	-17.79	
A 2111	15h	39m	37.21s	34d	25m	08.50s		-19.67	-18.70	S
A 2111	15h	39m	40.49s	34d	25m	27.30s	0.2282	-22.67	-21.51	E
A 2111	15h	39m	39.75s	34d	25m	23.10s		-19.57	-18.85	
A 2111	15h	39m	39.20s	34d	25m	11.50s		-21.13	-20.38	E
A 2111	15h	39m	39.39s	34d	25m	13.40s	0.2211	-21.34	-20.61	E
A 2111	15h	39m	36.23s	34d	25m	12.10s		-20.34	-19.21	S0
A 2111	15h	39m	34.90s	34d	25m	14.50s		-18.97	-18.02	
A 2111	15h	39m	40.27s	34d	25m	34.80s		-20.07	-21.06	
A 2111	15h	39m	38.15s	34d	25m	18.10s		-20.21	-19.01	S0
A 2111	15h	39m	37.53s	34d	25m	18.70s		-19.62	-18.72	S
A 2111	15h	39m	36.64s	34d	25m	29.00s		-18.96	-18.34	
A 2111	15h	39m	33.61s	34d	25m	34.00s		-18.48	-17.78	
A 2111	15h	39m	36.79s	34d	25m	39.10s	0.2312	-20.90	-19.65	S0
A 2111	15h	39m	39.69s	34d	25m	21.20s		-20.40	-19.70	
A 2111	15h	39m	31.27s	34d	25m	40.00s		-20.24	-19.65	

A 2111	15h	39m	38.68s	34d	25m	38.90s		-18.16	-17.04	
A 2111	15h	39m	37.29s	34d	25m	45.90s		-18.49	-17.33	
A 2111	15h	39m	36.42s	34d	25m	50.10s		-20.46	-19.50	E
A 2111	15h	39m	41.20s	34d	25m	50.90s		-20.53	-19.36	S0
A 2111	15h	39m	40.18s	34d	25m	50.80s		-18.60	-17.90	
A 2111	15h	39m	33.99s	34d	25m	51.30s		-19.30	-18.23	
A 2111	15h	39m	37.44s	34d	25m	54.80s		-20.12	-18.98	E
A 2111	15h	39m	39.52s	34d	25m	56.90s		-19.23	-18.23	
A 2111	15h	39m	39.91s	34d	25m	57.20s		-18.53	-17.69	
A 2111	15h	39m	41.69s	34d	26m	01.70s		-18.03	-16.89	
A 2111	15h	39m	31.72s	34d	26m	07.20s		-20.49	-19.37	S0
A 2111	15h	39m	36.84s	34d	26m	07.20s		-20.44	-19.68	I
A 2111	15h	39m	38.07s	34d	26m	09.50s		-18.64	-19.00	
A 2111	15h	39m	34.11s	34d	26m	19.20s		-20.80	-20.58	S
A 2111	15h	39m	34.26s	34d	26m	12.50s	0.2289	-21.97	-21.11	S0
A 2111	15h	39m	38.18s	34d	26m	06.90s		-19.72	-19.53	
A 2111	15h	39m	32.26s	34d	26m	12.80s		-19.25	-18.22	
A 2111	15h	39m	38.58s	34d	26m	28.20s		-20.23	-19.24	S
A 2111	15h	39m	39.03s	34d	26m	38.10s		-19.29	-19.48	
A 2111	15h	39m	38.70s	34d	26m	38.80s	0.2246	-20.85	-20.29	S
A 2111	15h	39m	37.81s	34d	26m	35.90s		-18.12	-17.73	
A 2111	15h	39m	31.99s	34d	26m	36.10s		-18.39	-18.00	
A 2111	15h	39m	35.47s	34d	26m	43.70s		-20.70	-19.87	S0
A 2111	15h	39m	41.19s	34d	26m	41.30s		-20.27	-20.24	I
A 2111	15h	39m	40.90s	34d	26m	45.40s		-19.28	-19.45	
A 2111	15h	39m	37.59s	34d	26m	44.20s		-18.92	-18.91	
A 2111	15h	39m	33.13s	34d	26m	45.60s		-19.25	-18.91	
A 2111	15h	39m	37.16s	34d	26m	45.70s		-18.26	-17.93	
A 2111	15h	39m	38.38s	34d	26m	50.50s		-18.01	-17.13	
A 2111	15h	39m	32.78s	34d	24m	22.40s		-19.21	-18.31	
A 2111	15h	39m	41.34s	34d	24m	34.30s	0.2294	-20.97	-20.81	S
A 2111	15h	39m	41.81s	34d	24m	42.70s	0.2292	-22.61	-22.18	E
A 2111	15h	39m	42.27s	34d	24m	40.40s		-19.08	-20.81	
A 2111	15h	39m	41.26s	34d	24m	43.60s		-20.43	-22.04	S
A 2111	15h	39m	47.09s	34d	27m	37.90s	0.2368	-21.25	-20.57	S0
A 2111	15h	39m	42.81s	34d	27m	44.60s		-19.68	-19.55	I
A 2111	15h	39m	52.99s	34d	27m	48.60s	0.2297	-20.98	-19.94	S0
A 2111	15h	39m	54.29s	34d	25m	06.60s		-18.05	-17.24	
A 2111	15h	39m	51.92s	34d	25m	18.80s		-18.85	-18.83	
A 2111	15h	39m	44.40s	34d	25m	22.70s		-19.46	-19.41	
A 2111	15h	39m	44.15s	34d	25m	21.30s		-18.78	-20.66	
A 2111	15h	39m	54.03s	34d	25m	24.60s		-18.87	-18.31	
A 2111	15h	39m	53.10s	34d	25m	26.50s		-18.75	-17.73	
A 2111	15h	39m	47.96s	34d	25m	32.10s		-20.49	-19.52	E
A 2111	15h	39m	52.98s	34d	25m	41.10s		-19.31	-18.24	
A 2111	15h	39m	43.94s	34d	25m	46.70s		-19.45	-19.01	

A 2111	15h	39m	42.69s	34d	25m	52.10s		-18.13	-16.99	
A 2111	15h	39m	42.04s	34d	26m	04.00s		-19.44	-18.39	
A 2111	15h	39m	42.02s	34d	25m	59.60s		-18.96	-20.78	
A 2111	15h	39m	44.85s	34d	25m	58.50s		-19.19	-19.08	
A 2111	15h	39m	47.82s	34d	26m	00.00s		-19.08	-18.05	
A 2111	15h	39m	53.40s	34d	25m	59.60s		-18.94	-18.56	
A 2111	15h	39m	52.50s	34d	26m	02.20s		-20.40	-19.62	S
A 2111	15h	39m	47.49s	34d	26m	11.10s		-18.84	-18.00	
A 2111	15h	39m	42.59s	34d	26m	14.00s		-19.82	-18.96	
A 2111	15h	39m	43.06s	34d	26m	23.00s		-18.42	-17.36	
A 2111	15h	39m	42.02s	34d	26m	30.30s	0.2258	-22.09	-20.96	E
A 2111	15h	39m	43.25s	34d	26m	32.90s		-19.02	-18.04	
A 2111	15h	39m	48.31s	34d	26m	36.70s		-18.79	-18.43	
A 2111	15h	39m	49.35s	34d	26m	41.50s	0.2299	-21.54	-21.03	S
A 2111	15h	39m	50.11s	34d	26m	44.40s		-19.48	-19.02	
A 2111	15h	39m	52.85s	34d	26m	46.80s		-20.45	-19.95	E
A 2111	15h	39m	42.09s	34d	26m	49.20s		-19.55	-18.52	
A 2111	15h	39m	45.75s	34d	26m	57.40s	0.2292	-21.07	-20.05	E
A 2111	15h	39m	42.98s	34d	27m	00.30s		-18.40	-18.28	
A 2111	15h	39m	42.30s	34d	27m	02.60s		-18.20	-17.92	
A 2111	15h	39m	52.55s	34d	27m	07.50s		-19.06	-20.58	
A 2111	15h	39m	52.04s	34d	27m	07.60s		-19.01	-21.29	
A 2111	15h	39m	52.15s	34d	27m	12.20s		-21.13	-21.23	S
A 2111	15h	39m	42.28s	34d	27m	17.10s		-20.12	-19.17	
A 2111	15h	39m	51.51s	34d	27m	31.30s		-19.54	-18.61	
A 2111	15h	39m	48.27s	34d	27m	34.80s		-18.70	-18.45	
A 2111	15h	39m	47.70s	34d	25m	16.40s		-19.85	-18.96	
A 2111	15h	39m	47.89s	34d	27m	39.90s		-20.28	-19.32	E
A 2111	15h	39m	47.34s	34d	25m	10.20s	0.2309	-21.07	-20.81	E
A 2111	15h	39m	47.26s	34d	25m	15.90s		-20.43	-20.38	S
A 2658	23h	44m	47.99s	-12d	18m	46.20s		-19.12	-18.24	
A 2658	23h	44m	55.21s	-12d	18m	37.00s		-18.98	-18.20	
A 2658	23h	44m	49.55s	-12d	18m	34.40s		-19.65	-18.99	
A 2658	23h	44m	49.62s	-12d	18m	31.90s		-18.68	-18.01	
A 2658	23h	44m	50.35s	-12d	18m	25.50s		-21.89	-21.06	S
A 2658	23h	44m	49.13s	-12d	18m	19.80s		-19.29	-18.34	
A 2658	23h	44m	47.27s	-12d	18m	13.40s		-19.24	-19.14	
A 2658	23h	44m	46.97s	-12d	18m	10.40s		-20.94	-20.12	S0
A 2658	23h	44m	49.36s	-12d	18m	07.90s		-18.44	-17.53	
A 2658	23h	44m	52.22s	-12d	18m	04.60s		-19.99	-18.90	E
A 2658	23h	44m	54.99s	-12d	18m	05.60s		-18.08	-17.23	
A 2658	23h	44m	54.27s	-12d	17m	59.30s		-21.42	-20.39	E
A 2658	23h	44m	50.42s	-12d	17m	56.40s		-19.39	-18.41	
A 2658	23h	44m	51.64s	-12d	17m	53.30s		-18.71	-18.11	
A 2658	23h	44m	47.44s	-12d	17m	47.40s		-20.92	-19.87	E
A 2658	23h	44m	50.34s	-12d	17m	32.70s		-18.84	-20.30	

A 2658	23h	44m	49.28s	-12d	17m	38.20s	-18.19	-19.65	
A 2658	23h	44m	50.26s	-12d	17m	20.90s	-21.07	-20.35	S0
A 2658	23h	44m	49.84s	-12d	17m	26.70s	-21.32	-20.95	E
A 2658	23h	44m	49.80s	-12d	17m	39.50s	-22.39	-22.02	E
A 2658	23h	44m	54.96s	-12d	17m	38.80s	-18.80	-18.35	
A 2658	23h	44m	55.87s	-12d	17m	37.60s	-18.22	-17.40	
A 2658	23h	44m	51.86s	-12d	17m	35.30s	-19.57	-18.55	
A 2658	23h	44m	47.85s	-12d	17m	31.10s	-18.14	-17.23	
A 2658	23h	44m	50.96s	-12d	17m	19.10s	-20.24	-19.17	E
A 2658	23h	44m	55.84s	-12d	17m	17.60s	-20.18	-19.15	S0
A 2658	23h	44m	51.40s	-12d	17m	11.00s	-18.35	-18.28	
A 2658	23h	44m	56.18s	-12d	17m	07.50s	-21.14	-20.31	S
A 2658	23h	44m	51.13s	-12d	16m	48.00s	-20.61	-19.49	E
A 2658	23h	44m	46.13s	-12d	16m	49.10s	-18.82	-18.35	
A 2658	23h	44m	49.65s	-12d	16m	35.80s	-20.56	-19.43	S0
A 2658	23h	44m	47.99s	-12d	16m	36.20s	-18.29	-17.66	
A 2658	23h	44m	51.63s	-12d	16m	28.80s	-18.70	-17.79	
A 2658	23h	44m	53.27s	-12d	16m	23.60s	-18.27	-17.77	

Appendix B

Surface Brightness Fit of the NOT clusters galaxies

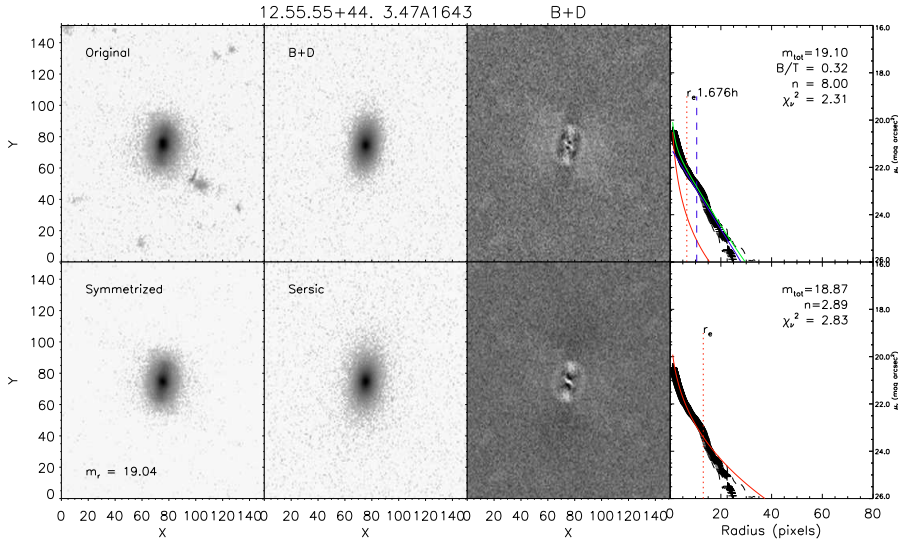

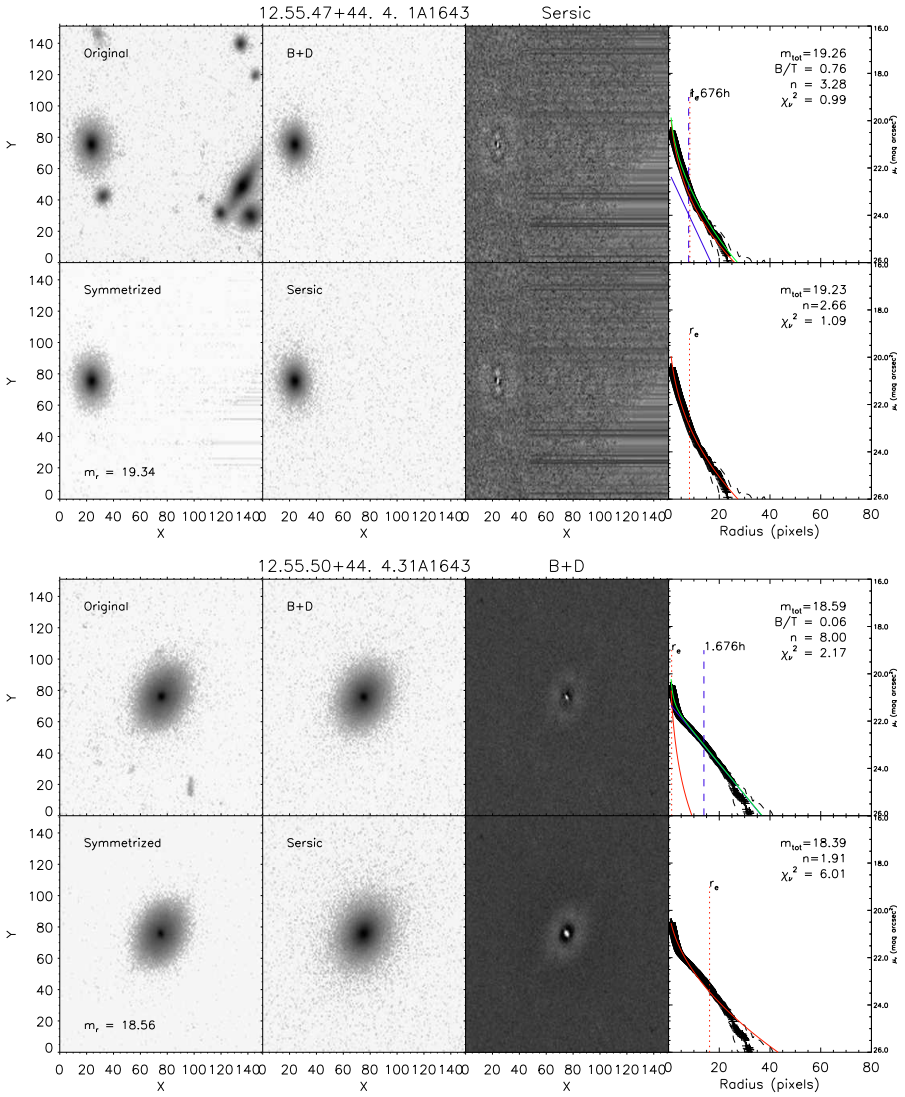
12.55.47+44. 4. 1A1643
Sersic
Original
B+D
Symmetrized
Sersic
m_r = 19.34
m_tot=19.26
B/T = 0.76
n = 3.28
χ_ν² = 0.99
r_e
1.676h
m_tot=19.23
n=2.66
χ_ν² = 1.09
X
Y
Radius (pixels)
12.55.50+44. 4.31A1643
B+D
Original
B+D
Symmetrized
Sersic
m_r = 18.56
m_tot=18.59
B/T = 0.06
n = 8.00
χ_ν² = 2.17
r_e
1.676h
m_tot=18.39
n=1.91
χ_ν² = 6.01
r_e
X
Y
Radius (pixels)

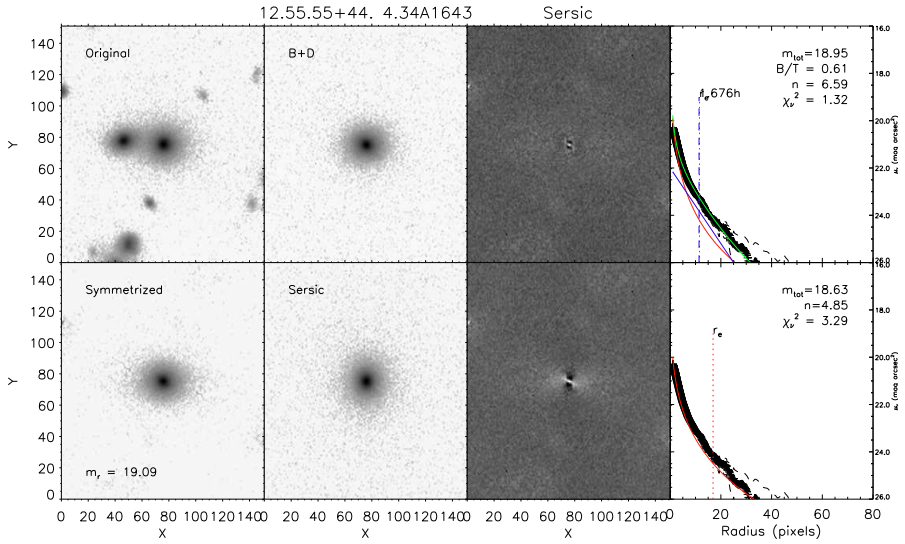
12.55.55+44. 4.34A1643
Sersic
Original
B+D
Symmetrized
Sersic
m_r = 19.09
m_tot=18.95
B/T = 0.61
n = 6.59
χ_ν² = 1.32
r_e.676h
m_tot=18.63
n=4.85
χ_ν² = 3.29
r_e
X
Y
Radius (pixels)

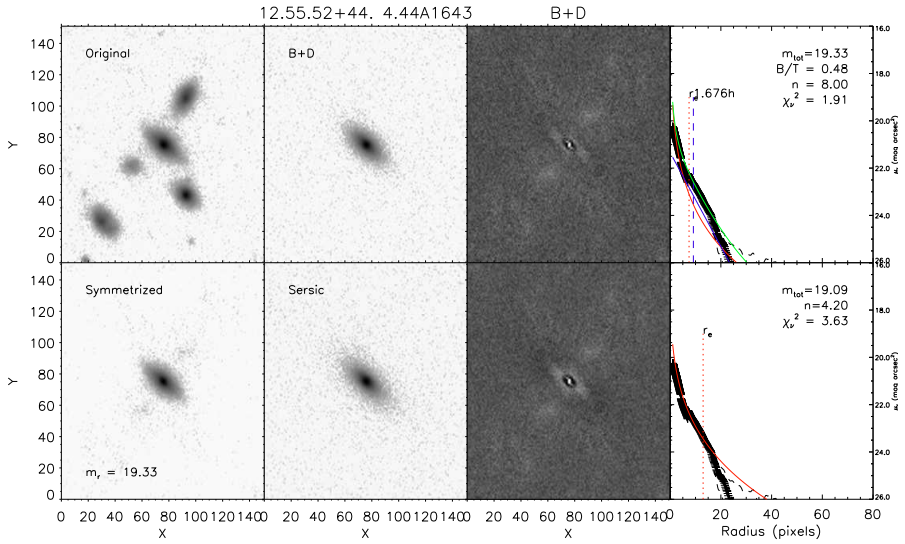
12.55.52+44. 4.44A1643
B+D
Original
B+D
Symmetrized
Sersic
m_r = 19.33
m_tot=19.33
B/T = 0.48
n = 8.00
χ_ν² = 1.91
r_e.676h
m_tot=19.09
n=4.20
χ_ν² = 3.63
r_e
X
Y
Radius (pixels)

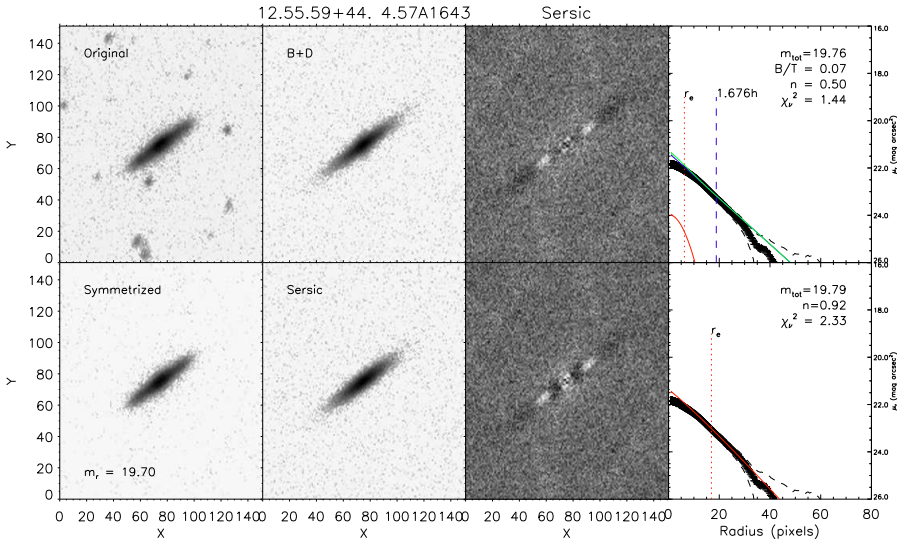
12.55.59+44. 4.57A1643
Sersic
Original
B+D
Symmetrized
Sersic
m_r = 19.70
m_tot=19.76
B/T = 0.07
n = 0.50
χ_ν² = 1.44
1.676h
m_tot=19.79
n=0.92
χ_ν² = 2.33
X
Y
Radius (pixels)

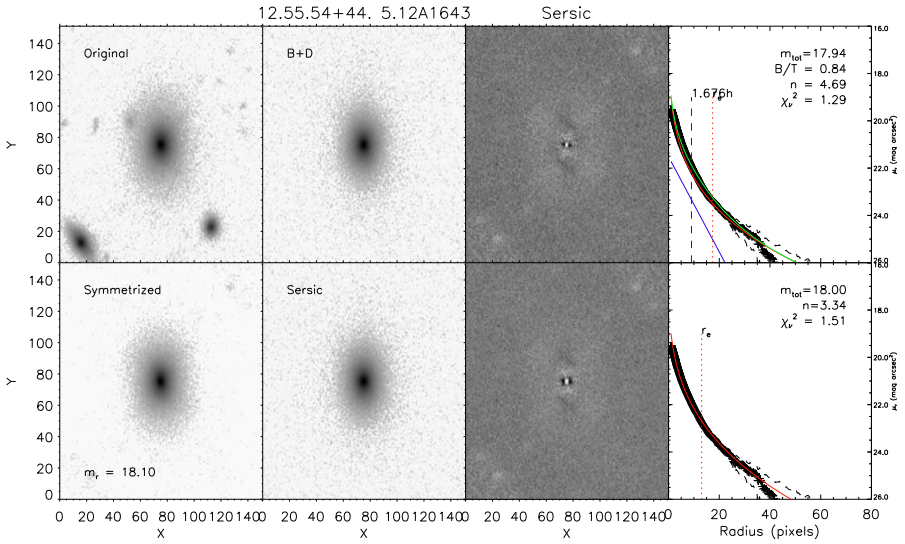
12.55.54+44. 5.12A1643
Sersic
Original
B+D
Symmetrized
Sersic
m_r = 18.10
m_tot=17.94
B/T = 0.84
n = 4.69
χ_ν² = 1.29
1.676h
m_tot=18.00
n=3.34
χ_ν² = 1.51
X
Y
Radius (pixels)

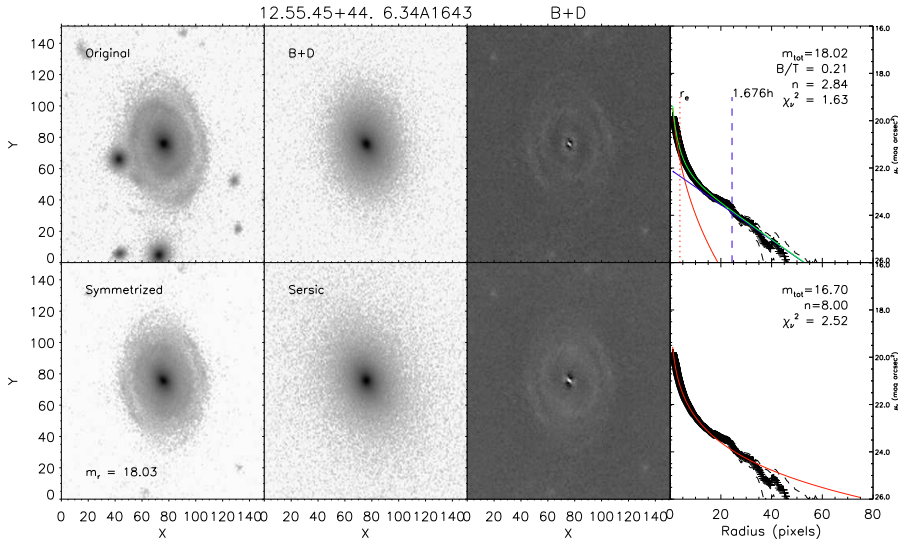
12.55.45+44. 6.34A1643
B+D
Original
B+D
Symmetrized
Sersic
m_r = 18.03
m_tot=18.02
B/T = 0.21
n = 2.84
χ_ν² = 1.63
1.676h
m_tot=16.70
n=8.00
χ_ν² = 2.52
X
Y
Radius (pixels)

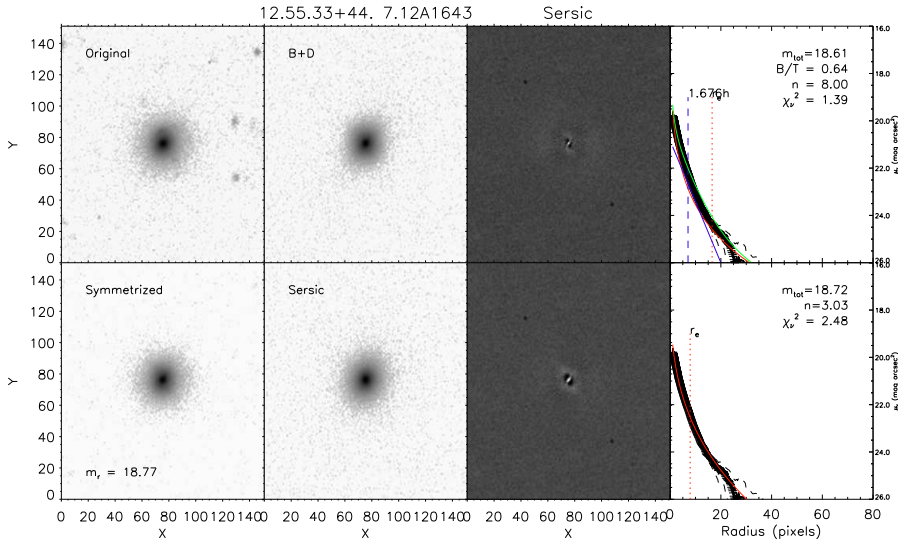
12.55.33+44. 7.12A1643
Sersic
Original
B+D
Symmetrized
Sersic
m_r = 18.77
m_tot=18.61
B/T = 0.64
n = 8.00
χ_ν² = 1.39
1.676h
m_tot=18.72
n=3.03
χ_ν² = 2.48
X
Y
Radius (pixels)

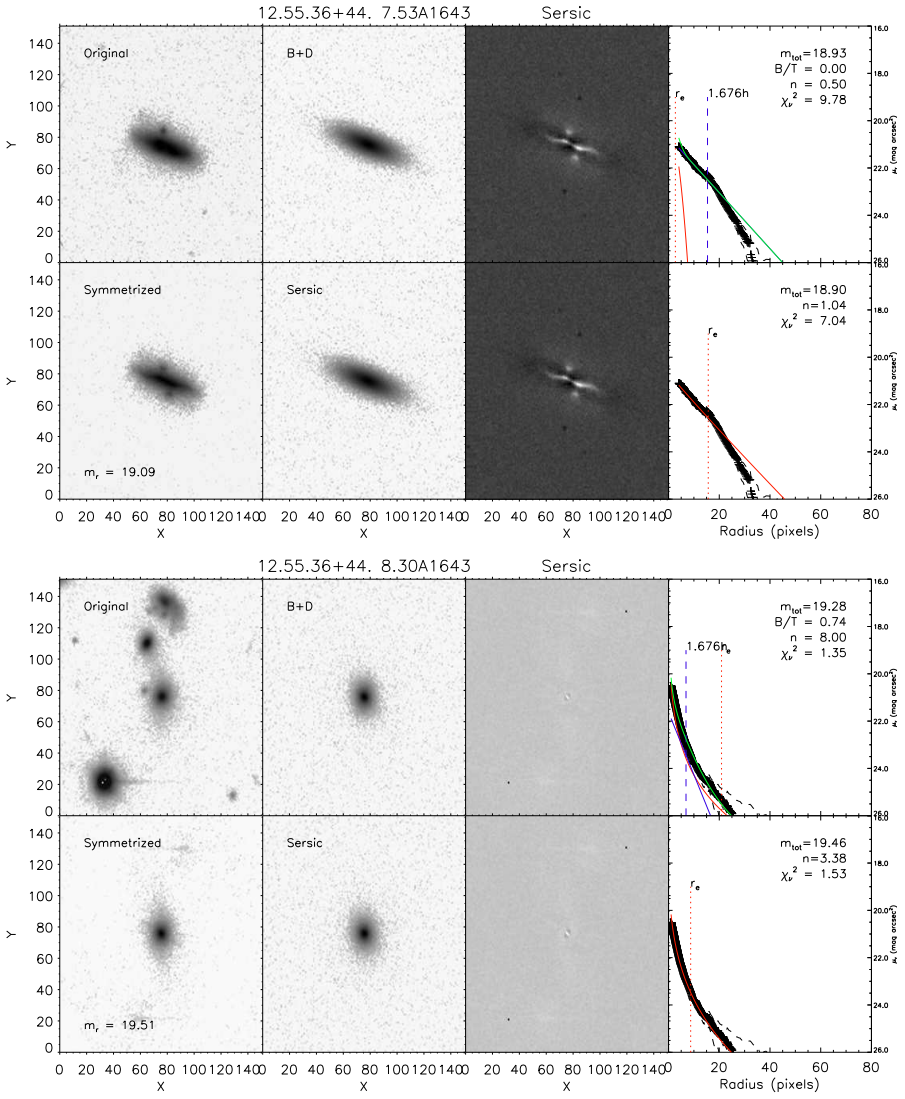
12.55.36+44. 7.53A1643
Sersic
Original
B+D
Symmetrized
Sersic
m_r = 19.09
m_tot=18.93
B/T = 0.00
n = 0.50
χ_ν² = 9.78
1.676h
m_tot=18.90
n=1.04
χ_ν² = 7.04
12.55.36+44. 8.30A1643
Sersic
Original
B+D
Symmetrized
Sersic
m_r = 19.51
m_tot=19.28
B/T = 0.74
n = 8.00
χ_ν² = 1.35
1.676h_e
m_tot=19.46
n=3.38
χ_ν² = 1.53
X
Y
Radius (pixels)

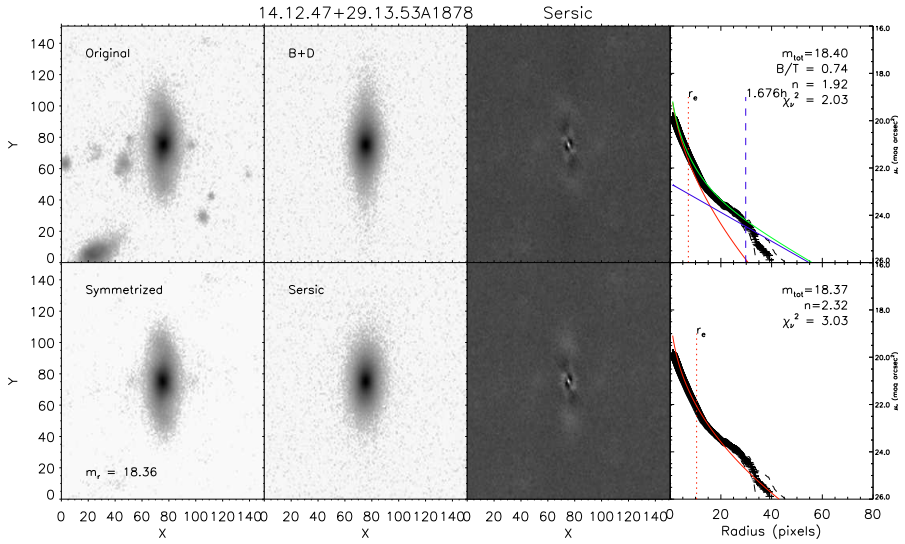
14.12.47+29.13.53A1878
Sersic
Original
B+D
Symmetrized
Sersic
m_r = 18.36
m_tot=18.40
B/T = 0.74
n = 1.92
χ_ν² = 2.03
1.676h
r_e
m_tot=18.37
n=2.32
χ_ν² = 3.03
X
Y
Radius (pixels)

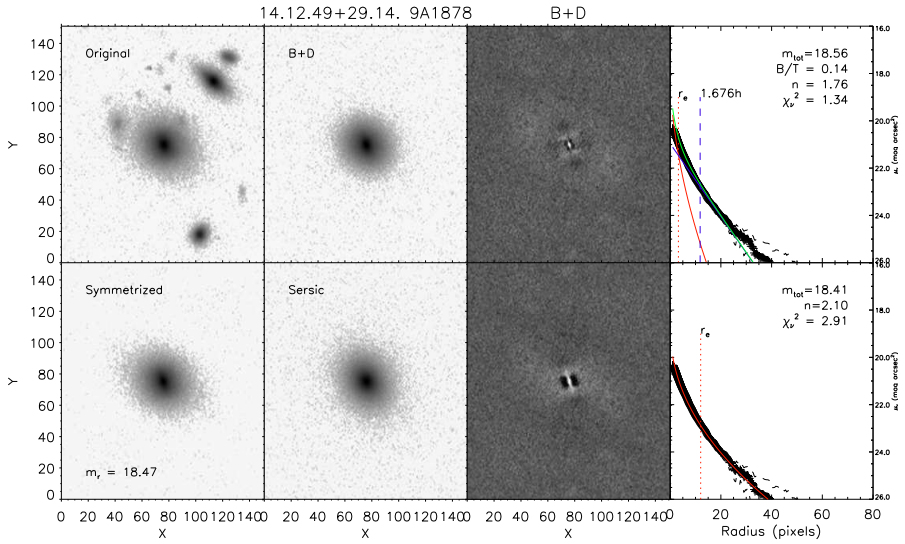
14.12.49+29.14. 9A1878
B+D
Original
B+D
Symmetrized
Sersic
m_r = 18.47
m_tot=18.56
B/T = 0.14
n = 1.76
χ_ν² = 1.34
1.676h
r_e
m_tot=18.41
n=2.10
χ_ν² = 2.91
X
Y
Radius (pixels)

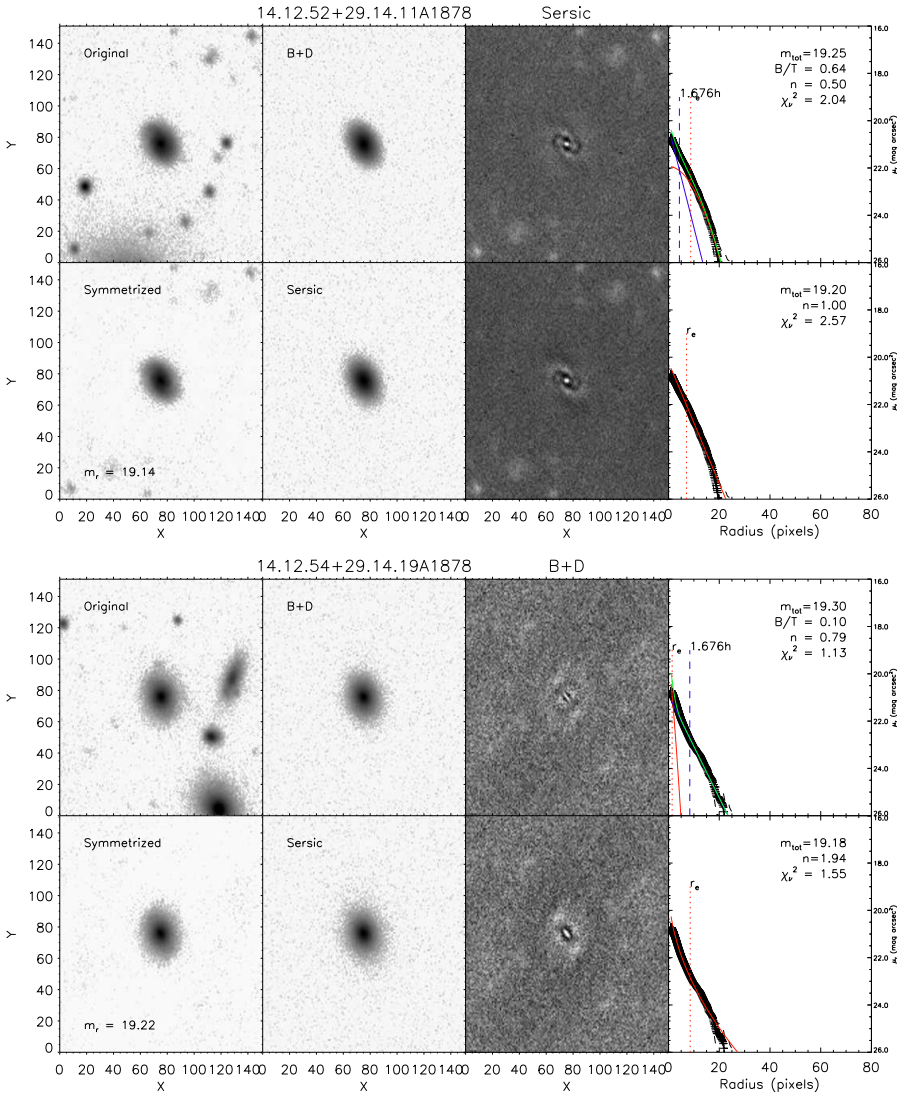
14.12.52+29.14.11A1878
Sersic
Original
B+D
Symmetrized
Sersic
m_r = 19.14
m_tot=19.25
B/T = 0.64
n = 0.50
χ_ν² = 2.04
1.676h
m_tot=19.20
n=1.00
χ_ν² = 2.57
r_e
Radius (pixels)
14.12.54+29.14.19A1878
B+D
Original
B+D
Symmetrized
Sersic
m_r = 19.22
m_tot=19.30
B/T = 0.10
n = 0.79
χ_ν² = 1.13
r_e 1.676h
m_tot=19.18
n=1.94
χ_ν² = 1.55
r_e
Radius (pixels)
X
Y

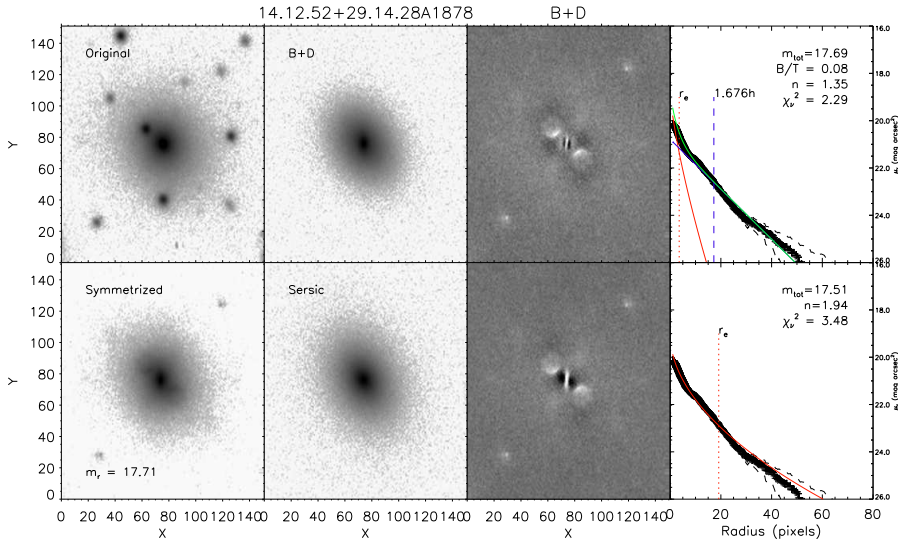
14.12.52+29.14.28A1878
B+D
Original
B+D
Symmetrized
Sersic
m_r = 17.71
m_tot=17.69
B/T = 0.08
n = 1.35
χ_ν² = 2.29
1.676h
m_tot=17.51
n=1.94
χ_ν² = 3.48
X
Y
Radius (pixels)

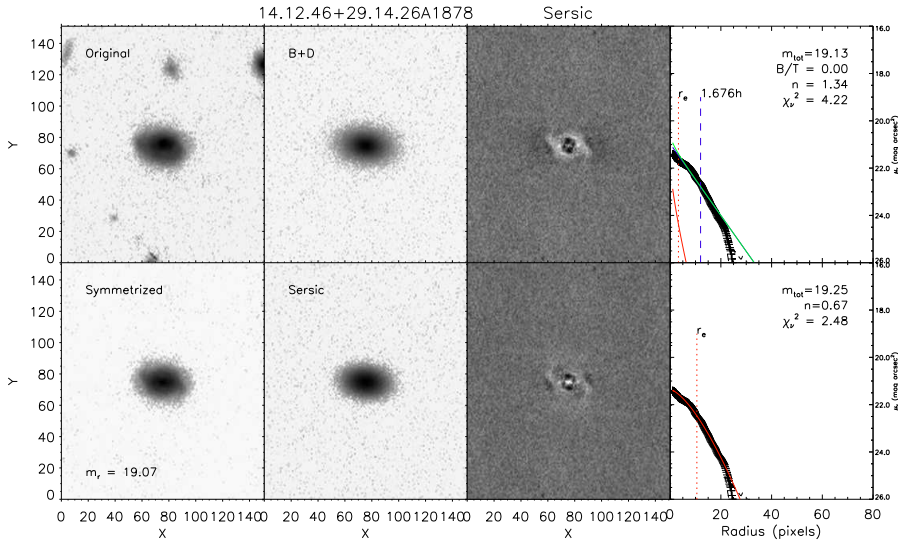
14.12.46+29.14.26A1878
Sersic
Original
B+D
Symmetrized
Sersic
m_r = 19.07
m_tot=19.13
B/T = 0.00
n = 1.34
χ_ν² = 4.22
1.676h
m_tot=19.25
n=0.67
χ_ν² = 2.48
X
Y
Radius (pixels)

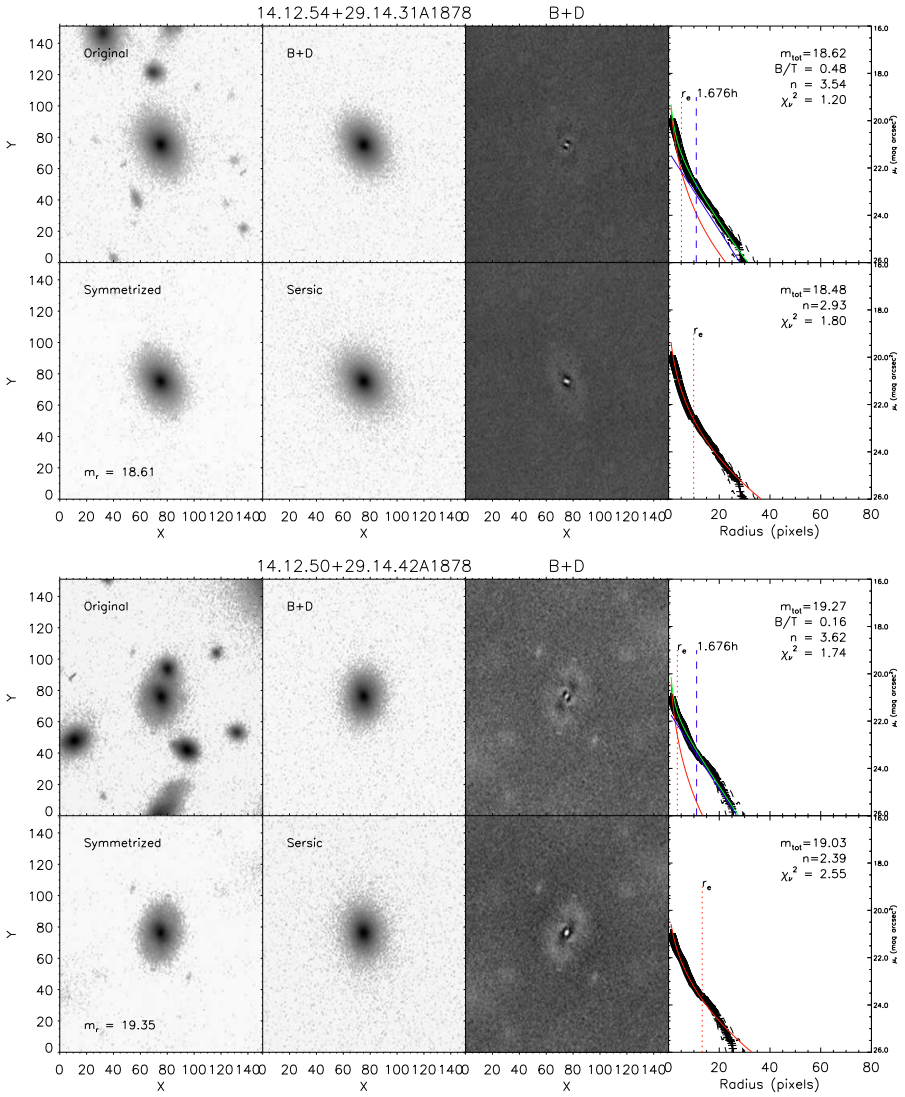
14.12.54+29.14.31A1878
B+D
Original
B+D
Symmetrized
Sersic
m_r = 18.61
m_tot=18.62
B/T = 0.48
n = 3.54
χ_ν² = 1.20
r_e 1.676h
m_tot=18.48
n=2.93
χ_ν² = 1.80
r_e
Radius (pixels)
14.12.50+29.14.42A1878
B+D
Original
B+D
Symmetrized
Sersic
m_r = 19.35
m_tot=19.27
B/T = 0.16
n = 3.62
χ_ν² = 1.74
r_e 1.676h
m_tot=19.03
n=2.39
χ_ν² = 2.55
r_e
Radius (pixels)

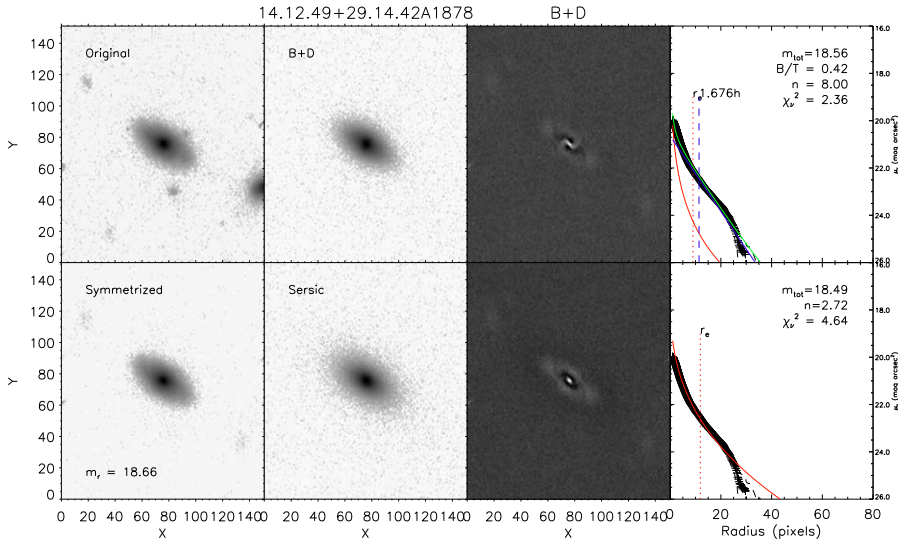
14.12.49+29.14.42A1878
B+D
Original
B+D
Symmetrized
Sersic
m_r = 18.66
m_tot=18.56
B/T = 0.42
n = 8.00
χ_ν² = 2.36
r_e
1.676h
m_tot=18.49
n=2.72
χ_ν² = 4.64
Radius (pixels)
X
Y

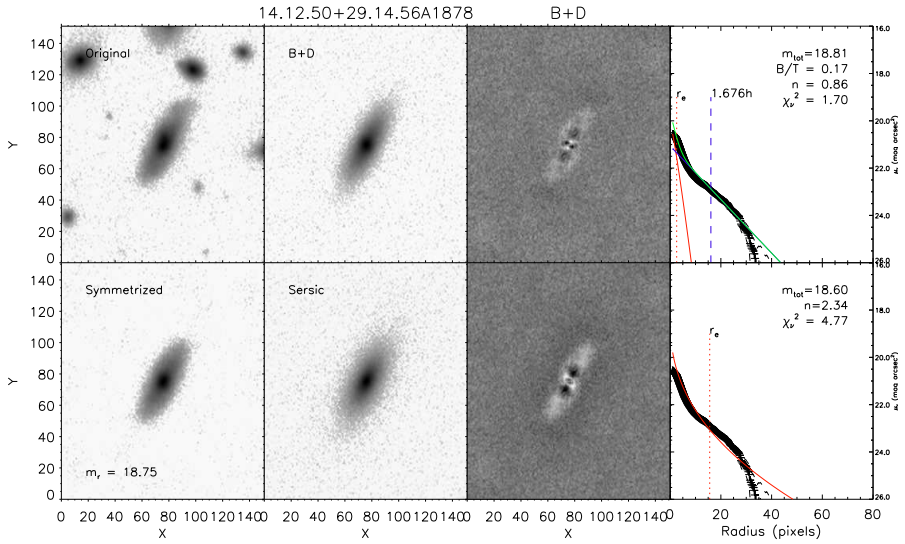
14.12.50+29.14.56A1878
B+D
Original
B+D
Symmetrized
Sersic
m_r = 18.75
m_tot=18.81
B/T = 0.17
n = 0.86
χ_ν² = 1.70
r_e
1.676h
m_tot=18.60
n=2.34
χ_ν² = 4.77
Radius (pixels)
X
Y

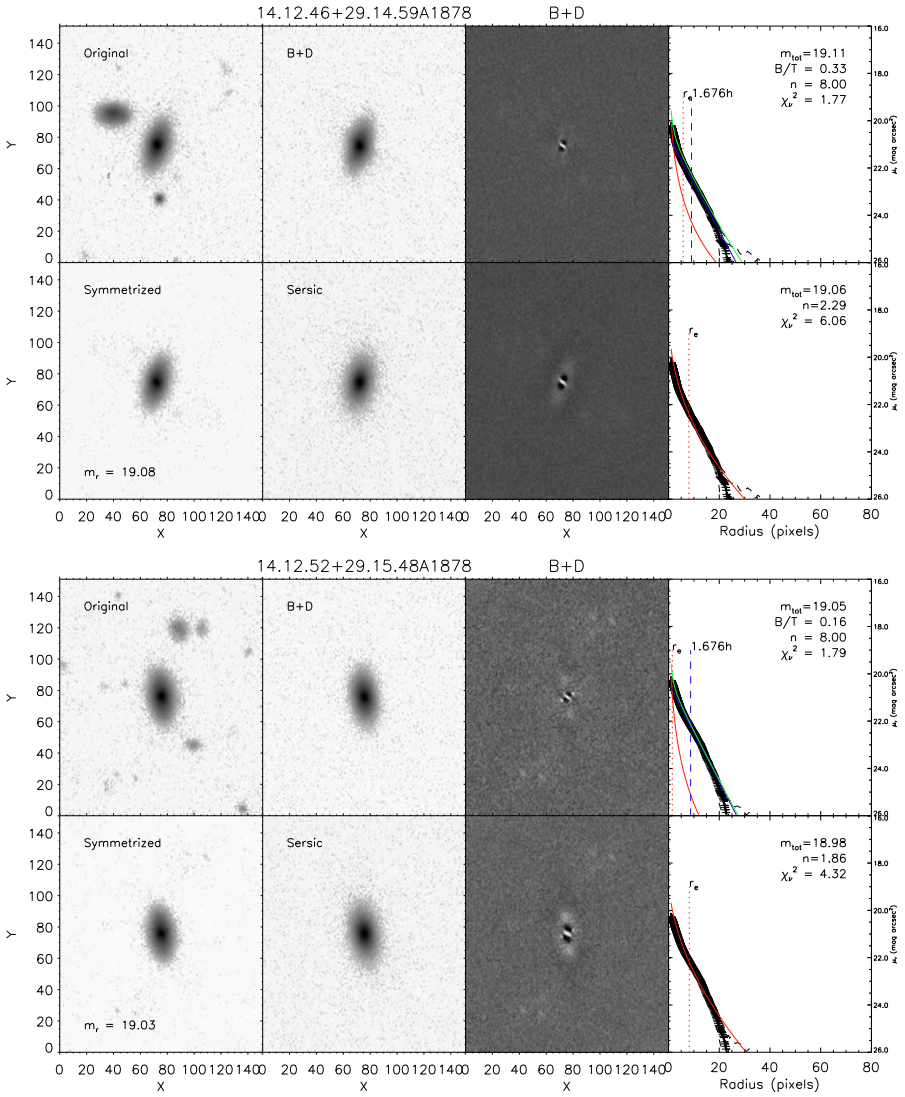
14.12.46+29.14.59A1878
B+D
Original
B+D
Symmetrized
Sersic
m_r = 19.08
m_tot=19.11
B/T = 0.33
n = 8.00
χ_ν² = 1.77
r_e 1.676h
m_tot=19.06
n=2.29
χ_ν² = 6.06
r_e
X
Y
Radius (pixels)
14.12.52+29.15.48A1878
B+D
Original
B+D
Symmetrized
Sersic
m_r = 19.03
m_tot=19.05
B/T = 0.16
n = 8.00
χ_ν² = 1.79
r_e 1.676h
m_tot=18.98
n=1.86
χ_ν² = 4.32
r_e
X
Y
Radius (pixels)

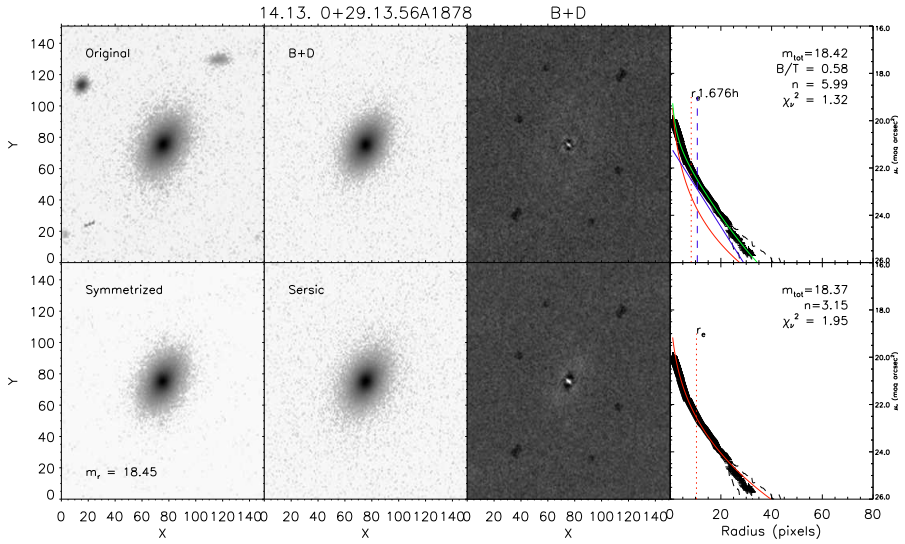
14.13. 0+29.13.56A1878
B+D
Original
B+D
Symmetrized
Sersic
m_r = 18.45
m_tot=18.42
B/T = 0.58
n = 5.99
χ_ν² = 1.32
r_e1.676h
m_tot=18.37
n=3.15
χ_ν² = 1.95
r_e
X
Y
Radius (pixels)

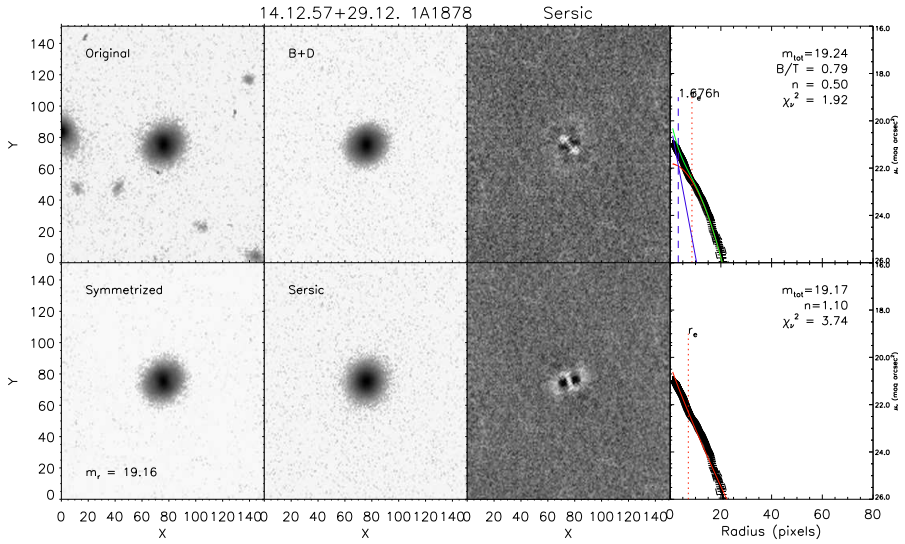
14.12.57+29.12. 1A1878
Sersic
Original
B+D
Symmetrized
Sersic
m_r = 19.16
m_tot=19.24
B/T = 0.79
n = 0.50
χ_ν² = 1.92
1.676h
m_tot=19.17
n=1.10
χ_ν² = 3.74
r_e
X
Y
Radius (pixels)

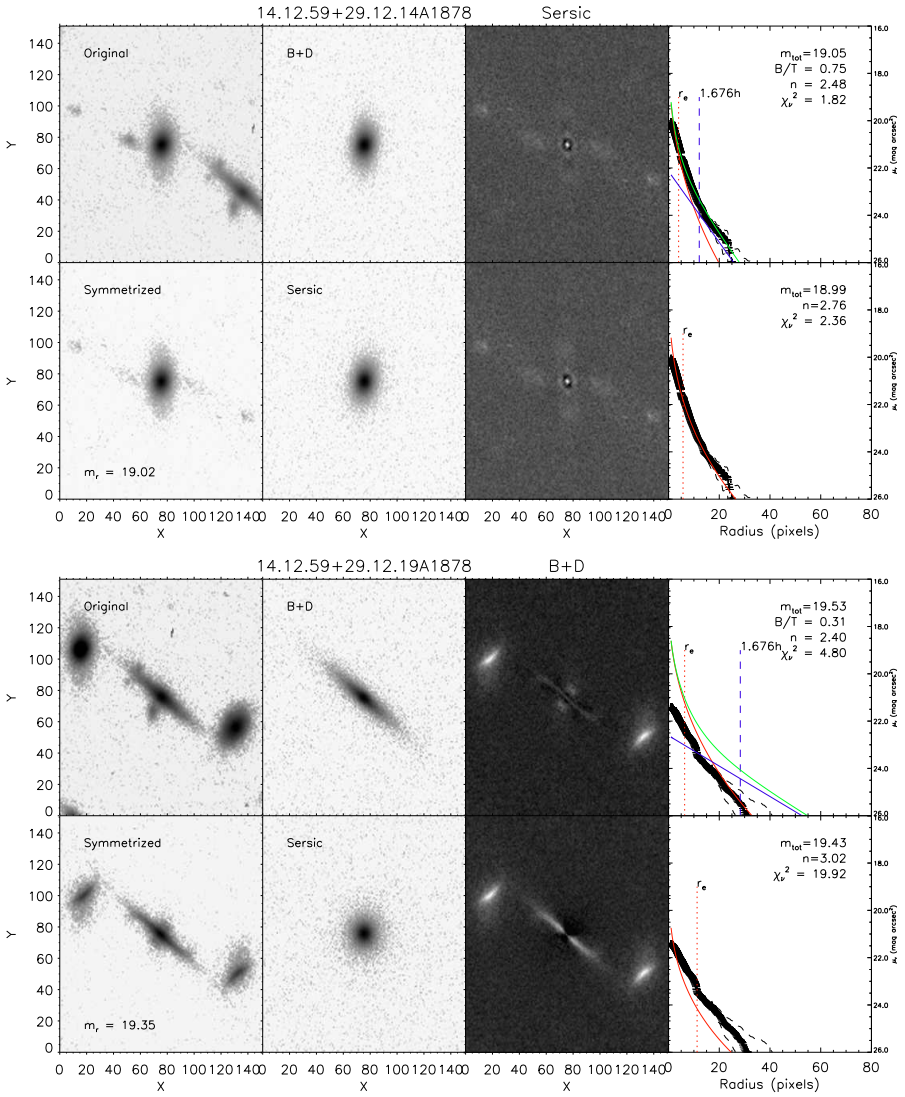
14.12.59+29.12.14A1878
Sersic
Original
B+D
Symmetrized
Sersic
m_r = 19.02
m_tot=19.05
B/T = 0.75
n = 2.48
χ_ν² = 1.82
1.676h
m_tot=18.99
n=2.76
χ_ν² = 2.36
14.12.59+29.12.19A1878
B+D
Original
B+D
Symmetrized
Sersic
m_r = 19.35
m_tot=19.53
B/T = 0.31
n = 2.40
χ_ν² = 4.80
1.676h
m_tot=19.43
n=3.02
χ_ν² = 19.92
X
Y
Radius (pixels)

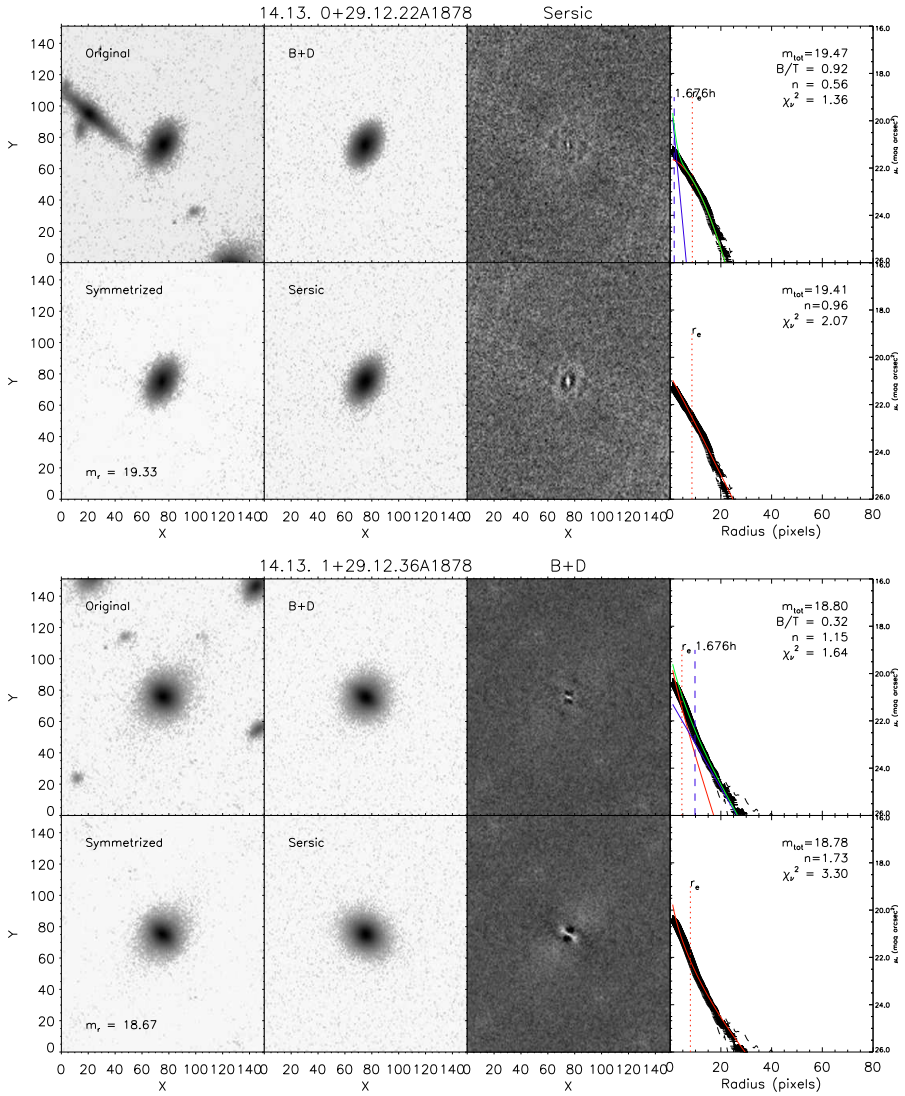
14.13. 0+29.12.22A1878 Sersic
Original
B+D
Symmetrized
Sersic
m_r = 19.33
m_tot=19.47
B/T = 0.92
n = 0.56
χ_ν² = 1.36
1.676h
m_tot=19.41
n=0.96
χ_ν² = 2.07
r_e
Y
X
Radius (pixels)
14.13. 1+29.12.36A1878 B+D
Original
B+D
Symmetrized
Sersic
m_r = 18.67
m_tot=18.80
B/T = 0.32
n = 1.15
χ_ν² = 1.64
r_e 1.676h
m_tot=18.78
n=1.73
χ_ν² = 3.30
r_e
Y
X
Radius (pixels)

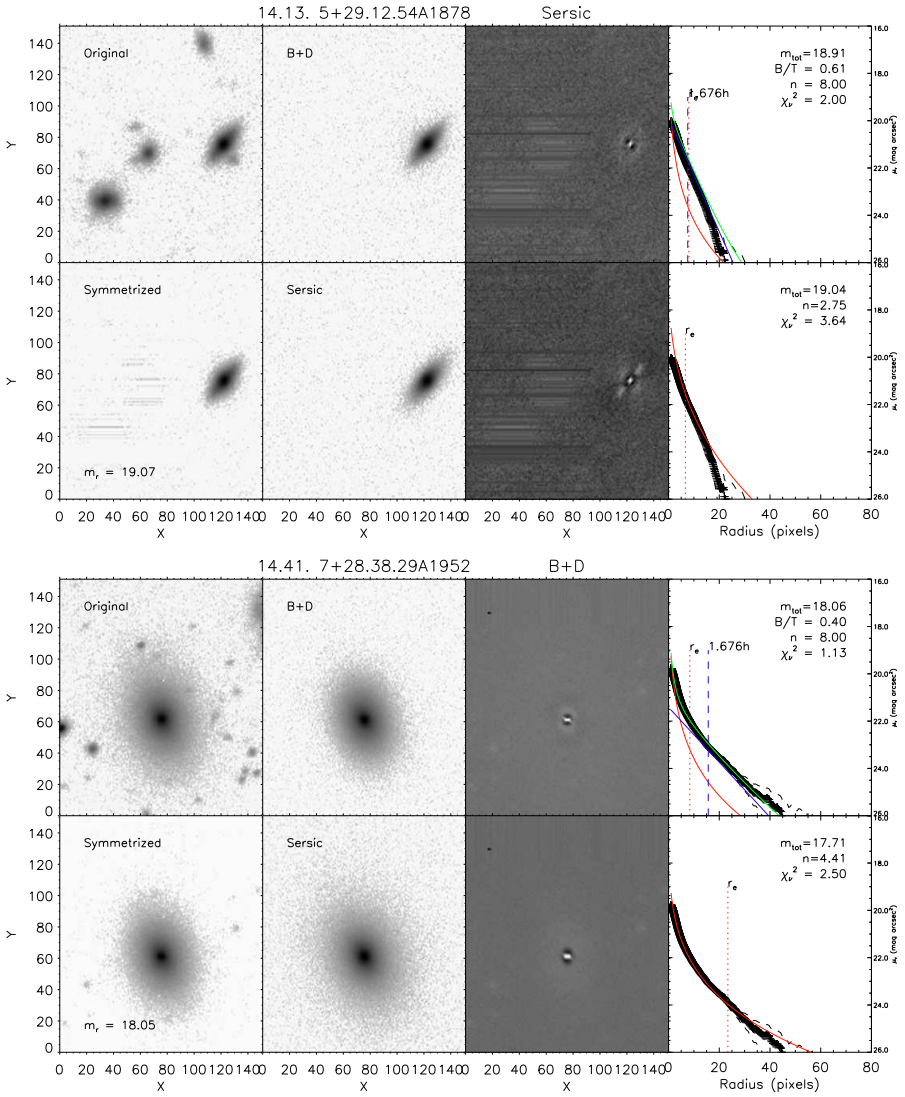
14.13. 5+29.12.54A1878
Sersic
Original
B+D
Symmetrized
Sersic
m_r = 19.07
m_tot=18.91
B/T = 0.61
n = 8.00
χ_ν² = 2.00
r_e 676h
m_tot=19.04
n=2.75
χ_ν² = 3.64
r_e
X
Y
Radius (pixels)
μ_r (mag arcsec⁻²)
14.41. 7+28.38.29A1952
B+D
Original
B+D
Symmetrized
Sersic
m_r = 18.05
m_tot=18.06
B/T = 0.40
n = 8.00
χ_ν² = 1.13
r_e 1.676h
m_tot=17.71
n=4.41
χ_ν² = 2.50
r_e
X
Y
Radius (pixels)
μ_r (mag arcsec⁻²)

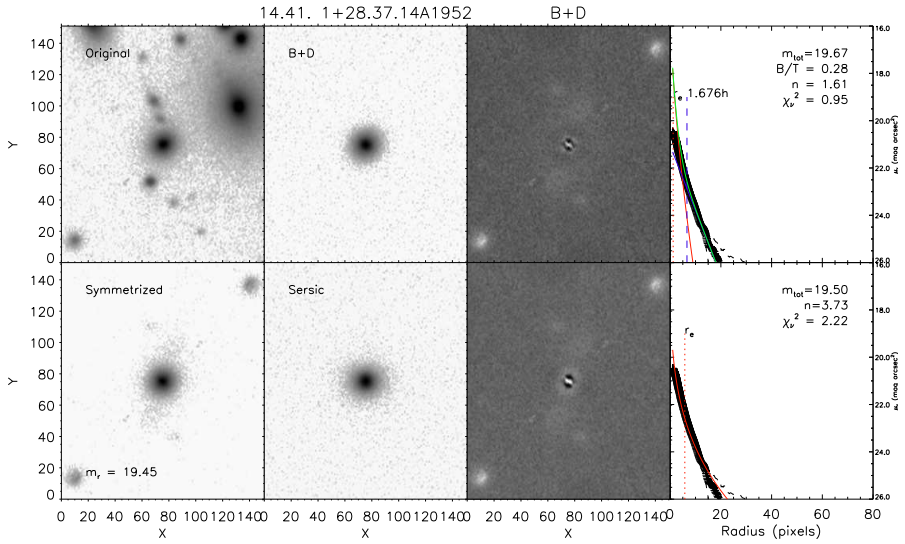
14.41. 1+28.37.14A1952
B+D
Original
B+D
Symmetrized
Sersic
m_r = 19.45
m_tot=19.67
B/T = 0.28
n = 1.61
χ_ν² = 0.95
r_e 1.676h
m_tot=19.50
n=3.73
χ_ν² = 2.22
r_e
X
Y
Radius (pixels)

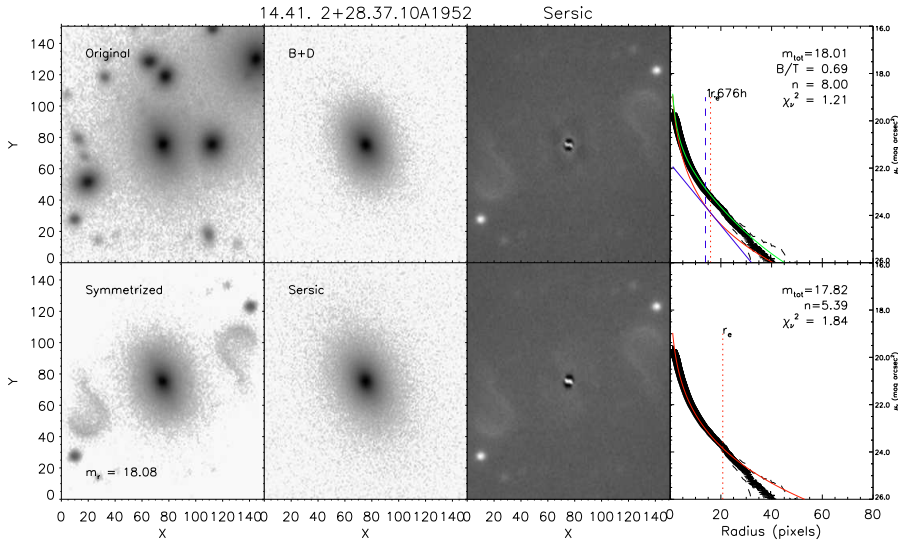
14.41. 2+28.37.10A1952
Sersic
Original
B+D
Symmetrized
Sersic
m_r = 18.08
m_tot=18.01
B/T = 0.69
n = 8.00
χ_ν² = 1.21
r_e 1.676h
m_tot=17.82
n=5.39
χ_ν² = 1.84
r_e
X
Y
Radius (pixels)

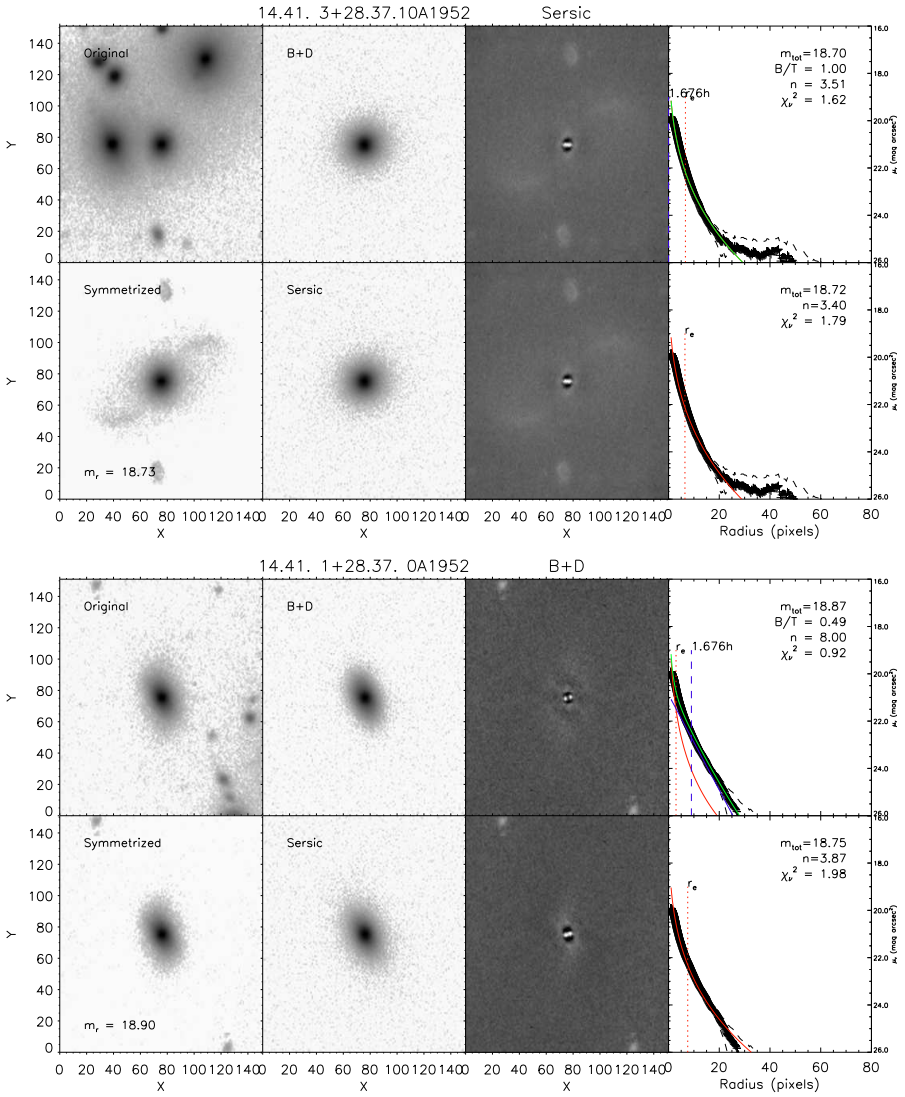
14.41. 3+28.37.10A1952
Sersic
Original
B+D
Symmetrized
Sersic
m_r = 18.73
m_tot=18.70
B/T = 1.00
n = 3.51
χ_ν² = 1.62
1.676h
m_tot=18.72
n=3.40
χ_ν² = 1.79
r_e
14.41. 1+28.37. 0A1952
B+D
Original
B+D
Symmetrized
Sersic
m_r = 18.90
m_tot=18.87
B/T = 0.49
n = 8.00
χ_ν² = 0.92
r_e 1.676h
m_tot=18.75
n=3.87
χ_ν² = 1.98
r_e
X
Y
Radius (pixels)

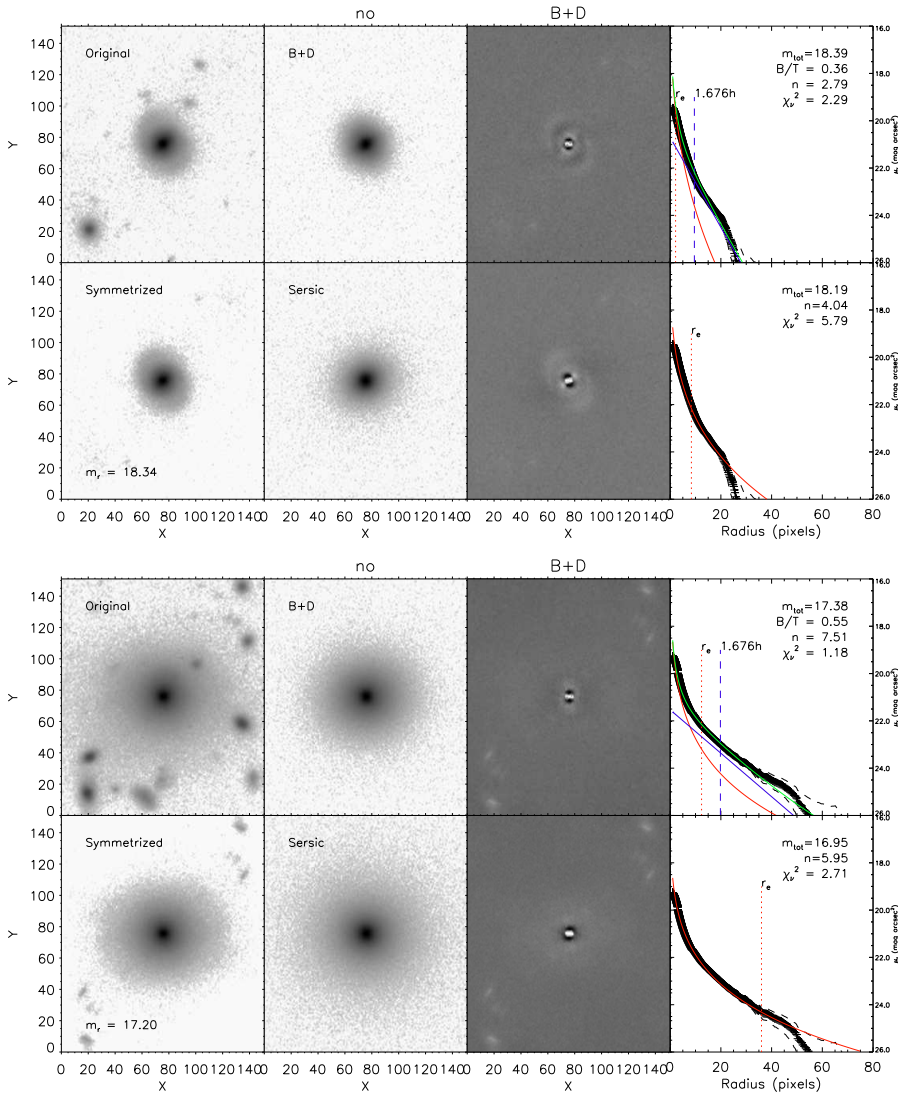
no
B+D
Original
B+D
Symmetrized
Sersic
m_r = 18.34
m_tot=18.39
B/T = 0.36
n = 2.79
χ_ν² = 2.29
r_e
1.676h
m_tot=18.19
n=4.04
χ_ν² = 5.79
X
Y
Radius (pixels)
μ_r (mag arcsec⁻²)
no
B+D
Original
B+D
Symmetrized
Sersic
m_r = 17.20
m_tot=17.38
B/T = 0.55
n = 7.51
χ_ν² = 1.18
r_e
1.676h
m_tot=16.95
n=5.95
χ_ν² = 2.71
X
Y
Radius (pixels)
μ_r (mag arcsec⁻²)

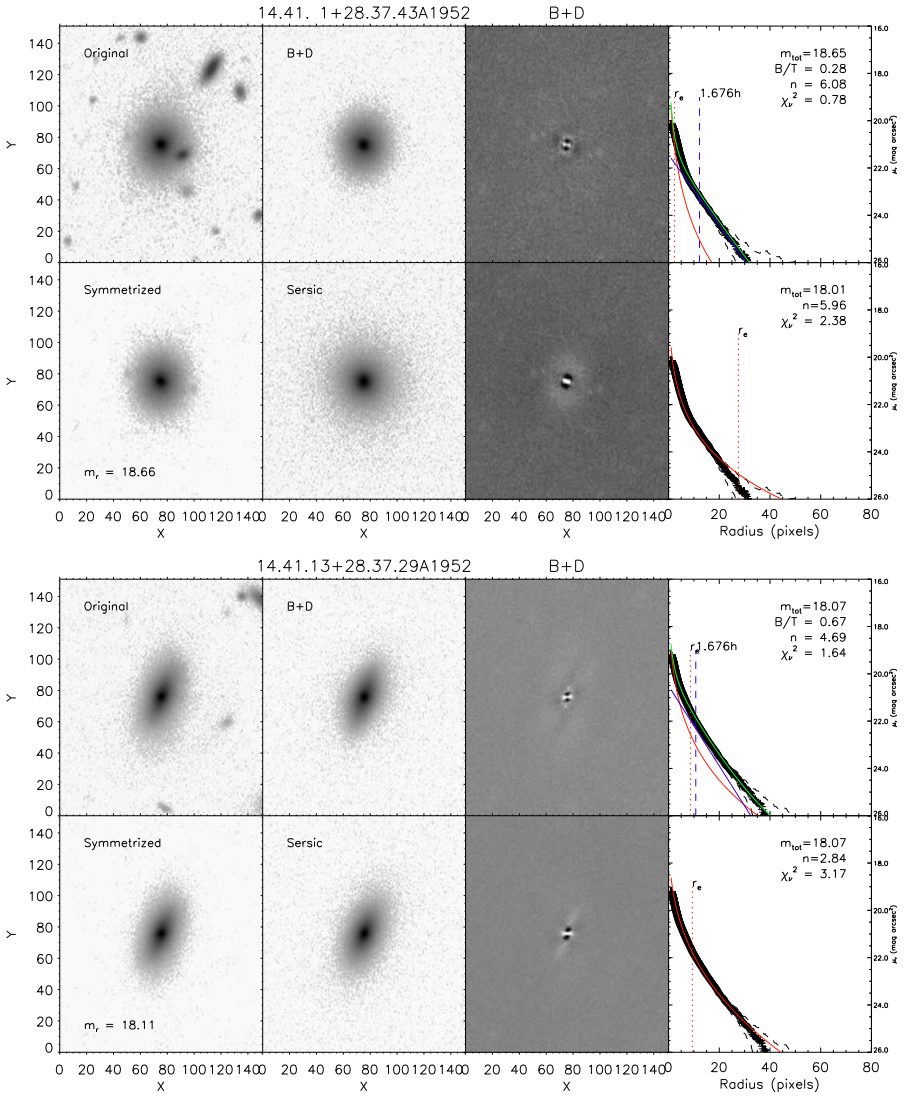
14.41. 1+28.37.43A1952
B+D
Original
B+D
Symmetrized
Sersic
m_r = 18.66
m_tot=18.65
B/T = 0.28
n = 6.08
χ_ν² = 0.78
r_e
1.676h
m_tot=18.01
n=5.96
χ_ν² = 2.38
r_e
Y
X
Radius (pixels)
μ_r (mag arcsec²)
14.41.13+28.37.29A1952
B+D
Original
B+D
Symmetrized
Sersic
m_r = 18.11
m_tot=18.07
B/T = 0.67
n = 4.69
χ_ν² = 1.64
r_e
1.676h
m_tot=18.07
n=2.84
χ_ν² = 3.17
r_e
Y
X
Radius (pixels)
μ_r (mag arcsec²)

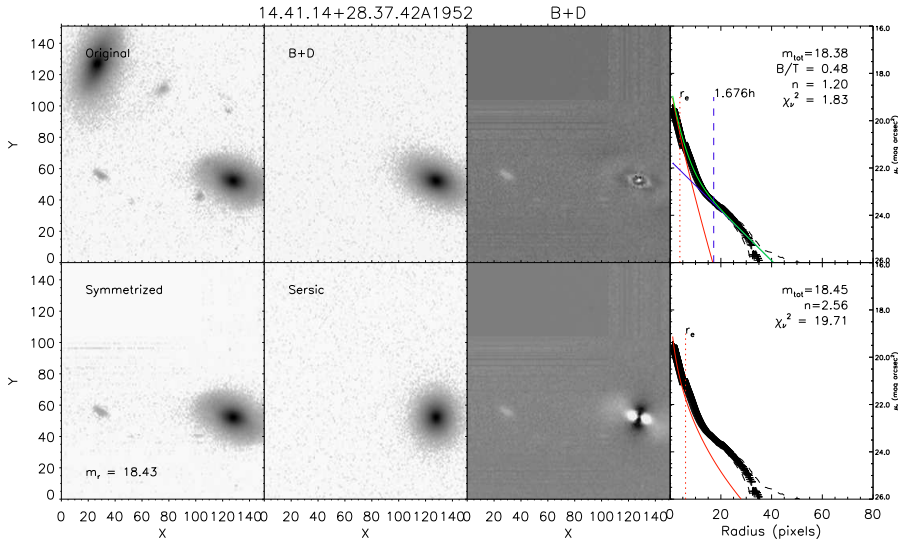
14.41.14+28.37.42A1952
B+D
Original
B+D
Symmetrized
Sersic
m_r = 18.43
m_tot=18.38
B/T = 0.48
n = 1.20
χ_ν² = 1.83
1.676h
m_tot=18.45
n=2.56
χ_ν² = 19.71
X
Y
Radius (pixels)

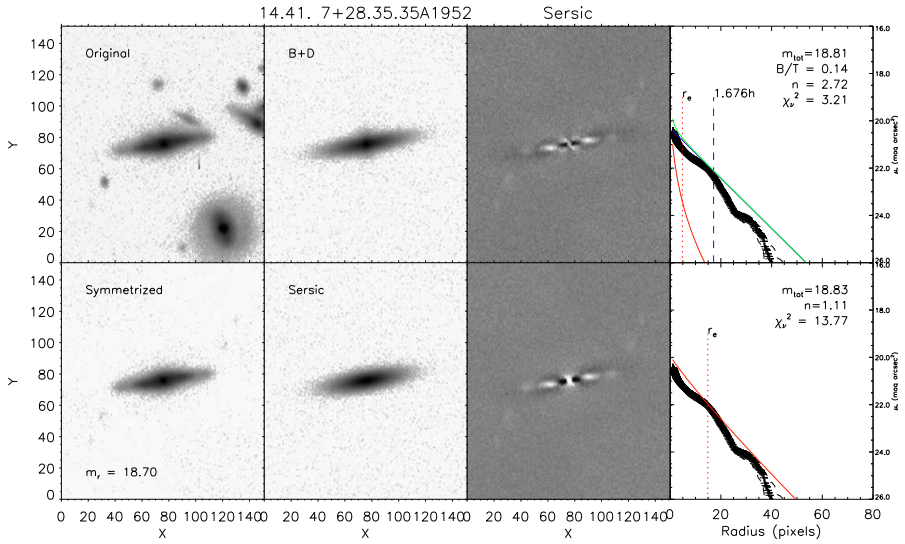
14.41. 7+28.35.35A1952
Sersic
Original
B+D
Symmetrized
Sersic
m_r = 18.70
m_tot=18.81
B/T = 0.14
n = 2.72
χ_ν² = 3.21
1.676h
m_tot=18.83
n=1.11
χ_ν² = 13.77
X
Y
Radius (pixels)

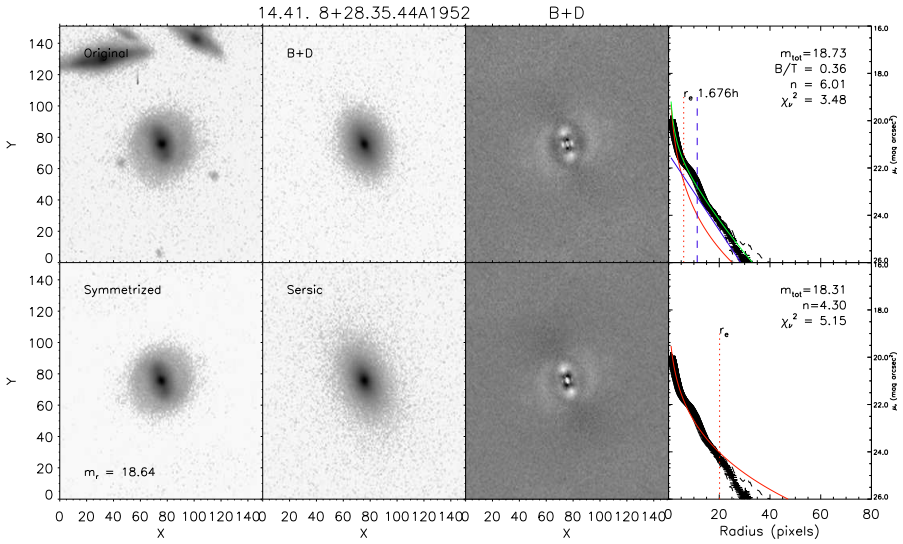
14.41. 8+28.35.44A1952
B+D
Original
B+D
Symmetrized
Sersic
m_r = 18.64
m_tot=18.73
B/T = 0.36
n = 6.01
χ_ν² = 3.48
r_e 1.676h
m_tot=18.31
n=4.30
χ_ν² = 5.15
r_e
X
Y
Radius (pixels)

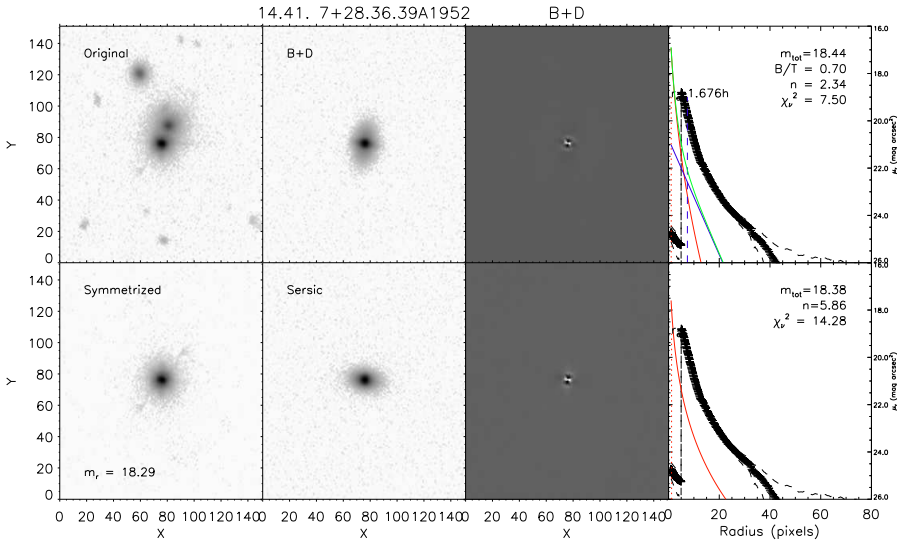
14.41. 7+28.36.39A1952
B+D
Original
B+D
Symmetrized
Sersic
m_r = 18.29
m_tot=18.44
B/T = 0.70
n = 2.34
χ_ν² = 7.50
1.676h
m_tot=18.38
n=5.86
χ_ν² = 14.28
X
Y
Radius (pixels)

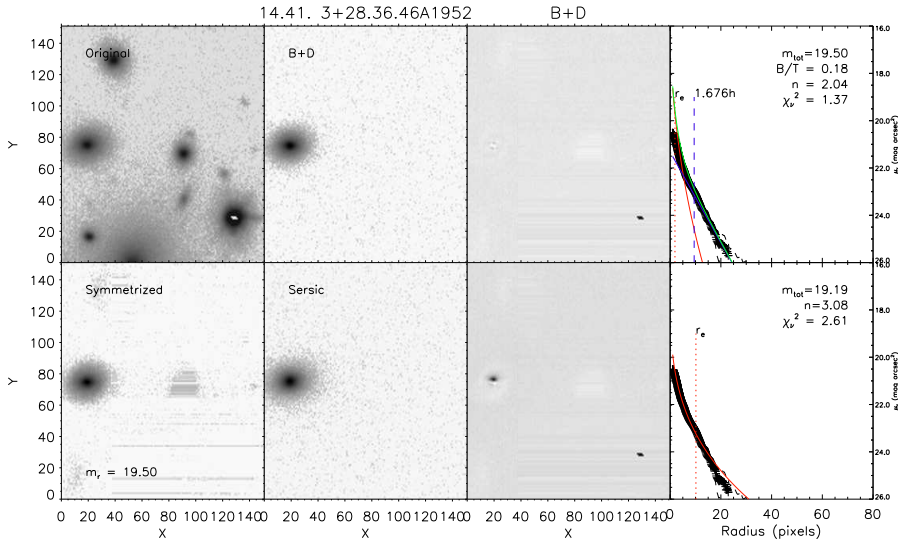
14.41. 3+28.36.46A1952
B+D
Original
B+D
Symmetrized
Sersic
m_r = 19.50
m_tot=19.50
B/T = 0.18
n = 2.04
χ_ν² = 1.37
r_e
1.676h
m_tot=19.19
n=3.08
χ_ν² = 2.61
X
Y
Radius (pixels)

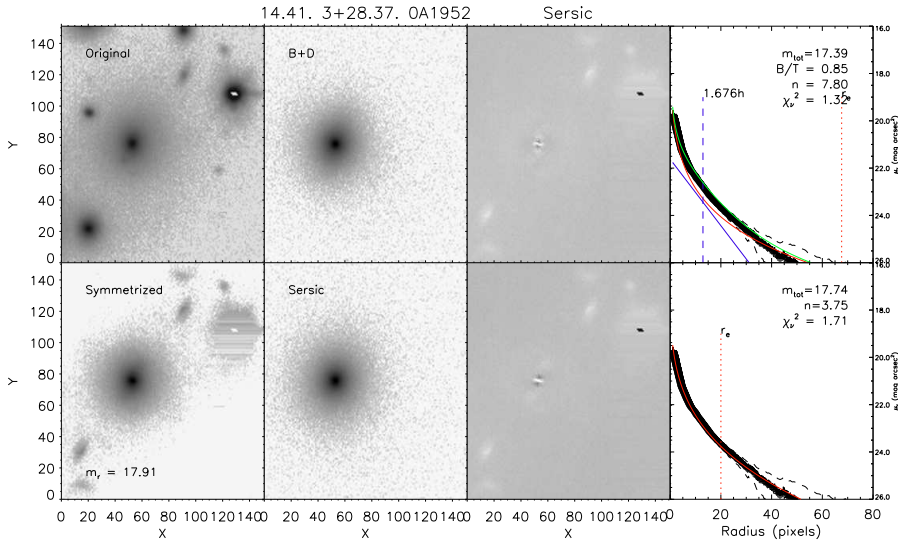
14.41. 3+28.37. 0A1952
Sersic
Original
B+D
Symmetrized
Sersic
m_r = 17.91
m_tot=17.39
B/T = 0.85
n = 7.80
χ_ν² = 1.32
1.676h
r_e
m_tot=17.74
n=3.75
χ_ν² = 1.71
X
Y
Radius (pixels)

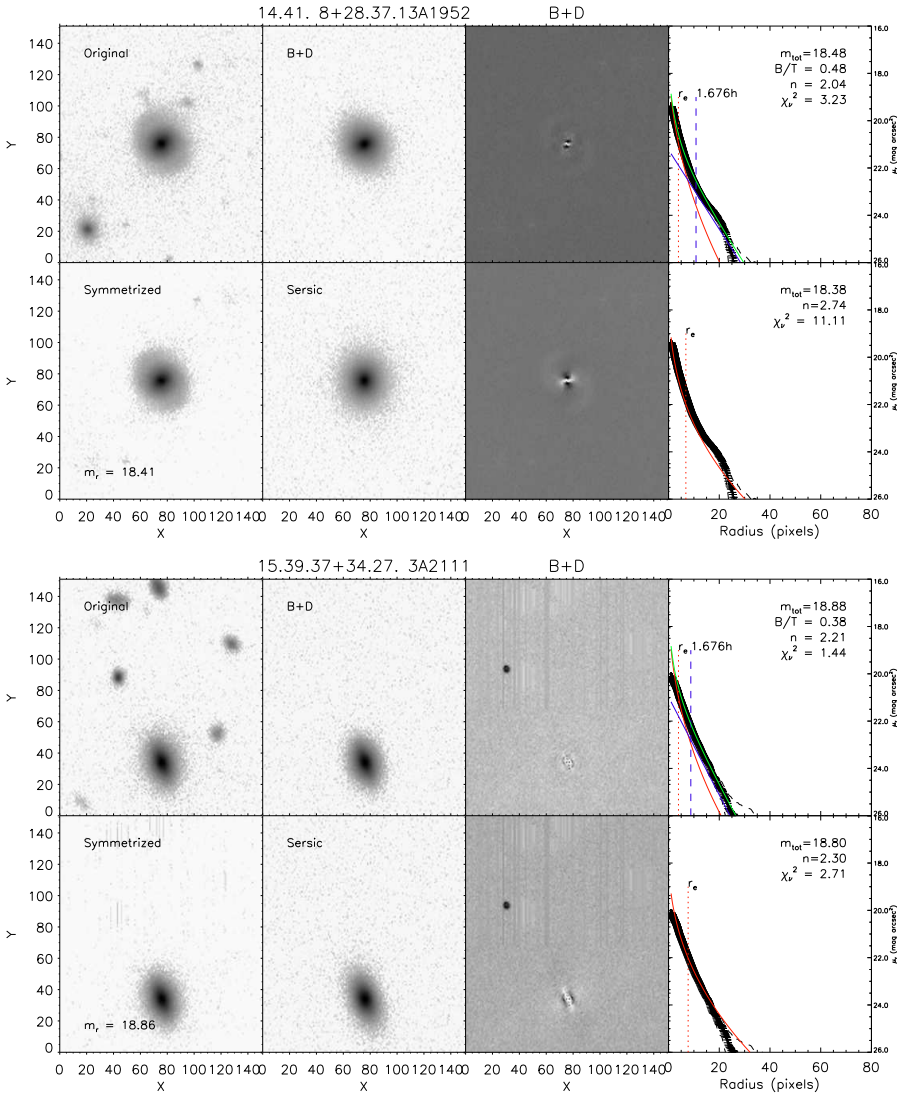
14.41. 8+28.37.13A1952
B+D
Original
B+D
Symmetrized
Sersic
m_r = 18.41
m_tot=18.48
B/T = 0.48
n = 2.04
χ_ν² = 3.23
r_e 1.676h
m_tot=18.38
n=2.74
χ_ν² = 11.11
r_e
Y
X
Radius (pixels)
μ_r (mag arcsec⁻²)
15.39.37+34.27. 3A2111
B+D
Original
B+D
Symmetrized
Sersic
m_r = 18.86
m_tot=18.88
B/T = 0.38
n = 2.21
χ_ν² = 1.44
r_e 1.676h
m_tot=18.80
n=2.30
χ_ν² = 2.71
r_e
Y
X
Radius (pixels)
μ_r (mag arcsec⁻²)

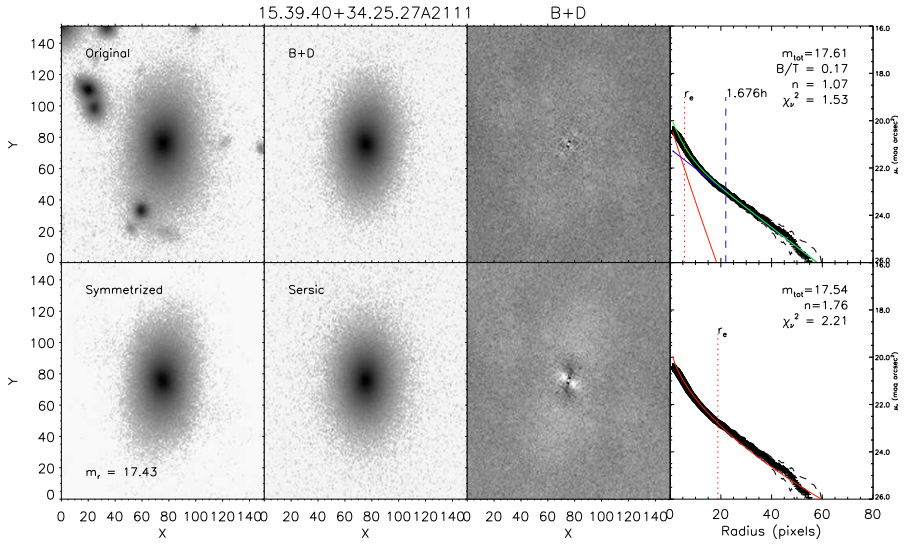
15.39.40+34.25.27A2111
B+D
Original
B+D
Symmetrized
Sersic
m_r = 17.43
m_tot=17.61
B/T = 0.17
n = 1.07
χ_ν² = 1.53
1.676h
r_e
m_tot=17.54
n=1.76
χ_ν² = 2.21
X
Y
Radius (pixels)

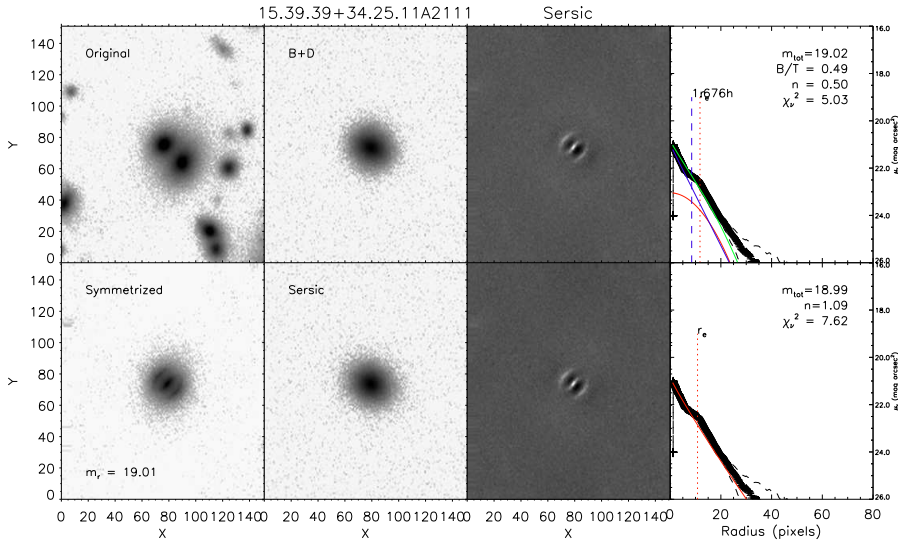
15.39.39+34.25.11A2111
Sersic
Original
B+D
Symmetrized
Sersic
m_r = 19.01
m_tot=19.02
B/T = 0.49
n = 0.50
χ_ν² = 5.03
1.676h
r_e
m_tot=18.99
n=1.09
χ_ν² = 7.62
X
Y
Radius (pixels)

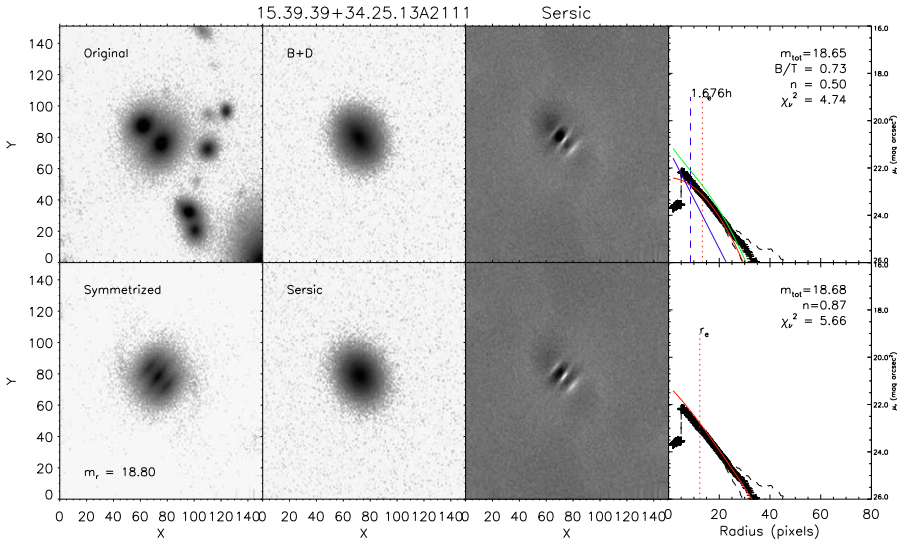
15.39.39+34.25.13A2111
Sersic
Original
B+D
Symmetrized
Sersic
m_r = 18.80
m_tot=18.65
B/T = 0.73
n = 0.50
χ_ν² = 4.74
1.676h
m_tot=18.68
n=0.87
χ_ν² = 5.66
r_e
X
Y
Radius (pixels)

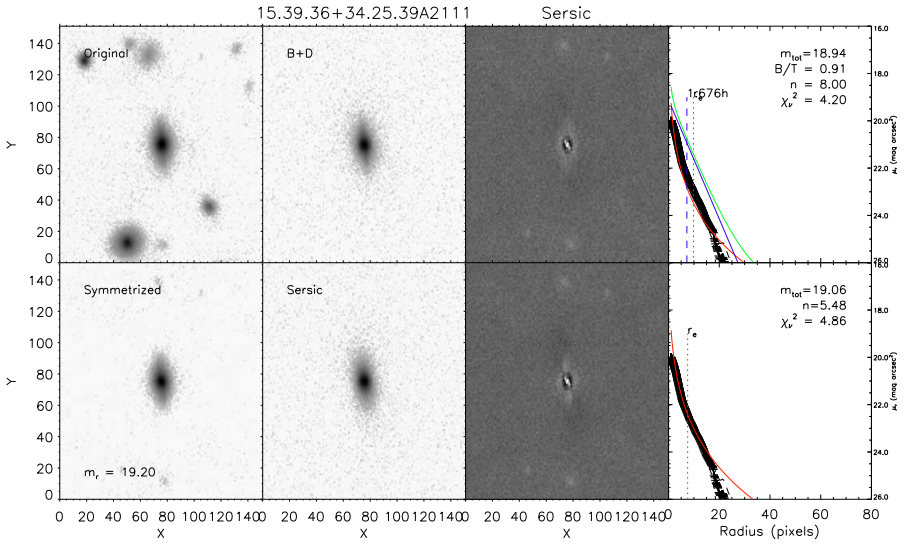
15.39.36+34.25.39A2111
Sersic
Original
B+D
Symmetrized
Sersic
m_r = 19.20
m_tot=18.94
B/T = 0.91
n = 8.00
χ_ν² = 4.20
1.676h
m_tot=19.06
n=5.48
χ_ν² = 4.86
r_e
X
Y
Radius (pixels)

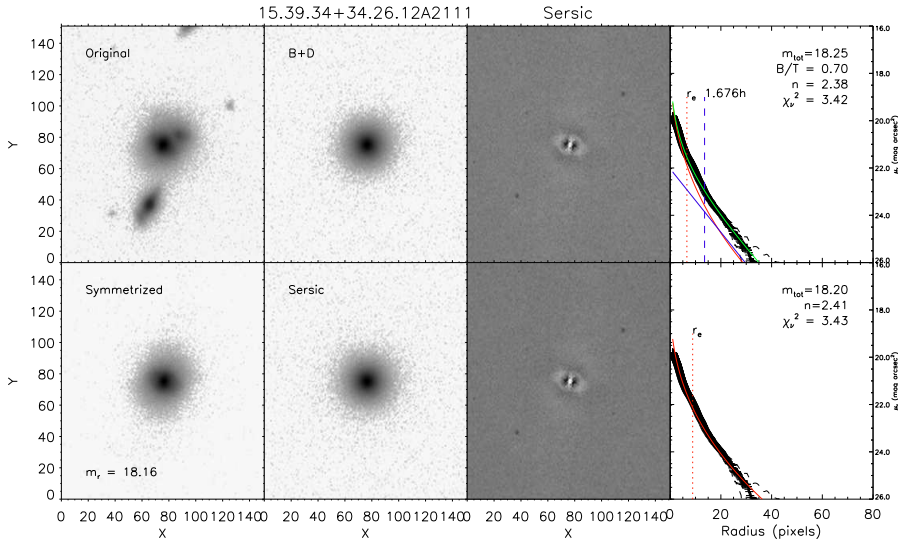
15.39.34+34.26.12A2111
Sersic
Original
B+D
Symmetrized
Sersic
m_r = 18.16
m_tot=18.25
B/T = 0.70
n = 2.38
χ_ν² = 3.42
r_e 1.676h
m_tot=18.20
n=2.41
χ_ν² = 3.43
r_e
X
Y
Radius (pixels)

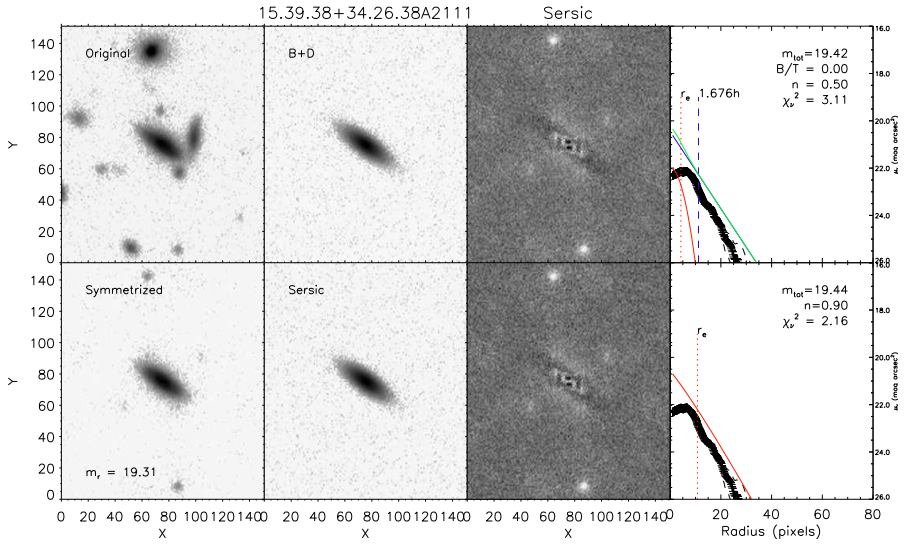
15.39.38+34.26.38A2111
Sersic
Original
B+D
Symmetrized
Sersic
m_r = 19.31
m_tot=19.42
B/T = 0.00
n = 0.50
χ_ν² = 3.11
r_e 1.676h
m_tot=19.44
n=0.90
χ_ν² = 2.16
r_e
X
Y
Radius (pixels)

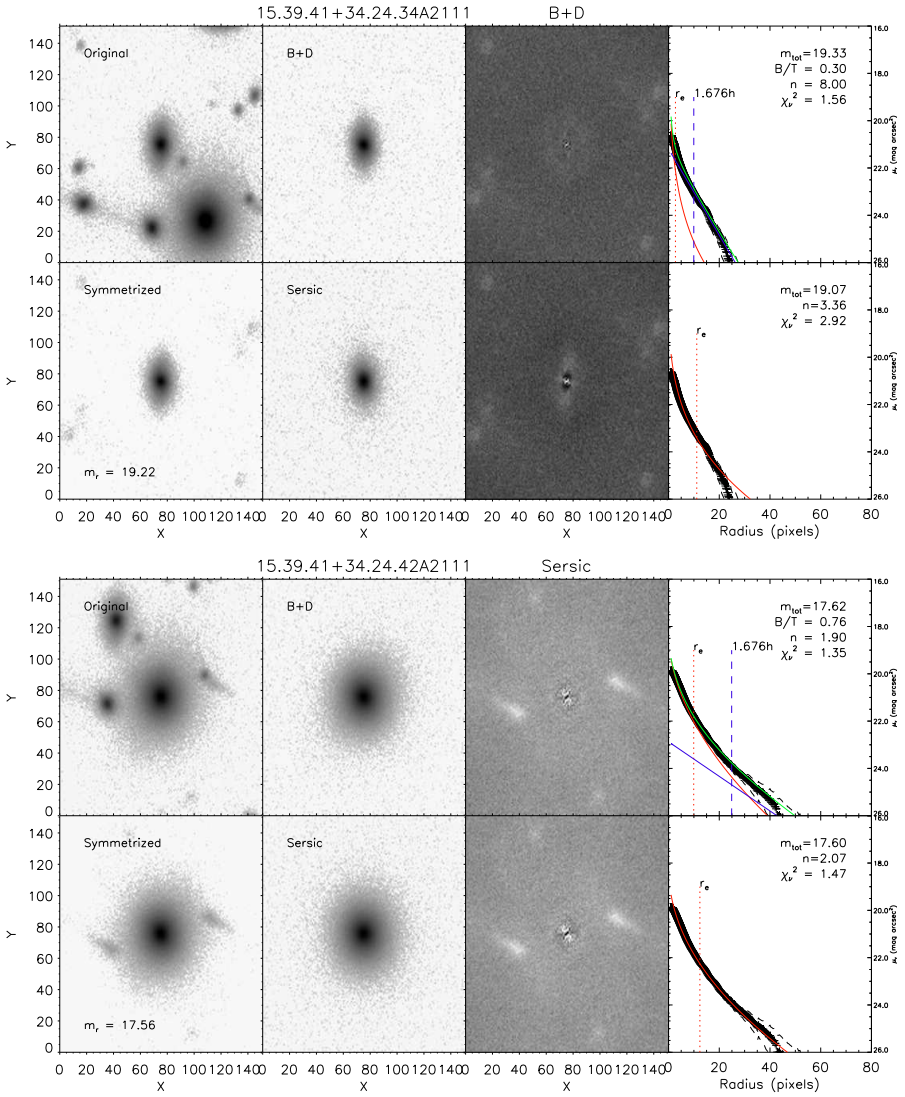
15.39.41+34.24.34A2111
B+D
Original
B+D
Symmetrized
Sersic
m_r = 19.22
m_tot=19.33
B/T = 0.30
n = 8.00
χ_ν² = 1.56
r_e
1.676h
m_tot=19.07
n=3.36
χ_ν² = 2.92
Radius (pixels)
15.39.41+34.24.42A2111
Sersic
Original
B+D
Symmetrized
Sersic
m_r = 17.56
m_tot=17.62
B/T = 0.76
n = 1.90
χ_ν² = 1.35
1.676h
m_tot=17.60
n=2.07
χ_ν² = 1.47
Radius (pixels)
X
Y

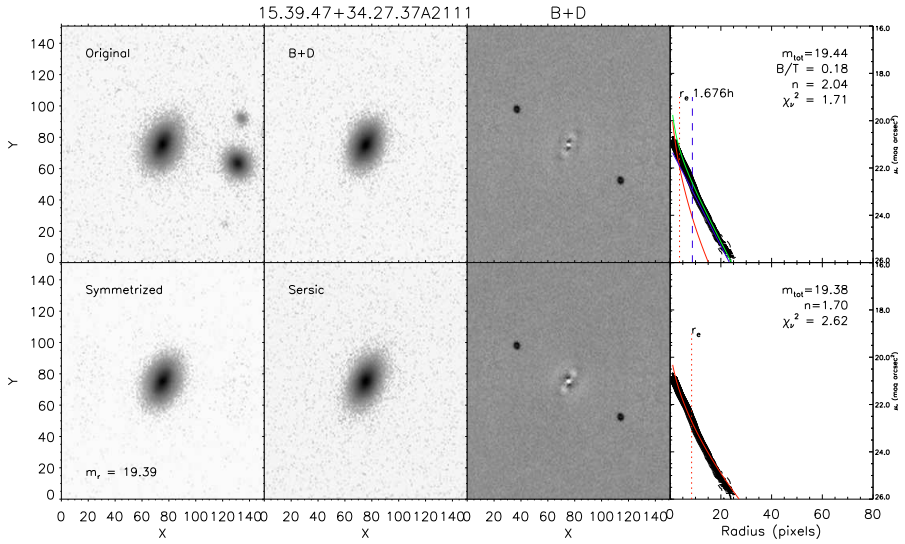
15.39.47+34.27.37A2111
B+D
Original
B+D
Symmetrized
Sersic
m_r = 19.39
m_tot=19.44
B/T = 0.18
n = 2.04
χ_ν² = 1.71
r_e 1.676h
m_tot=19.38
n=1.70
χ_ν² = 2.62
r_e
X
Y
Radius (pixels)

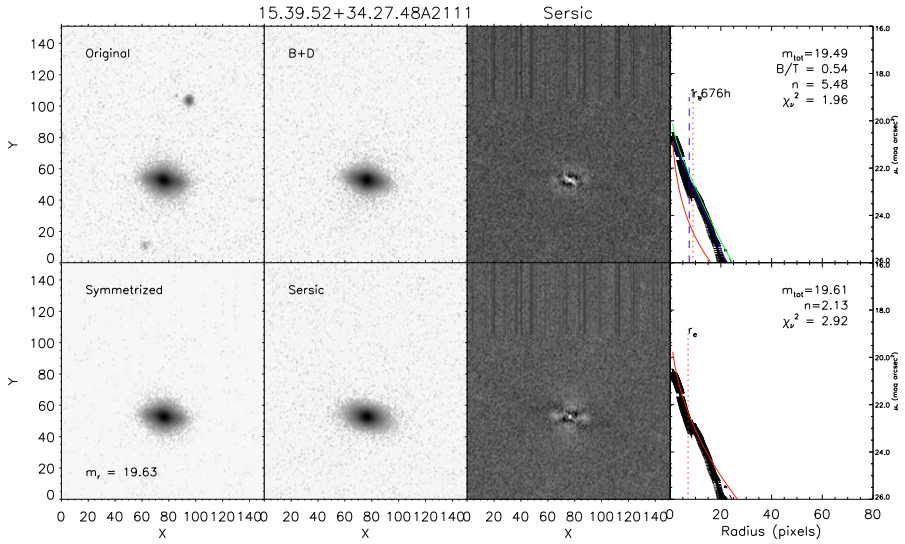
15.39.52+34.27.48A2111
Sersic
Original
B+D
Symmetrized
Sersic
m_r = 19.63
m_tot=19.49
B/T = 0.54
n = 5.48
χ_ν² = 1.96
r_e 1.676h
m_tot=19.61
n=2.13
χ_ν² = 2.92
r_e
X
Y
Radius (pixels)

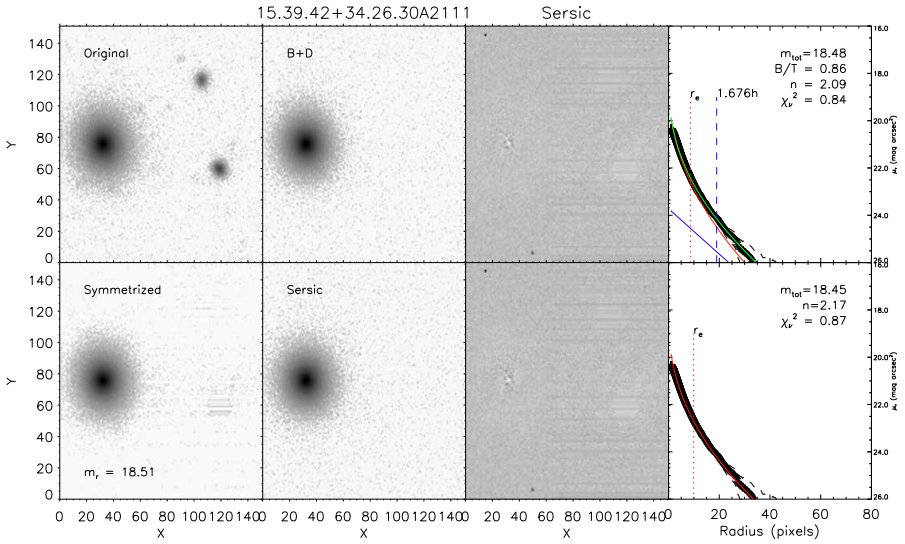
15.39.42+34.26.30A2111
Sersic
Original
B+D
Symmetrized
Sersic
m_r = 18.51
m_tot=18.48
B/T = 0.86
n = 2.09
χ_ν² = 0.84
1.676h
m_tot=18.45
n=2.17
χ_ν² = 0.87
X
Y
Radius (pixels)

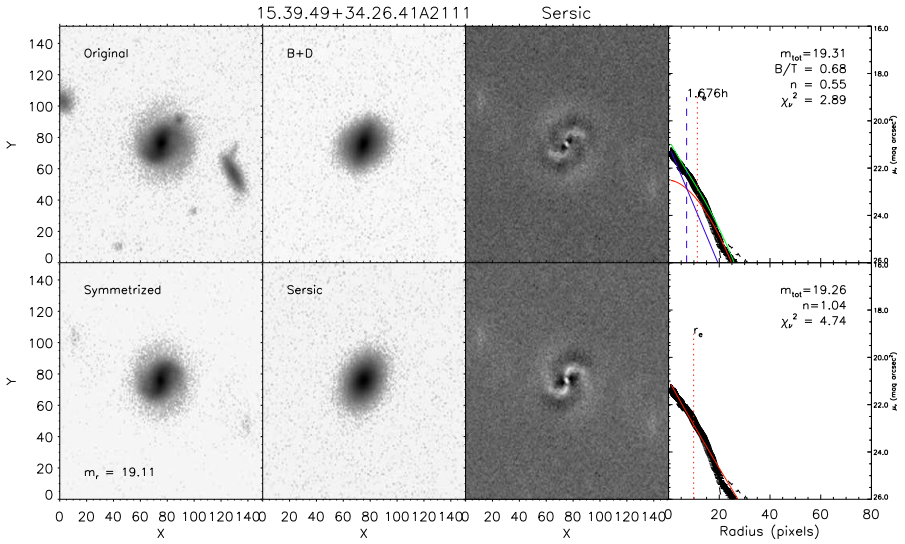
15.39.49+34.26.41A2111
Sersic
Original
B+D
Symmetrized
Sersic
m_r = 19.11
m_tot=19.31
B/T = 0.68
n = 0.55
χ_ν² = 2.89
1.676h
m_tot=19.26
n=1.04
χ_ν² = 4.74
X
Y
Radius (pixels)

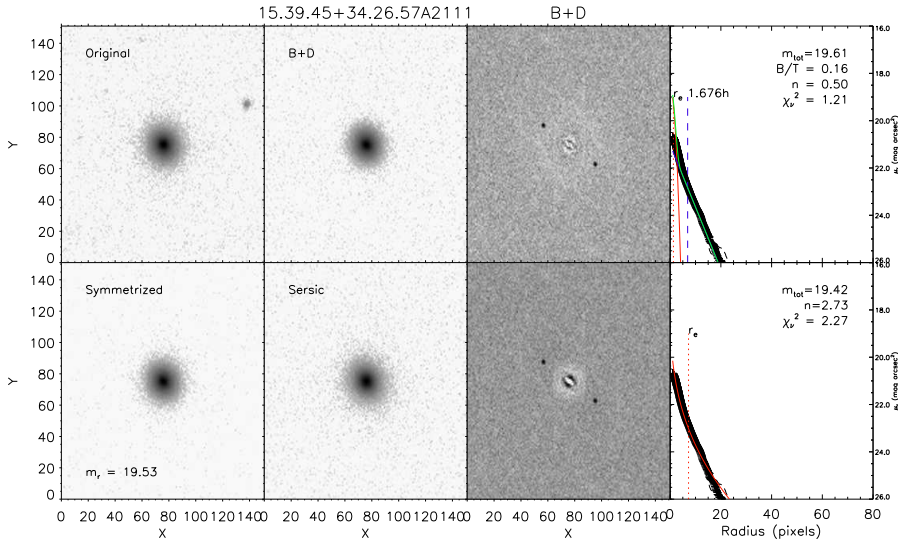
15.39.45+34.26.57A2111
B+D
Original
B+D
Symmetrized
Sersic
m_r = 19.53
m_tot=19.61
B/T = 0.16
n = 0.50
χ_ν² = 1.21
r_e 1.676h
m_tot=19.42
n=2.73
χ_ν² = 2.27
r_e
X
Y
Radius (pixels)
15.39.52+34.27.12A2111
Sersic
Original
B+D
Symmetrized
Sersic
m_r = 19.57
m_tot=19.87
B/T = 0.90
n = 0.57
χ_ν² = 1.32
r_e 1.676h
m_tot=19.77
n=1.01
χ_ν² = 1.65
r_e
X
Y
Radius (pixels)

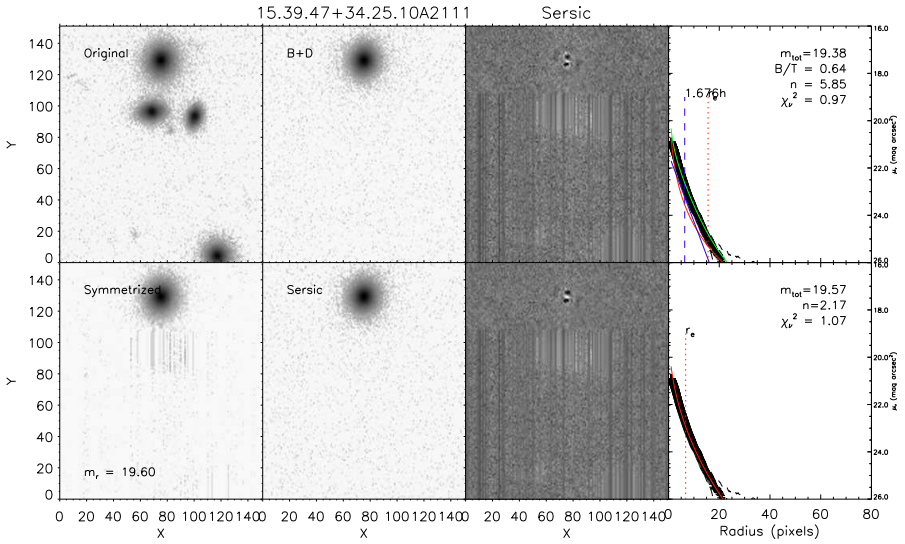
15.39.47+34.25.10A2111
Sersic
Original
B+D
Symmetrized
Sersic
m_r = 19.60
m_tot=19.38
B/T = 0.64
n = 5.85
χ_ν² = 0.97
1.676h
m_tot=19.57
n=2.17
χ_ν² = 1.07
r_e
X
Y
Radius (pixels)

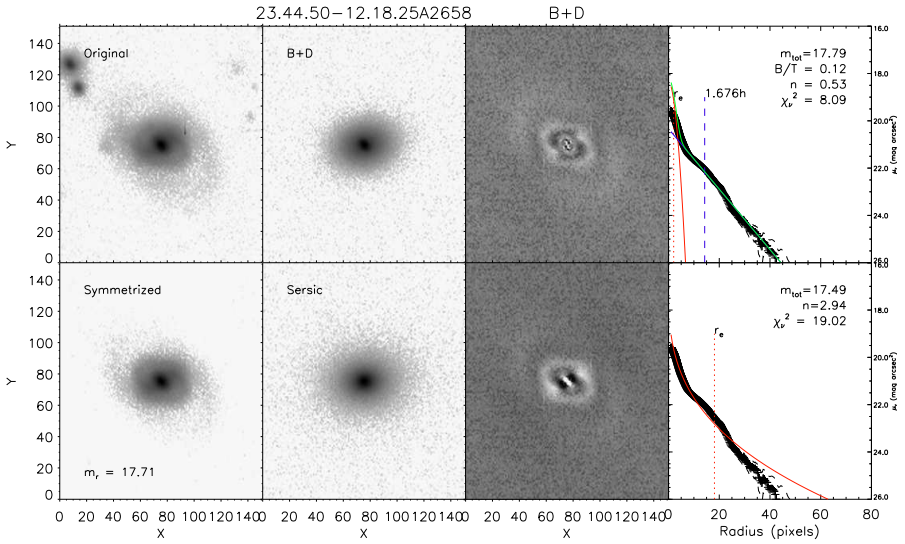
23.44.50−12.18.25A2658
B+D
Original
B+D
Symmetrized
Sersic
m_r = 17.71
m_tot=17.79
B/T = 0.12
n = 0.53
χ_ν² = 8.09
1.676h
r_e
m_tot=17.49
n=2.94
χ_ν² = 19.02
X
Y
Radius (pixels)

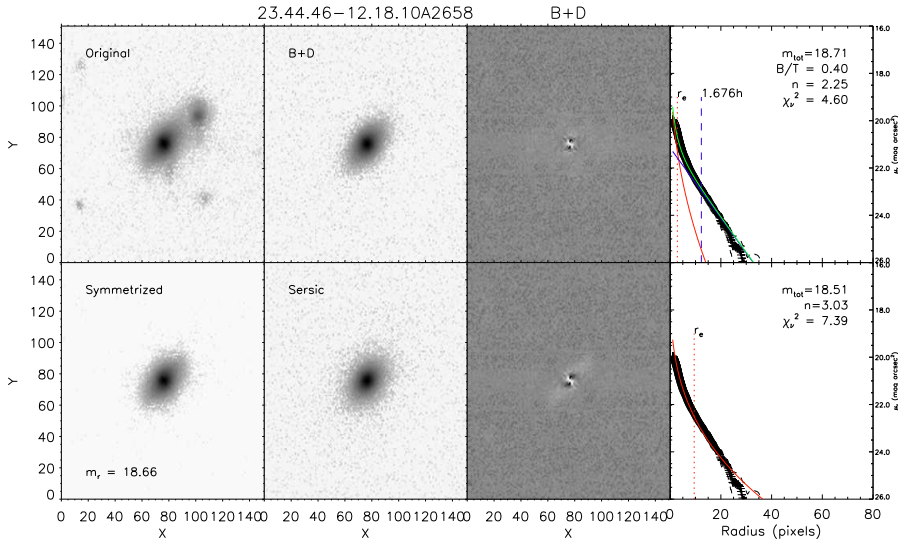
23.44.46−12.18.10A2658
B+D
Original
B+D
Symmetrized
Sersic
m_r = 18.66
m_tot=18.71
B/T = 0.40
n = 2.25
χ_ν² = 4.60
r_e
1.676h
m_tot=18.51
n=3.03
χ_ν² = 7.39
X
Y
Radius (pixels)

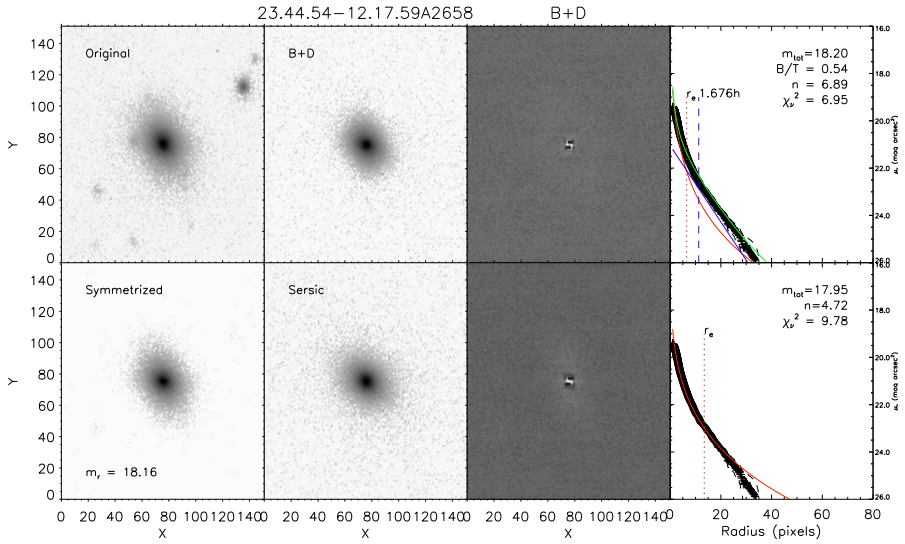
23.44.54−12.17.59A2658
B+D
Original
B+D
Symmetrized
Sersic
m_r = 18.16
m_tot=18.20
B/T = 0.54
n = 6.89
χ_ν² = 6.95
r_e
1.676h
m_tot=17.95
n=4.72
χ_ν² = 9.78
X
Y
Radius (pixels)

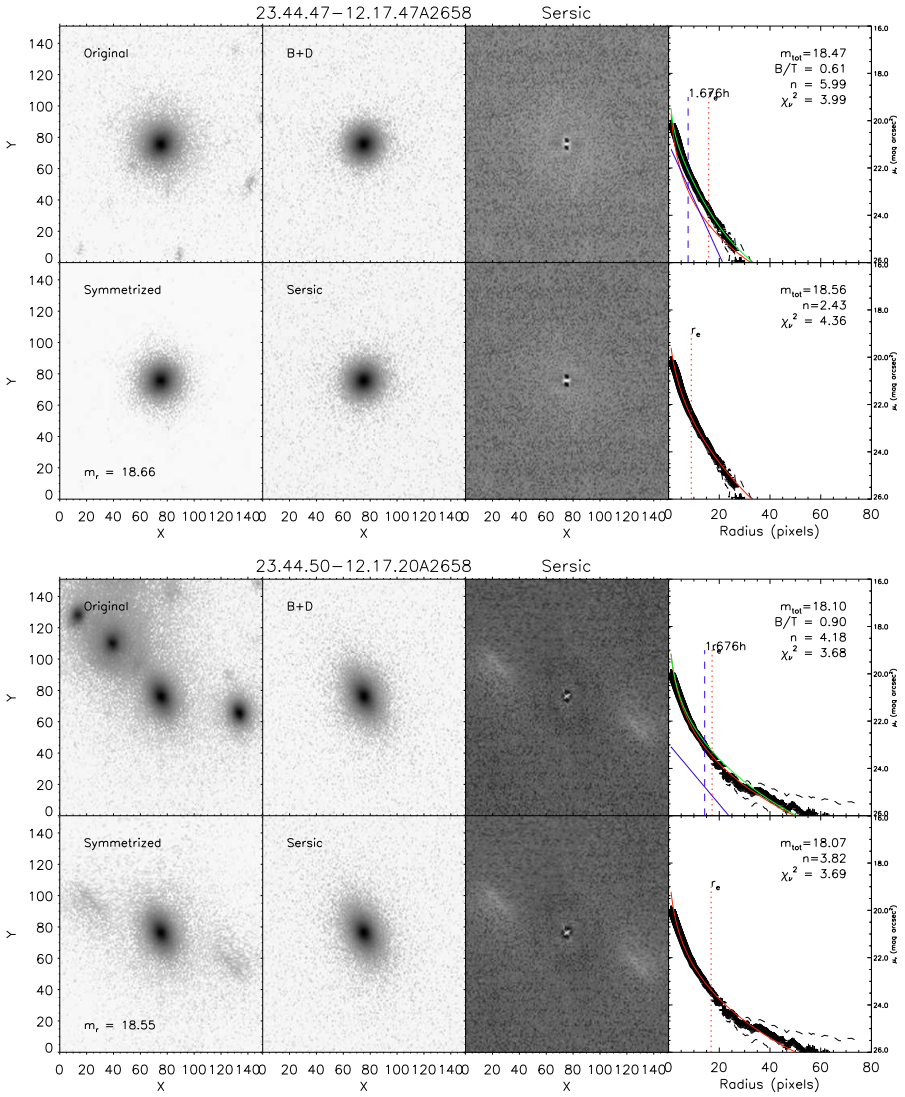
23.44.47−12.17.47A2658
Sersic
Original
B+D
Symmetrized
Sersic
m_r = 18.66
m_tot=18.47
B/T = 0.61
n = 5.99
χ_ν² = 3.99
1.676h
m_tot=18.56
n=2.43
χ_ν² = 4.36
r_e
23.44.50−12.17.20A2658
Sersic
Original
B+D
Symmetrized
Sersic
m_r = 18.55
m_tot=18.10
B/T = 0.90
n = 4.18
χ_ν² = 3.68
1.676h
m_tot=18.07
n=3.82
χ_ν² = 3.69
r_e
X
Y
Radius (pixels)

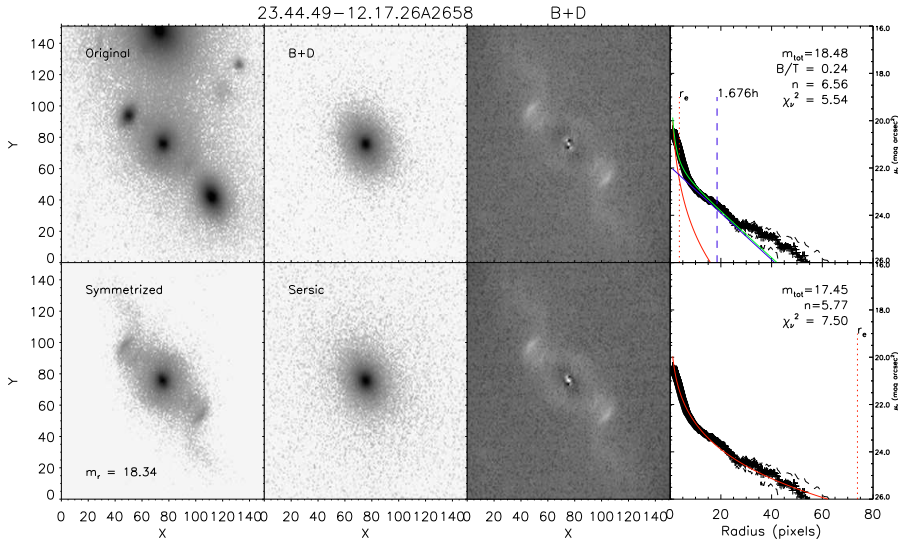
23.44.49−12.17.26A2658
B+D
Original
B+D
Symmetrized
Sersic
m_r = 18.34
m_tot=18.48
B/T = 0.24
n = 6.56
χ_ν² = 5.54
r_e
1.676h
m_tot=17.45
n=5.77
χ_ν² = 7.50
r_e
X
Y
Radius (pixels)

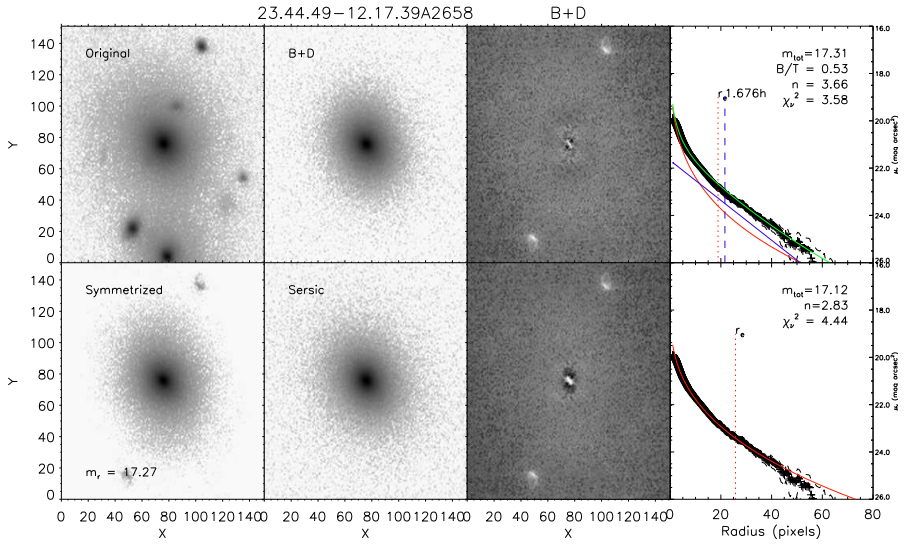
23.44.49−12.17.39A2658
B+D
Original
B+D
Symmetrized
Sersic
m_r = 17.27
m_tot=17.31
B/T = 0.53
n = 3.66
χ_ν² = 3.58
r_e1.676h
m_tot=17.12
n=2.83
χ_ν² = 4.44
r_e
X
Y
Radius (pixels)

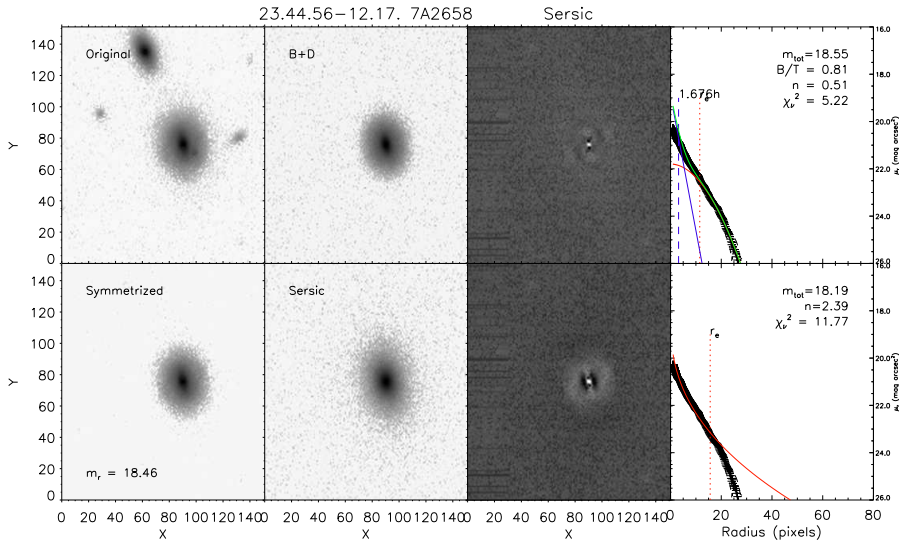

Figure B.1: Upper row: (From left to right). Original Galaxy, Sersic+Exponential model, Sersic+Exponential Residual and 1-Dimensional Profile with the Sersic+Exponential model profile. Bottom row: (From left to right). Original Galaxy, Sersic model, Sersic Residual and 1-Dimensional Profile with the Sersic model profile.

Appendix C

NOT BCGs subtraction

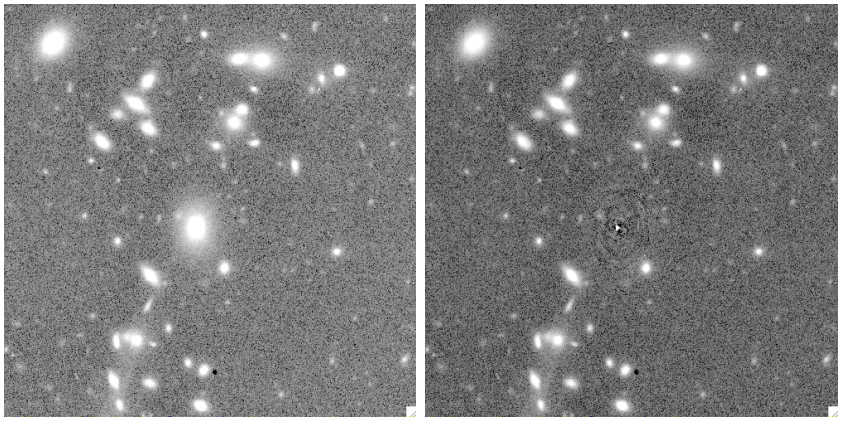

Figure C.1: A1643 BCGs subtraction in Gunn-r filter. Left panel: original BCG. Right panel: BCG subtracted

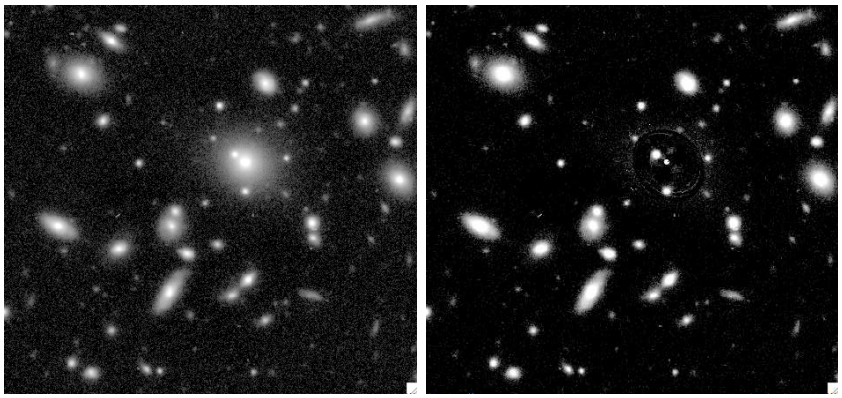

Figure C.2: A1878 BCGs subtraction in Gunn-r filter. Left panel: original BCG. Right panel: BCG subtracted

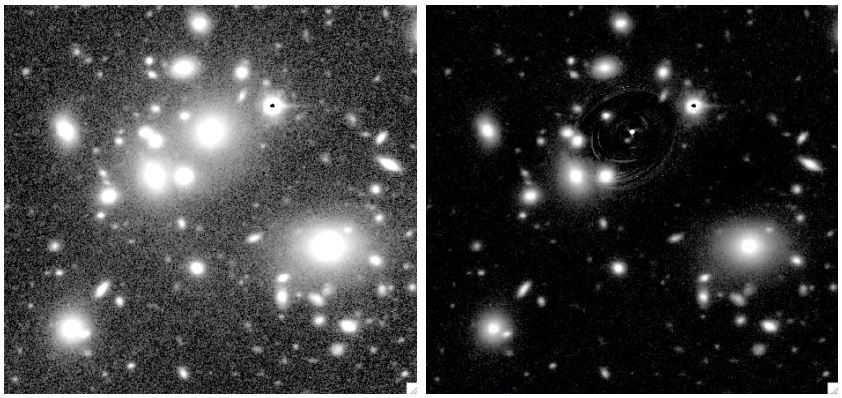

Figure C.3: A1952 BCGs subtraction in Gunn-r filter. Left panel: original BCG. Right panel: BCG subtracted

Figure C.4: A2111 BCGs subtraction in Gunn-r filter. Left panel: original BCG. Right panel: BCG subtracted.

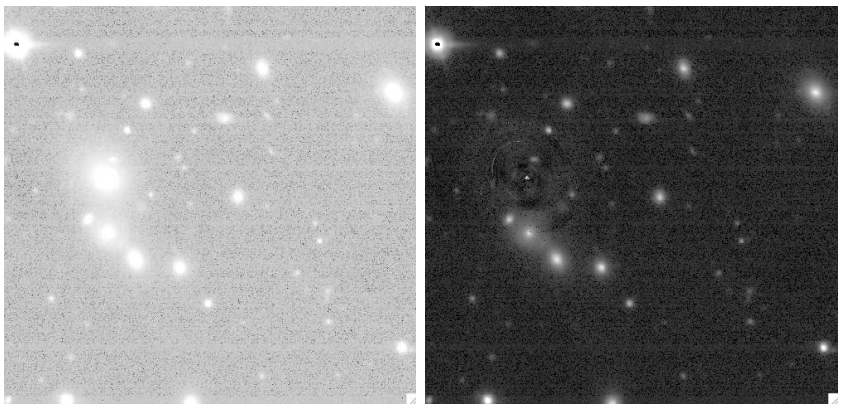

Figure C.5: A2658 BCGs subtraction in Gunn-r filter. Left panel: original BCG. Right panel: BCG subtracted.

Appendix D

ACS BCGs subtraction

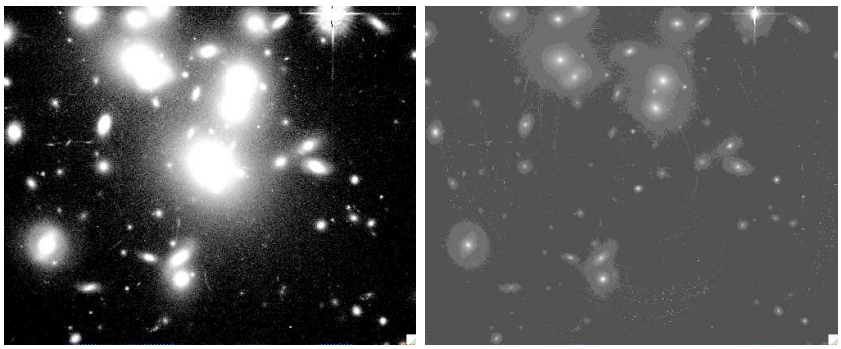

Figure D.1: A1689 BCGs subtraction in Gunn-r filter. Left panel: original BCG. Right panel: BCG subtracted.

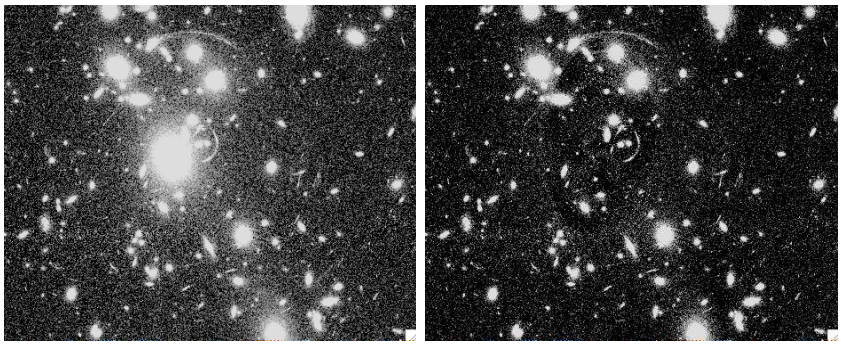

Figure D.2: A1703 BCGs subtraction in Gunn-r filter. Left panel: original BCG. Right panel: BCG subtracted.

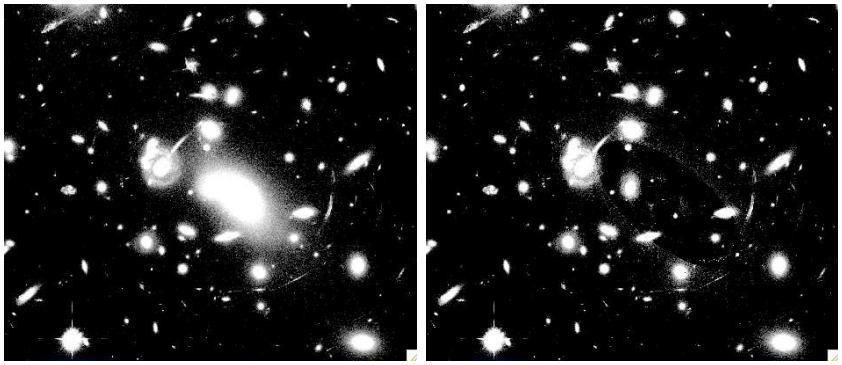

Figure D.3: A2218 BCGs subtraction in Gunn-r filter. Left panel: original BCG. Right panel: BCG subtracted.

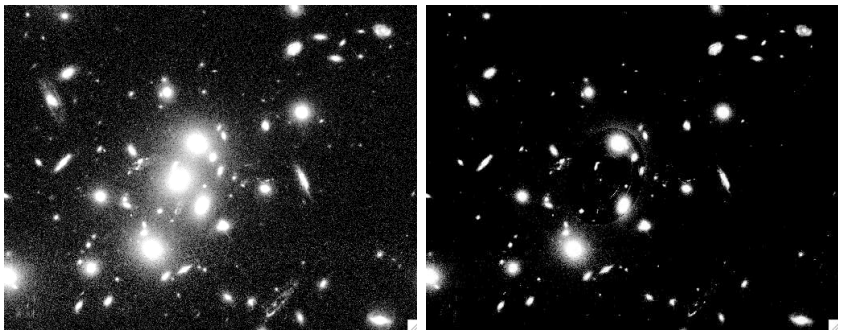

Figure D.4: CL0024 BCGs subtraction in Gunn-r filter. Left panel: original BCG. Right panel: BCG subtracted.

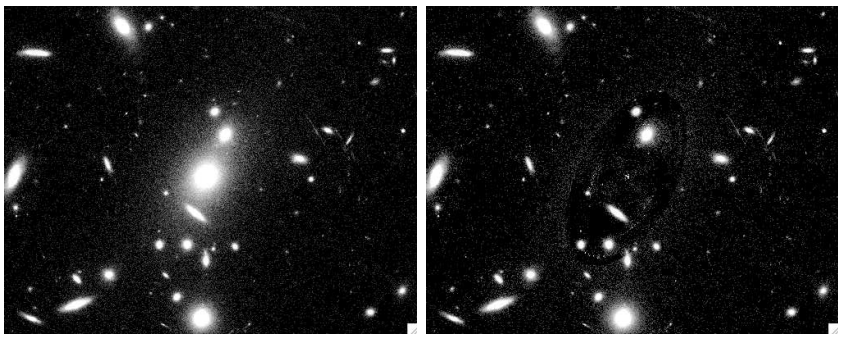

Figure D.5: MS1358 BCGs subtraction in Gunn-r filter. Left panel: original BCG. Right panel: BCG subtracted.